



HAL
open science

Exploring non-collinear spin structures in thin magnetic films with Nitrogen-Vacancy Scanning magnetometry

Isabell Gross

► **To cite this version:**

Isabell Gross. Exploring non-collinear spin structures in thin magnetic films with Nitrogen-Vacancy Scanning magnetometry. Optics [physics.optics]. Université Paris Saclay (COmUE), 2017. English. NNT : 2017SACLN064 . tel-01792316

HAL Id: tel-01792316

<https://theses.hal.science/tel-01792316>

Submitted on 15 May 2018

HAL is a multi-disciplinary open access archive for the deposit and dissemination of scientific research documents, whether they are published or not. The documents may come from teaching and research institutions in France or abroad, or from public or private research centers.

L'archive ouverte pluridisciplinaire **HAL**, est destinée au dépôt et à la diffusion de documents scientifiques de niveau recherche, publiés ou non, émanant des établissements d'enseignement et de recherche français ou étrangers, des laboratoires publics ou privés.

Exploring non-collinear spin structures in thin magnetic films with Nitrogen-Vacancy Scanning magnetometry

Thèse de doctorat de l'Université Paris-Saclay
préparée à l'École normale supérieure de Cachan

École doctorale n°572 Ondes et Matière
Spécialité de doctorat : Nanophysique

Thèse présentée et soutenue à Montpellier, le 5 décembre 2017, par

Isabell Gross

Composition du Jury :

Aléxandra Mougin Directeur de recherche, CNRS (LPS)	Président
Olivier Klein Directeur de recherche, CEA (Spintec)	Rapporteur
Jan Vogel Directeur de recherche, CNRS (Institut Néel)	Rapporteur
Vincent Cross Directeur de recherche, CNRS (UMP, Thales)	Examineur
Toeno Van der Sar Professeur des Universités, Delft University	Invité
Jean-François Roch Professeur des Universités, CNRS (ENS Cachan)	Directeur de thèse
Vincent Jacques Chargé de recherche, CNRS (Laboratoire Charles Coulomb)	Co-Directeur de thèse

to Mr. and Mrs. Kellerer

Acknowledgements

I would like to thank all the people who contributed in some way to the work described in this thesis. First and foremost, I thank my academic advisers. I want to thank my professor and thesis adviser Jean-François who I fortunately came across at a conference in Hong Kong in 2013. Already at that time I felt his enthusiasm for science and the positive ambience of his group. I am very grateful that he accepted me as a PhD student. I owe my deepest gratitude to my supervisor Vincent for the guidance of my Ph.D. research. He offered his continuous advice and encouragement and was a great support for preparing this manuscript. I have high respect for his scientific achievements, for the way he leads his group and for the way he cares for his students.

Every result described in this thesis was accomplished with the help and support of colleagues and collaborators. I am very grateful for the scientific advice and fruitful collaboration provided by Ales and Stan from LPS. I also want to thank our colleagues in Basel who made my multiple stays in their group a great pleasure. I would like to thank the various members of UM de physique CNRS/Thales, IEF and CEA who contributed to the work in this thesis.

I am grateful to my colleagues Luis and Waseem for their advice, for scientific discussions and for the good time we spend together while working in the lab. I wish you all the best for your futures! In addition to these persons, I want to thank all the members of our group in Montpellier. I enjoyed the atmosphere in our team and I had a great time with all of them. I want to express my gratitude to Jean-Philippe who was an outstanding teacher at the early stage of my thesis and my colleague Thomas with his high spirits and enthusiasms. Thank you to all the members of our old group at the ENS Cachan and all the members of the Laboratoire Charles Coulomb.

I am also very thankful to Olivier Klein and Jan Vogel for being my thesis referees, to Vincent Cros, Alexandra Mougin and Toeno van der Saar who have accepted to be members of the thesis jury and all other participants of my thesis defense.

Finally, I want to thank my family for their trust and support, my math and physics teachers and professors for helping to arouse my enthusiasm for physics and all my friends, for all the good times we spent together outside of the lab.

Contents

Introduction	1
1 Principle of scanning nitrogen-vacancy magnetometry	5
1.1 A color center in diamond as a nanoscale magnetic field sensor	6
1.1.1 The negatively charged NV center	6
1.1.2 Optical detected magnetic resonance on a single spin	8
1.1.3 The NV center in a magnetic field	10
1.2 The implementation of scanning NV magnetometry	14
1.2.1 Working principle of the scanning setup	15
1.2.2 Engineering and adjusting the sensor of the magnetometer	17
1.2.3 Characterization of the sensor	22
1.3 Magnetic field imaging modes	28
1.3.1 Demonstration of different sensing schemes on domain walls	28
1.3.2 High precision quantitative magnetic field imaging	30
1.3.3 All optical magnetic sensing of high fields	32
1.4 Conclusion	35
2 Direct measurement of the interfacial DMI in X CoFeB MgO heterostructures	37
2.1 The basic physics of magnetic domain walls in ultra thin films	38
2.1.1 Elements of micromagnetism	39
2.1.2 Magnetic domain walls in thin films with perpendicular anisotropy	42
2.1.3 The Dzyaloshinskii-Moriya Interaction in thin films	46
2.2 Measuring the DMI strength with the NV magnetometer	48
2.2.1 The challenges of a precise DMI measurement	48
2.2.2 Measuring DMI via local magnetic stray fields	48
2.2.3 Measurement precision	53

2.3	Engineering the DMI strength in different heterostructures	54
2.3.1	Bloch domain wall in Ta CoFeB MgO	55
2.3.2	The effect of nitrogen doping and thickness of the Ta underlayer	55
2.3.3	Néel domain walls in W CoFeB MgO	57
2.4	Other methods to measure the DMI and the virtues of NV magnetometry	60
3	The effect of disorder in thin magnetic films on skyrmion morphology	63
3.1	Magnetic skyrmions - History and physical properties	64
3.1.1	Brief history of magnetic skyrmions	64
3.1.2	Physical properties of skyrmions	66
3.2	Characterization of skyrmions in a [Ni Co Ni] bilayer	69
3.2.1	A bilayer magnetic structure designed as host medium for skyrmion	69
3.2.2	Preliminary characterization with MFM and observation of the skyrmion Hall effect	71
3.3	All optical imaging of magnetic skyrmions in bilayer film	73
3.3.1	Skyrmions and their host medium	73
3.3.2	Imaging skyrmions with NV magnetometry	74
3.3.3	Revealing the skyrmion nucleation process	75
3.3.4	The effect of disorder on skyrmion morphology	77
3.4	The future of skyrmionics	81
4	Real-space imaging of non collinear antiferromagnetic order in the multiferroic BFO	84
4.1	The antiferromagnetic multiferroic bismuth ferrite	85
4.1.1	Investigating antiferromagnetics and multiferroics	85
4.1.2	Crystal structure and magnetoelectric coupling	87
4.1.3	Electric and magnetic properties	89
4.2	Measuring and controlling the spin spiral of thin film BFO	93
4.2.1	Sample fabrication and characterization	93
4.2.2	Ferroelectric state revealed by piezoresponse force microscopy	93
4.2.3	First magnetic real space image uncovering the interplay between polarization and magnetization	94
4.3	Controlling the magnetic structure with electric fields	96
4.3.1	Observation of the switching of the spin spiral propagation direction	98
4.3.2	Amplitude of spin density wave revealed by qualitative stray field analysis	98
4.4	Conclusion and outlook	103
	Summary and Conclusion	107
	Appendix	109

A Stray field simulations	109
A.1 Calculating the magnetic field from a magnetization pattern	109
A.2 Simulation of the magnetic field from a random magnetization pattern	109
A.3 The ODMR response of the NV center	111
A.4 Photoluminescence response of the NV center to a static magnetic field	111
B Error calculation	114
B.1 Probe to sample distance	114
B.1.1 Uncertainty in the probe to sample distance	114
B.2 Amplitude of the spin density wave in BFO	115
C Derivation of the analytical formula for the magnetic field produced by the spin spiral in BFO	117
C.1 General Methodology	117
C.2 Magnetization pattern	118
C.3 Analytical description of the magnetic field	119
C.4 Comparison with numerical simulations	121
C.5 Effect of the cycloid chirality.	121
Bibliography	123

Introduction

With billions of interconnected devices worldwide gathering and analyzing around 20 petabytes [1] of data every minute, fast, dense and low-energy consuming storage devices are indispensable. Until now, data storage capacity has been increased by the continuous miniaturization of CMOS (complementary metal-oxide semiconductor) as predicted by Moore in 1965 [2, 3]. By 2017, a transistor size of 10 nm and a density of 100 million/mm² had been announced [4]. After further downscaling feature sizes to a few tens of atoms, the electron behavior will become governed by quantum uncertainty that makes transistors unreliable. In addition, the high device density will increase power dissipation per chip area and thus threatens to render circuits inoperable.

An increasing effort is being invested into alternative technologies to replace CMOS. Non-volatile memories and fast logic gates based on nanometer-sized magnetic elements show great promise. Using the spin degree of freedom should lead to lower power consumption, improved data processing speed and a high integration density. In 1988, the discovery of giant magnetoresistance (GMR) opened the way to efficiently controlling spin-polarized charge flow with the help of magnetic fields. This laid the foundation for sensitive and fast read heads and the magnetic hard disk drive (MHDD). The development of this *spintronic* technology marked an important step toward devices based on the electron spin rather than on charge transport.

Cutting-edge research now brings completely new propositions for spintronic memory and storage devices. These include architectures that rely on the displacement of magnetic domain walls along a ferromagnetic nanowire. In this *domain wall racetrack*, data is encoded as an array of magnetic domains. Spin-polarized current moves the entire pattern of domain walls coherently along the length of the wire and past read and write elements [5]. Such memories are expected to have the performance and reliability of conventional solid-state memory but at the relatively low cost of conventional MHDD storage. Another approach is based on skyrmions. Skyrmions are nanometer-sized whirls of spins and behave as particles that can be moved, created and annihilated, making them suitable for applications in information storage and logic technologies. Recently, they have been stabilized in thin films at room temperature [6, 7]. A skyrmion racetrack memory may utilize these 2D quasi-particles that can move unperturbed and even faster than domain walls along nanotracks [8]. Beyond standard ferromagnetic materials, multiferroics are also considered as new spintronic data storage media [9]. This intriguing class of materials simultaneously exhibits antiferromagnetism and ferroelectric order. These two properties are coupled to each other, allowing the magnetization to be switched with electric fields.

Utilizing this functionality may pave the way to a memory device with electrical writing and non-destructive magnetic reading operations, increasing writing speeds and reducing energy consumption. Moreover, such a device produces less heat and, due to vanishingly small stray fields, does not interact with its environment.

The successful implementation of these propositions relies on a profound microscopic understanding and detailed characterization of the materials. However, the small dimensions of nanoscale magnetic structures - e.g. only a few tens of nanometers in the case of skyrmions - require a sensor with nanoscale spatial resolution. Other systems, like antiferromagnetic multiferroics, have a vanishing net magnetization due to their antiferromagnetic spin arrangement and require nanoscale field sensitivity. In addition, the optimal sensor needs to operate at room temperature and cannot have any magnetic influence on the materials.

We will utilize the outstanding magnetic field sensing capabilities provided by a sensor consisting of a single spin: The negatively-charged nitrogen vacancy (NV) center in diamond. A magnetometer based on a single NV defect was first proposed in 2008 [10, 11, 12, 13] and, until recently, work has been focusing on technical development [14, 15, 16, 17]. In their pioneering work, Tetienne et al. revealed the laser-assisted control of domain wall jumping in a thin-film magnetic material using a NV magnetometer [18] and thereby demonstrated the exceptional potential of this characterization technique in the field of nanomagnetism.

In this thesis, we directly measure the interfacial Dzyaloshinskii-Moriya interaction (DMI) in different thin-film heterostructures with the help of stray-field measurements over domain walls. We find that X|CoFeB|MgO-based materials with an X=W or X=Pt underlayer exhibit high DMI and are therefore a suitable material for efficient domain wall motion or to host magnetic skyrmions. Our results are discussed in light of the engineering of thin-film magnetic heterostructures and DMI measurement methods and can be found in Chapter 2. With the aim of revealing the behavior of magnetic skyrmions, our magnetometer had to be furnished with a new sensing probe. While former experiments have been performed with nanodiamonds attached to a conventional Akiyama atomic force microscope (AFM) probe, we used the all-diamond tips provided by our collaborators at the University of Basel [19] and could increase both the sensitivity and spatial resolution compared to previous work. Our results, described in Chapter 3, provide insights into skyrmion formation and show that: i) in contrast to the disorder-free medium, the skyrmion size and shape strongly vary; and ii) the skyrmion size and distribution depend on the magnetic field history. In Chapter 4, we demonstrate the full capacity of the NV magnetometer by imaging the collinear antiferromagnetic spin order in the multiferroic bismuth ferrite. Here, we resolve the 70-nm spin spiral in real space and show the switching of its propagation direction with electric field.

The insight gained from real-space imaging of the magnetic structure of different material systems helps us to understand fundamental problems in nanomagnetism, in order to tailor materials for specific purposes and, eventually, to engineer new devices for data storage applications. A detailed outline of the thesis is given in the following.

Outline of the manuscript

In **Chapter 1**, the NV center in diamond, the heart of our custom-built magnetometer, is introduced. Crucial to understanding its working principle, the electronic structure and the optical properties of the defect center are elucidated, and the experimental setup is described. After explaining the characteristics of the sensor, calibration methods crucial for the magnetometer are explained. Next, we take a closer look at the scanning probe utilized and distinguish two approaches to realizing an NV sensor: the combination of a nanodiamond hosting a single NV center and an all-diamond scanning probe. The differences, virtues and draw-backs of the two systems are described, and their fields of application are discussed. In a third section, different approaches to magnetic-field sensing are examined. Finally, the operating principle of the magnetometer and the different sensing modes are illustrated on a typical problem of nanomagnetism: magnetic domain walls in an ultrathin ferromagnetic wire with perpendicular magnetic anisotropy.

In the first part of **Chapter 2**, some fundamental terms of micro magnetism are introduced which will be used throughout this thesis. They help us to describe the internal structure of magnetic domain wall in ultrathin films. The DMI at interfaces and the concept of perpendicular magnetic anisotropy in thin-film magnetic heterostructures are described, and the effect on magnetic domains walls is discussed. These are key elements in understanding and modifying the domain wall structure. In this way we can design films, where, instead of *Bloch domain walls*, *Néel walls*, with their favorable dynamic properties, can be obtained. In the following, we present a method developed to determine the domain wall structure from which the strength of the DMI in a material system can be inferred. To do so, we use the NV magnetometer to make an in-depth analysis of the stray field over a domain wall. Evaluating the strength of the DMI in different heterostructures helps us to investigate the origin of this interaction. Such knowledge gives us the possibility to tune the interaction and eventually promotes the determination of promising systems for spintronic logic devices. This is essential to tune magnetic thin films, for example, to host magnetic skyrmions.

In **Chapter 3**, we move from magnetic domain walls to magnetic skyrmions, topologically non-trivial objects with unique properties. Unlike domain walls, whose existence in tracks is related to their boundaries, skyrmions can be freely manipulated in two dimensions and promise faster propagation speeds at low current densities. These characteristics make them exceptional and has led to ideas as the skyrmion racetrack. We introduce a special sample configuration hosting magnetic skyrmions in this chapter. After discussing the sample's properties and confirming the skyrmionic nature of the observed magnetic textures, the all-optical, quenching mode of the NV magnetic microscopy is utilized to investigate the morphology of isolated skyrmions. The skyrmion size and shape are found to be strongly affected by local pinning effects and magnetic field history. Micromagnetic simulations, including a static disorder based on the physical model of grain-to-grain thickness variations, reproduce all experimental observations and reveal the key role of disorder and magnetic history in the stabilization of skyrmions in ultra-thin magnetic films. In the conclusion, we comment on challenges that have to be tackled in order to realize skyrmionic devices.

Finally, in **Chapter 4**, we move to a different material system: the multiferroic bismuth ferrite (BFO). After introducing it in the broader framework of antiferromagnetic and multiferroic materials, its physical properties are discussed. We focus especially on its coexisting ferroelectricity and magnetism, and the interplay between them: it is the magnetoelectric coupling, or, in other words, the possibility to switch magnetization with the help of electric fields, that makes this material outstanding for low-power spintronic devices. Here, we focus on a thin-film BFO sample whose electric structure is revealed with a piezoresponse force microscope and is subsequently investigated with the NV magnetometer with an all-diamond scanning probe. In this way, we demonstrate the first real-space imaging and electric-field control of the cycloidal antiferromagnetic order in a BFO. In addition, we conduct an analysis of the magnetic stray field to get more insight into the material's magnetic structure. The outlook of this chapter considers open questions that can now be tackled in future work with the help of the real-space magnetic image that the NV magnetometer can provide.

Principle of scanning nitrogen-vacancy magnetometry

Contents

1.1	A color center in diamond as a nanoscale magnetic field sensor	6
1.1.1	The negatively charged NV center	6
1.1.2	Optical detected magnetic resonance on a single spin	8
1.1.3	The NV center in a magnetic field	10
1.2	The implementation of scanning NV magnetometry	14
1.2.1	Working principle of the scanning setup	15
1.2.2	Engineering and adjusting the sensor of the magnetometer	17
1.2.3	Characterization of the sensor	22
1.3	Magnetic field imaging modes	28
1.3.1	Demonstration of different sensing schemes on domain walls	28
1.3.2	High precision quantitative magnetic field imaging	30
1.3.3	All optical magnetic sensing of high fields	32
1.4	Conclusion	35

The detection of weak magnetic fields at the nanoscale is crucial for fundamental research, as well as for information storage technology. In order to investigate exotic magnetic structures in condensed matter systems, and to understand and develop new magnetic storage material, a sensitive magnetic field probe is indispensable. However, imaging magnetism at the nanoscale remains a challenging task. One approach consists in mapping the sample magnetization. Examples for experimental approaches are spin polarized STM [20] with a spatial resolution down to the atomic-scale, or transmission X-ray microscopy [21] with a resolution of a few tens of

nanometer. However, these techniques require complex experimental environments, such as ultrahigh vacuum or synchrotron facilities, and a dedicated sample preparation. To observe magnetic samples in their natural, unprepared state, a more practical approach consists in mapping the magnetic stray field generated outside the sample. For this approach, scanning probe-based techniques play a particularly important role. Their spatial resolution is only limited by the probe size and its distance to the sample. A prime example is the magnetic force microscope (MFM), which is routinely used in many laboratories to characterize ferromagnetic structures. It works under ambient conditions, and provides a spatial resolution below 50 nm. However, the non-negligible magnetic back-action on the sample is a major drawback of this method. Recent developments in scanning probe magnetometry have led to the development of functionalised scanning probes. Here, special sensing units are used, such as nanoscale superconducting quantum interface devices (SQUID) [22] or Hall-bars [23]. For further improvement of sensitivity and spatial resolution, a new generation of scanning probe magnetometers which employs a single spin [24, 25] as sensing unit was proposed. In this thesis, such a nanoscale quantum sensor is realized with the single spin of a defect center in diamond: The negatively charged nitrogen-vacancy (NV) center. This atomic-scale defect is brought into close vicinity to a magnetic sample which is scanned underneath. Local magnetic fields are detected by means of the Zeeman shift of the NV center electron spin sub-levels. This technique provides a high spatial resolution, in the order of a few tens of nanometers combined with high magnetic field sensitivity. Importantly, NV magnetometry does not induce any magnetic back action on samples.

In this chapter we explain the working principle of the scanning-NV magnetometer. In Section 1.1 we briefly discuss the NV center's outstanding characteristics, which make it suitable as a nanoscale magnetic sensor. In Section 1.2, we focus on the technical implementation of the NV center as a probe for scanning magnetometry. The experimental setup is explained and different scanning probe configurations are discussed. In the last Section 1.3, different approaches to magnetic field sensing are demonstrated through the study of magnetic domain walls in an ultrathin ferromagnetic wire with perpendicular magnetic anisotropy.

1.1 A color center in diamond as a nanoscale magnetic field sensor

This section aims at establishing the framework for scanning NV magnetometry. First, we introduce the main properties of the NV center in diamond. We start by exploring its diamond host matrix and its crystal structure and explain its optical and electronic properties (§1.1.1). Subsequently, we explain the mechanism of optical detected magnetic resonance (ODMR) and on a single NV electron spin (§1.1.2). In the last section, the behavior of the NV center in an external magnetic field is discussed (§1.1.3).

1.1.1 The negatively charged NV center

Diamond makes most people think of expensive gemstones rather than about a material with exceptional properties as unequalled hardness and thermal conductivity. The diamond lattice consists of covalently bond

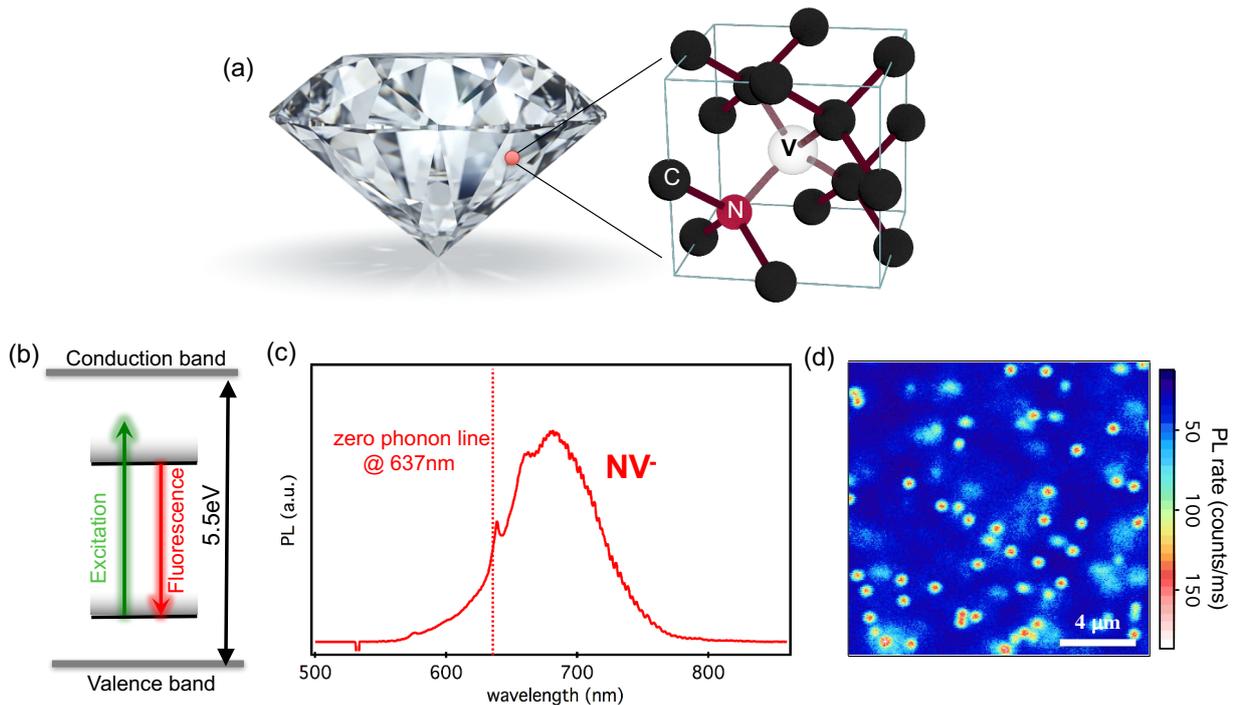


Figure 1.1 – **Crystal structure and optical properties of the NV center.** (a) The defect consists of a nitrogen (N) atom next to a missing carbon atom (V for vacancy). (b) Diamond is a semiconductor with a large band gap (5.5 eV). The discrete energy levels of the NV center are located deep in this gap. The schematic depicts the ground and excited state of the NV color center between which optical transitions can be induced. (c) Emission spectra of the negatively charged NV center. (d) Confocal microscope image recorded on a bulk diamond. The bright emitters correspond to single NV centers.

carbon atoms which form a face-centered (fcc) lattice structure. These covalent bonds make diamond very stiff. The saturated valence electrons lead to a bandgap of $E_g = 5.5$ eV. Due to this large bandgap, diamond is transparent from the ultraviolet to the far infrared spectrum. It is thus an ideal material to host optical active defects with energy levels deeply buried in the bandgap. Among more than 500 different color centers [26], the nitrogen-vacancy defect has attracted considerable attention due to its remarkable photophysical and spin properties. This defect consists of a substitutional nitrogen atom (N) and a vacancy (V) in a neighboring lattice site of the diamond matrix (Figure 1.1).

The NV center predominantly exists in two charge states. The neutral charge state (NV^0) possesses five electrons, which do not contribute to the covalent bonds. Three electrons are provided from the dangling bonds of the surrounding carbon atoms and one electron pair is provided from nitrogen. The negatively charged NV center (NV^-) holds one additional electron which is captured from a donor in the lattice [27, 28]. The NV^- thus has a total of six electrons [29]. The two electronic configurations of the NV centers lead to very different spin properties of NV^0 and NV^- . It is only the NV^- electron spin state that can be read-out optically. Since

this optical read-out is essential for applications such as magnetometry, we will focus on the negatively charged defect, which will be simply denoted as 'NV' center in the following.

The electronic structure of the NV center exhibits discrete energy levels that lie deep in the diamond band gap. The NV center can thus be considered as an artificial atom in the solid state. A simplified electronic structure of the NV center is depicted in Figure 1.1 (b). It consists of two energy levels, which are referred to as ground state and excited state. They are coupled by a dipole transition with a zero phonon line (ZPL) at 1.945 eV corresponding to a wavelength of $\lambda = 637$ nm [30]. This transition is usually excited off-resonance with a green laser at $\lambda = 532$ nm. Ensuing such an illumination, red photoluminescence (PL) is emitted by the NV center. A typical emission spectrum of the NV center under green laser illumination is shown in Figure 1.1 (c). Only a very few photons are emitted into the ZPL. Indeed, due to electron-phonon interaction the vast majority of the photons relax into sidebands which stretch from 637 nm to ~ 750 nm. Even a single NV center exhibits a fluorescence that can be detected with a conventional scanning confocal microscope and a sufficient sensible detector. Figure 1.1 (d) shows a confocal microscope image of a bulk diamond. The bright spots emitting ~ 100 kcounts/s correspond to single NV centers. Under continuous laser excitation, a constant emission rate is recorded from the NV centers. Blinking or bleaching is very rare. This perfect photostability, even at room temperature, is a distinctive characteristic of the NV center and makes it superior to other single emitters as quantum wells or fluorescence molecules [31, 32, 33, 34].

This property makes the NV center a highly robust single photon source [35]. This perfect photostability can also be exploited in biology, where NV defects in nanodiamonds are used as fluorescence markers [36]. Already in 1997 it was also demonstrated that optical detected magnetic resonance experiments on single NV centers are feasible. This paved the way for novel applications based on the NV center electron spin [37].

1.1.2 Optical detected magnetic resonance on a single spin

Among the six localized electrons of the defect, two are unpaired. This leads to spin triplet ($S=1$) and spin singlet ($S=0$) states of the electron spin. The energy level diagram of the NV defect is sketched in Figure 1.2 (a). The ground state is a spin triplet state, whose sub-levels are split by spin-spin interaction [38] into $|m_s = 0\rangle$ and $|m_s = \pm 1\rangle$, which are separated by $D \approx 2.87$ GHz in the absence of a magnetic field. Here, m_s denotes the spin state projection along the quantization axis of the NV center. The quantization direction lies along the axis joining the nitrogen atom and the vacancy and coincides with the [111] direction of the diamond lattice. In the following it will be denoted as $\mathbf{u}_{\text{NV}} = \mathbf{u}_z$ (Figure 1.2 (b)).

As already noted, the NV center can be optically excited from the spin triplet ground state into an excited state. The excited state is also a spin triplet and has a zero field splitting of $D_{\text{ex}} = 1.42$ GHz [39]. The energy structure of the NV center also includes a metastable singlet state ($S=0$) which lies between the excited and ground state [40]. Once optically excited, the NV defect relaxes back into the ground state. This can happen either through the same radiative transition, producing a broadband red photoluminescence, or, through a sec-

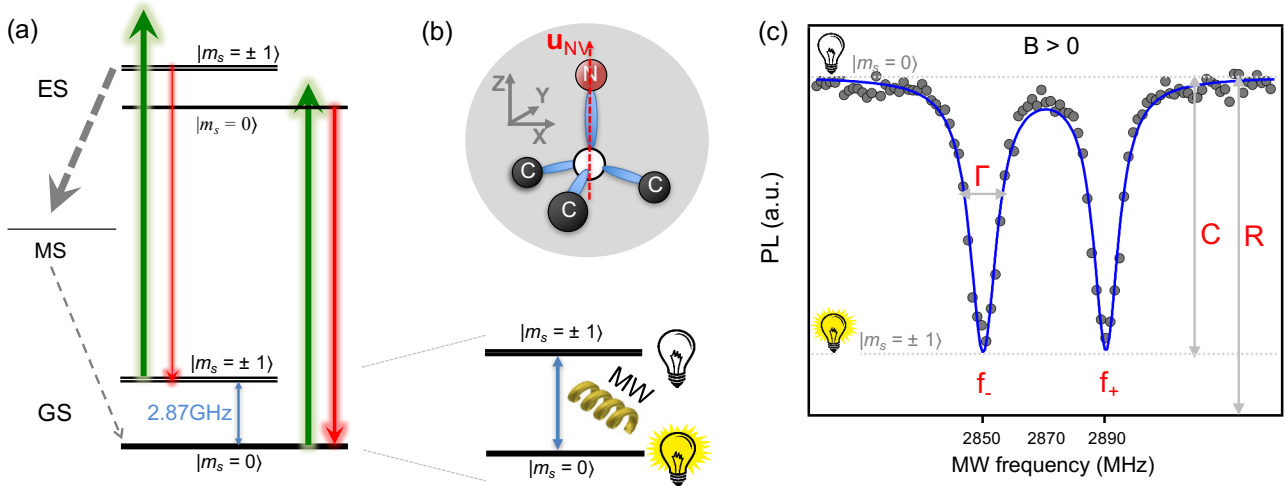


Figure 1.2 – **Energy diagram and principle of ODMR.** (a) The ground (GS) and excited state (ES) of the NV center are spin triplet states. Optical transitions between these states conserve the spin projection m_s along the NV axis. The green arrows in the graphic stand for an excitation at 532 nm and the red arrows depict the emitted photoluminescence from the color center. In addition to these optical transitions, a non-radiative, non-spin-conserving decay path over the meta stable singlet state (MS) is possible. The photoluminescence signal from $|m_s = \pm 1\rangle$ is $\sim 30\%$ weaker than from $|m_s = 0\rangle$. (b) The red arrow depicts the intrinsic quantization axis of the NV defect. It corresponds to the axis joining the nitrogen and the vacancy. (c) A typical ODMR spectrum from a single NV center in an external field, $B_z \approx 1$ mT. The photoluminescence is shown as a function of the applied microwave frequency. The off-resonance count rate R drops at the frequency f_{\pm} when transitions between $|m_s = 0\rangle$ and $|m_s = \pm 1\rangle$ can occur. The contrast C of this signal amounts up to 30%. The linewidth Γ is ultimately limited by the intrinsic parameters of the NV center but in practice depend on excitation power and microwave power [17].

ondary path involving a non radiative intersystem crossing (ISC) to the metastable state [41]. The metastable state plays a crucial role in the NV defect's spin dynamics. While optical transitions are primarily spin conserving ($\Delta m_s = 0$), the non-radiative relaxation through the metastable state does not conserve m_s and depends on its value. As sketched with grey arrows in Figure 1.2 (a), the probability to relax nonradiatively to the metastable state is higher for the $|m_s = \pm 1\rangle$ spin state. For this reason the $|m_s = \pm 1\rangle$ state is often referred to as 'dark' state. From the metastable state, relaxation occurs mainly towards to the $|m_s = 0\rangle$ ground state [29]. In contrary, the $|m_s = 0\rangle$ excited state has a high probability to relax radiatively into the ground state and is spin-conserving ($\Delta m_s = 0$). The $|m_s = 0\rangle$ state is therefore referred to as 'bright' state.

This leads to two important properties of the NV center:

- Under optical illumination, the total population is accumulated in the $|m_s = 0\rangle$ ground state. Thus, **the NV center can be polarized in the $|m_s = 0\rangle$ state, by optical pumping.**
- A NV center in the $|m_s = \pm 1\rangle$ state has a lower probability per excitation cycle for fluorescence than one in the $|m_s = 0\rangle$ state. Thus, **the NV center has a spin dependent fluorescence.**

The possibility to optically polarize and read out the NV center's electron spin, combined with the high stability of its photoluminescence, enables optical detected magnetic resonance (ODMR) experiments on a single NV center [37]. To perform ODMR, the NV defect is initially prepared in the $|m_s = 0\rangle$ state with a green laser. By applying a microwave field, it can then be driven to the $|m_s = \pm 1\rangle$ spin state. The increase in the population of this sublevel leads to a higher non-radiative decay rate and consequently to a reduction in the fluorescence rate R . To record an ODMR spectrum, the microwave frequency is swept while monitoring the NV center's fluorescence. A drop in photoluminescence will occur as soon as the oscillating magnetic field matches the electron spin resonance (ESR) frequencies (f_{\pm}). The contrast C , of this signal, can reach values up to 30% [11] and the linewidth Γ is in the order of several MHz.

External magnetic fields are detected by measuring the Zeeman shifts of the NV defect's electron spin sublevels $|m_s = 1\rangle$ and $|m_s = -1\rangle$. When an external magnetic field is present in the vicinity of the NV defect, the degeneracy of $|m_s = \pm 1\rangle$ spin sublevels is lifted (Figure 1.3 (b)). This leads to the appearance of two resonance lines in the ODMR spectrum as shown in Figure 1.2 (c). The exact response of the NV center to external magnetic fields will be detailed in the next section.

1.1.3 The NV center in a magnetic field

For magnetic sensing applications, it is important to understand the behavior of the NV center in an externally applied magnetic field. Under the influence of an external field the degeneracy of the electron spin sublevels, $|m_s = \pm 1\rangle$, is lifted due to the Zeeman effect. In order to determine the exact relationship between the ESR frequencies and the magnetic field amplitude, the ground state spin Hamiltonian of the NV defect is examined more closely. The goal is to precisely describe the spin resonance frequency f_{\pm} as a function of the external magnetic field B .

Neglecting the hyperfine interaction with nearby nuclear spins and the nuclear Zeeman terms, the ground state spin Hamiltonian in a magnetic field reads [42]

$$H = hD\hat{S}_Z^2 + hE(\hat{S}_X^2 + \hat{S}_Y^2) + g\mu_B\mathbf{B} \cdot \mathbf{S}, \quad (1.1)$$

where μ_B is the Bohr magneton, $g \sim 2$ the electron gyromagnetic ratio. $\hat{S}_X, \hat{S}_Y, \hat{S}_Z$, are the Pauli matrices, h is the Plank constant, Z is the NV defect quantization axis as shown in Figure 1.2 (b), D and E are the zero-field splitting parameters. The axial zero field splitting parameter D results from spin-spin interactions between the two unpaired electrons of the defect. It amounts to $D \approx 2.87$ GHz and corresponds to the energy difference between the $|m_s = 0\rangle$ and $|m_s = \pm 1\rangle$ state in zero field. E is the transverse zero-field splitting parameter caused by local strain. It is strongly influenced by the properties of the host matrix and can reach values between 100 kHz and 10 MHz.

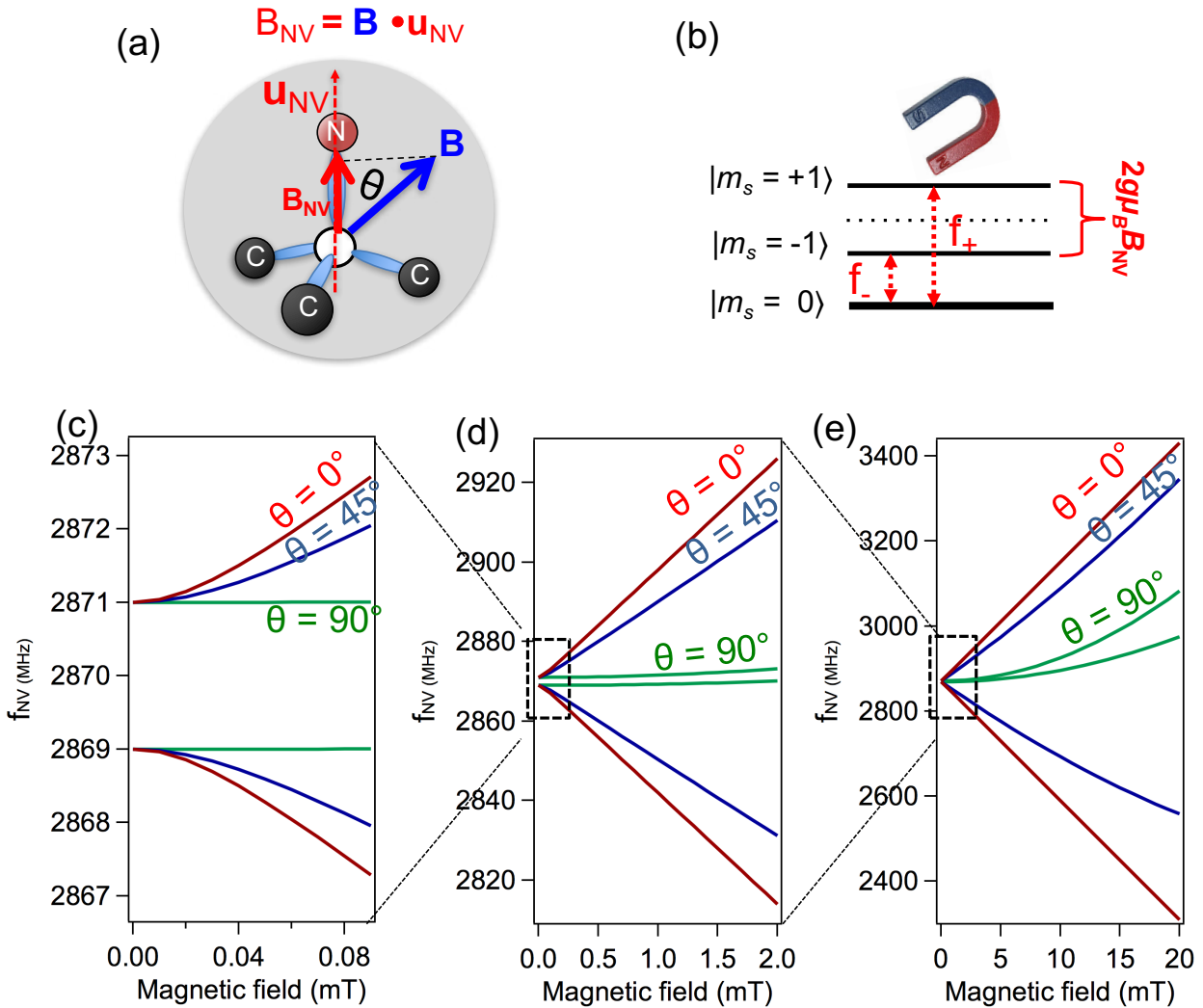


Figure 1.3 – **Energy level splitting in different magnetic field regimes.** (a) Schematic of the structure of the NV center. θ describes the angle between the external field B and the NV axis \mathbf{u}_{NV} . The red arrow represents the magnetic field and the blue arrow the projection of the field on the NV axis B_{NV} . (b) Splitting of the energy levels in a magnetic field. The red arrows stand for the two ESR frequencies f_{\pm} . (c-e) show the ESR frequencies f_{\pm} as a function of the magnetic field amplitude for different angles θ . The solid lines are obtained by diagonalizing the full Hamiltonian described by Equation 1.1.3, with $D = 2.87$ GHz and $E = 2$ MHz. (c) The graph on the left describes the very low field regime where the influence of the E parameter is important. (d) The second graph shows the weak magnetic field regime where the dependence of f_{\pm} are linear with the external field. (e) The last image leads up to high fields where the effect of off-axis magnetic fields leads to a non-symmetric behavior of the ESR splitting.

The Hamiltonian described by Equation 1.1.3 can be split into a parallel H_{\parallel} and a perpendicular H_{\perp} component with respect to the NV quantization axis:

$$H = \underbrace{hD\hat{S}_Z^2 - g\mu_B B_{NV}\hat{S}_Z + hE(\hat{S}_X^2 - \hat{S}_Y^2)}_{H_{\parallel}} + \underbrace{g\mu_B(B_X\hat{S}_X + B_Y\hat{S}_Y)}_{H_{\perp}} \quad (1.2)$$

The notation $B_Z = B_{NV}$ corresponds to the magnetic field projection along the NV center axis. By diagonalizing the Hamiltonian, the two ESR frequencies f_{\pm} can be calculated for any magnetic field B . For a linear polarized microwave source the two transitions cannot be distinguished and are denoted as f_+ for the higher transition frequency and f_- for the lower transition frequency. They are plotted in Figure 1.3 (c-d) as a function of the magnetic field amplitude. Different field ranges and angles θ (between field and NV axis) are shown.

In the next paragraph we will discriminate between two important field regimes.

Weak magnetic fields: $H_{\perp} \ll H_{\parallel}$

First, we examine the weak magnetic field regime, where $H_{\perp} \ll H_{\parallel}$. In this limit, the diagonal terms of the Hamiltonian dominate and the position of the ESR frequencies is determined by considering the projection of the external field on the NV axis only. The transition frequencies are then given by

$$f_{\pm}(B_{NV}) = D \pm \sqrt{\left(\frac{g\mu_B}{h}B_{NV}\right)^2 + E^2}. \quad (1.3)$$

This formula may be used when the transverse component of the external field $B_{\perp} = \sqrt{B_X^2 + B_Y^2}$ is such that $B_{\perp} \ll \frac{Dh}{g\mu_B}$. In practice, Equation 1.1.3 is a good approximation for field amplitudes smaller than 5 mT. In this regime the ESR frequencies evolve linearly as long as $B_{NV} \gg \frac{Eh}{g\mu_B}$. This is shown in Figure 1.3 (d), where the spectral position of f_- and f_+ are plotted as a function of the external magnetic field amplitude.

However, in the case of very weak fields, the intrinsic parameter E starts to play an important role. When $B_{NV} \sim \frac{Eh}{g\mu_B}$ the ESR frequencies evolve quadratically (Figure 1.3 (c) on the right). In the extreme case of $B_{NV} \ll \frac{Eh}{g\mu_B}$ they are independent of the external field,

$$f_{\pm} \approx D \pm E \quad (1.4)$$

As we can see, from formula 1.4, a measurement in zero external field allows to extract the D and E parameter of the NV center. An ODMR measurement at zero field is shown in Figure 1.4. The graph shows the behavior for fields smaller than 0.01 mT, in the case of $E = 2$ MHz. Due to the high strain in nanodiamonds, a large E parameter of 5 MHz and more is common. In high-purity, monocrystalline diamond, E is expected to be in the range of 100 kHz. A host diamond with high strain thus renders the NV center insensitive to small fields. However, this limitation can be avoided by either choosing NV center with a small E parameter, or by applying a bias field $B_{\text{bias}} \gg hE/g\mu_B$. In this way, the strain-induced splitting is compensated and a linear dependence

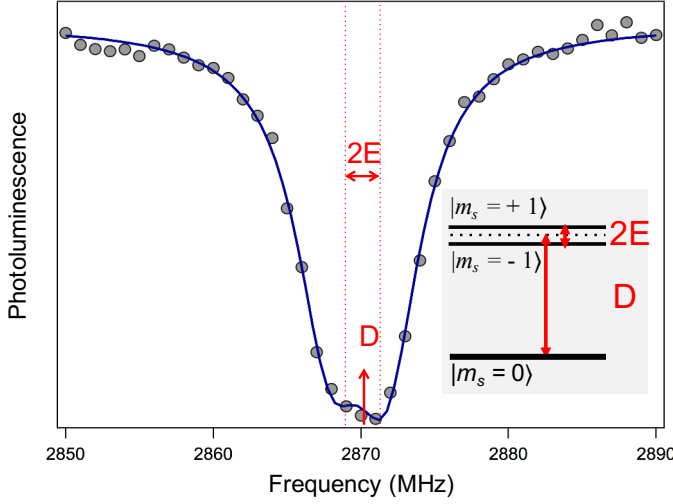


Figure 1.4 – **Determining the zero-field splitting parameters.** The graph shows an ODMR spectrum of a single NV center in zero field. In the case of this NV center, strain causes a ~ 3 MHz splitting of the ODMR lines. This splitting is described by the E parameter. The parameter D describes the zero field transition frequency between the spin sublevels without external field or strain. The inset depicts the energy levels of the ground state in zero field. Here D and E are visualized with red arrows.

of the ESR frequencies with magnetic field is reached

$$f_{\pm} = D \pm g\mu_B B_{NV}/h. \quad (1.5)$$

This is the ideal regime for NV magnetometry. A quantitative measurement of the field is achieved by tracking the spectral position of one ESR line.

Strong magnetic fields: $B_{\perp} \sim \frac{Dh}{g\mu_B}$

In strong fields, when the condition $H_{\perp} \ll H_{\parallel}$ is no longer fulfilled, m_s is not a good quantum number anymore. The external field induces mixing of the electron spin states and imposes the quantization axis on the NV center. This is the case starting from $B_{\perp} \gtrsim 5$ mT. Here, the ESR frequencies no longer evolve symmetrically with respect to D (Figure 1.3 (e)). Also, the dependence $f_{\pm}(B)$ is more complex than under weak fields. In this regime, it is not sufficient to measure only one ESR frequency to determine B_{NV} . Furthermore, the frequencies highly depend on the angle θ of the NV axis with respect to the external field. The relationship between field amplitude and ESR frequency ($E \ll D$) now reads as follows [11]:

$$\mathbf{B}^2 = \frac{1}{3}(f_+^2 + f_-^2 - f_+f_- - D^2 - 3E^2) \quad (1.6)$$

$$\cos(2\theta) = \frac{7D^3 + 2(f_+ + f_-)(2(f_+^2 + f_-^2) - 5f_+f_- - 9E^2) - 3D(f_+^2 + f_-^2 - f_+f_- + 9E^2)}{9D(f_+^2 + f_-^2 - f_+f_- - D^2 - 3E^2)} \quad (1.7)$$

Consequently, it is still possible to extract (B, θ) by recording the full ESR spectrum [43].

The spin state mixing also leads to strong modifications of the NV defect spin dynamics under optical illumination. In particular, the optically-induced spin polarization and spin-dependent photoluminescence of the NV defect become inefficient and the contrast of optically detected ESR vanishes when a large transverse field

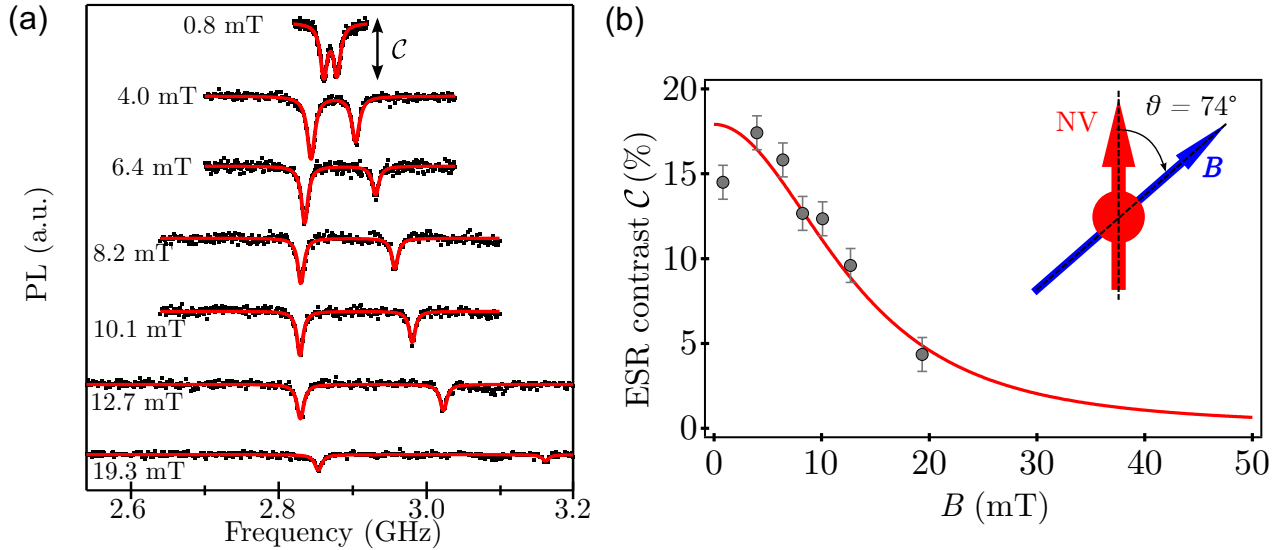


Figure 1.5 – **ODMR in the high field regime.** (a) ODMR spectra of a single NV center in bulk for different magnetic fields with lorentzian fit. The magnetic field is applied with an angle of $\theta = 74^\circ$ with respect to the NV center. The different spectra become asymmetric around D and the contrast diminishes with higher field. (b) ODMR contrast as function of magnetic field amplitude. The contrast reduces drastically in high fields and makes data acquisition time consuming or even impossible.

is applied to the NV defect. Figure 1.5 (a) shows typical ODMR spectra recorded for fields up to ~ 20 mT, with $\theta = 74^\circ$. The contrast is drastically decreased at high fields. In Figure 1.5 (b), this vanishing contrast is plotted against the magnetic field for $\theta = 74^\circ$. In this regime, magnetic field imaging through the optical detection electron spin transition frequencies implies excessively long data acquisition times. Practically, the application of quantitative field imaging is not applicable for $B_\perp \gg 10$ mT. This is an important limitation of NV magnetometry. However, we will see in Section 1.3.3 how the changes in the fluorescence properties of the NV center can be utilized as an indicator for strong fields, while operating the NV magnetometer in the fluorescence quenching mode.

In the next section we will show how the NV defect can be integrated in a scanning geometry.

1.2 The implementation of scanning NV magnetometry

To use the NV center as magnetometer in a scanning geometry, a single NV defect is integrated onto the tip of an atomic force microscope (AFM). A confocal microscope and a microwave antenna are combined with the AFM to record the spin-dependent photoluminescence of the NV defect. Figure 1.6 shows a schematic of the NV scanning setup as realized in our lab. The aim of the following sections is to describe the principle of this experiment in detail. We will start by presenting the basic setup, composed of the AFM and a confocal microscope (§1.2.1). Two different approaches for realizing the sensor of the magnetometer are described (§1.2.2)

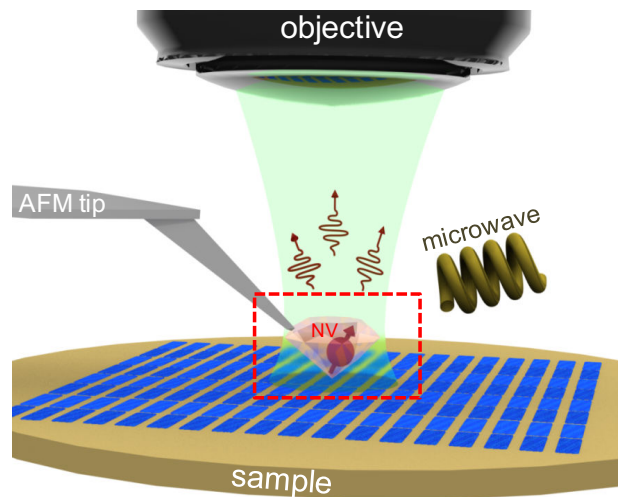


Figure 1.6 – **The scanning magnetometer setup.** (a) Schematic image of the principle piece of the set up: A scanning tip hosting the NV center, the objective through which a green laser is focused on the NV and its photoluminescence is collected. A microwave antenna to excite the NV center and underneath a magnetic sample.

and compared (§1.4). Lastly, we will show how these magnetic sensors are characterized with respect to their magnetic field sensitivity and spatial resolution (§1.2.3).

1.2.1 Working principle of the scanning setup

A photo of the setup, as mounted in the laboratory, is shown in Figure 1.7 (a). The installation of the system was the work of two former PhD students in our group, Loïc Rodin and Jean-Philippe Tetienne [15, 16]. In vicinity to a magnetic sample, the NV center feels the emanating magnetic stray fields. This causes a shift of the associated electron spin resonances (see Figure 1.7(b)), which are read out via ODMR. With the help of nano-positioning instrumentation the NV is scanned while mapping the stray field at each position over the sample. Engineering the NV center in the apex of a scanning tip can be achieved through two different approaches: A nanodiamond attached to an AFM tip and a full-diamond scanning probe (discussed in detail in Section 1.2.2).

As mentioned above, signals coming from the NV center are detected optically. The detection configuration is a home-built confocal microscope as shown in Figure 1.8 (a). A green laser at 532 nm is focused on the NV center with a high numerical aperture (NA: 0.9) objective. Its working distance of 1 mm is large enough to include an AFM tip between the sample and the objective. The NV center’s photoluminescence response is collected through the same objective and separated from the excitation path with a dichroic mirror. A confocal microscope configuration with a pinhole of 50 μm diameter is used to isolate the signal from single defects with a high signal to noise ratio. The collected light is filtered and finally recorded using an avalanche photo diode (APD) working in the single photon counting regime. A stirring mirror is implemented in the setup to scan the laser over a sample surface and retrieve an image of the optical response of the sample. A typical example

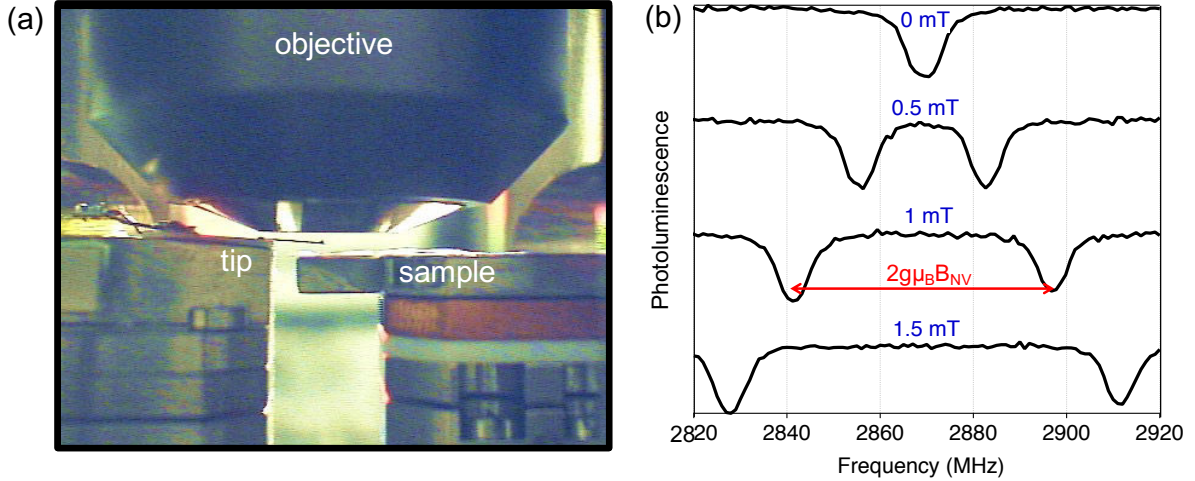


Figure 1.7 – **The scanning magnetometer setup.** (a) A photo of the setup as installed in the laboratory. On top, the objective with the scanning probe (tower on the right) and underneath the sample (tower on the left). (b) ODMR spectra of a single NV center for different magnetic fields B_{NV} along the NV axis, in the weak field regime. In this regime, the external magnetic field is directly proportional to the spacing between the two ODMR lines and can be determined with the relation: $B_{NV} = \Delta f_{NV} / (2g\mu_B)$.

of a photoluminescence scan from nanodiamonds deposited on a quartz plate is shown in Figure 1.8 (b). It is furthermore possible, to record simultaneously the topography of a sample with the AFM (Figure 1.8 (c) and (b))

The tuning-fork based AFM setup (attoAFM/CFM, Attocube Systems) consists of two independent towers. One for the sample and the other one for the scanning tip. Both towers consist of a 3-axis micrometer positioner ($3 \times 3 \times 2.5 \text{ mm}$) and a 3-axis piezoelectric scanner, allowing to scan areas up to $30 \times 30 \mu\text{m}^2$. In this configuration, the sample, as well as the AFM tip, can be positioned independently relative to the laser focus. For magnetometry experiments, the tip tower stays fixed. In this way, the laser can be focused on the tip hosting the NV center, while the sample is scanned underneath. The central element of the AFM is the scanning tip, which contains the magnetic sensor. At the same time, it is used in a conventional way to scan the topography of a sample. We use AFM tips of the brand Akiyama, made of doped silicon provided from NANOSENSORS [44]. The signal from the AFM cantilever is detected electrically to prevent any intervention with the optical NV detection scheme. It is thus possible to follow the topography of a surface while detecting fluorescence from a sample, using the confocal microscope.

In summary our system is a combination of AFM and confocal microscope and capable of detecting photoluminescence signal and topography at the same instance. This magnetometer detects magnetic fields through ODMR on its probe spin. It works under ambient conditions and is non-invasive. In the next section we take a closer look at how to functionalize the AFM tip with a single NV center.

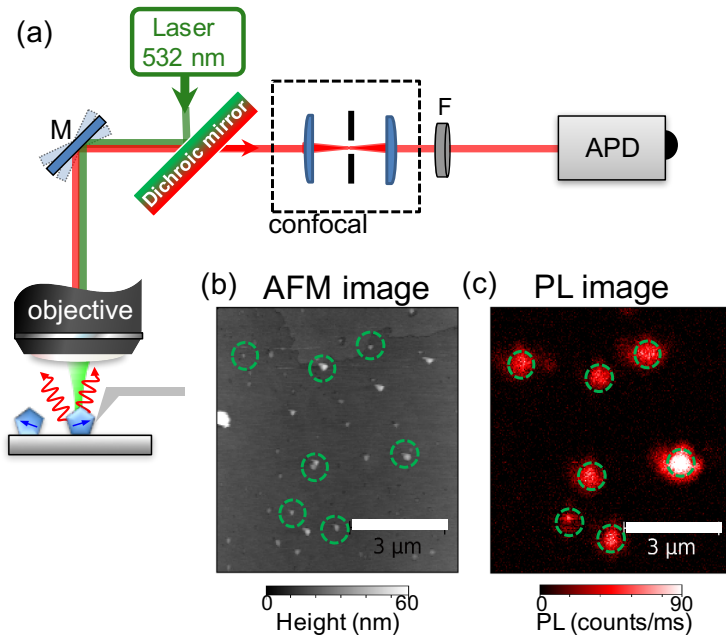


Figure 1.8 – **Optical setup.** (a) Schematic of the confocal setup, used for exciting the NV center and collecting its photoluminescence. A laser with a wavelength of 532 nm is focused on the NV center through an air objective. The red photoluminescence emitted by the NV center is collected through the same objective and then separated from the excitation path by a dichroic mirror. The light on the detection path is led through a pinhole to achieve a sufficient optical spatial filtering. After a spectral filter the photons are sent to an avalanche photo diode (APD) used as photon counters. AFM image (b) and confocal image (c) of a glass slide that has been spin coated with nanodiamonds. The laser beam was aligned with the AFM tip and the sample was scanned underneath. In this way topography and fluorescence images are obtained simultaneously.

1.2.2 Engineering and adjusting the sensor of the magnetometer

A crucial point for implementing scanning magnetometry with the NV center consists in functionalizing the scanning tip. For this purpose, the defect's properties, especially its density and position, have to be adjusted, with the goal of having a single NV center scanning close to the sample surface. One approach is the utilization of a nanodiamond containing a single NV center which is attached to the apex of an AFM scanning tip. Another approach consists in using all-diamond AFM scanning-probes in which a single NV defect is created through ion implantation. In the framework of this thesis, we will use these two approaches.

Nanodiamonds A very intuitive way to functionalize the AFM tip, is to attach a nanodiamond hosting a single NV center to its apex. In a first step, compatible nanodiamonds have to be fabricated. The realization of nanodiamonds with single NV centers was the object of a study of several years, realized in the group of Jean-François Roch in Paris and detailed in this reference [15]. The process can be summarized as follows: A commercial, highly nitrogen doped nanodiamond powder, is electron irradiated, so that vacancies are formed. Annealing at 800°C favors the formation of NV defects through the migration of vacancies. The resulting powder is freed from surface graphite layers with acid cleaning, as to facilitate the stabilization of the NV defect in the negatively charged state [45]. In this way, mono-disperse nanodiamonds, containing in average one NV center, can be formed. The diameter of the utilized nanodiamonds accounts to a few tens of nanometers.

To functionalize the AFM tip, the nanodiamonds have to be dispersed in a solution which is subsequently spin coated on a quartz cover slip. The dilution and spin coating procedure were optimized, in order to find

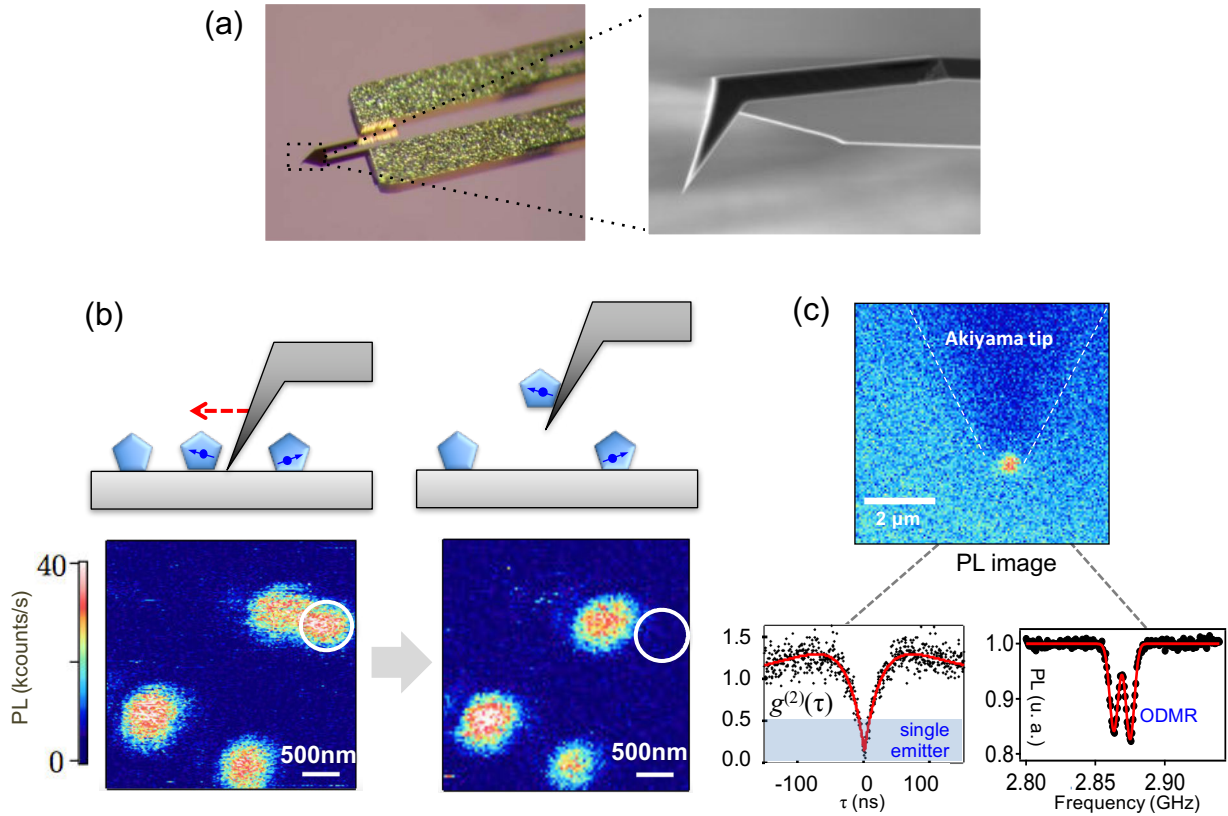


Figure 1.9 – **Functionalization of Akiyama AFM scanning probes.** (a) Microscope image of the cantilever of the Akiyama AFM scanning probe and electronic microscope image of its tip (Images from the site of the producer [44]). (b) In order to attach a chosen nanodiamond, the AFM tip is positioned close to it. The tip is brought in contact with the sample and scanned over the nanocrystal until it is attached. Underneath, the photoluminescence image of an area with several nanodiamonds are shown. In the first image, four are visible. After the attachment, one nanodiamond has vanished from the photoluminescence image. It has been attached to the Akiyama tip. This is confirmed in (c), which shows a photoluminescence image of the end of the Akiyama scanning probe. A bright emitter residues at its tip. The $g^{(2)}(\tau)$ and ODMR measurement confirm that the emitter on the tip is a single NV defect.

isolated nanodiamonds with a reasonable density on the quartz surface. Such a sample is then placed under the confocal microscope and the NV centers in the nanodiamonds are rendered visible via photoluminescence imaging. We use the tools of quantum optics to ensure the unicity of the NV center in the nanocrystal. A Hanbury Brown and Twiss (HBT) experiment is performed to show the effect of photon antibunching in the correlation function ($g^{(2)}(\tau)$) of the photoluminescence intensity. A drop of the $g^{(2)}(\tau)$ function at zero delay τ is the signature of single photon emission from a single emitter ($g^{(2)}(0) < 1/2$, Figure 1.9 (c)). Once, the single atom nature of the defect is tested, an ODMR measurement is conducted in order to characterize spin properties. Having identified different nanodiamonds with single NV center, one with satisfactory characteristics is chosen.

In order to attach it, the pre-characterized nanodiamond is placed into the optical focus of the microscope and is identified with the AFM by scanning over it. In addition to the standard AFM topography image the optical signal is also recorded. Consequently, scanning the tip results not only in an AFM topography image but also in an optical image of the focused area. If the density of nanodiamonds on the substrate is sufficiently low, a single diamond nanoparticle can be identified unambiguously in the laser focus. For the attachment procedure, the AFM tip is positioned above the nanodiamond. Then, the tip is scanned over it and pressed on the center of the particle in contact mode. Simultaneously the fluorescence is observed [46]. This procedure is sketched in Figure 1.9 (b). If the attachment procedure was successful, the trapping of the nanodiamond manifests itself as a sudden persistent increase in the optical signal while scanning and then drops back to background level after the tip is retracted. A photoluminescence image of the tip then reveals a bright emitter at its end. This corresponds to the attached nanodiamond (Figure 1.9 (c)). Once more, we confirm the unicity of the NV center with a HBT measurement. Also an ODMR spectrum is recorded to determine the NV center's intrinsic properties. For nanodiamonds with dimensions smaller than 20 nm, it can be beneficial to immerse the AFM tip in poly-L-lysine before the attachment process since the cationic polymer facilitates the attachment of the negatively-charged surface of the nanodiamond. Before using a readily functionalized tip as magnetometer it needs to be characterized to determine spatial and magnetic field resolution and hence its possible scope of application. Their precise characterization will be discussed in 1.2.3.

Diamond scanning probes While first experiments aimed at implementing scanning-NV microscopes by grafting diamond nanocrystals on AFM tips [11, 47], a recent approach is to use the full potential of a bulk-NV in the scanning geometry [48]. To this end monolithic diamond nanopillars hosting individual NV center have been developed as scanning probes. We utilized all-diamond scanning probes fabricated by Patrick Maletinsky's group at the university of Basel [19]. In the framework of this thesis, multiple stays in Basel allowed me to learn about the fabrication procedure, to precharacterize and to mount all-diamond scanning probes compatible with our setup requirements. In the following, the fabrication of the single-crystalline probes is outlined, starting from the nanofabrication performed by our collaborators in Basel. Subsequently, the mounting procedure and integration of the devices in our AFM setup is described.

In a first step, commercially available high purity 500 μm thick diamond plates (Element six [N] < 5 ppb, B < 1 ppb, (001) oriented) are thinned down to $\sim 50 \mu\text{m}$ thick plates by laser cutting and polishing. The plates are then cleaned successively by boiling acid and solvents. Since mechanical polishing of diamond can lead to crystal damages in the top layers, a few micrometers of the surface is removed by inductively coupled reactive ion etching. In the next step, NV centers are artificially created by ion implantation (Figure 1.10 (a)). Nitrogen ions are implanted with an energy of 6 keV and a dose of $3 \times 10^{11} \text{ cm}^{-2}$. This should result in a stopping depth of the nitrogen atoms of $\sim 9 \pm 4 \text{ nm}$ from the diamond surface (Estimation with the SRIM software [49]). The diamond plate is annealed to convert defects and nitrogen to NV centers. Then, the diamond plate is thinned to a several micron thick membrane which is suspended in the surrounding 50 μm thick diamond (Figure 1.10 (b)).

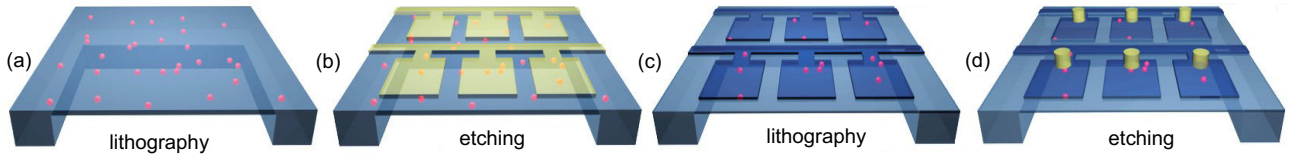


Figure 1.10 – **Fabrication process of diamond scanning probes.** (a) In a first step the membrane is implanted with shallow NV centers (red). (b) Electron beam lithography is utilized to structure the cantilever and holding bar pattern. (c) Transverse holding bars with $20\ \mu\text{m}$ long, $3\ \mu\text{m}$ wide cantilevers are connected via $500\ \text{nm}$ wide bridges. The structure is transferred into diamond via ICP RIE. (d) Afterwards diamond pillars are fabricated at one end of the cantilevers via lithography and subsequent etching. In this way the cantilever is thinned down, with only the pillar remaining on top. Image adapted from [19].

The cantilevers containing the scanning pillars are fabricated by consecutive electron beam lithography and patterning via induced coupled plasma reactive-ion etching (ICP-RIE). In a first step, electron beam lithography is used to form the holding bar pattern (Figure 1.10 (c)). Subsequently, the pillar pattern is aligned with the cantilevers, and transferred into the diamond. As only the pillars are protected by a hydrogen silsesquioxane resist mask, the earlier defined pattern, including the membrane, is thinned down during the etching (Figure 1.10 (d)). This step is carried on until the membrane is thinned to a point where all-diamond material in between the cantilevers has been removed and the cantilevers remain free-standing [19]. After this last fabrication step, hundreds of cantilevers are connected to a holding bar in the membrane by $500\ \text{nm}$ wide bridges. An optical microscope image of the holding bar is shown in Figure 1.11 (a), with a close-up on a few cantilevers on the right. The bridges connecting the cantilevers to the membrane are strong enough to reliably hold them, but allow at the same time an easy, individual break out. The scanning diamond nanopillars have typical diameters of $200\ \text{nm}$ and a length of $1\ \mu\text{m}$ and are positioned on the $20\ \mu\text{m}$ long, $3\ \mu\text{m}$ wide diamond cantilevers. The straight cylindrical shape of the pillars helps to enable efficient collection of the NV fluorescence signal. In Figure 1.11 (b) a microscope image of the front of the cantilever is shown where the pillar can be recognized by a white circular spot. The corresponding photoluminescence image reveals a bright emitter located inside the pillar.

In order to employ the scanning probes for imaging, the individually characterized cantilevers have to be transferred to an AFM tuning fork. However, prior to the attachment procedure, a preliminary characterization is carried out. In this way, pillars with single NV centers and good ODMR contrast are located. Around 30 % of the fabricated diamond nanopillars contain single NV centers. Using a tapered quartz micropipette, with an end diameter of $3\ \mu\text{m}$, a small droplet of UV curable glue is applied to the free standing end of the chosen cantilever. After the glue has cured, the cantilever is removed from the holding structure by mechanically breaking the connection by small movements with the quartz rod. On the bottom of Figure 1.11 (a) the attachment of a cantilever to a glass rod is sketched. In the last step the quartz tip is glued to the side of a tuning fork using ultra violet (UV) curable optical glue. Finally, the excess quartz rod is cut with a diamond cutter. The

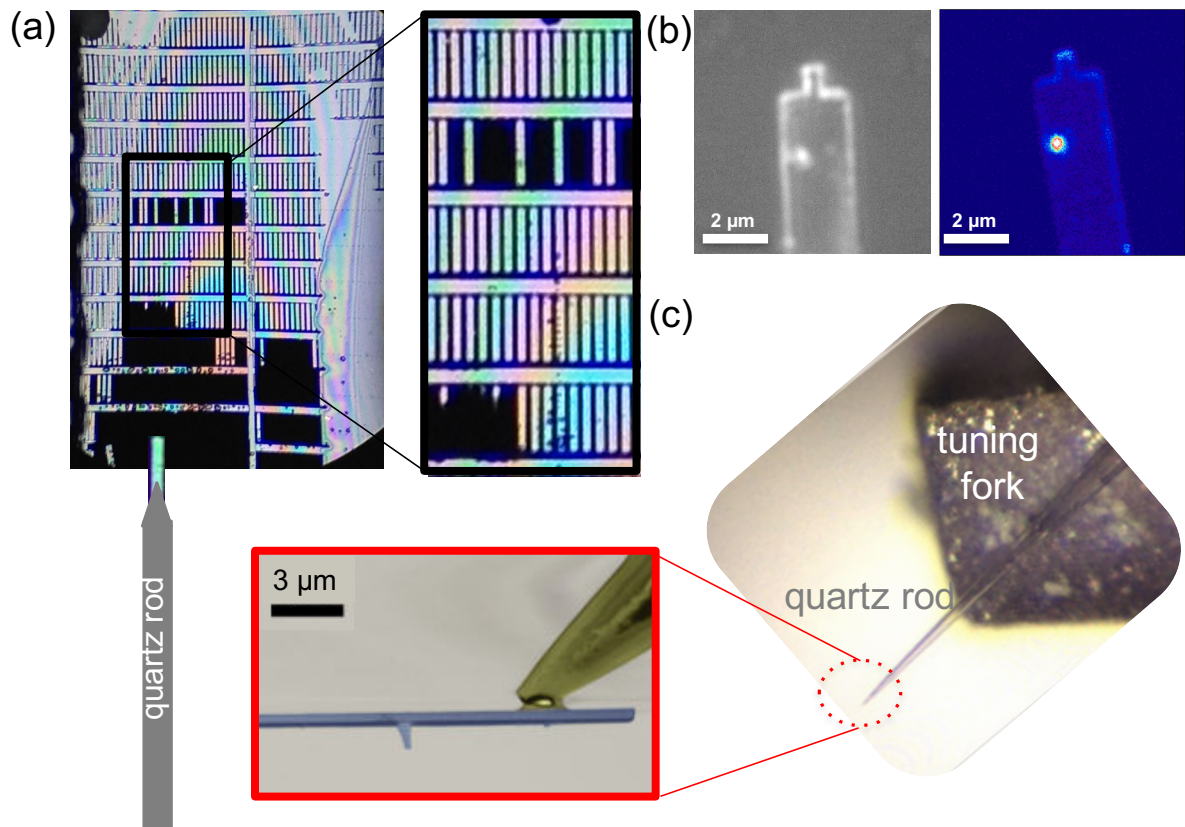


Figure 1.11 – **All diamond scanning probes.** (a) Microscope image of the cantilevers in the diamond membrane after the fabrication process. On the right, a zoom on the membrane, where the single cantilevers are clearly visible is shown. Each cantilever is still attached to the diamond frame by a thin bridge at the top. A glass rod which was tapered as to terminate in a $2\ \mu\text{m}$ thin end is glued from above to one of the cantilevers and is then cautiously swayed in order to break it out. (b) Camera image next to a photoluminescence image of the topview of a diamond tip. In the camera image the position where the pillar is located can be recognized by the white contrast. From the photoluminescence image it is clear that an emitter is located in this pillar. (c) The glass rod is attached to one side of the tuning fork using UV glue. The all-diamond tip is located at the very end of the quartz rod and is mounted in a way that the cantilever will later be parallel to the sample surface. The zoom shows a SEM image of the ready diamond tip (Image provided by P. Maletinsky).

right image in Figure 1.11 (c) shows a representative scanning electron microscope (SEM) image of a readily mounted single-crystalline diamond scanning probe and the image to its right displays a photo of the quartz rod which has been transferred to an AFM tuning fork. This method is very robust and the geometry can easily be adjusted to fit specific setup requirements.

The utilization of all-diamond scanning probes has considerable advantages. Due to a light guiding effect in the pillar, the collection efficiency of the NV photoluminescence is enhanced, leading to a higher fluorescence count rate. Furthermore, diamond tips enhance the spatial resolution due to the proximity of the NV center to

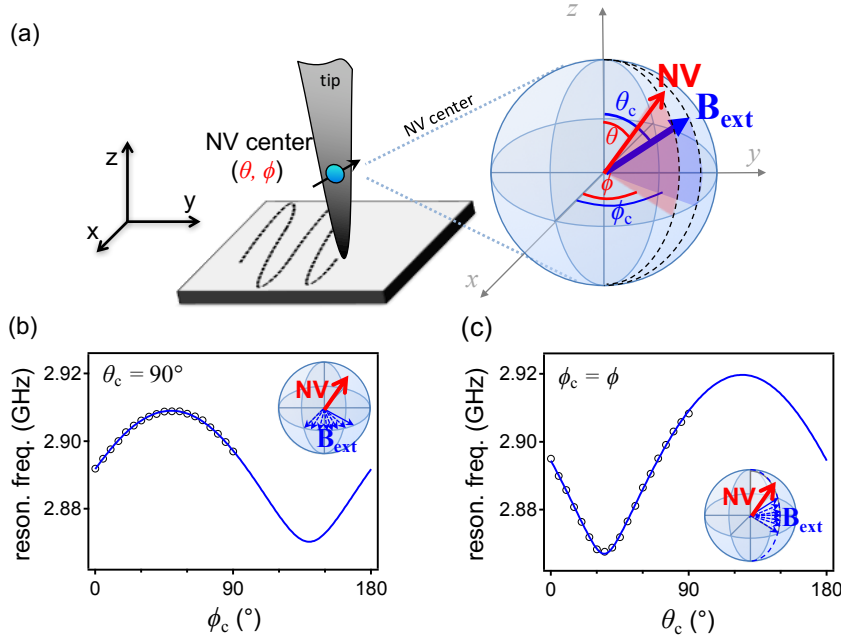


Figure 1.12 – **Measurement of the NV center orientation.** (a) Definition of the coordinate system. The NV center orientation is given by the angles ϕ (measured from the x axis) and θ (measured from the sample normal, z) which are defined in the laboratory frame. The direction of external magnetic fields is described with the same conventions. (b) θ and ϕ are determined by recording the ODMR splitting for different field directions applied with a set of three calibrated coils. While θ_c is fixed, the field with a defined strength is rotated with steps of $\Delta\phi_c = 5^\circ$ from 0° to 90° . ϕ_c is then fixed to the angle which produced the highest splitting in the ESR frequencies and the procedure is repeated for $\Delta\theta_c = 5^\circ$ from 0° to 90° . By fitting the two obtained curves the NV axis angles are obtained.

the apex of the diamond pillar and thus to the sample. This will be further discussed in the next section.

1.2.3 Characterization of the sensor

We want to utilize the NV center as sensitive scanning probe with nanometer spatial resolution. The confocal microscope setup combined with an AFM permits to detect the Zeeman splitting of an atomic size defect. Two approaches to implement the NV defect into the setup have been described in the previous section. In the following, the performance of these two configurations will be characterized. Its specifications will determine its adaptability to different samples.

NV center orientation As explained in the previous section, the detected magnetic field is the one projected along the NV quantization axis B_{NV} . It hence depends on the orientation of the defect with respect to the external field. The important determination of the NV centers orientation with respect to the laboratory frame is described in the following.

The spherical angles ϕ and θ describe the NV orientation in our laboratory frame (x, y, z) , which is defined

with respect to the translation axis of the AFM. First, a zero field ODMR spectrum is recorded and the intrinsic NV parameters D and E (defined in Section 1.1.3) are determined. The method to determine the NV angles is described in Figure 1.12. An external magnetic field with calibrated amplitude is applied along a direction, defined by the angles ϕ_c and θ_c , is varied (Figure 1.12 (a)). Due to this field, the resonance frequencies f_+ and f_- are shifted as a function of the projected field along the NV axis $B_{NV} = |\mathbf{B} \cdot \mathbf{u}_{NV}|$. This projection is defined by the angles ϕ and θ . In a first step, the orientation of the field is changed around a quarter of the horizontal plane (x, y) by increasing ϕ_c in steps of 5° while θ_c remains fixed. The ODMR spectrum is recorded at each step and the ESR frequency e.g. f_+ is tracked. This leads eventually to a graph as shown in Figure 1.12 (b). By choosing the highest shift in f_+ , the angle ϕ is extracted. Next, $\phi_c = \phi$ and θ_c is varied from $\theta_c = 90^\circ$ to $\theta_c = 0^\circ$. Another curve is obtained as shown in Figure 1.12 (c). By simultaneously evaluating the shift described by the two curves a single possible couple of parameters $(\phi, \theta) \in [0, \pi]^2$ is obtained. The standard error of this measurement is typically about $\pm 1^\circ$.

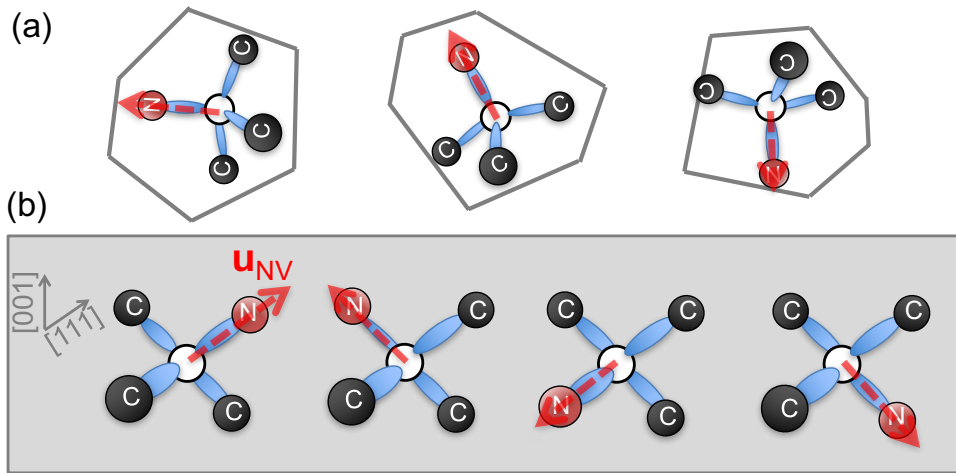


Figure 1.13 – **NV center orientation in nanodiamonds and bulk diamond.** (a) Schematically depicts nanocrystals which can be rotated and consequently can show any NV center orientation. (b) In bulk diamond, the NV center axis along the $[111]$ directions and has thus four possible orientations.

This angle measurement is performed each time a new sensor is installed in the setup. In case of a NV defect in a nanodiamond, the host nanocrystal is attached to the AFM with a random orientation and thus all combinations of ϕ and θ are possible (see Figure 1.13 (a)). Once attached, the orientation stays fixed unless the nanodiamond is released, or the AFM tip encounters a shock, in which case the orientation measurement has to be repeated. If a certain orientation is desirable an attached nanodiamond can be released and attached several times as to obtain the matching result.

The all-diamond tips hosting a NV in the scanning nanopillar were fabricated using (001) oriented diamond material. The NV center axis lies parallel along one of the $[111]$ directions (Figure 1.13 (b)). In this case only

$\theta \approx 125^\circ$ and $\theta \approx 55^\circ$ are possible. Four different orientations of the NV axis in the x, y plane with a relative offset of 90° are possible. Resulting in two different possible values for $\phi \approx 0^\circ$ and $\phi \approx 90^\circ$, in our coordinate system. This is visualized in Figure 1.13 (b). In addition, the cantilever exhibits tilts which can change θ and ϕ by several degrees. Once the diamond tip is installed, the orientation of the NV center cannot be changed.

Sensitivity of the scanning probe An important characteristic of the magnetometer is its sensitivity η [T/\sqrt{Hz}] to magnetic fields. In the case of the NV center, it corresponds to the minimal ESR frequency shift δf_{NV} that can be detected in a given acquisition time Δt . In the weak magnetic field regime ($\lesssim 5$ mT) where f_{\pm} varies linearly with B_{NV} , the sensitivity η can be written as [42]:

$$\eta \approx \frac{h}{g\mu_B} \frac{\Gamma}{C\sqrt{R}}. \quad (1.8)$$

The magnetic field sensitivity is thus dependent on the ODMR contrast C , the photon count rate R and the resonance linewidth Γ . These parameters depend on each other: By increasing the power of the microwave excitation the contrast C may be increased at the expense of increasing the linewidth Γ due to power broadening. Likewise, the linewidth Γ may be decreased by lowering the excitation power to reduce power broadening. However, this decreases at the same time the number of photons collected per measurement time R . For experiments, these parameters are optimized in order to achieve the best sensitivity. The linewidth Γ depends mostly on the measurement protocol. For the continuous ODMR sequence utilized in this thesis, it lies in the range of 5 MHz but may ultimately be decreased by a pulsed ODMR scheme [50]. The contrast C is given by the photo-physical parameters of the NV center and cannot be increased over $\sim 30\%$. The parameters R and Γ can vary in a certain range depending on the NV center and its host matrix. R is limited by the radiative transition rate of the NV center and the photon collection efficiency of the optical system. The radiative transition rate may be enhanced by using resonant cavity exploiting the Purcell effect [51] and the collection efficiency can be optimized by using appropriate photonic micro structures, e.g. diamond pillars [52]. In this way it is possible to enhance R by a factor of ten. Due to the differences in the host matrices in nanodiamonds and diamond tips, the NV centers' characteristic parameters differ, leading to different magnetic field sensitivities.

In nanodiamonds the photon emission rate R is typically in the order of 50 kcounts/s (see Figure 1.14 (a)) measured with our confocal microscope. The contrast C of the ODMR lines can vary from nanodiamond to nanodiamond, however it rarely overpasses 20%. The option to preselect a nanodiamond before attaching it as sensor helps to choose a NV with sufficient contrast C . As discussed in Section 1.1.3, the E parameter can also influence the sensitivity or, more precisely, it can obstruct entirely the detection of magnetic fields if these are smaller than $B \ll \frac{Eh}{g\mu_B}$. E in nanodiamonds often has values of around 10 MHz and thus renders the NV little sensitive to fields inferior to 0.2 mT if no bias field is applied. The linewidth Γ is in the range of ~ 6 MHz and in our experiments it is mostly limited by power broadening and not by the intrinsic NV parameters. This leads to a minimal magnetic field sensitivity in the order of $\eta \sim 10 \mu T/\sqrt{Hz}$ in the case of a NV defect embedded in

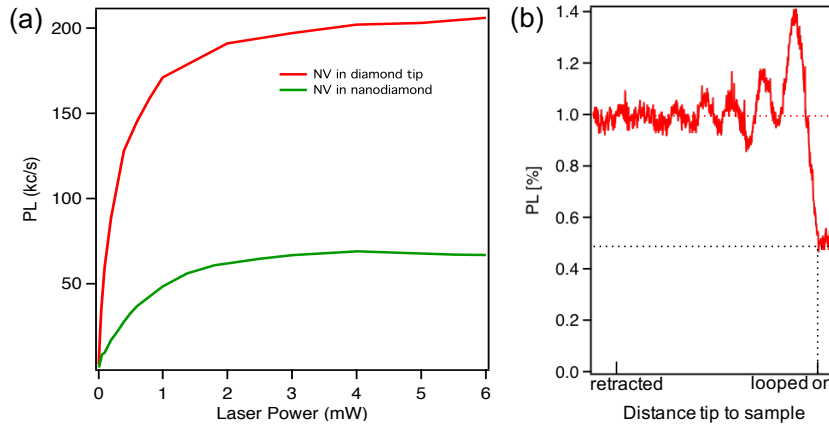


Figure 1.14 – **Saturation curves.** (a) Saturation curve for a NV center in the pillar (red curve) of a all-diamond tip and in a nanodiamond attached to the apex of an AFM tip (green curve) (b) photoluminescence emission from the NV center in the diamond tip while bringing the probe close to sample ('loop on'). The NV fluorescence was normalized to the fluorescence rate $R=200$ kcounts/s when the NV center was far from the sample, which is the case on the left side of the graph. During the approach the photoluminescence from the NV oscillates and drops to about 50% when engaged with the sample. This curve is always observed if the NV center is close to the apex of the tip. In the case of a sharp Akiyama scanning probe with nanodiamonds this effect is rarely observed.

a nanodiamond.

In the case of NV defects in all-diamond scanning probes, the photon waveguiding through the nanopillar [53] leads to a typical saturation emission rate of 200 kcounts/s or higher (see Figure 1.14 (a)). However, it has to be noted that a drastic decrease in photoluminescence counts has been observed when engaging the tip with the sample as shown in Figure 1.14 (b). This partial fluorescence quenching occurs on magnetic and non-magnetic surfaces (silicon, gold, graphite) and seems to be related to the geometry of the scanning pillar. It was especially pronounced when the NV center was close to the apex of the nanopillar. The contrast C in diamond tips reaches values up to the optimum of 30% and is generally higher than in the case of nanodiamonds. Since the NV center in the diamond tip is quasi in a bulk environment, also the zero field splitting induced by strain E is lower (0.5 MHz). However, in some rare cases, a E of 10 MHz is observed, probably when the NV is located close to one side of the pillar and thus the surface. In this case the strain induced splitting has to be countered with a static external field in order to achieve a good field sensitivity. The linewidth Γ , as in the case for nanodiamonds, is typically ~ 6 MHz, limited by power broadening. Especially the higher photon count rate and the high contrast enhances the sensitivity of NV centers in a full diamond scanning probe to $\eta \sim 1 \mu T / \sqrt{Hz}$.

Spatial resolution New proposals for future information storage devices are based on tiny magnetic structures that are stabilized in carefully engineered thin magnetic films. In order to investigate such materials, not only the magnetic field sensitivity, but also the spatial resolution of the magnetometer is a crucial parameter.

Since the NV center is a defect whose electron spin wave function is localized over just a few lattice sites, the ultimate spatial resolution of the NV center is atomic. In the following we distinguish between the spatial resolution of the magnetic field measured in a recorded image and the resolving power of the magnetization distribution. The spatial resolution of the magnetic field map first depends on the cell size of the raster scan. It is limited by the precision in the positioning of the AFM tip. In our case, this is in the order of one nanometer. The magnetization structure in a sample can be derived from the stray field distribution above the sample. Here, the critical limitation in resolving power lies in the probe to sample distance d and thus in the distance of the NV center to the magnetic layers of the sample. The probe-to-sample distance d is an important parameter which is a priori unknown. It depends on the utilized scanning probe.

A method to determine the probe-to-sample distance d has been developed in our group during the PhD of Thomas Hingant [54]. It is used in order to determine the spatial resolution provided by each scanning probe. The distance d between the NV spin sensor and the sample surface is inferred by recording the magnetic stray field produced above the edges of an uniformly magnetized ferromagnetic wire. As explained in Section 1.2.1, we track one ESR frequency, while scanning the NV sensor over the magnetic stripe. The recorded ODMR spectra are fitted and the Zeeman shift of the ESR frequency shift Δf_{NV} is extracted (black data points in Figure Figure 1.15 (b) and (c)).

For an ultrathin magnetic layer t , infinite in the y-direction, the field \mathbf{B}^{bd} is described by an analytical formula

$$\begin{cases} B_x^{bd}(x, z) = \frac{\mu_0 M_s t}{2\pi} \left(\frac{z}{x^2 + z^2} \right) \\ B_y^{bd}(x, z) = 0 \\ B_z^{bd}(x, z) = -\frac{\mu_0 M_s t}{2\pi} \left(\frac{x}{x^2 + z^2} \right) \end{cases} \quad (1.9)$$

This field depends on the magnetization of the sample M_s and the distance to the sample z . This distance $z = d$ of the NV center determines the spatial resolving power. By fitting formula (1.9) to the quantitative measurement of the stray field, we can determine the magnetization M_s and the probe-to-sample distance d . For the measurement of the stray field, the NV probe is scanned over the magnetic wire and an ODMR spectrum is recorded at each position. From the shift in the resonance frequency we can determine the shift from the zero field position in the weak field regime $\Delta f_{NV} = D \mp f_{\pm}$. The relation

$$B_{NV} = \Delta f_{NV} / (2g\mu_B) \quad (1.10)$$

converts the frequency shift Δf_{NV} to the measured field along the NV axis B_{NV} .

A schematic of the measurement procedure is shown in Figure 1.15 (a) and a typical Zeeman-shift profile recorded while scanning the NV defect across the edges of a 500-nm-wide wire of Pt|Co(0.6nm)|AlO_x is shown in Figure 1.15 (b) and (c). The probe to sample distance is then extracted by fitting the experimental data with

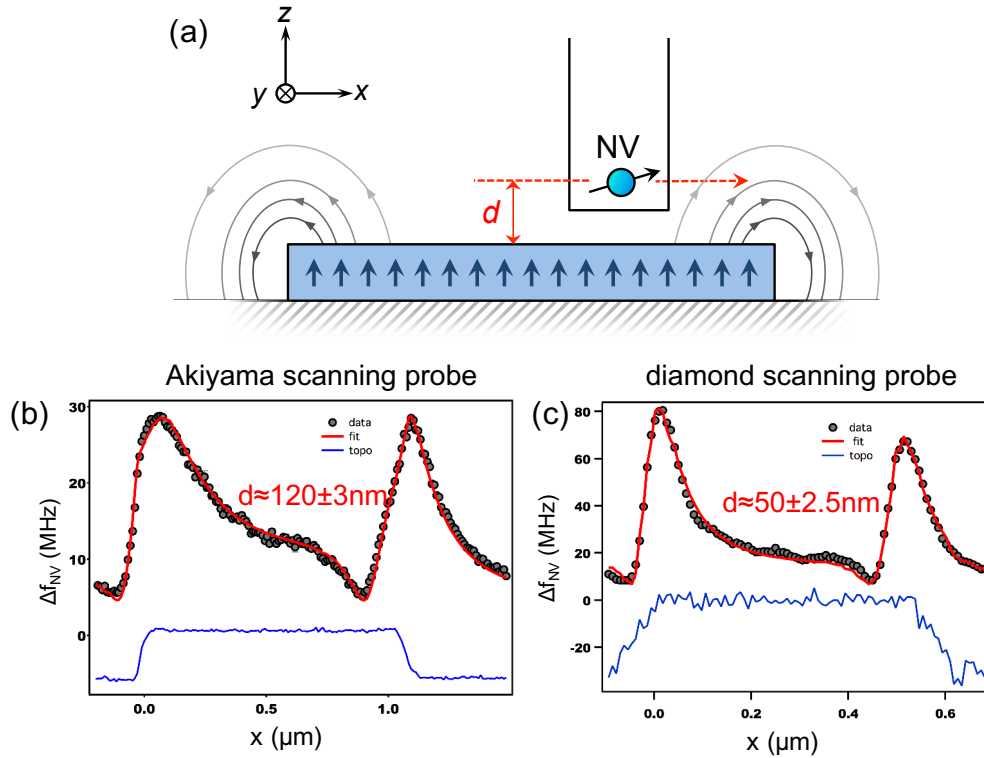


Figure 1.15 – Principle of the measurement of the probe-to-sample distance d . (a) The scanning NV magnetometer is used to measure the magnetic field (grey arrows) produced at the edges of an uniformly magnetized ferromagnetic wire (blue arrows). (b) and (c) Typical Zeeman-shift profile measured by scanning the NV defect across the edges of a wire of Pt|Co(0.6nm)|AlO_x with perpendicular magnetic anisotropy. The markers are experimental data and the red solid line is the data fitting from which d is extracted [54]. (b) is the measurement for a nanodiamond and (c) for a diamond tip.

the analytical formula. Two such measurements are shown in Figure 1.15 in case for an Akiyama probe with an attached nanocrystal (b) and the diamond tip (c). The measurement technique can be applied in the same way for both cases. The only difference lies in the slightly higher error in the measured distance when utilizing a diamond tip. Due to its rather broad end (in comparison with the sharp Akiyama tip) the beginning and the end of the magnetic stripe for each linecut cannot be determined as precisely. This results in a uncertainty of about 5% in the probe to sample distance, while it is about 2.5% in the case of the Akiyama scanning probe. Since the uncertainty in the probe to sample distance translates into the biggest error in measured stray fields a precise error analysis of this measurement is carried out in the Annexe B.1.1. For the two measurements, shown in Figure 1.15 (b) and (c) the fit of the stray field profile results in $d=120 \text{ nm} \pm 3 \text{ nm}$ for the nanodiamond and in $d=50 \text{ nm} \pm 2.5 \text{ nm}$ for the diamond tip. This is a representative result for the two scanning probes: While for diamond tips the extracted probe to sample lies mostly in the order of 50 nm (lowest d measured in our case was 40 nm and the highest 80 nm), the height of the attached nanodiamonds lies in most cases in the range of 100 nm or more (the lowest d measured was 80 nm and the highest 150 nm).

The size of the nanocrystals, in average 40 nm in diameter, should ensure the proximity of an NV center to the sample. It is however not necessarily attached to the very end of the scanning tip, which leads to greater and varying distances compared to the nanodiamond radius. In the case of diamond tips, the implantation dose should guarantee a probe to sample distance of ~ 10 nm, but since the exact positioning is a random process the depth of the created NV centers is not well-defined (straggle effect during the implantation process) the actual implantation depth can vary by 10-20 nm. In addition, scanning diamond nanopillars can gather contamination at the end of the tip, which can increase the height additionally by a few tens of nanometers [48].

In summary, the resolving power of the two scanning probes is limited by the probe to sample distance d and is in the order of 50 nm in case of the all-diamond scanning probe and around 100 nm for AFM tips functionalized with nanodiamonds. This difference between the two scanning probes can be the decisive factor when it comes to a measurability of a sample. For example, if a sample exhibits magnetic feature smaller than a few tens of nanometer, a probe to sample distance of $d < 50$ nm is required. The usage of diamond tips becomes necessary.

1.3 Magnetic field imaging modes

After having introduced the magnetometer and the sensing probes, we will now have a closer look at different magnetic field detection schemes. Namely, the quantitative magnetic field detection mode based on ODMR (also referred to as 'full B') and the detection of fields based on photoluminescence quenching (referred to as 'quenching mode' or 'all optical' detection mode). In the first part of this section, we will briefly introduce qualitative features of magnetic domain walls as they will serve as a prime example for the different detection modes (§1.3.1). We have already shortly encountered the quantitative field imaging mode in the previous section and will describe it more precisely in the following (§1.3.2). The purely optical detection scheme of magnetic fields will be introduced (§1.3.3). It is especially useful when high off-axis field prevent quantitative field imaging. Both imaging modes are demonstrated above magnetic domain walls in ultrathin ferromagnetic wires.

1.3.1 Demonstration of different sensing schemes on domain walls

Towards the development of new data storage architectures, a lot of attention in recent years has been paid to ultrathin magnetic heterostructures. In magnetic materials, the minimization of the free energy leads to the formation of domains. A magnetic domain denotes a region where the magnetization is uniform and the region separating two domains with opposite orientation is called a domain wall. The domain wall can be understood as a quasi-particle. It can be manipulated for instance by an external magnetic field, a spin-polarized current and by variations in the sample geometry. The ultrathin films studied in this work are in general heterostructures of different materials with thicknesses in the range of ~ 1 nm and perpendicular magnetic anisotropy.

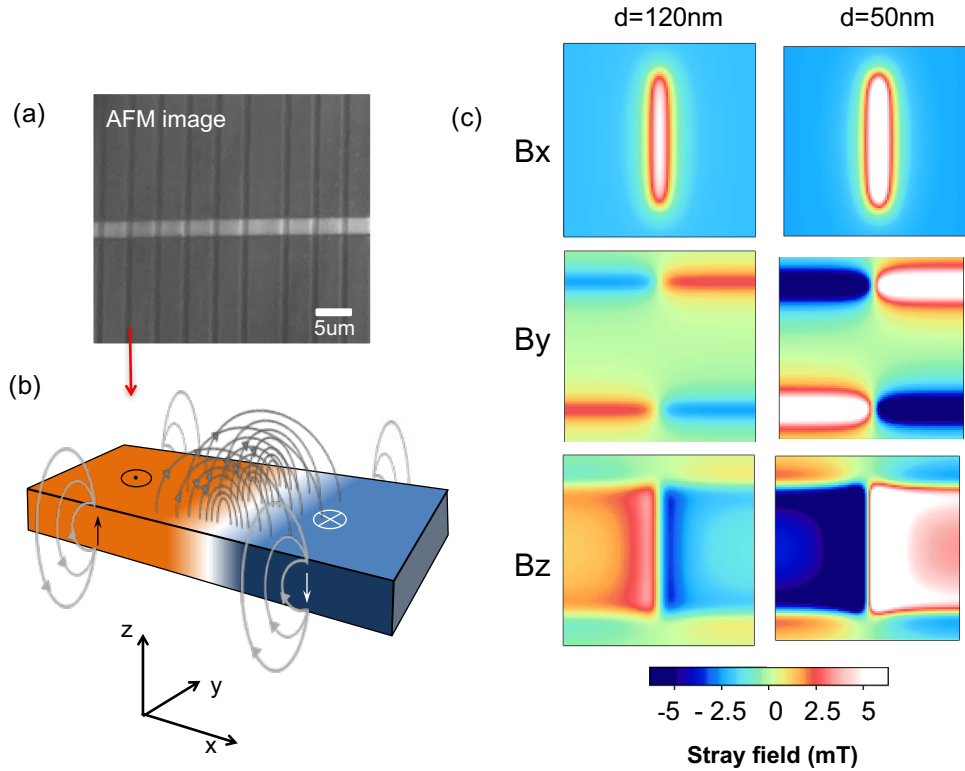


Figure 1.16 – **Magnetic field of domain walls.** (a) Microscope image of a sample with several $1\ \mu\text{m}$ broad magnetic stripes. A gold microwire is located in the middle of the sample in order to perform ODMR measurements and nucleate domain walls. (b) Schematic of a magnetic wire with a domain wall. The stray field that is emitted by such a structure is sketched by the grey arrows. It arises from the change in magnetization at the edges of the stripe and over the domain wall. (c) Images of the calculated stray field B_x , B_y and B_z for typical sample parameters ($M_s = 1\ \text{MA/m}$ and $t = 1\ \text{nm}$), for $d = 120\ \text{nm}$ on the right and $d = 50\ \text{nm}$ on the left. The maximum field for a probe to sample distance over the domain wall is $\sim 3\ \text{mT}$. In case of $d = 50\ \text{nm}$ fields of $8\ \text{mT}$ are reached and we start to leave the quantitative imaging regime of the NV center. More details for the calculation of stray field is given in Annexe A

Such thin films are advantageous, since very narrow domain walls are formed and can then be propagated with the help of small currents. They are consequently promising systems for high density storage devices with low power consumption. Magnetic domain walls are chosen as a prime example in nanomagnetism to demonstrate two different detection schemes of the NV scanning magnetometer. The related physics, leading to the domain walls exact internal structure will be described and studied in detail in Chapter 2. The magnetic stray field generated above a domain wall is sketched in Figure 1.16. We are in the following interested in the response of the scanning probe to this field. We will demonstrate two different magnetic field detection schemes and explain their characteristics and possible applications.

We consider an ultrathin ferromagnetic heterostructures (Ta|CoFeB(1nm)|MgO) grown by sputtering and structured by electron lithography and ion etching. A gold wire is deposited for the microwave excitation of

the NV center. A microscope image of such a structured sample is shown in Figure 1.16 (a). The samples are generally saturated with a electromagnet and subsequently domain walls are nucleated by applying a short current pulse through the gold antenna. First, a general look is taken at the expected stray field of a magnetic stripe containing a domain wall, which is schematically depicted in Figure 1.16 (b). An uniformly magnetized surface would not exhibit any stray field. In the magnetic wires the magnetization changes at its edges (to zero) and reverses its sign in the case of a domain wall. It is in these regions that a magnetic stray field is produced. The calculated stray field over a domain wall in a magnetic wire is shown in Figure 1.16 (c) for two probe to sample distances. The calculation is performed considering a probe to sample distance of $d = 120$ nm (typical for nanodiamonds) and $d = 50$ nm (typical for diamond tips). A magnetization of $M_s = 1$ MA/m and a magnetic layer thickness t of 1 nm, which are typical values in our ultra thin samples. The details of the stray field calculation is described in Annexe A. The B_x component is only present over the domain wall, while the component B_y is related to the field over the edges of the stripe. The B_z component is representative for the magnetization direction on both sides of the wall. In the quantitative imaging mode, the NV center detects the absolute value of the projection of the three stray field components along its axis:

$$B_{NV} = | \cos(\theta)B_z + \sin(\theta) \cos(\phi)B_x + \sin(\theta) \sin(\phi)B_y | . \quad (1.11)$$

In the quenching imaging mode, the component perpendicular to its quantization axis B_{\perp} is detected, as we will see in Section 1.3.3.

1.3.2 High precision quantitative magnetic field imaging

The principle of quantitative magnetic field imaging relies on the electron spin level splitting of the NV center due to the Zeeman effect. The principle and physics of this effect was explained in detail Section 1.1.2. Here, we focus on the technical details of the measurement procedure. For quantitative stray field mapping, the ODMR spectrum is recorded while scanning the sample under the sensor. At each pixel (pixel sizes of 10-20 nm² are common) the absolute magnetic field is extracted. For a faster data acquisition, only one of the two ESR frequency is recorded, corresponding to the $|m_s = 0\rangle \rightarrow |m_s = -1\rangle$ or $|m_s = 0\rangle \rightarrow |m_s = 1\rangle$ transition. By tracking the linear shift of the ODMR frequency, the absolute value of the field is determined at each point over the sample at the probe to sample distance d .

For a typical image, each pixel of the ODMR spectrum is composed of 10 bins with a bin size of 2 MHz and an integration time per bin of 100 ms (see Figure 1.17 on the right). This corresponds to an integration time per pixel of 1000 ms. Since the ODMR signal for NV centers in diamonds tips usually show a higher ODMR contrast, the imaging speed can be slightly increased compared to nanodiamonds. By fitting each of the obtained spectra, the peak value of the signal is extracted and consequently the total frequency shift and field along the NV center axis is determined. The error in the measured field resulting from this procedure is about ~ 0.3 MHz. As previously mentioned, the quantitative field imaging method is often executed while applying a bias field, in order to reach the linear sensing regime even in the presence of a high transverse zero-field splitting

E. Additionally, an externally applied bias field enables to detect the sign of the stray field with respect to the NV axis, since frequency shifts to lower and higher frequencies can be distinguished.

Full magnetic field imaging of a domain wall

The microwave frequency is swept over a range of 20-30 MHz around one of the transition frequencies f_{\pm} . It is recentered around its minimum after each pixel and consequently a tracking of the shift of the resonance is achieved. All recorded spectra are fitted with a Gaussian function to determine the minimum. This minimum gives the shift of the resonance frequency and the detected magnetic field $\Delta f_{NV} \propto B_{NV}$.

Figure 1.17 (c) shows a magnetic field map above a domain wall in a thin film ferromagnetic wire of Ta|CoFeB|MgO recorded with a NV center in a nanodiamond with $\theta = 102^\circ$ and $\phi = 27^\circ$. With this NV axis orientation, mainly along the x-direction, we clearly see the field over the domain wall and a small contribution from the edges of the wire. The probe to sample distance for this nanodiamond was in the range of 100 nm. At this distance, we are in the weak field sensing regime. The intrinsic width of the domain wall can not be determined from this image since the resolving power is limited by the probe to sample distance. As already mentioned, the recorded magnetic field is the one projected on the NV axis and depends thus on the NV center orientations (on the angles θ and ϕ). While the field over a domain wall in a magnetic stripe can be divided up in the three components described in 1.16 (c) only a projection of these was measured in Figure 1.17 (c). Since the orientation of a nanodiamonds on an AFM tip can be changed rather easily (however the attained angle is left to chance) different components of the field can be imaged. Such magnetic fields maps will be used in the

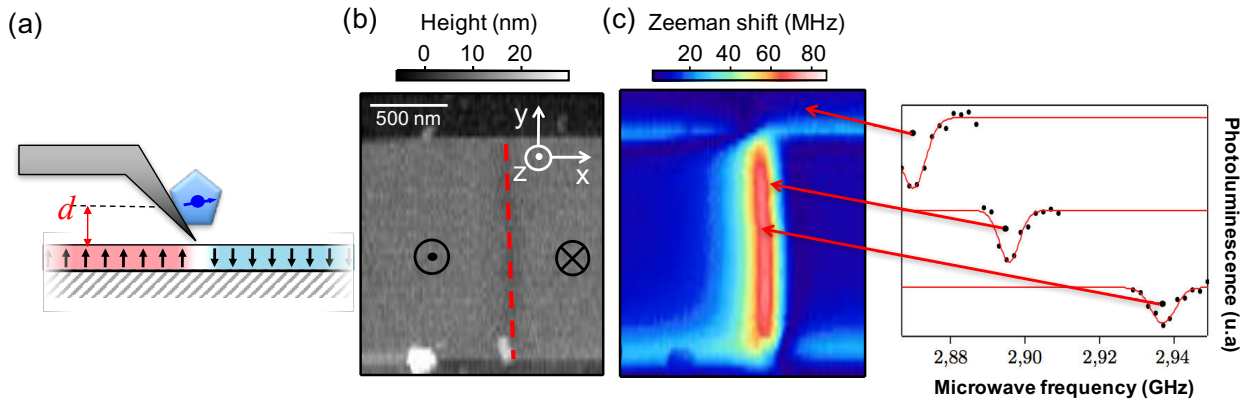


Figure 1.17 – **Full magnetic field measurement of a domain wall.** (a) A nanodiamond hosting a NV center is placed at the apex of an AFM tip and used to measure the magnetic stray field over a domain wall in a magnetic stripe. (b) AFM image of the ferromagnetic wire. (c) Corresponding full magnetic field image of a domain wall in a ferromagnetic wire (Ta|CoFeB|MgO). The color bar gives the shift of the resonance frequency of the NV center provoked by the field parallel to its axis. Each pixel on the color map corresponds to a recorded ODMR spectrum which was fitted with a Gaussian function to determine Δf_{NV} . Each spectrum consists of 11 points and a window of 20 MHz which leads to a good enough fit with a error in Δf_{NV} of about 0.3 MHz

following chapter to extract information about the domain wall structure on various magnetic heterostructures.

The lower bound for the field sensitivity of this quantitative sensing method is the one discussed in Section 1.1.3 and is approximately an order of magnitude better for NV centers in diamond tips ($\eta = 1 \mu\text{T}/\sqrt{Hz}$) than for NV centers in nanocrystals ($\eta = 10 \mu\text{T}/\sqrt{Hz}$). Also the maximal detectable field has its limitations. As seen in Section 1.1.3 the ESR frequency splitting is linear as long as $H_{\perp} \ll H_{\parallel}$. With increasing off-axis fields, m_s is not a good quantum number anymore and this condition is no longer fulfilled. We are in the strong field regime. In this case NV magnetometry can be operated in an all optical quenching regime, as discussed in the next section.

1.3.3 All optical magnetic sensing of high fields

As discussed in Section 1.1.3, the presence of a strong magnetic field perpendicular to the NV axis B_{\perp} , leads to a reduction of the ODMR signal contrast and inhibits quantitative NV magnetometry. Especially, when the proximity of the NV center to the sample is required to ensure a high spatial resolution, quickly a regime is reached where the above-described qualitative ODMR imaging mode is no longer applicable. High fields transverse to the NV axis alter the global optical properties of the color center. In the presence of high B_{\perp} a mixing of the spin-levels in the optical ground and excited states of the NV center provokes an increase in the mean probability for non-radiative transitions and at the same time suppresses the spin dependence in shelving from the excited state to the metastable singlet state. Spin polarization and spin dependent fluorescence - the key features normally enabling optical detected spin resonance - become inefficient and the ODMR contrast is significantly reduced [55]. The decrease of the ODMR contrast of a NV center with angle θ in an external magnetic field was shown in Figure 1.5. For fields bigger than 15 mT the ESR contrast drops to under 5% and data acquisition becomes long and cumbersome.

A concurrent effect of high transverse magnetic fields is a drop in the NV center's fluorescence rate, as recorded in the graph in Figure 1.18. It is this drop in emitted photons that can be adopted as an all-optical

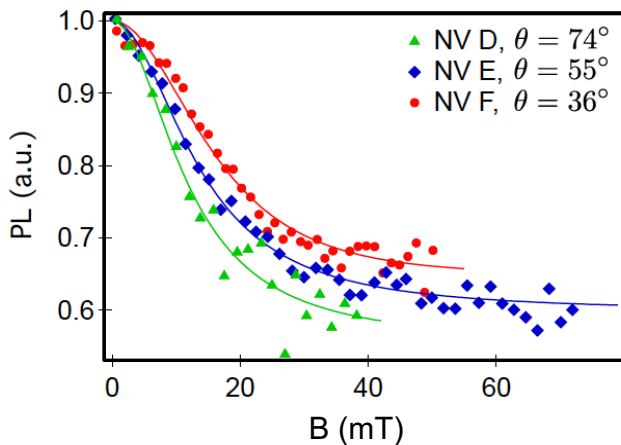


Figure 1.18 – **Magnetic quenching of the NV fluorescence.** Count rate R measured as function of the amplitude of an external applied field for three different NV centers. Not only the contrast, but also the photoluminescence response from the NV center decreases significantly in high fields which are not aligned with the NV axis. The angle θ describes the orientation of the magnetic field B with respect to the NV axis. Starting from 10 mT a significant decrease in the count rate for all three NV centers is observed. The data was adjusted from a former work in our group [55]

detection technique to discriminate between low and high magnetic field regions. In order to model the magnetic quenching response of the NV center a seven level model of its energy levels is used. The photodynamics resulting in the magnetic quenching and this simulations are explained in the Annex A.4.

In order to apply the drop in fluorescence as detection technique, the experimental setup remains unchanged and the microwave excitation becomes obsolete. Merely the change in photon counts per seconds is detected at every point over the sample. With an integration time of 100 ms per pixel, good images can be obtained with a speed 10 times faster than with the full magnetic field imaging mode. However, this imaging mode is not qualitative. Nevertheless, due to its simplicity and speed this proves a suitable technique for samples with high magnetization where the exact magnetization shape and not the absolute strength of the field are of interest. This sensing scheme is primary interesting in combination with the all-diamond scanning probes where the sensor close to the surface guarantees a high spatial resolution.

All optical magnetic field imaging of a domain wall

To test the quenching regime of the NV center on domain walls we use all-diamond scanning probes. In the diamond tip which was used to record Figure 1.19 (c), the NV center is ~ 30 nm close to the sample. Stray fields at this distance over the domain wall in this sample (Ta| CoFeB|MgO) are large enough to provoke a quenching in the NV fluorescence. Without applying any RF signal, we scan the tip with the NV over a domain wall and detect its photoluminescence signal. The photoluminescence rate drops at the sides of the wire and over the domain wall, where high stray fields cause high off-axis fields. The inverse happens when B_{\perp} is reduced. The sample itself shows several small bright areas in between the magnetic stripes which add to the photolumi-

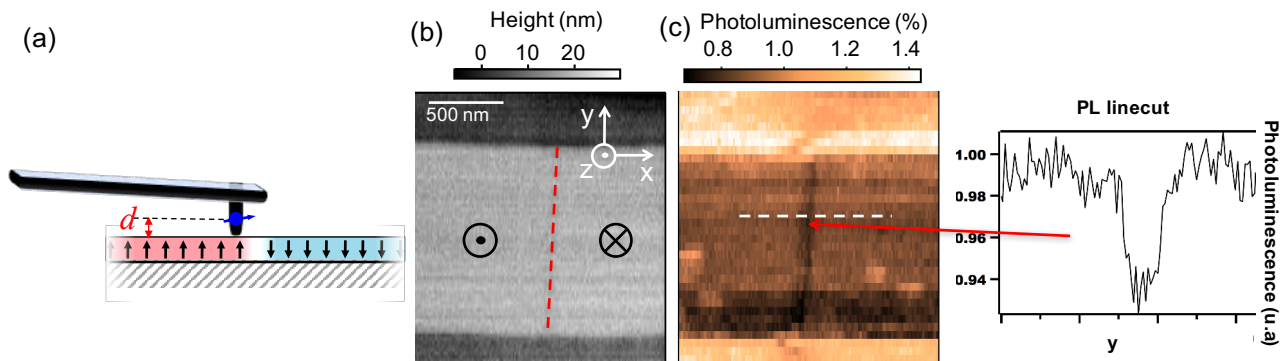


Figure 1.19 – **Quenching image of a domain wall.** (a) In this measurement a diamond tip with a NV center approximately 30 nm from the surface was used to perform quenching images over a magnetic domain wall. (b) is the simultaneously recorded AFM image. (c) shows the NV fluorescence counts observed when scanning an NV in a diamond nanopillar over the sample. The photoluminescence signal was normalized to the average fluorescence intensity of $S \sim 100$ kc/s when the tip was in contact to the sample on a non-magnetic area. Dark areas appear when the NV is scanned over magnetic features that enhance B_{\perp} . A linecut of the photoluminescence counts above the domain wall is shown on the left which reveals a drop in fluorescence of $\sim 10\%$.

nescence counts from the NV and are not related with the magnetic features of the sample. Furthermore, the fluorescence quenching caused by off-axis fields is superposed with the distance dependent change of the NV fluorescence with topographic features on the sample. As shown before in Figure 1.14 (b), when approaching the NV to the sample, the total NV fluorescence collected through the pillar changes and is at a certain probe to sample distance even intensified. In Figure 1.19 (c) such an enhancement in fluorescence can be seen on the upper side of the stripe. In this area the nanopillar recording the AFM image is still scanning on the stripe while the NV center, probably located on the other side of the pillar, is placed over the lower sample. In this way, the topography causes the mean distance between the NV center and the sample to change, which in turn causes variations in the collected NV fluorescence rate. The same effect can be observed when scanning over dust particles on the sample surface.

The assets of this all optical technique are demonstrated in Figure 1.20 (a)-(c). Due to the small probe to sample distance, the domain wall can be resolved with a very high spatial resolution. In image (a) the drop in fluorescence has merely the range of 1-2 pixels which translates into ~ 20 nm and is close to the intrinsic domain wall width in this sample. Image (b) shows an image with two domain walls, or a single domain wall hopping from one pinning side to another. The two magnetic structures are solely separated by a tens of nanometers and exhibit both a characteristic shape. The quenching imaging is ideal to image samples with dense, small magnetic features and the exact shape of nano-size magnetic objects (see Chapter 3). Image (c) shows another area of application of this simple imaging method: As reported in [18] domain walls can move between pinning site, a movement which is activated thermally. In order to study such dynamics it can be advantageous to apply an imaging method were not even a microwave excitation is necessary. In this way it is ensured, that the sample

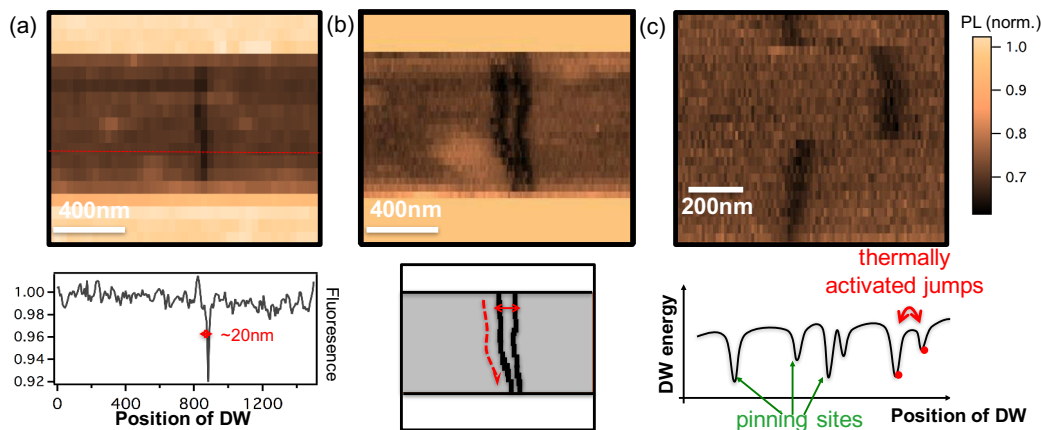


Figure 1.20 – **Application of the all optical imaging mode.** (a) Close probe to sample distances of the diamond tip (in this case 10-20 nm) can resolve the exact position of domain walls. (b) the high resolution and the absence of other overlapping disconcerting magnetic features allows to see the exact shape of magnetic objects and to resolve them even if they are close to each other. (c) The quenching imaging mode is ideal to study the dynamics of nanoscale magnetic objects as laser induced domain wall hopping.

properties are in no way altered by the measurement method and the study of other effects, as the influence of currents or microwave excitation is possible. The fact that this imaging mode is rather fast (a few minutes for micrometer big images) permits to study dynamics properties of magnetic features in some samples.

Although not qualitative in view of magnetic field sensing, this microwave free, pure optical quenching imaging mode provides a non-perturbative and fast measurement method at room temperature and can expand the sensing capacity of the NV center up to higher fields. The advantages of the fluorescence quenching method is its high localization accuracy of magnetic features related to the small probe to sample distance and the absence of other disconcerting magnetic features. No microwaves excitation is needed, which renders sample fabrication and setup extremely simple and robust. The non-perturbative method is capable to study the dynamics of nanoscale magnetic objects, even in soft magnetic materials where other techniques are likely to alter their shape and dynamics. It will be applied in Chapter 3 to study the effect of disorder on size and shape of magnetic skyrmions in ultrathin ferromagnetic samples.

1.4 Conclusion

In this chapter we have described the working principle of a scanning NV magnetometer. Its outstanding properties include:

- the possibility to quantitatively measure the magnetic field projection along the NV axis B_{NV}
- an atomic size intrinsic detection volume.
- the operation under ambient conditions.
- the non-invasive magnetic field detection scheme.

Other characteristics, such as magnetic field sensitivity and resolving power depend on the utilized scanning probe. Two different scanning probes have been introduced in Section 1.2. In the last part of this chapter we give a conclusive comparison between them.

Nanodiamonds provide a very accessible way to realize a NV scanning magnetometer since no complicated nanofabrication process is necessary. Commercially available nanocrystals with single NV centers can selectively be attached to a conventional AFM scanning probe. Any desired NV axis orientation can be obtained. For ferromagnetic samples that are emitting high stray fields, the quantitative magnetic field imaging mode can be utilized to obtain field maps of the sample. The magnetic field sensitivity is $\sim 10\mu T/\sqrt{Hz}$. All optical imaging is hardly adaptable due to the general high probe to sample distances. Efficient light collection from nanodiamonds on scanning probe tips is difficult. It lengthens data acquisition and limits the sensitivity. In addition, it has proven challenging to ensure close NV-to-sample separations. Even for small nanocrystals the NV is scanning around 100 nm from the sample surface, limiting resolving power of the scanning probe imaging.

PROPERTY	DIAMOND TIP		NANODIAMOND
	full B	PL imaging	full B
ODMR contrast C	20-30%	-	10-20%
Count rate R	200-500 kcounts/s	200-500 kcounts/s	~ 50 kcounts/s
Zero field splitting E	~ 1 MHz	~ 1 MHz	~ 5 MHz
Probe to sample distance d	40-70 nm ($\pm 5\%$)	40-70 nm	70-150 nm ($\pm 2.5\%$)
Acquisition time (per pixel)	~ 800 ms/pixel	~ 80 ms/pixel	~ 1000 ms/pixel
Sensing range (B)	0.01-5 mT	5-20 mT	0.2-5 mT
Spatial resolution (M)	~ 50 nm	~ 50 nm	~ 100 nm
DC sensitivity η	$1 \mu T/\sqrt{Hz}$	-	$10 \mu T/\sqrt{Hz}$

Table 1.1 – **Comparison of diamond tips and nanodiamond scanning probes.** Overview of the main characteristics of NV centers hosted in all diamond scanning probes and nanodiamonds (white). Summary of the specifications of the magnetometer, working in full B and quenching imaging method. All properties apply for ambient conditions.

In order to detect very small fields and to improve the resolving power, a reduction in distance between the NV center and the sample is desirable. For such cases, **diamond tips** are the preferable choice. These scanning probes are very robust and once installed on the setup, can last for months without altering their properties. The ODMR contrast C and count rate R are better than in the case of nanodiamonds and allow for lower acquisition times. The magnetic field sensitivity is $\sim 1\mu T/\sqrt{Hz}$. A slightly worse AFM scanning performance occurs due to the larger apex of the diamond tip (compared to a sharp Akiyama probe). However this problem might be resolved by improving the fabrication process. Poor AFM scans go hand in hand with a bigger uncertainty in the probe to sample distance (for the protocol described in this thesis, see Section 1.2.3). We have seen (Figure 1.14) that a (non-magnetic) quenching can occur close to the sample. For the all optical detection scheme the confluence of distance-dependent fluorescence changes and magnetic induced changes in fluorescence can be cumbersome. The samples measured with a diamond scanning probe in Chapter 3 and 4 are flat and such effects have not to be taken into account. Both, full magnetic field imaging (see Section 1.3.2) and all optical imaging (see Section 1.3.3) can be exerted with diamond tips. For samples emitting high fields, as in the case for ferromagnetic films, the proximity of the NV center might prevent ODMR experiments. For samples showing low magnetization and nanoscale magnetic features the combination of high spatial resolution and high field sensitivity provided by all-diamond scanning probes is a key prerequisite for field imaging.

In the following chapters, we will choose the one or the other scanning probe to investigate the nanomagnetic properties of different thin film samples. In Chapter 2 we continue the discussion on magnetic domain walls. We utilize a NV center in a nanodiamond to deduce characteristic material parameters by performing quantitative magnetic field imaging over domain walls. In Chapter 3 we aim to resolve magnetic whirls with a size of a few tens of nanometer. The necessity for a nanoscale spatial resolution in combination with high stray fields emitted from the ferromagnetic film require a measurement with a diamond tip in the quenching imaging mode. In Chapter 4 we utilize a diamond tip in the quantitative magnetic field imaging mode in order to resolve the noncollinear, antiferromagnetic structure of a multiferroic material.

Direct measurement of the interfacial Dzyaloshinskii-Moriya interaction in X|CoFeB|MgO heterostructures

Contents

2.1	The basic physics of magnetic domain walls in ultra thin films	38
2.1.1	Elements of micromagnetism	39
2.1.2	Magnetic domain walls in thin films with perpendicular anisotropy	42
2.1.3	The Dzyaloshinskii-Moriya Interaction in thin films	46
2.2	Measuring the DMI strength with the NV magnetometer	48
2.2.1	The challenges of a precise DMI measurement	48
2.2.2	Measuring DMI via local magnetic stray fields	48
2.2.3	Measurement precision	53
2.3	Engineering the DMI strength in different heterostructures	54
2.3.1	Bloch domain wall in Ta CoFeB MgO	55
2.3.2	The effect of nitrogen doping and thickness of the Ta underlayer	55
2.3.3	Néel domain walls in W CoFeB MgO	57
2.4	Other methods to measure the DMI and the virtues of NV magnetometry	60

Thin film magnetic heterostructures with perpendicular anisotropy have attracted a lot of attention as materials for novel spintronic technologies. By controlling the magnetization with local electric currents, instead of externally applied magnetic fields, unprecedented possibilities open up for low power consuming devices. Magnetic domain walls in such films have a characteristic size of ~ 10 nm and are thus extremely suited as high density data storage medium. A fast speed of data recording and readout is ensured by their high velocities

(>100m/s) even at low currents densities [56]. These properties inspired the use of magnetic domain walls in a 'racetrack memory' configuration as proposed by Parkin *et al.* [5]. However, there is still a debate on the underlying mechanisms of domain wall motion. In 2011 astonishing high domain wall speeds were observed in Pt|Co|AlO_x heterostructures [57] and a movement against the electron flow was observed in Ta|CoFe|MgO and Pt|CoNiCo|Pt samples [58, 59]. With these discoveries, former models explaining the interaction between electrical current and domain wall propagation were called into question and a major academic debate sparked off. The key to this debate is the structure of the walls which dramatically affects the efficiency of the different proposed current motion mechanisms [60, 61]. The most stable domain wall configuration, Bloch walls, are expected to move with lower speeds and always with the electron flow. It was recently proposed that an interfacial interaction in the thin films - the Dzyaloshinskii-Moriya interaction (DMI) - could force domain walls to be of Néel type rather than Bloch. This would have a considerable impact on their dynamic properties because Néel type domain walls can be efficiently moved by a spin orbit torque (SOT) induced by the spin Hall effect. To understand the mechanism underlying the origin of domain wall motion, a measurement technique revealing the domain wall structure and the DMI strengths is necessary. Yet, the relatively small number of spins at the wall center makes direct imaging of its inner structure a very challenging task. In this chapter we will show how to infer the domain wall structure and the strength of the DMI in thin film heterostructures with the help of NV scanning magnetometry.

In the first part of this chapter, the basic physics of domain walls are introduced (Section 2.1). The elements of the micromagnetic formalism are explained and the influence of the DMI on domain walls is discussed. In Section 2.2, we show how NV magnetometry can be used to measure the DMI strength. The general principle of the experiment is elucidated by showing how stray field measurements above a domain wall enable us to infer its inner structure. We introduce typical samples and describe how the DMI evolves while changing the heavy metal underlayer ($X=\text{Ta, TaN, W}$) in X|CoFeB|MgO heterostructures. At the end of this section the accuracy of this technique is discussed. In Section 2.3, the experimental results obtained with scanning NV magnetometry on the different thin film heterostructures are presented. Different strength of DMI are retrieved for different heavy metal underlayers in the samples. Lastly we discuss the results and compare our DMI measurement method with other techniques (Section 2.4).

2.1 The basic physics of magnetic domain walls in ultra thin films

In this section we introduce the basic micromagnetic elements that are used throughout this thesis (§2.1.1). We show how the interplay between different energy terms stabilizes Bloch domain walls in ultrathin films with perpendicular anisotropy (§2.1.2). By taking into account the DMI, present in thin films with broken inversion symmetry and strong spin orbit coupling, the internal structure of the domain wall is altered and Néel walls can be stabilized (§2.1.3).

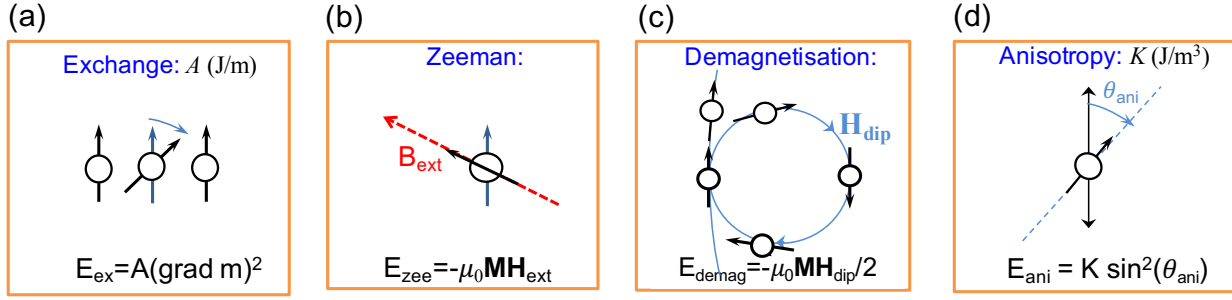


Figure 2.1 – **Illustration of the main magnetic energy terms.** (a) The exchange energy favors a parallel alignment of neighboring spins and thus leads to a uniform magnetization configurations. (b) The Zeeman energy describes the energy of the magnetization in an external field. (c) The demagnetization energy describes the fact that the magnetic dipole moments are aligned by the field created by the magnetization itself. It tends to make magnetic poles disappear by producing flux closing magnetic fields. (d) The anisotropy energy favors the alignment of the magnetization parallel to certain axis depending on the crystal structure of the material.

2.1.1 Elements of micromagnetism

In nanometer thin films, an atomic description of magnetism is not feasible. However, it is possible to grasp the physics of such materials on a micro and nanometer scale by treating them with a micromagnetic approach. In this formalism the macroscopic properties are simulated by using a continuum description of the magnetic material. The resulting micromagnetic equations can be solved numerically even for relatively large systems. The magnetization is assumed to be a continuous vector field

$$\mathbf{M}(\mathbf{r}) = M_s \mathbf{m}(\mathbf{r}), \quad (2.1)$$

with $|\mathbf{m}(\mathbf{r})| = 1$, \mathbf{r} being the position vector and M_s the saturation magnetization of the material. The basic micromagnetic approach formulates the magnetic energy in terms of the continuous magnetization vector fields. In order to determine stable magnetization configurations this energy is minimized. The different energy terms are in the following described for the case of thin magnetic films [62].

Exchange Energy

This quantum mechanical contribution arises from the Pauli exclusion principle and the short-range Coulomb interaction. Its basic consequence is that adjacent magnetic moments prefer to align collinearly (see Figure 2.1.1 (a)). Any deviation from this ideal case induces an energy penalty. In the approximation of continuous magnetization, the expression for the microscopic exchange energy density is written as

$$E_{\text{ex}} = A(\nabla \mathbf{m})^2. \quad (2.2)$$

This simple, microscopic form, of the exchange interaction describes the energy cost for two adjacent moments \mathbf{m}_i and \mathbf{m}_j to be rotated out of their collinear alignment. The exchange constant $A[\text{J/m}]$ can be measured with

ferromagnetic resonance experiment in bulk materials. In ultra thin films, A is difficult to access and can only be determined with a high uncertainty [63, 64]. In the case for cobalt thin films, as studied in this thesis, A is in the range of $\sim 10^{-11}$ J/m

Zeeman Energy

An external field H_{ext} has the tendency to align the magnetic moments along its direction (see Figure 2.1.1 (b)). The energy of this interaction is the Zeeman energy

$$E_{\text{zee}} = -\mu_0 \mathbf{M} \cdot \mathbf{H}_{\text{ext}} \quad (2.3)$$

where μ_0 is the magnetic permeability in vacuum.

Demagnetization Energy

All magnetic moments inside a material are themselves sources of a magnetic dipolar field H_{dip} . The magnetic moments are aligned along this field (See Figure 2.1.1 (c)). This is why the demagnetization energy has the same nature as the Zeeman energy, but the origin of the field are the magnetic moments themselves. Its energy density can be written as

$$E_{\text{demag}} = -\frac{\mu_0}{2} \mathbf{M} \mathbf{H}_{\text{dip}}, \quad (2.4)$$

where H_{dip} is the dipolar field (or demagnetization field) created by dipoles inside the material. Since the field of a dipole does not align itself, its contribution has to be excluded. This term is thus similar to the Zeeman energy with the difference of a factor 1/2. Generally, the demagnetizing field of an arbitrarily shaped object is very difficult to calculate. For simple geometries, such as uniformly magnetized ellipsoid, cylinders or plane films, the field can be expressed analytically by using the linear relation to the magnetization by a geometry dependent constant called the demagnetizing factor,

$$\mathbf{H}_{\text{dip}} = \mathbf{N} \mathbf{M} = N_x M_x + N_y M_y + N_z M_z = M_s (N_x m_x + N_y m_y + N_z m_z), \quad (2.5)$$

where x, y, z are the axis describing the volume and N_i are the demagnetization factors, which are tabulated for various geometries [65], such that $\sum N_i = 1$. In this case, the microscopic dipolar energy is written as

$$E_{\text{demag}} = -K_d \sum_{i \in x, y, z} N_i m_i^2 \quad (2.6)$$

where $K_d = \mu_0 M_s^2 / 2$, is defined as the boundary value for the maximum demagnetization energy.

The competition between exchange and demagnetization energy is expressed by the characteristic exchange length $\Lambda = \sqrt{A/K_d}$. For distances smaller than the exchange length, the magnetic moments can hardly deviate from the direction of their neighbors. For materials with dimension bigger than Λ , a subdivision into magnetic domains is observed. In this way the exchange is satisfied on the small scale, while globally the demagnetization

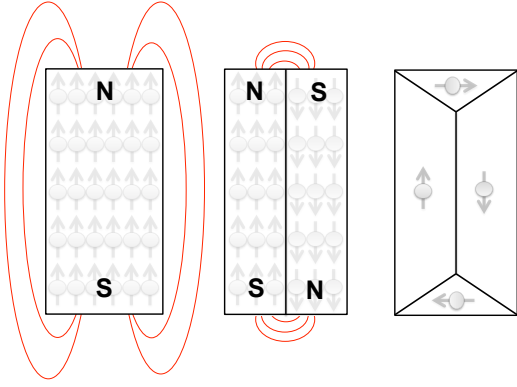


Figure 2.2 – | **Formation of domains.** The demagnetization energy decreases from left to right as magnetic domains are formed and dipolar stray fields are reduced. This happens at the cost of a higher exchange which want to align the spins in a collinear way and anisotropy energy. The characteristic parameters describing which domain structure dominates is the exchange length Λ which describes the competition between exchange and dipolar energies.

interaction is minimized. This is illustrated in Figure 2.2. In ultra thin films the thickness of the films is smaller than the characteristic length $\Lambda \approx 10$ nm and the magnetization does not vary within the thickness of the film.

Anisotropy Energy

The magneto crystalline anisotropy energy E_{ani} takes into account that the magnetization preferentially orientates along certain 'easy' axis in a material. These axes are linked to the symmetry of the crystal lattice (see Figure 2.1.1 (d)). The energy is intrinsic to the material and has its origins on the atomic level. In materials with a large anisotropy, a strong coupling between the spin and orbital angular momenta within an atom prevails [66]. To rotate the magnetization away from the easy direction in a perpendicular magnetized sample the energy

$$E_{\text{ani}} = K \sin^2(\theta_{\text{ani}}) \quad (2.7)$$

has to be paid. Here, θ_{ani} is the angle between the magnetization and the easy axis, and $K[J/m^3] > 0$ is the first order anisotropy constant. The anisotropy energy K includes contributions from various sources and is therefore sometimes referred to as effective anisotropy K_{eff} . The expression for the anisotropy energy has a pure phenomenological origin, but it is able to describe anisotropy effects with a high accuracy. In practical applications, the energy expressions are often reduced to the lowest order term which will be sufficient for the ultrathin layers studies in this manuscript.

In general, the anisotropy of thin films is remarkably different from the ones in bulk material. This is caused by the particular layered shape of magnetic thin films heterostructures, as well as the presence of symmetry breaking elements such as surfaces and interfaces. By varying layer thickness and heterostructure composition, it is possible to manipulate the magnetic anisotropy and to change the preferential direction from the commonly observed in-plane configuration to the out of plane direction. This phenomenon is referred to as perpendicular magnetic anisotropy (PMA). The two main sources of the magnetic anisotropy are the magnetic dipolar interaction and the spin-orbit interaction. Whereas the dipolar interaction leads to an in-plane magnetization in thin films, the spin-orbit interaction induces a small orbital momentum which couples the magnetic moment to the crystal axes and thus results in a total energy that depends on the relative orientation of magnetization and crystalline axis [67]. This contribution is strongly modified by lowered symmetry at a surface and leads to

a so called surface anisotropy, as described by Néel [68]. For the analysis of the anisotropy in thin films and multilayers, it has proven useful to distinguish the magnetic anisotropy energy K phenomenologically in a volume contribution K_v (J/m^3) and a contribution from the interfaces K_s (J/m^2), which contribution diminishes with the thickness t of the material. The magnetic anisotropy is then expressed as

$$K = K_v + \frac{K_s}{t}, \quad (2.8)$$

with $K_s \sim 10^{-3} \text{J}/\text{m}^2$ and $K_v \sim 10^4 \text{J}/\text{m}^3$. In bulk material the anisotropy is thus generally dominated by the volume term. With smaller thickness t the surface term dominates. At the same time, this effect increases the demagnetization energy, since magnetic poles appear at the material surface and create high demagnetization fields. This results in an artificial decrease in the anisotropy due to the demagnetization field

$$K_{\text{eff}} = K_v + \frac{K_s}{t} - K_d N_{\perp} \quad (2.9)$$

where $N_{\perp} = 1$ is the demagnetization coefficient for a plane [69]. It is only in ultrathin films with thicknesses of several Ångström where perpendicular anisotropy can become energetically favorable.

Several interfaces can lead to a perpendicular anisotropy in thin films: Interfaces with a heavy metal (Pt,Pd) with strong spin orbit coupling or recently also interfaces with an oxide layer (MgO) are utilized. All samples studies in this work fall into one of these categories.

Total magnetic energy

Finally, the total magnetic energy \mathcal{E} is calculated by summing all energy terms and integrating over the volume of the material

$$\mathcal{E} = \int_V (E_{\text{ex}} + E_{\text{Zee}} + E_{\text{demag}} + E_{\text{anis}} + \dots) dV. \quad (2.10)$$

The magnetic behavior of a material depends on the detailed balance between all these energy contributions. Once the total energy of a system is calculated, the main task of the micromagnetic approach is to find the magnetization distribution that minimizes the energy. Apart from analytic solutions, numerical solvers such as the OOMMF code have been developed to perform energy minimization calculations. In the case of ultra thin films additional interactions arising at the interface may have to be considered.

2.1.2 Magnetic domain walls in thin films with perpendicular anisotropy

Domain walls are the boundaries between regions with collinearly aligned magnetic moments. Their number and size are determined by the competition between relevant energies. At the domain wall, magnetic dipoles moments have to reorient themselves. This reorientation of the spins does not happen instantaneously: A too abrupt change of magnetization causes a high exchange energy penalty and consequently it is advantageous to reorient the spins across multiple spacings. This in return causes a deviation of several moments from the

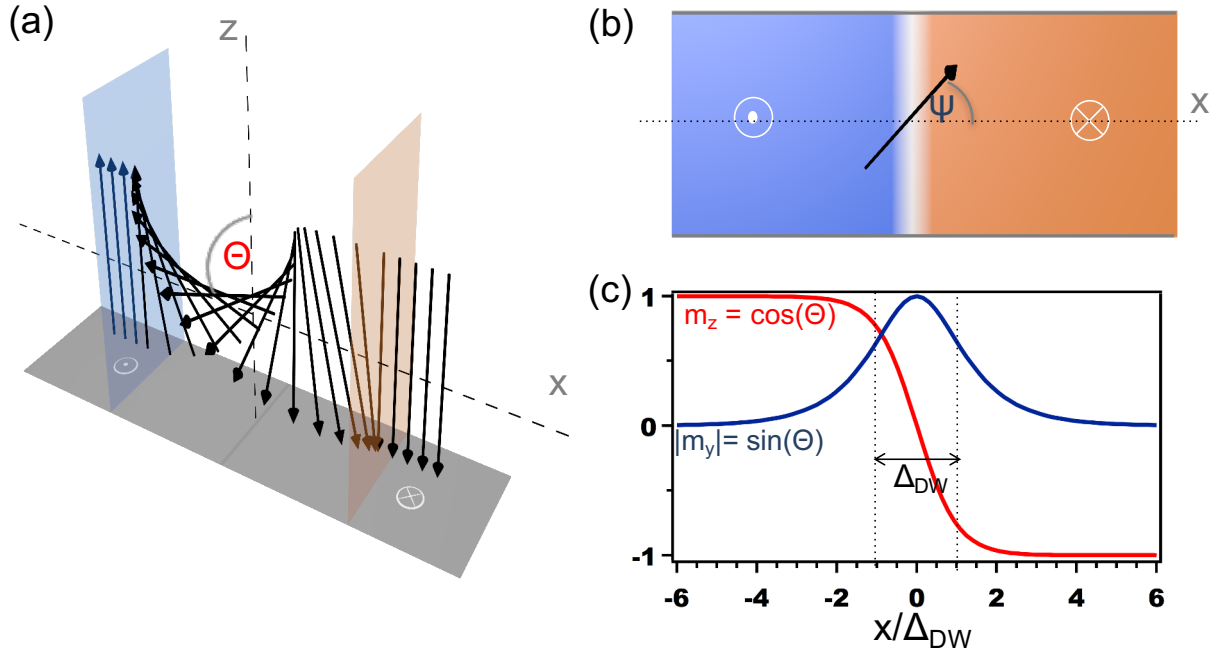


Figure 2.3 – **Domain wall configuration in ultra thin films.** Different types of domain walls can exist in ultra thin films with perpendicular anisotropy. They are defined by the angle $\Theta(x)$ which describes the tilt from the film normal z as depicted in (a). The angle ψ is the tilt measured from the normal of the domain wall x as shown in (b). The angle ψ defines the in-plane magnetization in the domain wall and is the tilt from x . (c) The m_z and the m_x component of the magnetization over a Bloch domain wall. Its characteristic length is defined by domain wall width $\Delta_{DW} = \sqrt{A/K_{eff}}$

easy magnetization axis and consequently increases the anisotropy energy. In ultrathin films, the thickness of the material is smaller than all the characteristic interaction length scales. The characteristic exchange length $\Lambda = \sqrt{A/K_d}$ is in the range of 10 nm and consequently the magnetization cannot vary in the thickness of the material. As a result, only a limited number of transition possibilities from one magnetization direction to another exist. Only the in-plane component of the magnetization is not imposed by the anisotropy and thus determines the domain wall structure.

Domain walls are described by the angle $\Theta(x)$, the tilt from the vertical z -axis, and $\psi(x)$ the tilt from the x -axis (Figure 2.3 (a) and (b)). The magnetic wire has the thickness t and width $w \gg t$. The wire's long axis lies parallel to the x -axis in the lab frame. A domain wall in such a wire is considered to lie straight along the y -axis. Its width, defined as $\Delta_{DW} = \sqrt{A/K_{eff}}$, is much smaller than the width w of the stripe. Here, K_{eff} is the effective anisotropy constant corresponding to the magneto crystalline anisotropy reduce by the demagnetization energy term associated with M_z which normally favors a planar magnetization (see Equation 2.9). The magnetization lies along the z -direction and is expected to be uniform along the stripe. When considering w as infinite, the description of the domain wall is reduced to a one dimensional problem in which the variables only depend on the x direction.

Domain wall energy

The energetic cost of a domain wall \mathcal{E}_{DW} is proportional to its length l_{DW} and the film thickness t . It is in the following described by the surface energy density σ , which in the one dimensional case is expressed as [70]

$$\sigma = \sigma_0 + \sigma_{\text{demag}} + \sigma_{\text{ext}}.$$

where

- $\sigma_0 = 4\sqrt{AK_{\text{eff}}}$ expresses the intrinsic energy cost due to the exchange and effective anisotropy.
- $\sigma_{\text{demag.}} = 2\Delta_{DW}N_xK_d \cos^2(\psi)$ is the demagnetization coefficient associated with the in-plane component m_x of the wall (see [69]). With $N_x \approx \ln(2)t/(\pi\Delta_{DW}) \ll 1$ and $K_d = \mu_0M_s^2/2$ it can be written as

$$\sigma_{\text{demag.}} = \frac{\mu_0M_s^2t \ln 2}{\pi} \cos^2 \psi. \quad (2.11)$$

- σ_{ext} represents supplementary terms that may have to be included to describe the energy of the wall as for example the Zeeman energy in case of an external field.

The total energy is generally described as follows:

$$\mathcal{E}_{DW} = t \times l_{DW} \left[4\sqrt{AK_{\text{eff}}} + \frac{\mu_0M_s^2t \ln 2}{\pi} \cos^2 \psi + \sigma_{\text{ext}} \right] \quad (2.12)$$

In the case of $\sigma_{\text{ext}} = 0$ the energy is minimized for an angle $\psi = \pm \frac{\pi}{2}$.

$$\frac{\delta\sigma}{\delta\psi} = 0 \Rightarrow \psi = \pm \frac{\pi}{2} \quad (2.13)$$

This kind of magnetic domain wall is called a Bloch wall (Figure 2.4 (a)). Its helical rotating magnetization components are shown in Figure 2.3 (c). In thin films with PMA it is the most stable domain wall configuration because it minimizes volume magnetic charges: Since $w \gg \Delta_{DW}$, no magnetic charges are present at the wall itself. It can be considered that the wall has no demagnetisation energy costs and hence, its profile is only determined by the competition of exchange and anisotropy. The analytic formula for this domain wall profile can be derived analytically [71].

It was mentioned above, that in several thin film samples with PMA, very high domain wall speeds were observed. This is the case for example in Pt|Co|AlO_x heterostructures. Such high speeds cannot be explained with Bloch domain walls that are predicted by our model so far. Up to now, $\sigma_{\text{ext}} = 0$ was considered. In the next section we will see that in thin films with strong spin orbit coupling and broken inversion symmetry, we have to take into account the effect of the Dzyaloshinskii-Moriya interaction. In this case, $\sigma_{\text{ext}} \neq 0$ and a different type of domain wall can be stabilized.

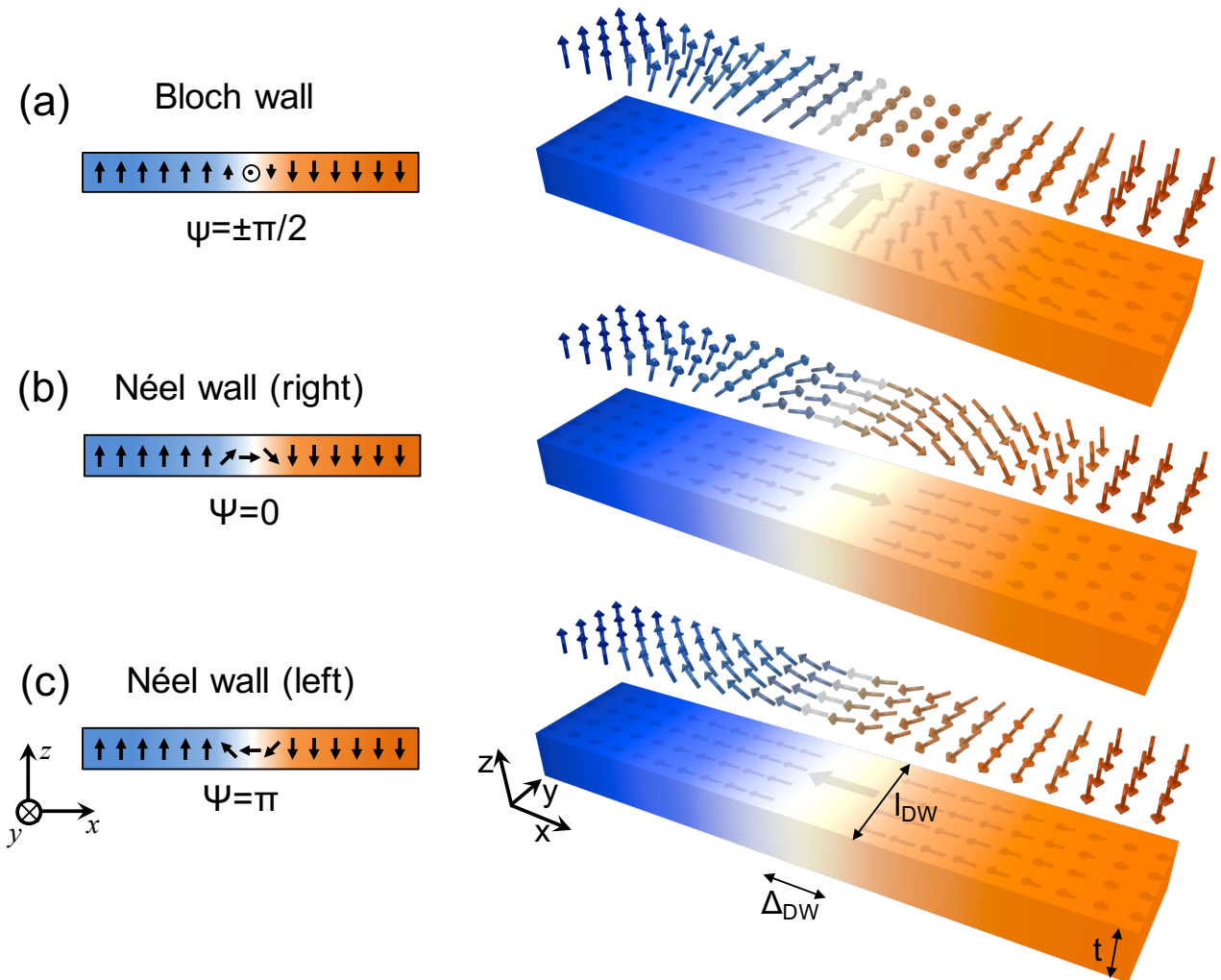


Figure 2.4 – **Domain wall structures in thin films with PMA.** Domain walls can be classified as Bloch walls ((a)) in which spins rotate within the plane of the wall, and Néel walls ((b) and (c)) - in these walls spins rotate in the plane perpendicular to the plane of the wall. On the left, the simple side view and the out of plane component of the wall texture is shown. On the right, the three dimensional spin structure is depicted above the stripe with the in-plane component projected on its surface. For the Néel wall as well as for the Bloch wall a left- and a right-handed case exist.

2.1.3 The Dzyaloshinskii-Moriya Interaction in thin films

The search for a medium that allows high information storage density combined with low power consumption, has motivated the study of low dimensional magnetic systems [72, 5, 73, 8]. In some of these materials, lowered symmetry gives rise to a new category of interactions, whose interplay leads to exotic magnetization patterns [74, 75]. One practical example of such systems are magnetic thin film multilayers, as perpendicularly magnetized X|CoFeB|MgO heterostructures. In these films, lacking inversion symmetry gives rise to the interfacial DMI [76, 77, 78], an antisymmetric exchange interaction occurring at the interface between a ferromagnetic layer and a heavy metal substrate with large spin-orbit coupling.

The DMI has the following form:

$$\mathcal{E}_{\text{DM}} = \mathbf{D}_{ij} \cdot (\mathbf{S}_i \times \mathbf{S}_j) . \quad (2.14)$$

where \mathbf{S}_i and \mathbf{S}_j are atomic spins. The interfacial DMI is arising from the interplay of the atomic spins of a ferromagnet and a neighboring atom in a non-magnetic layer with a large spin-orbit coupling, combined with a reduced symmetry. The latter condition is notably fulfilled in ultra thin films with a lack of inversion symmetry. The interaction gives rise to a resulting DMI vector, \mathbf{D}_{ij} , which points outwards from the plane of the atoms as depicted in Figure 2.5. The magnitude and sign of \mathbf{D}_{ij} is fixed by the properties of the interfaces and the involved materials. Using the micromagnetic model, the volumic energy density of the DMI term is derived [79] as follows:

$$E_{\text{DM}} = D_{\text{DM}} \left[\left(m_x \frac{\partial m_z}{\partial x} - m_z \frac{\partial m_x}{\partial x} \right) + \left(m_y \frac{\partial m_z}{\partial y} - m_z \frac{\partial m_y}{\partial y} \right) \right]. \quad (2.15)$$

Here, D_{DM} is the DMI constant of the magnetic layer (J/m^2), which is indirectly proportional to the film thickness $D_{\text{DM}} \propto 1/t$. In ultra thin films the energy contribution of the DMI can reach the same order of magnitude as the volumic energy terms introduced in the previous section and hence has to be taken into account for the description of the domain wall energy and structure.

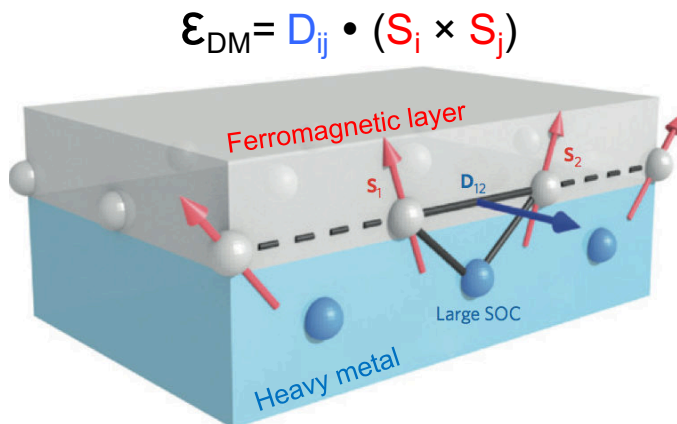


Figure 2.5 – **Interfacial Dzyaloshinskii-Moriya interaction.** This schema illustrates the DMI arising at the interface of a magnetic material (grey) and a material with strong spin orbit coupling (blue). This chiral interaction tends to deviate the spins from their collinear alignment. The vector D_{ji} describes the DMI strength and is perpendicular to the axis which links the two spins \mathbf{S}_i and \mathbf{S}_j (Figure adapted from reference [8]).

Next, we will see how the DMI influences the domain wall energy and consequently the domain wall's internal structure. It has been shown [61], that the interfacial DMI does not significantly affect the profile $\Theta(x)$ of a domain wall, nor its width Δ_{DW} . By integrating Equation 2.15, the equation for the surface energy σ (Equation 2.12) is modified by the term

$$\sigma_{\text{ext}} = \sigma_{\text{DM}} = -\pi D_{\text{DM}} \cos(\psi). \quad (2.16)$$

Here, ψ is the in-plane magnetization orientation (see Figure 2.3 (b)). The total energy of the domain wall consequently reads

$$\sigma = 4\sqrt{AK_{\text{eff}}} + \frac{\mu_0 M_s^2 t \ln 2}{\pi} \cos^2 \psi - \pi D_{\text{DM}} \cos(\psi). \quad (2.17)$$

The demagnetization field in competition with the interfacial DMI determines the angle ψ of the in-plane magnetization of the domain wall. It should be noted that the DMI acts on the domain wall as an effective magnetic field along x with the amplitude $H_{\text{DM}} = \frac{D_{\text{DM}}}{\Delta_{\text{DW}} M_s \mu_0}$. The wall configuration can hence be determined by minimizing the energy of Equation (2.17) with respect to the parameter ψ . This leads to

$$\psi = \begin{cases} 0 & \text{if } D_{\text{DM}} > D_c \\ \pm \arccos \left[\frac{D_{\text{DM}}}{D_c} \right] & \text{when } |D_{\text{DM}}| \leq D_c \\ \pi & \text{if } D_{\text{DM}} < -D_c, \end{cases} \quad (2.18)$$

where $D_c = 2\mu_0 M_s^2 t \ln 2 / \pi^2$. In the limit where $|D| \ll D_c$, the domain wall is of Bloch-type, as already described in Section 2.1.2. Conversely, if $|D_{\text{DM}}| \geq D_c$, the DMI strength is large enough to fully stabilize the domain wall into a Néel configuration, with a chirality fixed by the sign of D_{DM} . Here, the magnetization between the two domains turns cycloidal and has an in-plane magnetization perpendicular to the wire axis. This Néel wall is shown in Figure 2.4 (b) and (c) for $\psi = 0$ (Néel right) and $\psi = \pi$ (Néel left). The two different possible chiralities are energetically not equivalent. In opposite to the Bloch wall, the Néel wall shows magnetic charges on both sides of the wall, creating an additional demagnetization field. This chiral domain wall type with its magnetization along the nanowire axis permits a uniform motion with very high efficiency induced by the spin Hall effect [80]. The two different chiralities (left and right) define the propagation direction (against or with the electron flow). In the intermediate regimes, $D_{\text{DM}} < D_c$, the domain wall moments reorient gradually towards the Bloch configuration as the DMI strength decreases. The angle ψ can reach any possible value $0 < \psi < \pi$ through the competition of the different energies.

2.2 Measuring the DMI strength with the NV magnetometer

An exact measurement of the DMI strength is important but not easy to achieve. In the following, we will discuss the challenges of a precise DMI measurement (§2.2.1). We have seen, that this interaction gradually changes Néel walls to Bloch domain walls. A measurement of the domain wall type can consequently reveal the strength of the DMI interaction. We will see how this can be done by analyzing the stray field created above a domain wall (§2.2.2). In the last paragraph we examine the precision of our DMI measurement method (§2.2.3).

2.2.1 The challenges of a precise DMI measurement

As explained in the previous sections, the DMI is an interfacial interaction and is mediated by the spin-orbit coupling arising from the heavy metal underlayer of the samples. A large number of experiments to date have relied on the analysis of domain wall motion under magnetic fields [81, 82] and currents [59, 58, 60, 83] to determine the strength of the DMI in ultrathin ferromagnetic films. However, such methods rely heavily on assumptions concerning the internal spin structure of the domain wall and its dynamics, owing to the large number of spin torques involved in the domain wall dynamics [84] as well as the influence of pinning effects in the creep regime [85, 86].

It was recently demonstrated that direct measurements of the DMI strength can be obtained by monitoring the non-reciprocal propagation of spin waves with Brillouin light spectroscopy in the Damon-Eshbach geometry [87, 88]. Although accurate, these measurements are always averaged over length scales of several microns, and thus can not be used to investigate local variations of the magnetic properties in the samples. An alternative strategy to draw conclusions on the DMI consists in measuring the inner structure of domain walls with the aim of observing the transition from a Bloch to a Néel configuration induced by the DMI [89, 90, 91]. In a former work in our group, it was demonstrated that the nature of domain walls in ultrathin ferromagnets can be inferred through quantitative stray field measurements with the NV based scanning magnetometer [92]. We will use this approach to determine the DMI strength with the help of the NV magnetometer. Without making any assumptions on domain wall dynamics, this technique enables direct measurements of the domain wall structure under ambient conditions.

2.2.2 Measuring DMI via local magnetic stray fields

In the sample geometries with broken inversion symmetry, the strength of the interfacial DMI can be large enough to modify the inner structure of the domain wall as described in Section 2.1.3. The latter is characterized by the angle ψ between the in-plane domain wall magnetization and the x -axis perpendicular to the domain wall (Figure 2.6 (a)). For a Bloch domain wall, $\psi = \pm\pi/2$ and the magnetization rotates as a spiral while crossing the domain wall as was visualized in Figure 2.4 (a). A Néel domain wall corresponds to $\psi = 0$ or $\psi = \pi$, leading to a cycloidal rotation of the magnetization (Figure 2.4 (b)). In both cases, the two possible

values of ψ determine the chirality (right or left) of the domain wall.

The interplay between the domain wall structure and the DMI can be inferred by considering the surface energy density σ [J/m²]. We remind that in the case of thin films with perpendicular anisotropy it is expressed as [81]

$$\sigma = 4\sqrt{AK_{\text{eff}}} + \frac{\mu_0 M_s^2 t \ln 2}{\pi} \cos^2 \psi - \pi D \cos \psi . \quad (2.19)$$

Here A is the exchange constant, K_{eff} is the effective anisotropy. M_s is the saturation magnetization, t is the thickness of the magnetic layer and D_{DM} is the micromagnetic DMI constant. The domain wall structure is obtained by minimizing the domain wall energy with respect to ψ . This leads to the relation $D_{\text{DM}}(\psi)$ as described by Equation 2.18.

The domain wall structure, and thus the DMI strength, can be determined through quantitative measurements of the stray field above the domain wall [93, 92]. Here, the out-of-plane magnetization component M_z of a Néel wall, and consequently also the generated magnetic stray field \mathbf{B}^\perp , is considered identical to the one of a Bloch wall. This is schematically depicted in the first row of Figure 2.6 (b). In the second row, the difference between the stray field of a Bloch and a left and right Néel wall is illustrated. The magnetic stray field \mathbf{B}^\parallel , induced

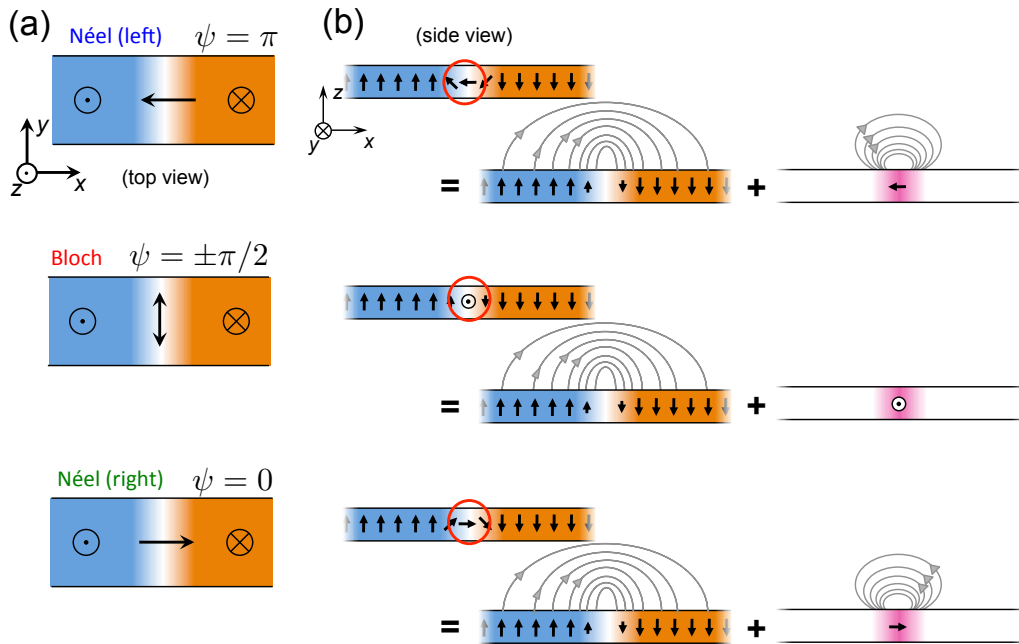


Figure 2.6 – **Stray field over different domain walls.** (a) Top view of the magnetization pattern in left Néel, Bloch and right Néel walls. The important difference is the behavior of the magnetization inside the wall, which is characterized by the angle ψ . (b) The angle ψ is linked to the in-plane component of the magnetization in a domain wall and thus to the stray field over a domain wall. The magnetic field over each domain wall can be divided into the contribution from the out-of-plane component and the in-plane component, which differs for different DMI strengths. Consequently the DMI strength can be determined by measuring the stray field over a domain wall.

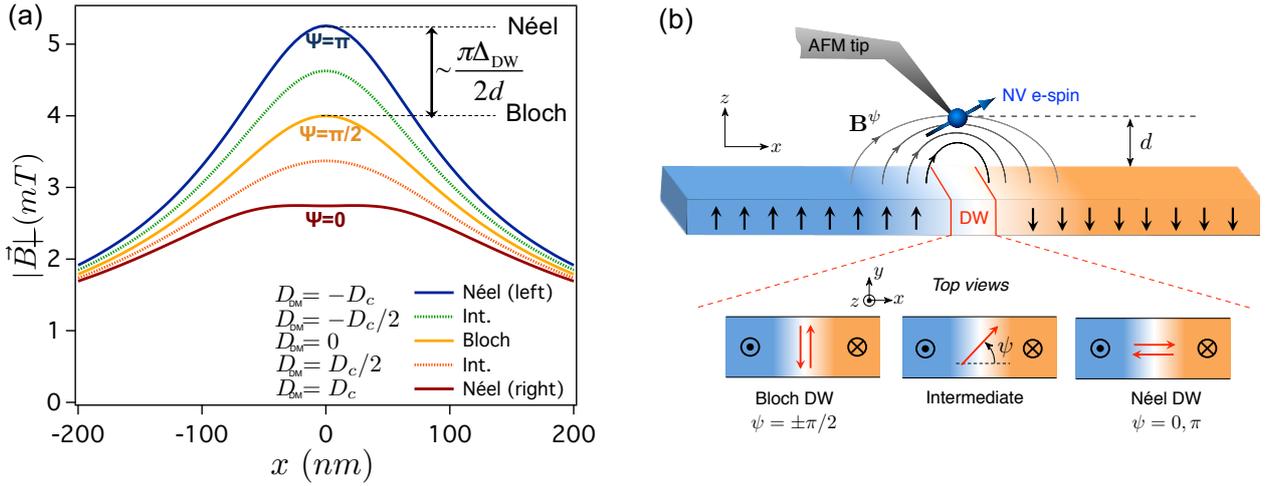


Figure 2.7 – **Principle of the experiment.** (a) A scanning NV magnetometer is used to measure the stray field \mathbf{B}^ψ produced by a domain wall in a perpendicularly magnetized ferromagnetic wire (black arrows). The bottom panels show top views of the magnetization for various domain wall structures, characterized by the angle ψ between the in-plane magnetization (red arrows) and the x -axis. (b) Stray field component $B_x^\psi(x)$ calculated for different values of the DMI strength, corresponding to different ψ angles. The calculation is performed at a distance $d = 100$ nm from a magnetic layer with thickness $t = 1$ nm, saturation magnetization $M_s = 1$ MA/m and domain wall width $\Delta_{\text{DW}} = 20$ nm. With these parameters $D_c = 0.17$ mJ/m².

by the in-plane magnetization, differs for different wall types. Considering a one-dimensional model with an infinitely long domain wall along the y axis, the total stray field can be described as [92]

$$\mathbf{B}^\psi(x) = \mathbf{B}^\perp(x) + \mathbf{B}^\parallel(x) \cos \psi. \quad (2.20)$$

Over the domain wall, field is divided into the two contributions \mathbf{B}^\perp and \mathbf{B}^\parallel . \mathbf{B}^\perp (resp. \mathbf{B}^\parallel) results from the variation of the out-of-plane (resp. in-plane) magnetization while crossing the domain wall along the x direction. The field \mathbf{B}^\perp arising from the out-of-plane component of the magnetization can be considered as an abrupt transition of the magnetization $M_z = M_s \tanh(x/\Delta_{\text{DW}})$ at the wall position. This situation is similar to the field above the edge of a magnetic wire as described in Chapter 1, simply with twice the amplitude. Consequently, the stray field components \mathbf{B}^\perp at a distance d above the domain wall located at $x = 0$ are given by

$$\begin{cases} B_x^\perp(x) = \frac{\mu_0 M_s t}{\pi} \frac{d}{x^2 + d^2} \\ B_y^\perp(x) = 0 \\ B_z^\perp(x) = -\frac{\mu_0 M_s t}{\pi} \frac{x}{x^2 + d^2}. \end{cases} \quad (2.21)$$

The in-plane magnetization component is in general given by $\mathbf{M}_\parallel = M_\parallel(x) [\cos(\psi) \mathbf{u}_x + \sin(\psi) \mathbf{u}_y]$, where

$M_{\parallel} = M_s / \cosh(x/\Delta_{\text{DW}})$. We are especially interested in the component $M_{\parallel}(x)\cos(\psi)\mathbf{u}_x$ of the magnetization which defines the difference between Bloch and Néel wall.

$$\begin{cases} B_x^{\parallel}(x) = \frac{1}{2}\mu_0 M_s t \Delta_{\text{DW}} \frac{x^2 - d^2}{(x^2 + d^2)^2} \\ B_y^{\parallel}(x) = 0 \\ B_z^{\parallel}(x) = \mu_0 M_s t \Delta_{\text{DW}} \frac{xd}{(x^2 + d^2)^2} \end{cases}, \quad (2.22)$$

where $\Delta_{\text{DW}} = \sqrt{A/K_{\text{eff}}}$ is the domain wall width parameter. These simple analytic formulas are valid for $d \gg (\Delta_{\text{DW}}, t)$ [92]. This approximation is reasonable in our case since Δ_{DW} is in the order of tens of nanometers and t generally smaller than 1 nm, while the flying height of a nanodiamond attached to an AFM tip over the sample results in probe to sample distances in the order of ~ 100 nm. From Equation 2.22 the importance of a calibration measurement (see Figure 2.8 (c) or Section 1.2.3) becomes evident. Indeed, we need to determine the parameters M_s and d with high precision. Then the parameter Δ_{DW} defines the difference in stray field between Bloch and Néel wall.

In terms of amplitude, the component \mathbf{B}^{\parallel} is maximal for $\cos(\psi) = \pm 1$, which means for a Néel domain wall. Defining this maximal amplitude as \mathbf{B}_0^{\parallel} gives:

$$\mathbf{B}_{\text{DW}} = \mathbf{B}^{\perp} + \cos(\psi)\mathbf{B}_0^{\parallel}.$$

In the case of a Bloch wall $\mathbf{B}_{\text{DW}} = \mathbf{B}^{\perp}$ and $\cos(\psi) = 0$ which shows the similarity between the stray field measured over a Bloch wall and the one measured over the edge of a magnetic wire for the calibration. The difference between the maximal field \mathbf{B}^{\perp} produced by a Bloch wall and the one of a Néel wall $\mathbf{B}^{\perp} \pm \mathbf{B}_0^{\parallel}$ varies with $B_{0,\text{max}}^{\parallel}/B_{\text{max}}^{\perp} \sim \pi\Delta_{\text{DW}}/2d$. This dependence shows that a measurement closer (in distance) to the wall allows a better differentiation between Bloch and Néel wall. At a probe to sample distance $d \sim 100$ nm the difference is typically in the order of $\sim 10\%$. In the investigated thin film samples, the stray fields are in the order of a few militesla at a distance of 100nm and the difference in field of Bloch and Néel wall accounts to $\sim 100 \mu\text{T}$. The NV scanning magnetometer with a nanodiamond attached to the apex of a Akiyama AFM tip is thus the ideal probe for this type of measurement.

Figure 2.7 (a) shows the stray field component $B_x^{\psi}(x)$ for different values of D_{DM} at a distance $d = 100$ nm above the domain wall. This graph illustrates how local stray field measurements enable to infer the inner structure ψ of the domain wall, from which the sign and the strength of DMI can be extracted. More precisely, a value of D_{DM} can be obtained as long as $|D_{\text{DM}}| \leq D_c$. In ultrathin ferromagnets ($t < 1$ nm), D_c is typically in the range of 0.2 mJ/m^2 . The method is therefore sensitive to weak DMI strength. If $|D_{\text{DM}}| \geq D_c$, the domain wall is fully stabilized in the Néel configuration ($\psi = 0, \pi$) and stray field measurements can only give the sign of DMI and a lower bound on D_{DM} .

The experimental procedure is sketched in Figure 2.8. A diamond nanocrystal hosting a single NV defect is grafted at the apex of an atomic force microscope (AFM) and scanned above a domain wall in a thin ferromagnetic wire. At each point of the scan, the stray magnetic field is measured with a typical sensitivity of $10 \mu\text{T}/\text{Hz}^{1/2}$, by recording the Zeeman shift Δf_{NV} of the NV defect electronic spin sublevels through optical detection of the magnetic resonance [14]. In the weak magnetic field regime ($< 5 \text{ mT}$), the Zeeman shift follows

$$\Delta f_{\text{NV}} \approx \sqrt{\left(\frac{g\mu_B}{h} B_{\text{NV}}\right)^2 + E^2}, \quad (2.23)$$

where $\frac{g\mu_B}{h} \approx 28 \text{ GHz/T}$, E is the transverse zero-field splitting parameter of the NV defect, which is typically in the range of few MHz, and B_{NV} is magnetic field projection along the NV defect quantization axis \mathbf{u}_{NV} as

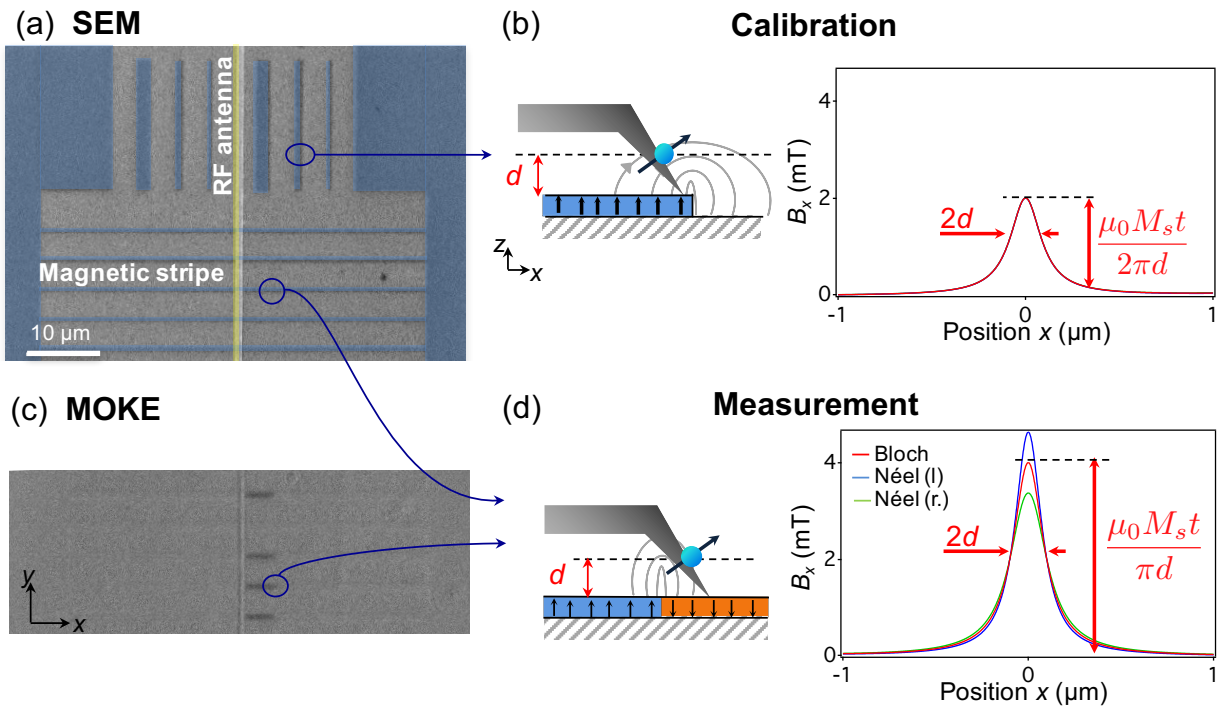


Figure 2.8 – **MOKE image of sample and measurement principle.** (a) Scanning electron microscope (SEM) image of a typical sample studied in this work with magnetic microwires. The gold stripline (yellow color) is used for domain wall nucleation and as a microwave antenna for scanning-NV magnetometry. (b) Before every experiment a calibration measurement is performed by measuring the magnetic field over the edges on a microwire parallel to the microwave antenna. In this way M_s and d are determined. (c) The MOKE image helps to localize domain walls in the sample. Close to the microwave wire a change in color in the magnetic stripes indicates the change in magnetization direction and consequently the position of a domain wall. (d) In the last step the actual domain wall measurement is performed at the location indicated by the MOKE image. The magnetic field is recorded as described in Section 1.3 and a full magnetic field map of the wall is obtained. The field from a Bloch wall should show two times more field than recorded over the edge of the micro wire in the calibration measurement.

discussed in Chapter 1. A summary of the measurement procedure is given in Figure 2.8. All the investigated **samples** are thin ferromagnetic heterostructures with perpendicular magnetic anisotropy grown on top of a heavy metal substrate that possesses a large spin-orbit coupling. A SEM image of a typical sample is shown in Figure 2.8 (a). Magnetic wires parallel and perpendicular with respect to the antenna were fabricated. This geometry is ideal to compare the field over an edge of a magnetic wire (parallel to gold antenna) to the domain wall stray field (nucleated in a wire perpendicular to the gold antenna). For an optimal measurement precision, a nanodiamond with an angle of $\theta \sim 90^\circ$ and $\phi \sim 0^\circ$ is desirable. Once a nanodiamond with a good orientation was attached, a **calibration measurement** as described in Chapter 1 is performed in order to infer M_s and d (Figure 2.8 (b)). We can now proceed to the **domain wall measurement**. With the help of a polar Kerr microscopy (MOKE) the domain wall position in the magnetic wires is located (Figure 2.8 (c)). A full magnetic field map of the domain wall is recorded. A linecut perpendicular to the wall shows the \sim two times higher stray field over a domain wall compared to the calibration measurement on the edge of a wire. (Figure 2.8 (d)). This measurement can now be compared with micromagnetic calculations in order to extract the inner structure of the domain wall.

2.2.3 Measurement precision

The crucial step to determine the DMI by a measurement of the stray field over a domain wall is the calibration of the experiment. It was mentioned that the field over a Bloch wall \mathbf{B}^\perp is twice as big as the field over the edge of a magnetic wire. By comparing the field over a wall and the field over the edge of the magnetic wire, the nature of the domain wall (and the chirality in case of a Néel wall) can directly be determined. Since we want to compare these two fields, and the NV measures only the projection of the field on its axis, it is highly important that the calibration wire and the domain wall are parallel. A sample with calibration stripes and domain walls can be seen in Figure 2.8 (a) and (b). Once such a measurement is performed, the uncertainty in distinguishing a Bloch and a no-Bloch wall lies solely in the magnetic field measurement precision which is in the order of $\sim 10 \mu\text{T}/\sqrt{\text{Hz}}$ per point.

To insure a high precision measurement, the projection of the field over a domain wall on the NV center axis should be as high as possible. To maximize the field B_x projected on \mathbf{u}_{NV} over a domain wall lying along the y-axis a NV oriented perpendicular to the domain wall ($\theta = 90^\circ, \phi = 0^\circ$) is advantageous. A nanodiamond is attached and reattached to the AFM tip until a desired direction of the NV orientation is achieved.

In these conditions, the most important error arises from the uncertainties of the parameters utilized to predict the field with the analytic formula in the case of a Néel wall. As illustrated by Equation 2.21 and 2.22, the stray field distribution above the domain wall strongly depends on d , $M_s t$ and Δ_{DW} . Any imprecision on these parameters directly translates into uncertainties on the measurement of the angle ψ , and thus of the DMI strength. The surface density of magnetic moments $M_s t$ and the distance d to the magnetic layer can be measured with high accuracy by recording the magnetic field distribution across the edge of a uniformly magnetized

ferromagnetic wire [54]. The error calculation for these parameters can be found in the Annex. The main source of uncertainties then comes from the imperfect knowledge of the domain wall width, $\Delta_{\text{DW}} = \sqrt{A/K_{\text{eff}}}$. In this expression, although the effective anisotropy K_{eff} can be measured with high precision, the exchange constant A has so far been difficult to determine accurately in ultra-thin films. For instance, measurements of this parameter vary from $A \approx 10$ pJ/m to $A \approx 30$ pJ/m in ultrathin CoFeB layers [63] and consequently are prone to an error in the order of 100%. This ultimately translates into an error of $\sim 10\%$ on the predicted field \mathbf{B}_0^{\parallel} . This is the main source of uncertainty in the measurement of the domain wall structure. The precise error calculation for this method can be found in the supplementary information of reference [92].

In conclusion, the important points to perform an accurate measurement are (i) the calibration on a stripe which is parallel to the domain wall, and (ii) a NV center with an axis perpendicular to the wall. The estimation for the field of a Bloch wall and the comparison to the measurement is more precise since the poorly known parameter A does not have to be taken into account. Applying this measurement method and error calculations the measurements and results on different samples will be presented in the following. An important point is the non-perturbative local magnetic probes, that does not induce any magnetic back-action on the sample. This is the key to quantify small changes in the spin structure, such as the internal spin arrangement within a magnetic domain wall, and to probe the local variations in magnetic properties such as the DMI.

2.3 Engineering the DMI strength in different heterostructures

In the following paragraphs we will present the result on perpendicularly magnetized X|CoFeB(1nm)|MgO heterostructures, with different metal underlayers, namely X=Ta, TaN and W. The investigated thin film samples were deposited by magnetron sputtering on a Si|SiO₂(100 nm) wafer and magnetic microwires were patterned onto the samples by using a combination of e-beam lithography and ion milling. E-beam lithography was performed in order to define a gold stripline, which is connected to a microwave generator and serves as an antenna to record the Zeeman shift of the NV defect magnetometer [42] and to nucleate domain walls in the microwires through the Oersted field produced by a current pulse. The geometry of the sample is shown in Figure 2.8 and a summary of the magnetic heterostructures studied is given in Table 2.1.

The work described in this section was performed in collaboration with

- M. Hayashi at the National Institute for Materials Science (NIMS) in Japan
- J.-V. Kim and J.P. Adam from the Institut d'Electronique Fondamentale in Orsay, France
- S. Rohart and A. Thiaville at LPS, Orsay, France

In the following we will show that for a X=Ta underlayer Bloch domain walls are stabilized (§2.3.1). In the case of nitrogen doping of the Ta underlayer (X=TaN) a light deviation toward the Néel case is observed (§2.3.2). For $X = W$ a right-handed Néel configuration is obtained (§2.3.3).

2.3.1 Bloch domain wall in Ta|CoFeB|MgO

The method presented in Section 2.2.2 is employed to measure the domain wall structure and extract the DMI constant in different magnetic heterostructures. The first studied sample (Sample A) has Ta as metal underlayer. Sample A is a Ta(5nm)|CoFeB(1nm)|MgO(2nm) trilayer stack as depicted in Figure 2.9 (a). A typical distribution of the Zeeman shift Δf_{NV} recorded with scanning NV magnetometry above a domain wall in a 1.5- μm -wide wire is shown in Figure 2.9 (c), together with the simultaneously recorded AFM image in Figure 2.9 (b). In order to extract the domain wall structure, the magnetic field distributions calculated with Equation 2.21 were first converted into Zeeman shift distributions while taking into account the NV defect quantization axis, and then compared to the experimental data [92]. A typical linecut of the magnetic field distribution across the domain wall is shown in Figure 2.9 (d) together with the theoretical predictions for various domain wall structures. Here the experimental data are very well reproduced with a pure Bloch-type wall structure. This result indicates that the DMI can be safely neglected in a Ta|CoFeB(1nm)|MgO trilayer stack, as already reported in previous studies [92, 83].

2.3.2 The effect of nitrogen doping and thickness of the Ta underlayer

It was recently shown that the magnetic properties of ultrathin CoFeB films can be significantly modified by doping the Ta underlayer with nitrogen. Such a doping leads to an enhanced interface perpendicular magnetic anisotropy [94]. In addition, current-driven domain wall motion experiments have suggested that the DMI strength could also be enhanced by using a TaN underlayer [83]. In the following, we analyze the effect of nitrogen doping on the DMI strength by measuring the structure of domain walls in Sample B, a TaN_{0.7%}(4nm)|CoFeB(1nm)|MgO(2nm) trilayer stack (Figure 2.10 (a)). The TaN underlayer was formed by mixing N₂ gas into the Ar gas atmosphere during sputtering of Ta. Here the ratio between the N₂ (S_{N_2}) and the Ar (S_{Ar}) gas flows is $Q = S_{\text{N}_2}/(S_{\text{N}_2} + S_{\text{Ar}}) = 0.7\%$, which results in an atomic composition of Ta₄₈N₅₂. The film was finally post-annealed at 300°C for one hour in vacuum.

The magnetic field distribution recorded with scanning NV magnetometry above a domain wall nucleated in a 1- μm -wide magnetic wire of sample B is shown in Figure 2.10 (b). Comparison with theoretical predictions indicates a small deviation of the domain wall structure towards a right-handed Néel configuration (Figure 2.10 (c)). This result confirms that the DMI strength is slightly enhanced through nitrogen doping of the Ta underlayer. The experimental data are well reproduced for a domain wall structure with $\psi = 75 \pm 5^\circ$, corresponding to a positive DMI strength $D_{\text{DM}} = 0.03 \pm 0.01 \text{ mJ/m}^2$. Similar results were obtained for two other domain walls in Sample B. We note that this value is one order of magnitude smaller than the one inferred by Torrejon *et al.* in the same sample through current-driven domain wall motion experiments [83]. This discrepancy is attributed to the difficult interpretation of domain wall motion experiments [81, 85], which require strong assumptions on the domain wall dynamics in order to quantify the current-induced spin torques at play (see Section 2.4 for a detailed discussion). Scanning-NV magnetometry rather provides a direct measurement of the DMI strength, with a domain wall at rest.

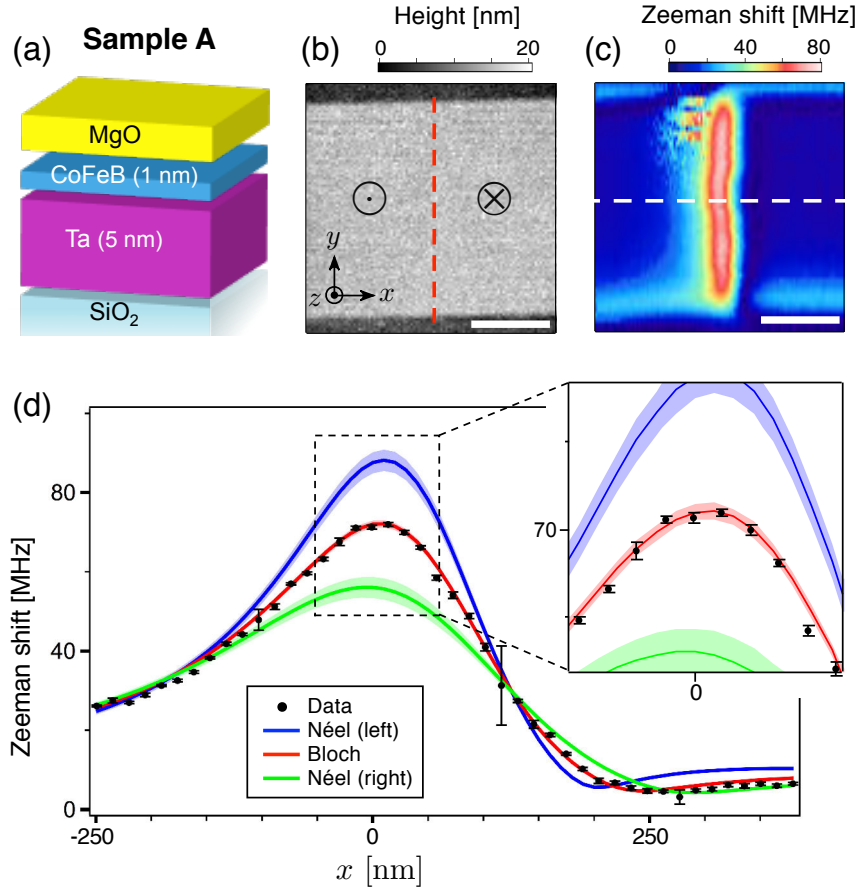


Figure 2.9 – **Ta as heavy metal underlayer.** (a) Sketch of sample A. (b) AFM image and (c) corresponding Zeeman-shift distribution recorded by scanning the NV magnetometer above a domain wall isolated in a $1.5\text{-}\mu\text{m}$ -wide wire of sample A. Scale bar: 500 nm. (d) Linecut extracted from the white dashed line in (c). The markers are experimental data and the solid lines are the theoretical predictions for a Bloch (red), a Néel left (blue) and a Néel right (green) domain wall structure. The shaded areas include all the uncertainties in the theoretical predictions, which are dominated by uncertainties on the exchange constant A (see main text). The quantization axis of the NV defect \mathbf{u}_{NV} is characterized by the spherical angles ($\theta = 62^\circ$, $\phi = -25^\circ$) in the laboratory frame of reference (x, y, z), the probe-to-sample distance is $d = 123 \pm 3$ nm and $M_s t = 930 \pm 30$ μA . We note that the Zeeman shift does not fall to zero far from the domain wall, because of the transverse zero-field splitting parameter of the NV defect E .

Next, the effect of the TaN underlayer thickness on the DMI strength is investigated. Current-induced domain wall motion experiments have indicated modifications of the DMI strength with TaN thickness [83], which could appear surprising owing to the interfacial origin of DMI. In order to check these results, scanning NV magnetometry was used to image domain walls in Sample C, a $\text{TaN}_{0.7\%}(1\text{ nm})|\text{CoFeB}(1\text{ nm})|\text{MgO}(2\text{ nm})$ stack shown in Figure 2.10(d). Here the TaN thickness is reduced to 1 nm. A typical magnetic field distribution recorded above a domain wall in a $1\text{-}\mu\text{m}$ -wide wire of Sample C is shown in Figure 2.10(e). Comparison with theoretical predictions reveals once again a deviation of the domain wall structure towards the right-handed Néel

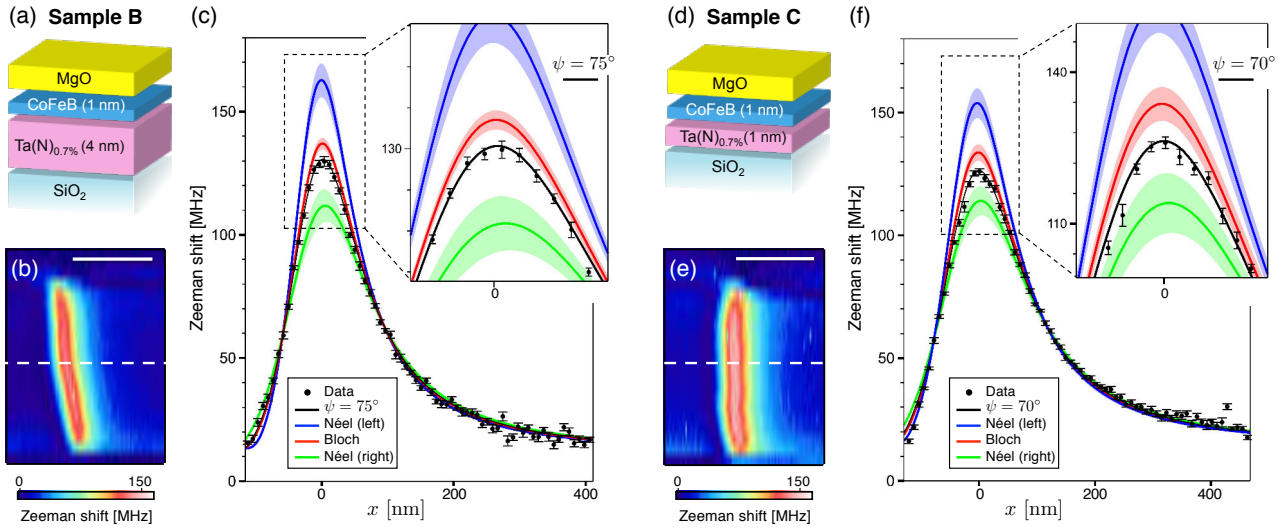


Figure 2.10 – **Effect of nitrogen doping of the Ta underlayer.** (a) Sketch of Sample B. (b) Zeeman-shift distribution recorded by scanning the NV magnetometer above a domain wall isolated in a $1\text{-}\mu\text{m}$ -wide wire of sample B. Scale bar: 500 nm . (c) Linecut extracted from the white dashed line in (b). The data (markers) are well reproduced by a domain wall structure with $\psi = 75^\circ$ (black solid line). The quantization axis of the NV defect \mathbf{u}_{NV} is characterized by the spherical angles ($\theta = 117^\circ$, $\phi = 12^\circ$) in the laboratory frame of reference (x, y, z), the probe-to-sample distance is $d = 61 \pm 6\text{ nm}$ and $M_s t = 800 \pm 80\ \mu\text{A}$. (d) Sketch of Sample C with a 1-nm -thick TaN underlayer. (e) Zeeman-shift distribution above a domain wall isolated in a $1\text{-}\mu\text{m}$ -wide wire of sample C. Scale bar: 500 nm . (f) Linecut extracted from the white dashed line in (e). The probe-to-sample distance is $d = 80 \pm 5\text{ nm}$ and $M_s t = 1040 \pm 50\ \mu\text{A}$. In (c) and (f), the shaded areas include all the uncertainties from the theoretical predictions.

configuration ($\psi = 70 \pm 5^\circ$), which corresponds to a DMI strength $D_{\text{DM}} = 0.06 \pm 0.02\text{ mJ/m}^2$ (Figure 2.10(f)). Similar results were inferred from two other domain walls in Sample C. This value is close to the one measured in Sample B with a 4-nm -thick TaN underlayer. We therefore conclude that the modification of the underlayer thickness does not translate into a significant change of the DMI strength for these particular samples. This is in good agreement with the interpretation of the DMI as a surface interaction occurring at the interface between the heavy metal substrate and the magnetic layer.

2.3.3 Néel domain walls in $\text{W}|\text{CoFeB}|\text{MgO}$

The last underlayer considered is W, in Sample D, a $\text{W}(1\text{nm})|\text{CoFeB}(1\text{nm})|\text{MgO}(2\text{nm})$ trilayer stack, which was post-annealed at 300°C for one hour in vacuum. The sample structure is shown in Figure 2.11 (a). The magnetic field distributions recorded above three different domain walls in $1\text{-}\mu\text{m}$ -wide wires of this sample are presented in Figure 2.11(b)-(d). The first domain wall is fully stabilized in the right-handed Néel configuration as can be seen in the graph in Figure 2.11 (b). In this case, a lower bound can be determined for the DMI constant $D_{\text{DM}} > D_c = 0.12\text{ mJ/m}^2$, in good agreement with the results obtained through current-induced domain wall motion experiments in the same system [83]. The second domain wall also exhibits a right-handed Néel configuration within the uncertainty of our technique (Figure 2.11 (c)). However, in the case of the third domain

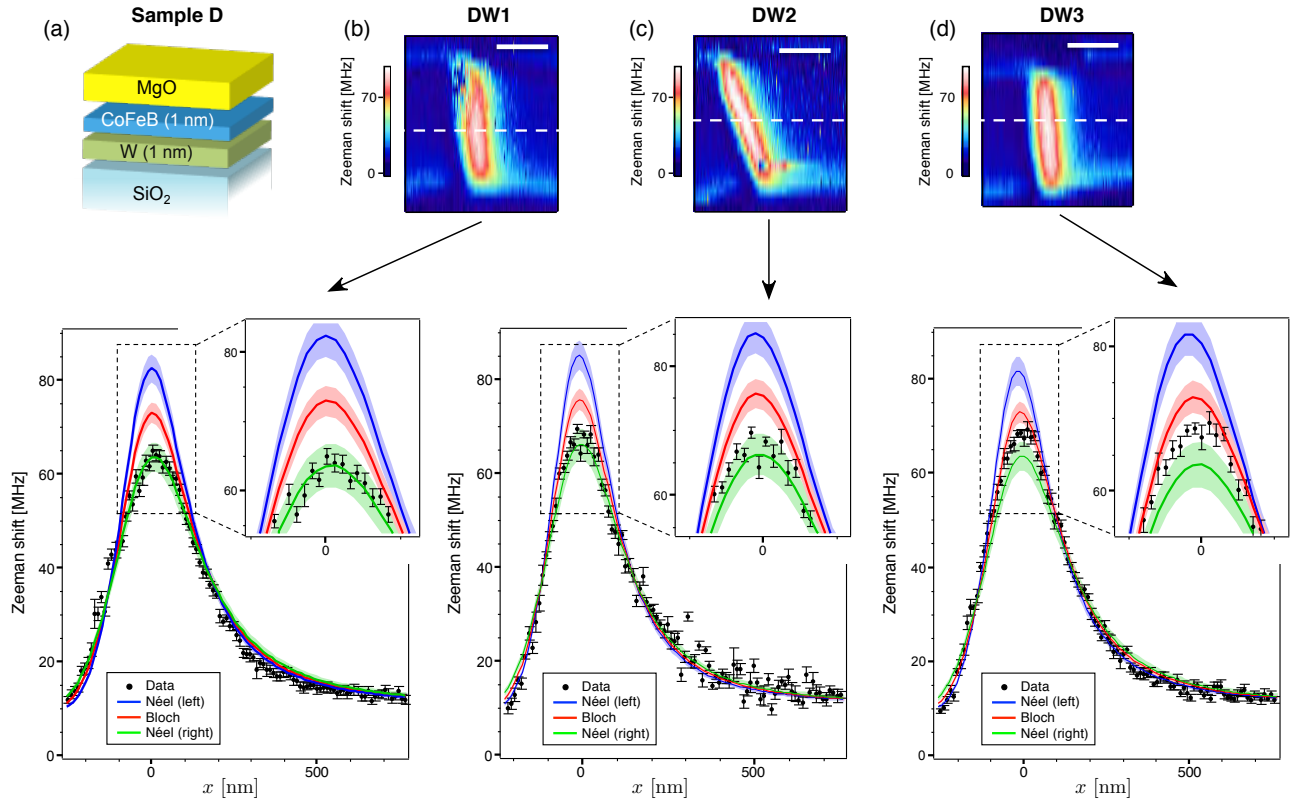


Figure 2.11 – **W as heavy metal underlayer.** (a) Sketch of Sample D. (b) to (d) Magnetic field distributions recorded above three different domain walls nucleated in 1- μm -wide wire of Sample D. Scale bar: 500 nm. The linecuts are extracted from the white dashed line in (b), (c) and (d). The shaded areas include all the uncertainties in the theoretical predictions. The quantization axis of the NV defect \mathbf{u}_{NV} is characterized by the spherical angles ($\theta = 110^\circ$, $\phi = 12^\circ$) in the laboratory frame of reference (x, y, z), the probe-to-sample distance is $d = 114 \pm 10$ nm and $M_s t = 820 \pm 100$ μA . It should be noted that the tilt angle of the domain wall is taken into account in the theoretical predictions [92].

wall, the magnetic field distribution clearly indicates a domain wall structure lying between the Bloch and the right-handed Néel configurations (Figure 2.11 (d)). Here, the magnetic field distribution is well reproduced for $\psi = 66 \pm 5^\circ$, corresponding to $D_{\text{DM}} = 0.05 \pm 0.02$ mJ/m².

Such a discrepancy between experimental results obtained in different areas of Sample D can have different origins. First, it could originate from local variations of the saturation magnetization M_s . However, such variations would lead to localized stray field components, as reported in Reference [54]. Since these features were not observed in our experiment, inhomogeneities in the magnetic moment density M_s can be excluded. Other possibilities are spatial variations of the effective anisotropy K_{eff} and/or the exchange constant A . Although D_c , hence ψ , would not be affected by such variations, it would however lead to a change of the domain wall width Δ_{DW} , and therefore of the stray field component \mathbf{B}^{\parallel} resulting from the variation of the in-plane component of the magnetization (see Equation 2.22). For example, the difference in stray field between a Bloch and a Néel-type wall would be reduced for a thinner domain wall. The data shown in Figure 2.11(d) could then be

Name	Sample composition	M_s [A/m] · 10 ⁵	Δ_{DW} [nm]	DW structure	D_{DM} [mJ/m ²]
A	Ta(5) Co ₄₀ Fe ₄₀ B ₂₀ (1) MgO(2)	9.3 ± 0.3	20 ± 5	Bloch	0 ± 0.01
B	TaN _{0.7%} (4) Co ₂₀ Fe ₆₀ B ₂₀ (1) MgO(2)	8.0 ± 0.8	8 ± 2	Bloch ^a	0.03 ± 0.01
C	TaN _{0.7%} (1) Co ₂₀ Fe ₆₀ B ₂₀ (1) MgO(2)	10.4 ± 0.5	8 ± 2	Bloch ^a	0.06 ± 0.02
D	W(1) Co ₂₀ Fe ₆₀ B ₂₀ (1) MgO(2)	8.2 ± 1	10 ± 2.5	Néel-right ^b	$D_{\text{DM}} > 0.12$
E	Pt(3) Co(0.6) AlO _x (2) [92]	11.2 ± 0.3	6 ± 1.5	Néel-left	$D_{\text{DM}} < -0.1$

Table 2.1 – **Overview of the samples studied in this work.** The saturation magnetization M_s is measured with scanning NV magnetometry following the procedure described in Ref. [54]. The domain wall width parameter Δ_{DW} is obtained by using measurements of K_{eff} with vibrating sample magnetometry and assuming an exchange stiffness $A = 22 \pm 10$ pJ/m [95]. The strength and the sign of DMI is calculated from Equation 2.18 using the measured angle ψ . Sample E was measured in a previous study [92]. The numbers in brackets correspond to the film thickness in nm.

^a slight deviation towards a right-handed Néel wall.

^b deviations within different domain walls in the sample.

explained if the domain wall width is reduced by roughly a factor of two. This is quite unexpected owing to the good homogeneity of M_s in the sample. Furthermore such a variation in Δ_{DW} would lead to large variations on the domain wall energy, which would create strong pinning sites for the domain wall. This is not consistent with the low depinning fields observed in domain wall motion experiments in the same trilayer system [88]. Another possible reason explaining the discrepancy between the experimental results is a spatial variation of the DMI strength in the sample. This variation of D_{DM} could result from local modifications of the interface between the heavy-metal substrate and the magnetic layer, which is highly probable in a sample deposited by sputtering. These experiments illustrate how scanning NV magnetometry enables measuring local modifications of the magnetic properties in ultrathin ferromagnets, which would be averaged out by using global techniques like Brillouin light spectroscopy [87].

Conclusively, we have demonstrated that the DMI is significantly increased when the Ta underlayer is replaced by W in perpendicularly magnetized X|CoFeB|MgO heterostructures. The DMI can even be strong enough to fully stabilize the domain walls onto the right-handed Néel configuration. We note that by changing the interface to Pt/Co, it was also demonstrated that the sign of DMI can be reversed and the domain walls then exhibit a left-handed Néel structure ($D_{\text{DM}} < -0.1$ mJ/m²) [92]. These experiments, which are summarized in Table 2.1, directly demonstrate how the strength and the sign of DMI can be tuned by engineering the interface between the heavy metal substrate and the ferromagnetic layer.

2.4 Other methods to measure the DMI and the virtues of NV magnetometry

The DMI can be seen as an effective in-plane chiral field $\mu_0 H_{\text{DMI}} = D_{\text{DM}}/M_s \Delta_{\text{DW}}$ acting on the domain wall. A well-established way to infer H_{DM} , and thus the DMI strength, is based on current-driven domain wall motion under applied magnetic fields [59, 60, 83]. In these experiments, H_{DMI} is determined by measuring the longitudinal field H_L at which the domain wall velocity goes to zero. The interpretation of the results requires to consider at least four different current-induced spin torques in the domain wall dynamics: the adiabatic and nonadiabatic torques related to spin-polarized current flow in the ferromagnetic layer, and the spin Hall and Rashba torques resulting from the current flow in the heavy metal substrate or at the heavy-metal/ferromagnet interface. These torques remain difficult to quantify precisely in experiments [84]. Furthermore, even if their relative strengths were known, one would also require detailed knowledge of how much of the electrical current flows in each of the metallic layers in the stack - a challenging current-in-plane problem from both experimental and theoretical points of view. Finally, the one-dimensional model used to evaluate DMI may not fully represent the current and field driven motions of domain walls. In particular, the in-plane field dependence of domain wall velocity found experimentally does not agree well with that predicted by the model for samples with strong pinning [83], which may influence the estimation of DMI. Determining the DMI field from current-driven domain wall motion is therefore prone to large uncertainties. It should also be noted that the current driven motion of domain walls probes the DMI of a moving domain wall whereas the NV-microscopy reveals that of a domain wall at rest.

The effective DMI field can also be inferred through field-driven domain wall motion. Although current-induced spin torques are not involved in this method, it still relies on the analysis of the domain wall dynamics. For dynamics under large fields, where the wall is driven into steady state motion, it is known that strong deformations in the lateral domain wall profile can appear in perpendicular anisotropy materials with weak damping. The wall structure then becomes jagged in the precessional regime where the precessing magnetization leads to dynamical Bloch and Néel wall states. This results in an anomalous behavior in the wall velocity versus field curve [95, 96]. If one were to interpret these curves with a standard one-dimensional wall model, one might mistakenly attribute the anomalous behavior to some fictitious internal field, which would be erroneous. As such, wall motion under fields alone can also be fraught with complications linked to the precise description of domain wall dynamics [85]. On the other hand in the creep regime, where the wall is pinned and motion occurs via thermal activation, the key parameter is the domain wall energy. Again, a number of strong assumptions are made to translate asymmetries in the wall velocities under applied fields to the DMI. Despite these general caveats, we remark here that recent measurements of the DMI strength obtained from domain wall creep gave similar results to those obtained in this work with scanning NV magnetometry for the same samples [88]. We note that for both methods, the accuracy of the measurement is limited by the imperfect knowledge of the domain wall width parameter Δ_{DW} .

Another strategy to determine the DMI strength relies on direct imaging of the magnetization at the wall position. This can be achieved either by spin-polarized scanning tunneling microscopy [90] or by spin-polarized low-energy electron microscopy [91]. However, these techniques, which require highly complex experimental apparatus with ultrahigh vacuum and a dedicated sample preparation, can hardly be used to study practical spintronic devices. Direct imaging of the domain wall structure can also be realized with photoemission electron microscopy combined with X-ray magnetic circular dichroism. This method was recently used to measure the chirality of magnetic skyrmions in ultrathin Pt|Co|MgO nanostructures [97]. Finally, the wall structure can be directly inferred through stray field imaging with a scanning NV magnetometer, as reported in this work. This technique operates under ambient conditions and can be used to estimate the DMI strength in any type of ultrathin ferromagnetic heterostructures, without making assumptions on the domain wall dynamics. This is an important advantage of this method. The drawback is the limited range of DMI strength that can be measured. Indeed, as soon as $|D_{\text{DM}}| \geq D_c$ the domain wall is fully stabilized in the Néel configuration and only a lower bound for D_{DM} can be extracted. This is a common drawback of all the methods based on direct imaging of the domain wall structure.

All the above-mentioned techniques rely on the study of domain walls nucleated in ultrathin ferromagnets. These domain walls are always stabilized at pinning sites, which result from structural defects of the magnetic structure that locally lower the energy cost of a domain wall [18]. Consequently, DMI measurements based on domain wall properties might be systematically biased by selecting particular regions of the sample producing stable pinning sites for domain walls, although we note that examination of pinned domain walls has a direct technological relevance for domain wall-based spintronic devices. This sampling bias can be circumvented by using Brillouin light spectroscopy (BLS). Here the DMI strength is obtained by measuring frequency shifts of spin waves propagating in opposite directions of the sample [98, 99, 100, 87]. This method probes DMI over a micrometer length scale and does not rely on the presence of a domain wall. Local fluctuations of the magnetic properties, like the one observed in Figure 2.11, are therefore averaged out. Recent BLS measurements in X|CoFeB|MgO heterostructures have systematically indicated larger D_{DM} values than those obtained by scanning NV magnetometry and field-driven domain wall motion in the creep regime [88]. As already indicated above, this observation could be explained by considering that the methods relying on the study of domain walls underestimate the DMI strength since the measurement is performed at stable pinning sites, corresponding to local defects of the sample which may degrade the interface. This suggests that the models used to interpret experimental results obtained with different methods still need to be refined when the aim is to obtain accurate measurements of the DMI strength. In the end, what is desirable both for physics and applications is not just the average value of D_{DM} , but rather its complete distribution.

In this chapter it was shown how scanning NV magnetometry is employed to probe the strength of the interfacial DMI at the domain wall positions in [Ta,TaN,W]|CoFeB|MgO ultrathin films as summarized in Figure 2.12. This was done by measuring the stray field emanating from domain walls in micron-long wires in these materials. A deviation from the Bloch profile for TaN and W underlayers is observed and that is

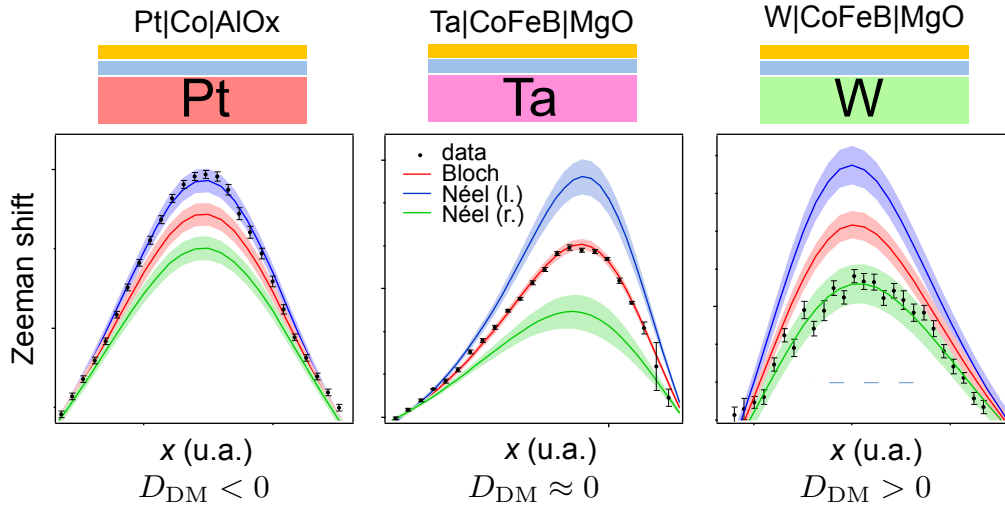


Figure 2.12 – **Tuning the DMI in magnetic heterostructures** The overview shows a summary of the different results in samples with Pt, Ta and W underlayer. The three different domain walls and DMI strength illustrate the possibility to tune this interaction by modifying the sample composition, in particular the heavy metal underlayer. The possibility to controllably tune the DMI ensure optimized materials for spintronic application.

consistent with a positive DMI value favoring right-handed chiral spin structures. While the overall trends are in accord with previous work involving current-driven wall dynamics, the study reveals important quantitative discrepancies. Moreover, the measurements suggest that the DMI constant might vary locally within a single sample, a possibility also considered in a recent study of current-driven skyrmions motion [7]. These results illustrate the importance of local probes of magnetic states and suggest certain hypotheses for extracting the DMI value from domain wall motion experiments require great care and depend strongly on assumptions made on the dynamics. Given its operability under ambient conditions, the NV scanning magnetometry offers important new ways to study the magnetism of ultrathin films. The existence of spatial variations in the DMI will certainly impact how past, present, and future experiments will be interpreted, and will also guide the design of future devices. Furthermore these results will have strong bearing on present research on chiral magnetization dynamics involving chiral domain walls and skyrmions, which are of both fundamental and applied interest. In materials with high D_{DM} the formation of so-called skyrmions - magnetic quasi particles with outstanding properties - is facilitated. Being able to tune magnetic heterostructures in a way to adjust characteristic parameters as the DMI strength will help to develop materials that can employ such chiral magnetic objects for spintronic applications. In the following, third chapter of this thesis, measurements on such materials hosting magnetic skyrmions will be presented.

The effect of disorder in thin magnetic films on skyrmion morphology

Contents

3.1	Magnetic skyrmions - History and physical properties	64
3.1.1	Brief history of magnetic skyrmions	64
3.1.2	Physical properties of skyrmions	66
3.2	Characterization of skyrmions in a [Ni Co Ni] bilayer	69
3.2.1	A bilayer magnetic structure designed as host medium for skyrmion	69
3.2.2	Preliminary characterization with MFM and observation of the skyrmion Hall effect	71
3.3	All optical imaging of magnetic skyrmions in bilayer film	73
3.3.1	Skyrmions and their host medium	73
3.3.2	Imaging skyrmions with NV magnetometry	74
3.3.3	Revealing the skyrmion nucleation process	75
3.3.4	The effect of disorder on skyrmion morphology	77
3.4	The future of skyrmionics	81

In this chapter we investigate ultra-small, whirl-like magnetic objects, so-called skyrmions. Due to their small size and their particular topology, they are outstanding candidates for spintronic technologies. A possible foundation for future devices is the current-induced motion of skyrmions in ultra-thin films, which has recently been demonstrated [101, 102, 103]. This efficient motion at small current densities should be facilitated by the skyrmions' limited interaction with disorder. However, recent experiments have shown that disorder in samples strongly alters the skyrmion dynamics, contrary to initial expectations. These observations motivate a more precise description of disorder in thin film magnetic materials and their effect on skyrmion morphology. In this chapter, we use NV center microscopy to probe the effect of disorder on skyrmions.

In Section 3.1, an overview of the fast evolving field of skyrmionics is given and the skyrmions' physical properties are explained. In Section 3.2 we introduce a particular bilayer material architecture. In this sample, skyrmions are stabilized by the DMI in combination with dipolar coupling. After discussing the skyrmion formation mechanism in this system, we present current induced propagation experiments. In Section 3.3 we reveal the condensation of skyrmions with the help of scanning NV magnetometry operating in the quenching detection mode. We discuss the effect of disorder on skyrmion shape and size by means of micromagnetic simulations. In the last Section 3.4, the results are summarized and an outlook is given.

All the work presented in this chapter has been realized in close collaboration with A. Hrabec, A. Thiaville and S. Rohart at the Laboratoire de Physique des Solides (LPS, Orsay).

3.1 Magnetic skyrmions - History and physical properties

In the first section, we will give a short overview on the research of magnetic skyrmions up to date and we will embed our work in this field (§3.1.1). Then, we briefly explain the basic properties that make magnetic skyrmions compelling for spintronic devices (§3.1.2).

3.1.1 Brief history of magnetic skyrmions

In recent years, much effort was invested in the research on magnetic skyrmions, a chiral phase evidenced in materials with broken inversion symmetry. Their first observation in bulk non-centrosymmetric magnets [104] was attributed to the presence of a high DMI in the crystal lattice without inversion symmetry. Since their first experimental observation a whole new field, denoted as skyrmionics, has evolved. Skyrmions are small in size and can be created and moved with ultra-low current densities. An example for an envisioned device is the skyrmion racetrack memory [8]. Here, the state of the bit is encoded by the existence or absence of a skyrmion (Figure 3.1 (a)). In addition, skyrmions may be moved electrically along a nanoscopic wire ('racetrack'). The key point for such applications is the creation of isolated skyrmions in thin films at room temperature. Until very recently, skyrmions had only been observed at low temperature and mostly under the application of very high magnetic fields. The development of multilayers with perpendicular magnetization, grown by sputtering, is a promising path towards room temperature devices. Lately, such thin magnetic heterostructures hosting individual skyrmions at room temperature have been identified [6, 7, 97, 105, 106]. By the breaking of the inversion symmetry at the interface combined with a large spin orbit coupling with an adjacent heavy metal layer, a large DMI can stabilize single skyrmions in these materials. Also, skyrmion displacement under current in nanotracks has been demonstrated with velocities up to ~ 100 m/s [7]. These advancements prove that, after not even two years since the first experimental proof of individual skyrmions in ultra-thin magnetic wires, we are already on a fast track towards the conceptual development of skyrmion based devices.

However, there are also still open questions and new challenges that have emerged along the way. These have to be tackled to make skyrmions a true candidate for spintronic technologies.

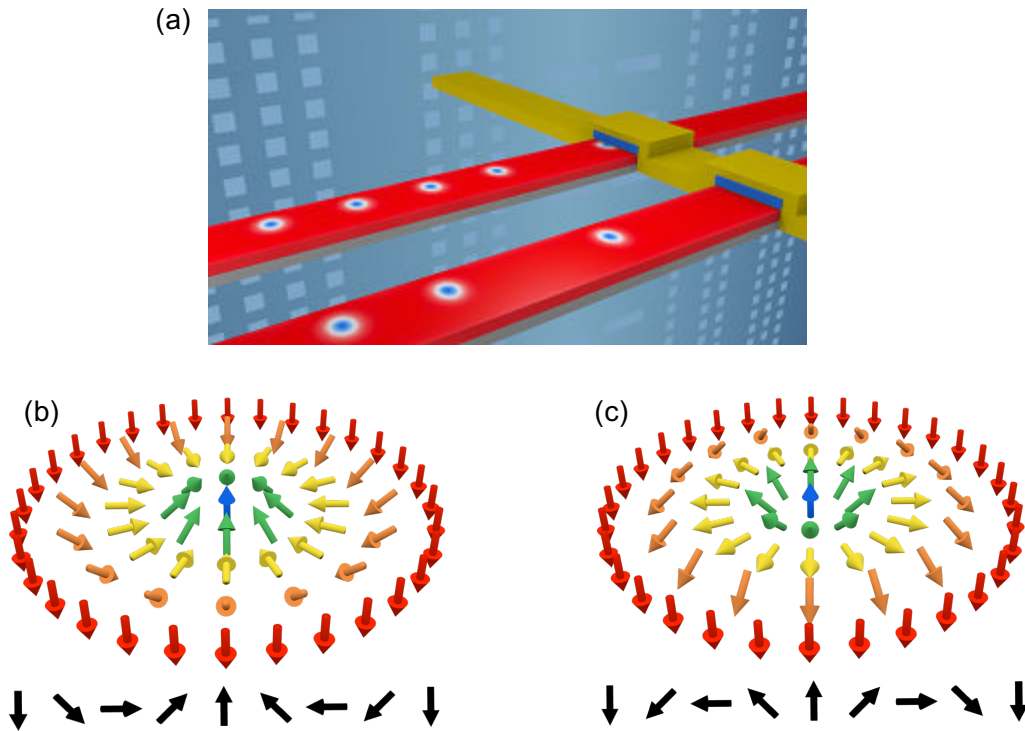


Figure 3.1 – **Skyrmion racetrack and Néel skyrmions.** (a) Schematic of a skyrmion racetrack memory [107]. (b,c) Configuration of spins in a Néel skyrmion with two different chiralities. The spins rotate in the radial planes from the core to the periphery. In the case of (b) this rotation is clockwise, as for the right handed Néel wall and in (c) counterclockwise, as for the left handed Néel wall. At the bottom the cross section of the skyrmion is depicted for both cases.

- First, there is the necessity to find a way to tailor the chirality and energy of domain walls, in order to nucleate isolated skyrmions that remain stable at room temperature. Furthermore, it is crucial to optimize and control skyrmion properties, as for example their size. In this regard, it is crucial to understand the influence of their host medium. It has already been demonstrated in Chapter 2 how NV magnetometry can help to examine properties of thin film magnetic heterostructures in order to find suitable host materials for skyrmions.
- Second, for devices as the racetrack memory, a reproducible, fast displacement of skyrmions is crucial for information transfer. Consequently, the efficient control of their motion in ultrathin films is the cornerstone of innovative applications. Our collaborators at the *Laboratoire de Physique des Solides* (LPS) in Orsay have developed a special sample structure in which they demonstrated skyrmion nucleation and propagation. However, in such a technologically relevant magnetic material, structural defects often result in considerable pinning and thus limit the propagation velocity of skyrmions. In this framework, we will in this investigate the sample grown and characterized at LPS with NV magnetometry and tackle the question of nucleation process and disorder.

3.1.2 Physical properties of skyrmions

A skyrmion is a local perturbation in a uniformly magnetized magnetic material [108]. As shown in Figure 3.1, its core is directed in the reversed magnetization direction and is surrounded by a circular domain wall. There are two typical types of magnetic skyrmions: Néel-type (shown in Figure 3.1) and Bloch-type skyrmions. We have seen in Chapter 2 that in thin films the asymmetric stacking of a ferromagnet between a heavy metal underlayer and an oxide leads to a broken inversion symmetry. The broken inversion symmetry in combination with a strong spin orbit coupling at the interface between the magnetic layer and heavy metal layer, induces the DMI. This interaction stabilizes the domain wall in a Néel configuration with a chirality fixed by its sign. Skyrmions are also predominantly stabilized by the DMI. This interaction defines their chiral spin structure, which in turn is essential for their sensitivity to spin orbit torques and thus their dynamic properties [109, 110, 111]. This indicates, that in general, skyrmion host media with a large DMI are desirable. In the following chapter we will concentrate on magnetic Néel skyrmions.

Eventually, it is the competition of different mechanisms contributing simultaneously, that leads to the generation of skyrmions in thin films. While the DMI interaction tends to cant the magnetic moments, leading to a chiral structure, the Heisenberg exchange interaction favors the collinear alignment of neighboring spins. As a result, a helical spin order is realized in the absence of an external field [112]. Another important mechanism is the magnetic dipole interaction. By the competition of long-range dipolar energy and domain wall energy, magnetic bubble phases are stabilized [113]. This competition, plus the application of a magnetic field normal to the thin film plane, results in the formation of magnetic skyrmions [114, 115] and defines their size [79]. Whereas a large DMI interaction stabilizes small skyrmions (10-200nm), the dipolar mechanism tends to stabilize bigger chiral bubbles (up to $\sim \mu m$). Apart from a large differences in size, the two systems exhibit a similar topological structure and thus, similar current-induced motions properties. The combination of different interactions can be exploited to tailor material properties and consequently to create magnetic skyrmions. This will be shown in Section 3.2.

Magnetic skyrmions are topologically non-trivial textures. This property is described with the topological charge, or skyrmion number

$$\Omega = \frac{1}{4\pi} \int \mathbf{m} \cdot (\partial_x \mathbf{m} \times \partial_y \mathbf{m}) \, dx dy, \quad (3.1)$$

where \mathbf{m} is the normalized magnetization vector. Ω is a measure of how many times the magnetization wraps around the unit sphere and equals to $\Omega = \pm 1$ for a chiral Néel skyrmion. It describes the fact that a skyrmions' magnetic configuration is stable and cannot be easily (only by overcoming an energy barrier) converted into a different magnetic structure. This topological protection is expected to drastically reduce the influence of defects, so that skyrmions can move in nanotracks without being destroyed by imperfections in the film or at the edges of the track.

The size of skyrmions in thin films ranges from some nanometers [116] to a few hundreds of nanometers [103], depending on the host materials parameters and the external magnetic field. Due to the small dimensions of skyrmions, it can be difficult to test their exact size, shape and properties. Common techniques to investigate skyrmion in thin films are: Kerr microscopy, magnetic force microscopy (MFM), scanning transmission X-ray microscopy (STXM), X-ray Magnetic Circular dichroism (XMCD) coupled to photoemission electron microscopy (PEEM) and Lorentz mode tunneling electron microscopy (TEM). While Kerr microscopy is a very accessible and non-invasive technique. Its spatial resolution lies at ~ 300 nm. The MFM works in a scanning configuration and has a high spatial resolution (~ 50 nm). However, it is an invasive technique since a magnetic probe is employed. In contrast to the other two methods, STXM, Lorentz mode TEM and XMCD PEEM offer a quantitative field measurement. Spatial resolution lies in the order of 20 nm (1 nm for Lorentz mode TEM). However, for STXM and XMCD PEEM synchrotron radiation is required and for Lorentz mode TEM dedicated samples have to be prepared. Often rather thick samples are necessary in order to detect enough signal from the magnetic material. This limits their application to bulk samples or multilayers. We note that XMCD PEEM [97] and NV center magnetometry [117] have recently been utilized to deduce the chirality of skyrmions.

A crucial point for applications are the skyrmions' dynamical properties. It has recently been shown that skyrmions can be created and moved by small electrical currents [102, 118, 7, 105], with current densities in the order of 10^6 A/m² [105]. This is five orders of magnitude smaller than the ones necessary for moving domain walls [8]. The motion of skyrmions is explained by spin transfer torques. These can be exerted either by a spin-polarized current flowing inside the ferromagnet, or by a non-spin polarized current in the heavy metal layer, via the spin Hall effect (SHE). Until 2011, spin textures were expected to be moved by in-plane spin transfer torques (STT) along the electron flow. With the discovery of unexpected high speeds of domain walls in certain materials [119], this model proved insufficient. In ultrathin films deposited on large spin orbit materials, a new torque related to the spin orbit coupling (SOT) was found and proposed to explain the motion of chiral objects [120, 61]. This torque describes the action of a non spin-polarized current in the non magnetic layer with large spin orbit coupling (see Figure 3.2). There, the spin Hall effect causes a spin accumulation with opposite polarities at each interface. When this spin accumulation flows into the ferromagnet, it interacts with the magnetic moment of the skyrmions [110, 121]. It produces a force which can be expressed as

$$\mathbf{F}_{\text{SH}} = \pm \frac{\hbar}{2e} \pi j \theta_{\text{SH}} b \mathbf{z} \times \mathbf{e}_{\mathbf{p}} \quad (3.2)$$

where j is the current density, θ_{SH} is the SHE angle (angle between skyrmion propagation direction and current direction, can be positive or negative) and b is a skyrmion characteristic length (about half its perimeter). The SHE induced spin accumulation is along the vector $\mathbf{e}_{\mathbf{p}} = \mathbf{n} \times \mathbf{j}$, with \mathbf{n} being the outer normal to the SHE layer at the considered interface. The force results in a steady motion of the skyrmion parallel to the track and thus parallel to the current. It is important to note that the \pm sign in Equation 3.2 described the chirality of the skyrmion ('-' stands for left-handed chirality). Hence, the direction of the force is determined by the skyrmion chirality.

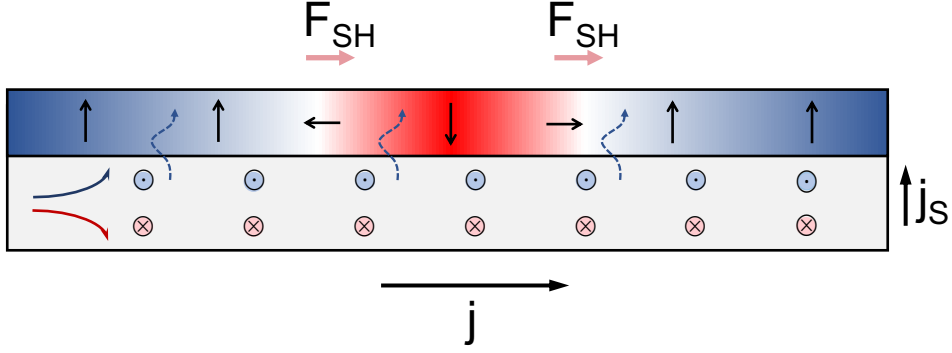


Figure 3.2 – **Schematic of the skyrmion motion due to the SHE.** A sketch showing the spin accumulation due to the electrical current j in the underlayer. If we assume Pt as underlayer with a positive spin Hall angle θ_{SH} , the resulting force \mathbf{F}_{SH} , defined by Equation 3.2, causes the left handed skyrmion to move against the electron flow.

Both of the torques described above (in-plane STT and SOT) may coexist. However, the SOT usually proves more efficient than the STT in ultrathin films. A big difference between STT and SOT is that for STT, the motion is only along the electron flow whereas for SOT the motion can be in any direction depending on the sign of the SHE angle and the chirality.

Another important influence on skyrmion dynamic has to be considered. A skyrmion will not move in a straight line parallel to the current direction. Due to its topological charge, it feels the Magnus force while moving and it is deviated perpendicular to its propagation direction. This effect is called the skyrmion Hall effect [103, 101]. The conventional Hall effect arises because a charge-carrying particle experiences a force perpendicular to its direction of motion when it travels through a magnetic field. Skyrmions have no charge, however, during current-induced displacements they have been predicted to undergo a deflection due to their topological charge. Consequently, an applied current not only induces longitudinal but also a transverse motion. The force acting on the skyrmions caused by the skyrmion Hall effect is described with the following equation

$$\mathbf{F}_G = \mathbf{G} \times \mathbf{v}, \quad (3.3)$$

where $\mathbf{G} = \left(0, 0, \frac{-\mu_0 M_s t}{\gamma_0} \Omega\right)$ is the gyrotropic vector, $\Omega = 4\pi S p$ with S the winding number and p the core polarity, which can for example be changed by inverting the external magnetic field. This equation shows how the topology of skyrmion is bound to its motion. The overall dynamics of skyrmion are described by the mass-less Thiele equation [7, 122]

$$\mathbf{G} \times \mathbf{v} - \alpha_G \mathcal{D} \cdot \mathbf{v} + \mathbf{F}_{SH} = 0 \quad (3.4)$$

where \mathbf{F}_{SH} is the force from the SHE (longitudinal movement), α the Gilbert damping and \mathcal{D} the dissipation tensor. The transverse motion of a skyrmion consequently provides a way to reveal its topological state.

3.2 Characterization of skyrmions in a [Ni|Co|Ni] bilayer

In the next sections we present a sample geometry in which a pair of coupled skyrmions with the same topological charge and opposite chiralities can be stabilized. The symmetric magnetic bilayer system combines DMI and dipolar coupling effects to stabilize skyrmions (§3.2.1). A preliminary characterization of the sample with MFM is shown and the skyrmion Hall effect is demonstrated (§3.2.2). These experiments have been performed by A. Hrabec and S. Rohart at LPS, Orsay.

3.2.1 A bilayer magnetic structure designed as host medium for skyrmion

In thin film materials with broken inversion symmetry, chiral magnetic structures can be stabilized. Such materials have been studied in Chapter 02 of this thesis. The aim was to find materials with high DMI, e.g. fast moving domain walls and eventually heterostructures that are ideal to host fast moving magnetic skyrmions. Lately published studies, revealing skyrmions stabilization, employ for example thin multilayer Pt|CoFeB|MgO stacks, since this material exhibits a large DMI at the Pt|CoFeB interface [101].

The high DMI necessary to stabilize skyrmions restricts the choice of possible materials and makes it more difficult to fine-tune sample parameters. Our collaborators at LPS have recently shown that a globally symmetrical structure in a magnetic bilayer with perpendicular magnetization can meet all the requirements to host skyrmions, without the need for a large DMI [102]. The investigated sample is a stack of Pt(5nm)|FM|Au(t_{AU})|FM|Pt(5nm). Two ferromagnetic layers (FM=Ni|Co|Ni) are separated by a thin gold spacer, and sandwiched between two Pt layers. The sample structure is depicted in Figure 3.3. Magnetometry and Brillouin light scattering experiments were performed on both stacking configurations Pt|FM|Au and Au|FM|Pt separately and reveal an opposite DMI constant, $D_{\text{DM}} = -0.21 \pm 0.01 \text{ mJ/m}^2$ and $D_{\text{DM}} = +0.24 \pm 0.01 \text{ mJ/m}^2$ respectively, with otherwise similar film properties. The DMI arising at the Pt|FM interfaces, combined with flux-closing dipolar fields [123], promotes the stabilization of superimposed skyrmions having identical topological charge and opposite chirality in each FM layer. The resulting skyrmion pairs are strongly coupled by dipolar fields and behave as a single magnetic quasiparticle, which are hereafter referred to as skyrmion. The strength of the dipolar coupling can be tuned by adjusting the spacer thickness t_{AU} , between the two layers [102].

In the following we take a close look at the skyrmion stabilization mechanism in this kind of bilayer heterostructure. The red, blue and green arrows in Figure 3.3 represent the relevant dipolar interaction and will be explained in the following. The micromagnetic energy of a domain wall in this system is described by following equation

$$\sigma = \sigma_0 - \pi D_{\text{DM}} + \sigma_{\text{N}} - \sigma_{\text{DW-DW}} - \sigma_{\text{D-DW}}. \quad (3.5)$$

The energy $\sigma_0 = 4\sqrt{AK_{\text{eff}}}$ includes the anisotropy and exchange energy. The domain wall energy is lowered by the DMI term πD_{DM} [61], as already discussed in Chapter 2 for domain walls in ultra thin magnetic films. The

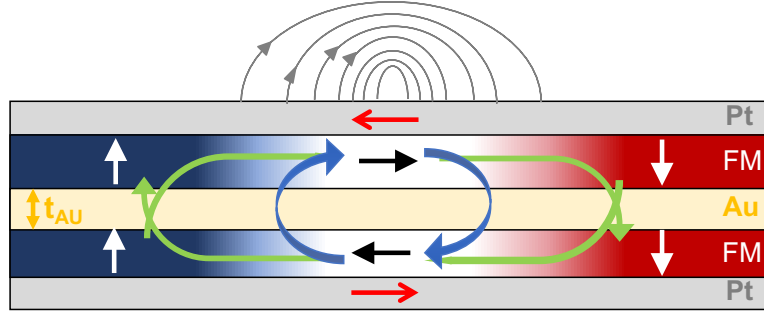


Figure 3.3 – **Schematic of the bilayer sample structure.** The magnetic sample is a symmetric bilayer system with a stack of Pt(5nm)|FM|Au(3nm)|FM|Pt(5nm), where FM=Ni(4Å)|Co(7Å)|Ni(4Å). The white arrows are the magnetization directions in the film. The black arrows are the directions of the magnetization in the domain wall, which is antiparallel in the two layers. The rest of the arrows represent the different dipolar interactions that stabilize chiral domain walls. Red stands for the demagnetization field from the Néel wall. The blue arrows show the interaction of the two superimposed domain walls and the green arrows the interaction of the stray field arising from the domains on the domain wall.

DMI favors a Néel wall structure which gives rise to magnetostatic charges on either side of the wall. These charges create a field opposed to the wall magnetization, as shown by the red arrows in Figure 3.3. This causes an increase in energy by σ_N . In Chapter 2 it has been shown that in thin films with PMA the transition between Bloch and Néel walls is determined by the competition between DMI and demagnetization field from the Néel wall, which is the only dipolar interaction term that needs to be taken into account.

For the bilayer system considered here, additional dipolar interactions have to be considered. The magnetostatic interaction of the two superimposed domain walls σ_{DW-DW} is depicted by blue arrows. If the spacer thickness t_{Au} is smaller than the domain wall width, the magnetostatic charges created by each wall are so close that σ_{DW-DW} is in absolute value approximately equal to σ_N . Thus, these two terms cancel out and can therefore be neglected. The dipolar coupling between domains acting on the domain wall gives rise to another contribution σ_{D-DW} , depicted by the green arrows. It leads to an energy decrease of the system and reinforces the chiral nature of the wall.

Finally, the domain wall energy reads as follows:

$$\sigma \simeq \sigma_0 \underbrace{-\pi D_{DM} - \sigma_{D-DW}}_{\pi D_e} \quad (3.6)$$

A part of the energy minimization is carried by the dipolar coupling and not the DMI. In this way the DMI is artificially increased to $\pi D_e = -(\pi D_{DM} + \sigma_{D-DW})$. This makes the necessity of high DMI obsolete. The ratio of the two energy contribution can also be tuned for example by changing the spacer thickness t_{Au} [102]. While the DW energy remains positive here, the dipolar coupling between the domains can efficiently lower the energy cost. Consequently, the bilayer sample spontaneously demagnetizes in a multiple domain state at zero field.

It should be noted that the interaction between the domains and the walls σ_{D-DW} naturally leads to an antiparallel alignment of the domain walls in the two layers of the sample [123]. Both DMI-induced wall chiralities have to be opposite in order to reinforce this antiparallel alignment. This is achieved by using the opposite stacking order of the Pt|FM and FM|Pt layer. The sign of D_{DM} at the Pt|FM interface defines the succession of FM and Pt layer. In this case, the spin-orbit layers (Pt) generating the interfacial DMI should be placed as outer layers since D_{DM} is negative.

3.2.2 Preliminary characterization with MFM and observation of the skyrmion Hall effect

The magnetic texture of the bilayer sample was first imaged by magnetic force microscopy. This technique scans a tip coated with a ferromagnetic material over the sample and is sensitive to magnetic field gradients. Figure 3.4 (a) shows the measurement principle. A non magnetic coating is applied to the tip in order to reduce its magnetic back action on the sample. The MFM measurement confirms that the bilayer is at remanence in a worm-like demagnetized state. The period in the worm phase is fixed by the competition between the domain wall energy and the dipolar coupling. The importance of the non-magnetic coating is visualized in Figure 3.4 (b) and (c). A non-coated tip interacts with the magnetic structure. It may allow the system to overcome an energy barrier such as to cut elongated domains into skyrmions. In image (b) this effect is reduced because of the non magnetic coating. By applying an out-of-plane magnetic field the domains should start to contract into skyrmions. In order to measure the magnetic field dependent condensation of skyrmions a completely noninvasive technique is advantageous. In Section 3.3.2, the results with all optical NV magnetometry will be presented.

For most application it is interesting to move skyrmions in nanostructures. In order to nucleate skyrmions

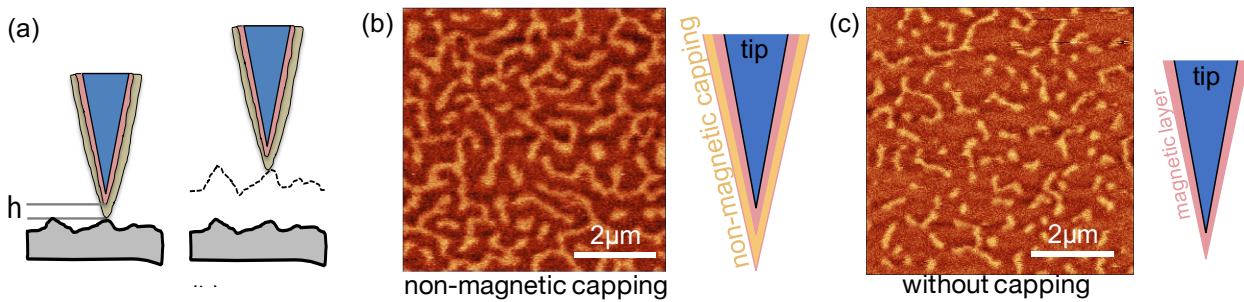


Figure 3.4 – **Imaging of the groundstate with MFM.** (a) shows the principle of the MFM measurement. A coated tip is first scanned to record the topography and after to measure the magnetic stray field from the sample. In (b) the magnetic domain structure of the bilayer sample is shown. The MFM tip was coated with a non-magnetic Cr layer. (c) Illustrates the perturbative character of a non-coated tip. The measurement with a MFM magnetic scanning tip can lead to perturbations in the magnetic structure of the sample. In order to monitor the exact skyrmion formation process while ramping an external magnetic field, it is important to perform a non-invasive measurement.

in nanowires several methods have been proposed [124, 105, 6, 125]. Here, current-induced nucleation was used. The current injection at the triangular contact (see Figure 3.5 (a)) leads to a disturbance of the magnetic configuration, due to the local concentration of the current, and skyrmions are injected into the track.

At this point, it is important to verify that the magnetic textures created in the bilayer system have the dynamic properties associated with skyrmions. As explained in Section 3.1.2 the skyrmion moves according to the force F_{SH} from the spin Hall effect acting on it. In the particular case of the symmetric bilayer sample with two stacked skyrmions, this effects manifests itself as well. As we have seen before, the sample is constructed in a way so that the stray field arising from the domains coupled to the domain wall magnetization in a flux-closure configuration, and promotes Néel walls with opposite chirality in both layers. When an electric current is applied through the Pt layers, a spin accumulation with opposite polarities takes place at each interface of the sample. The sign of the force F_{SH} on a skyrmion is set by its chirality. Since the spin accumulation and the chirality are both opposite at each interface of the bilayer, the forces acting on both stacked skyrmions point in the same direction (See Figure 3.5 (c), top). The skyrmions in both layers are therefore pushed in the same direction.

This is verified by applying short current pulses in the structure. Figure 3.5 (b) shows such a sequence of images where skyrmions are displaced by 3 ns long pulses. They move in the same direction as the current. Given the positive spin Hall angle of Pt and the left handed chiralities observed at Pt|Ni or Pt|Co interfaces, the motion is expected against the electron flow, as also demonstrated in reference [59, 126]. The skyrmion velocity is determined by measuring the displacement after the application of current pulses. The obtained

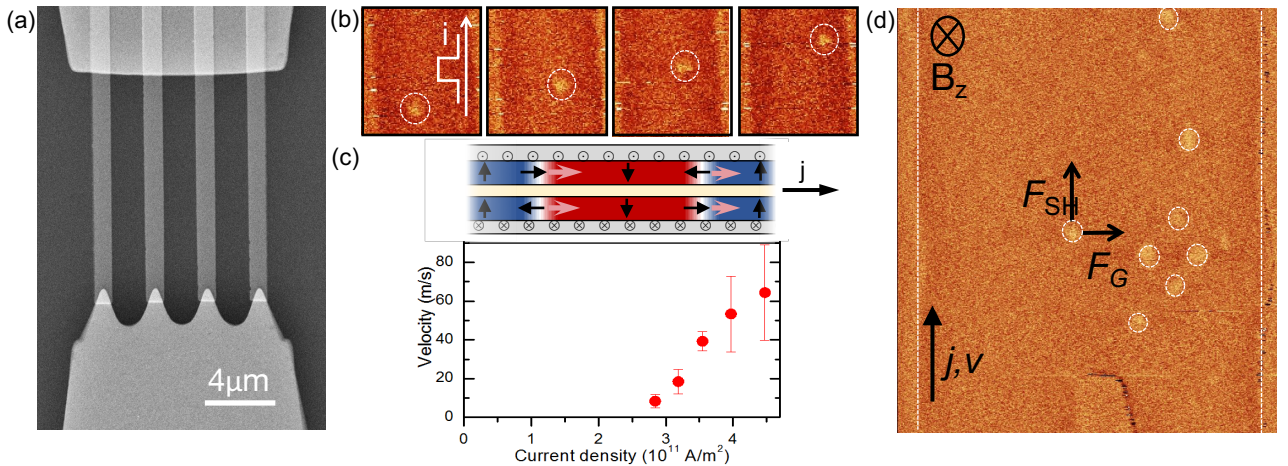


Figure 3.5 – **Skyrmion motion in the bilayer sample.** (a) AFM image of the device for skyrmion injection and movement. (b) MFM images showing the skyrmion move along a 1 μm wide track between 3 ns pulses of $j=3.9 \times 10^{11}$ A/m 2 . In this way the velocity/current curve is obtained as depicted in (c). Skyrmions reach velocities of 60 m/s. (d) MFM image of a 3 μm wide track after application of a series of 8 ns long pulses in an external field B_z and a current density of $j = 3 \times 10^{11}$ A/m 2 . The skyrmions are accumulated on the right side of the sample due to the skyrmion Hall effect.

velocity current graph is shown in Figure 3.5 (c) (bottom). It reveals skyrmion velocities of 60 m/s and critical currents of $\sim 2.5 \times 10^{11}$ A/m². The displacement after each pulse, even at larger current densities, is not equal. This can be explained by the potential landscape in the sample which influences the skyrmions' dynamic properties. Due to structural defects, skyrmions can get trapped at pinning sites rather than moving smoothly along the wire. Further effects of the sample inhomogeneity will be investigated with NV magnetometry in Section 3.3.

In order to demonstrate the presence of topological textures in this sample the skyrmion Hall effect was demonstrated. The experiment revealing this effect was conducted in 3 μ m wide strips where the skyrmions can move freely in the lateral direction. After skyrmion creation and movement with 8 ns long $j = 3 \times 10^{11}$ A/m² pulses, the image shown in Figure 3.5 (d) was recorded. It shows a deflection of the quasiparticles to the right. When reversing the magnetic field and consequently the polarity of the skyrmion core, a deflection to the left is observed. These measurements confirm that we observe nontrivial magnetic textures with $S > 0$, topology compatible with skyrmions.

3.3 All optical imaging of magnetic skyrmions in bilayer film

As we have seen in the previous section, skyrmions can be created and moved by an electric current in the symmetric bilayer sample. The predicted skyrmion Hall effect has been demonstrated [103, 101, 102]. In the next sections we investigate the impact of disorder on the size and shape of isolated skyrmions with the scanning NV magnetometer. First we shortly describe the relation of skyrmions and their host medium (§3.3.1). After, we explain the technique to image skyrmions with NV center magnetometry (§3.3.2). The skyrmion nucleation process is shown step by step (§3.3.3) and finally we quantify the effect of disorder on the skyrmion morphology (§3.3.4).

3.3.1 Skyrmions and their host medium

Despite their many promising properties discussed in Section 3.1, magnetic skyrmions are inseparably attached to their host medium. They inherit its properties, including imperfections. Importantly, the magnetic texture dynamics in ultra thin films are hindered by defects, extrinsic and intrinsic, limiting their velocity. Contrary to domain walls, which cannot bypass any defects along their track [127, 128], skyrmions should be able to move in two dimensions and avoid defects [8]. They are thus expected to display limited interaction with the disorder in their host medium. Recent, experiments in thin films however have shown that skyrmion dynamics are strongly affected by disorder of the host medium [105] and this fact is likely to influence the skyrmions dynamical properties [101]. Such a contradiction indicates that disorder have been oversimplified and that a better understanding of skyrmion dynamics requires a better description of disorder [129].

Whereas average magnetic properties of ultra thin films - magnetization, anisotropy, DMI, damping - can be routinely measured, the effects of structural disorder remains highly challenging to evaluate and model, both

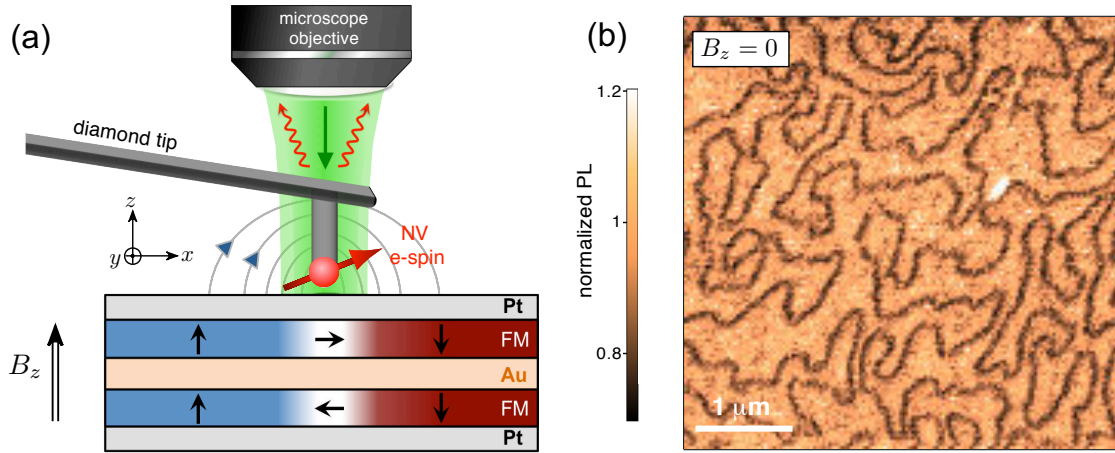


Figure 3.6 – **Principle of the experiment.** (a) A single NV defect placed at the apex of a diamond tip is employed as a non-invasive, scanning magnetometer operating under ambient conditions. A microscope objective is used both to excite (green arrow) and collect the magnetic-field dependent photoluminescence (PL) quenching of the NV defect (red wavy arrows). The magnetic sample is a symmetric bilayer system with a stack of Pt(5nm)|FM|Au(3nm)|FM|Pt(5nm), where FM=Ni(4Å)|Co(7Å)|Ni(4Å). (b) PL quenching image recorded in zero external field ($B_z = 0$). A drop in PL appears at the border between two oppositely magnetized domains where the stray field is highest. The bright spot with enhanced PL correspond to a dust on the sample, as verified on the simultaneously recorded AFM image.

concerning its magnitude and spatial distribution. Such a study would require high quality imaging of the skyrmion morphology. Conventional magnetic imaging techniques face either a lack of sensitivity or spatial resolution, or more problematically induce magnetic perturbations in the sample. In the next sections, we will show how scanning NV-magnetometry enables to investigate the impact of disorder on the morphology of skyrmions.

3.3.2 Imaging skyrmions with NV magnetometry

The symmetric magnetic bilayer sample Pt|FM|Au|FM|Pt described in Section 3.2 was studied with NV magnetometry to reveal the effects of disorder on the skyrmions morphology. From previous experiments we know that skyrmions sizes in the order of ~ 100 nm are expected. To ensure a sufficient spatial resolution of single skyrmions we use a diamond scanning-probe unit [48, 19], as sketched in Figure 3.6 (a). Once integrated into a tuning-fork based AFM, this device enables scanning of the NV sensor in close proximity to the sample. For the present study, a calibration process following the method described in Section 1.2.3 indicates a probe-to-sample distance of $d = 50$ nm. Static magnetic fields are usually measured by recording the Zeeman-shift of the NV defect electronic spin sublevels through optical detection of the magnetic resonance as described in Section 1.3. In this way, the exact magnetic field distribution over a magnetic texture can be determined. Such a measure-

ment protocol becomes highly challenging for magnetic fields larger than 15 mT, as discussed in Chapter 1. In this high-field regime, any off-axis magnetic field induces spin state mixing, leading to a drastic reduction in ODMR contrast [55]. This situation is inevitably reached as soon as the NV sensor is brought in close proximity to a ferromagnet, *i.e.* when high spatial resolution is required. As an example, magnetic simulations indicate a stray field amplitude larger than 15 mT at a distance $h = 50$ nm above a domain wall in the bilayer magnetic sample. For such fields, the ODMR contrast vanishes and quantitative magnetic field imaging cannot be performed with NV-based magnetometry. However, it has been shown that the decreased ODMR contrast is accompanied by an overall reduction of the NV defect photoluminescence (PL) intensity [130, 131]. This magnetic-field-dependent PL quenching can be exploited to map high magnetic field regions without the need of microwave excitation [55]. Although not fully quantitative, we show below that this all-optical imaging mode is ideally suited to study the morphology of ferromagnetic textures with high spatial resolution. Magnetic field imaging is thus performed in the quenching mode by recording the NV defects' PL intensity while scanning over the sample (See Section 1.3.3). A typical PL quenching image recorded at zero field is shown in Figure 3.6 (b). Sharp dark areas with a contrast greater than $\sim 25\%$ reveal regions of high stray magnetic fields, which correspond to domain walls. The demagnetized state of the bilayer sample is organized in a worm-like structure. Although very similar images could be obtained with MFM [102], the key advantage of NV-based magnetometry is the absence of magnetic back-action on the sample, which provides unambiguous field measurements.

3.3.3 Revealing the skyrmion nucleation process

We are now interested in the imaging of single skyrmions. Before this, simulations are conducted to learn about the expected NV quenching response to skyrmions in the bilayer sample. The magnetization pattern of a perfectly round skyrmion in a uniform bilayer film sample is modeled with Matlab for two different skyrmion sizes. The z-component of the magnetization pattern is shown in Figure 3.7 (a). We consider a domain wall width of $\Delta_{\text{DW}} = 25$ nm and a skyrmion radius of 150 nm and 50 nm. Within the domain wall the magnetization is considered to be zero. This is a good approximation for the bilayer sample with antiparallel in-plane component in the two layers.

The stray field at 50 nm above the texture is then calculated and projected on the NV center axis, whose orientation was determined beforehand ($\theta = 128^\circ, \phi = 80^\circ$). Figure 3.7 (b) shows the stray field component perpendicular to the NV center which is responsible for the PL quenching. This off-axis field is highest over the domain wall. Here it reaches a strength of 16 mT and is strong enough to significantly decrease the PL efficiency. In Figure 3.7 (c), a simulation of the NV quenching image of this magnetization pattern is presented. The NV center photo-physical parameters being adapted from reference [132] in order to calculate its PL response. Details of the simulation are given in the Annex A). The simulated images show a dark ring which corresponds to a drop in fluorescence of $\sim 30\%$ over the domain wall. This produces a dark contrast around the skyrmion core. With a probe to sample distance of 50 nm and a skyrmion radius of 150 nm a significant PL

rate is recovered at the skyrmion center: Since the skyrmion size remains much larger than the NV-to-sample distance ($d \sim 50$ nm) domain walls from opposite sides of the skyrmion can be easily resolved, leading to a dark ring in the PL quenching image. For smaller skyrmion sizes (and same probe to sample distance) the bright contrast in the middle would hardly be visible. This can be seen in Figure 3.7 (c) for a skyrmion with a radius of 50 nm. The quenching images reflect the perfect round shape as predetermined by the magnetization pattern. The slight deviation is caused by the orientation of the NV center.

Starting from the worm-like magnetization structure at zero field, as shown in Figure 3.6 (b), isolated skyrmions are obtained experimentally by applying an external magnetic field B_z perpendicular to the sample. The skyrmion nucleation step by step is shown in Figure 3.8 (a-d). For $B_z = 3$ mT, one type of domain starts to shrink but still a vast domain landscape is present and no skyrmions were formed (Figure 3.8 (b)). In a next step, a magnetic field with larger amplitude is applied during several seconds in order to release domain walls from pinning sites. The magnetic field image is subsequently recorded at $B_z = 3$ mT. As shown in Figure 3.8

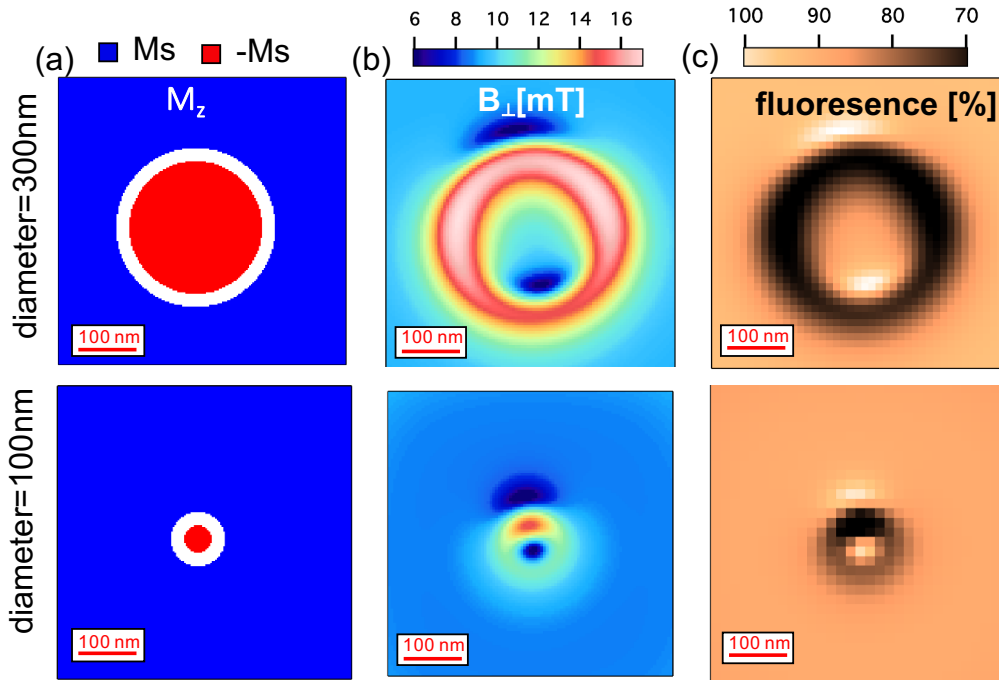


Figure 3.7 – **Simulation of skyrmion imaging.** The first images in (a) show a simulation of the magnetization pattern expected for a skyrmion in the bilayer sample. The images in the middle are the corresponding magnetic fields perpendicular to the NV axis, produced by this magnetization at the probe to sample distance $d = 50$ nm. The perpendicular field is highest at the domain wall and reaches values up to 16 mT. The last image shows the expected response in the NV fluorescence caused by the off-axis field. The maximum quenching is reached over the domain wall and leads to a drop in fluorescence of 30%. The simulations are performed for a skyrmion diameter of 300 nm (first row) and a skyrmion diameter of 100 nm (second row)

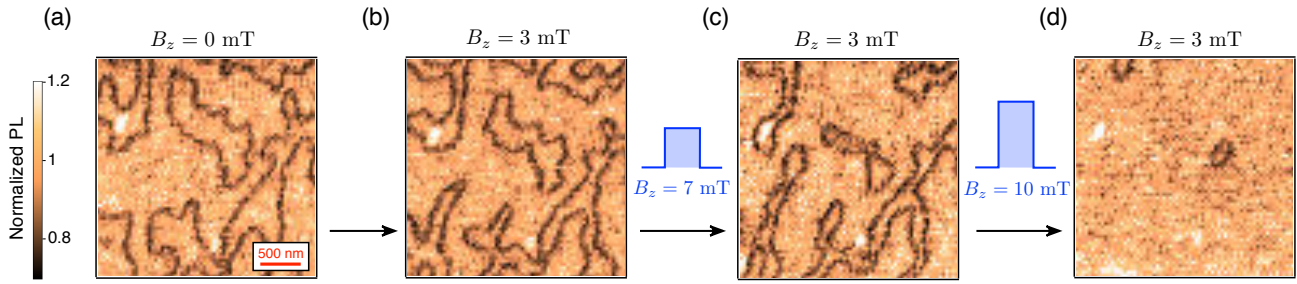


Figure 3.8 – **Skyrmion nucleation and relaxation.** Step-by-step formation of isolated skyrmions by applying an external out-of-plane magnetic field B_z . (a) PL quenching images recorded at zero field and (b) $B_z = 3$ mT. (c,d) Images recorded at $B_z = 3$ mT after applying a 10 s field pulse of (c) 7 mT and (d) 10 mT. The bright PL spots correspond to particles on the sample which serve as position references.

(c), a field pulse of 7 mT considerably compresses the magnetic domains, but it is only after a 10 mT pulse that the wormy domain structure completely collapses, as shown in Figure 3.8 (d). Since our measurement method imposes no magnetic back action on the sample, we use exclusively the magnet pulses to collapse the domains and nucleate skyrmions, which subsequently relax and stay stable in the applied constant field. All over the sample, a 10 mT depinning pulse was necessary in addition to the constant field, for observing isolated skyrmions. These are higher depinning fields than observed when characterizing the same sample with MFM. This is related to the fact that the magnetic tip stray field facilitates the collapse of the worms and thus the skyrmion condensation.

3.3.4 The effect of disorder on skyrmion morphology

Magnetic skyrmions were extensively imaged over the sample in order to obtain their size and shape distributions. Whereas perfectly circular skyrmions would be expected owing to the in-plane symmetry of the magnetic energy, we observe significant distortions of the magnetic texture as shown in Figure 3.9 (a). As illustrated before by simulation, it is not the NV orientation that does distort the shape of the skyrmion, neither the non-invasive measurement technique itself. The different observed skyrmion shapes are intrinsic to the sample and illustrate the key role of disorder in the stabilization of skyrmions. Indeed, as analyzed below, these observations can be well explained by pinning effects induced by disorder in the sample.

The characteristic skyrmion size is inferred by measuring the area \mathcal{A} enclosed by the dark ring observed in the PL images. The effective diameter d_s is then defined as $d_s = 2\sqrt{\mathcal{A}/\pi}$, corresponding to a conversion of the distorted skyrmion geometry into a perfectly rounded shape. Measurements of a set of 27 isolated skyrmions leads to $d_s = 268 \pm 63$ nm (Figure 3.9 (b)). In order to understand these results, micromagnetic simulations including disorder were carried out with the MuMax3 code [133]. The calculations have been realized by J. Sampaio and S. Rohart *et al.* at LPS. The MuMax3 code solves the space dependent magnetization evolution in nanoscale magnets using a finite-difference discretization [133]. We use magnetic parameters extracted

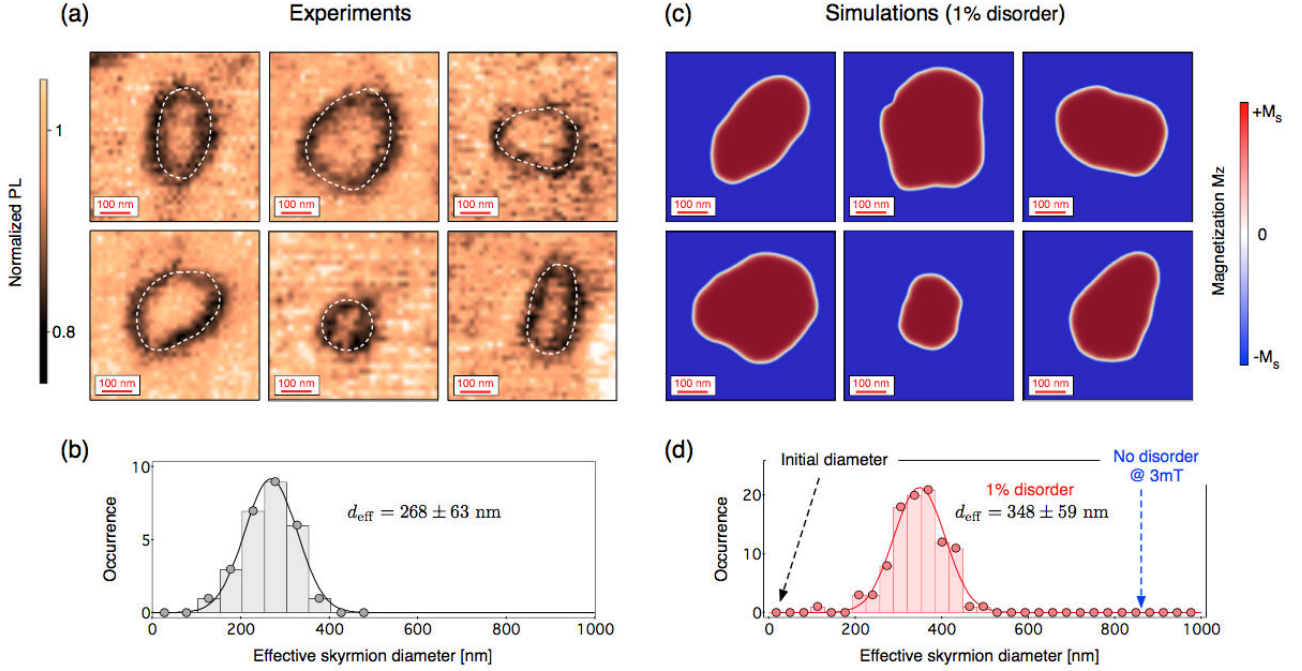


Figure 3.9 – **Patchwork of skyrmions in the bilayer sample.** (a) PL quenching images recorded above isolated skyrmions over the sample. These experiments are performed at $B_z = 3$ mT after applying a field pulse of 10 mT. The white dashed lines indicate the PL quenching ring from which the skyrmion area \mathcal{A} is extracted. (b) Histogram of the effective skyrmion diameter d_s extracted from measurements over a set of 27 skyrmions. The solid line is a fit with a Gaussian distribution. (c) Typical micromagnetic simulations of the skyrmion spin texture by including thickness fluctuations with a relative amplitude of 1%. (d) Histogram of the effective skyrmion diameter obtained for a large number of randomly picked disorder configurations. The blue dashed arrow indicates the skyrmion diameter for a disorder-free sample (860 nm) and the black dashed arrow shows the initial skyrmion size in the simulation (40 nm) before expansion in a 3 mT field.

from previous measurements [102]: interfacial anisotropy $K_s = 1.5$ mJ/m², saturation magnetization $M_s = 0.85$ MA/m and exchange constant $A = 12$ pJ/m. The code was modified for the particular problem of the bilayer sample where two magnetic layers ($t_0 = 1.5$ nm) are separated by a vacuum ($t = 3$ nm) which allows to put a different interfacial DMI constant in the top and bottom layers ($D_{\text{DM}} = \pm 0.2$ pJ/m² with a positive respectively negative sign). The meshing size was $1.5\text{nm} \times 1.5\text{nm} \times 1.5\text{nm}$, fixing the layer thickness t_0 utilized in the simulations. Disorder is included by a random fluctuation of the FM layer thickness t between columnar grains arranged in a Voronoi fashion [134, 135, 136, 129]. The average lateral grain size is fixed to 15 nm, which corresponds to the one observed in high resolution AFM measurements as shown in Figure 3.10. The thickness variation between grains is assumed to follow a normal distribution. Since micromagnetic simulations require a computation cell with a constant thickness t_0 all over the sample, the saturation magnetization is varied from grain to grain as $M_s t / t_0$. Averaged over the thickness, the uniaxial anisotropy K_u and the effective

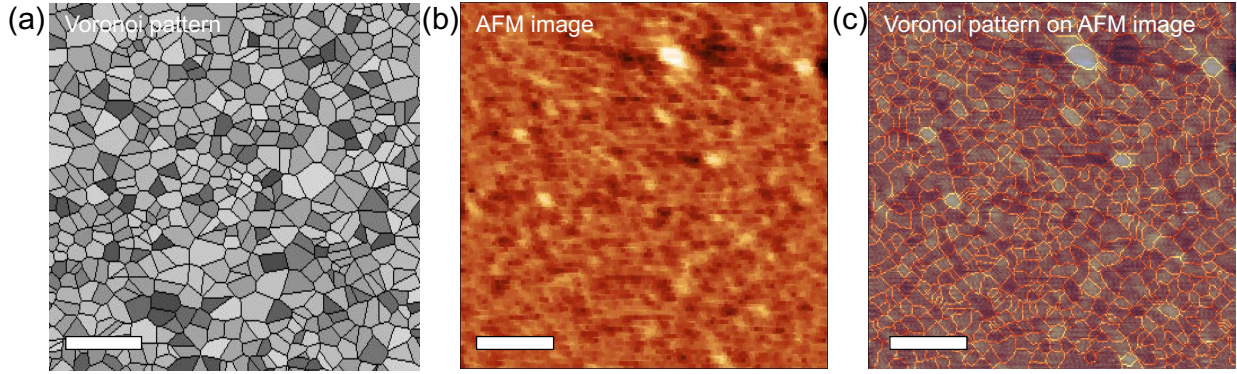


Figure 3.10 – **Voronoi model for thickness fluctuations.** (a) Example for a Voronoi grain distribution. The colors (dark grey to white grains correspond to thickness fluctuations of $\pm 1\%$). The white bar corresponds to 100 nm. (b) AFM image of the bilayer sample in which the average lateral grain size is 15 nm. (c) visualization of how the Voronoi model fits the grains visible from the AFM image.

DMI constant D_{eff} are also directly modified in each grain, *i.e.* $K_u = K_s/t$ and $D_{\text{eff}} = D_{\text{DM}}/t$. The thickness fluctuations are therefore mimicked by locally varying the micromagnetic parameters K_u , M_s , D_{eff} .

In a disorder-free medium, magnetic simulations lead to circular skyrmions with a diameter of 860 nm in a 3 mT field, which is much larger than the experimental observation. However, measurements are performed after a field pulse of 10 mT, which means that skyrmions are imaged after a compression of their diameter, followed by relaxation at 3 mT. To account for such a magnetic history, 40 nm diameter round skyrmions, corresponding to the skyrmion size for a 10 mT field in a disorder-free medium, are first generated and then relaxed in a 3 mT field while including disorder. Figure 3.9 (c) shows typical results of the simulation for thickness fluctuations with a relative amplitude of 1%. The calculated skyrmion morphology is similar to the one observed in the experiments, revealing the key role of disorder and magnetic history in the stabilization of isolated skyrmions. A statistic performed over a large number of randomly chosen disorder distributions leads to an effective skyrmion diameter $d_s^{[1\%]} = 348 \pm 59$ nm (see histogram for Figure 3.9 (d)). A similar analysis performed by slightly tuning the disorder amplitude to 2% and 0.5% thickness fluctuations lead to $d_s^{[2\%]} = 136 \pm 55$ nm and $d_s^{[0.5\%]} = 577 \pm 44$ nm, respectively (Figure 3.11 (a)).

It should be emphasized that the impact of disorder on the skyrmion morphology is very strong, even for relatively small thickness fluctuations considered. The key parameter fixing the skyrmion size is the domain wall energy σ , which involves all magnetic parameters [79]. For a single magnetic layer, $\sigma = 4\sqrt{AK_{\text{eff}}} - \pi D_{\text{eff}}$ with $K_{\text{eff}} = K_u - \frac{1}{2}\mu_0 M_s^2$ the effective anisotropy. Note that in the sample studied in this work, the bilayer behavior makes the relation slightly different, without any simple analytical formula (see Equation 3.6) [102]. Media adapted for skyrmion stabilization are generally optimized to display a low effective anisotropy in order to decrease the domain wall energy to few mJ/m². As a result, tiny thickness fluctuations are converted into large fluctuations of the effective anisotropy and domain wall energy, respectively. As an example, a 1%

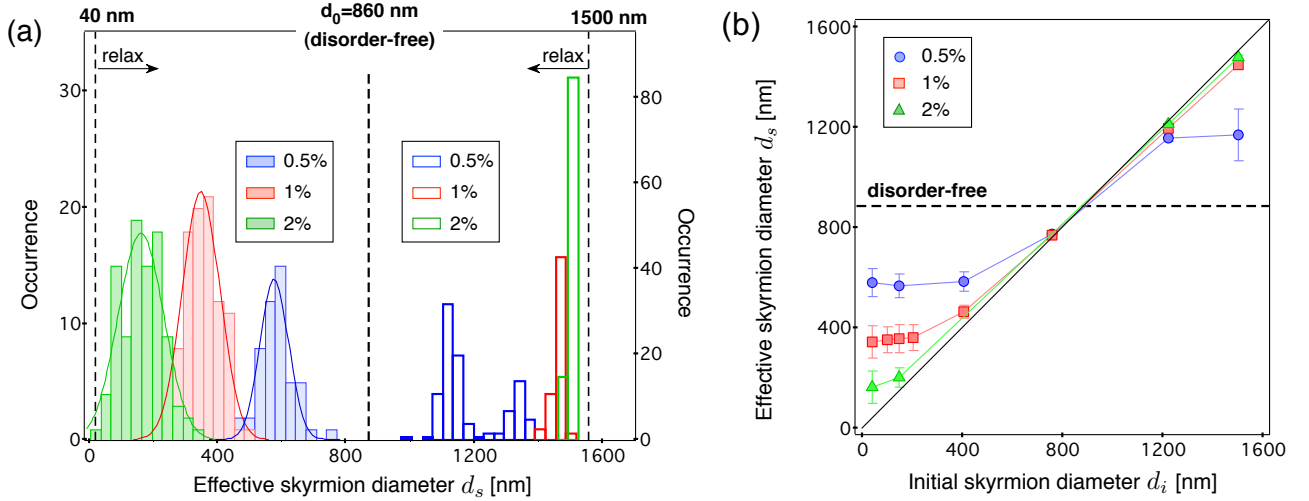


Figure 3.11 – (a) Simulation of the effective skyrmion size distribution obtained for different strength of disorder after relaxation in a 3 mT field while starting with a skyrmion diameter of $d_i = 40$ nm (left, filled bars) and $d_i = 1500$ nm (right, empty bars). The black dashed line in the middle indicates the skyrmion diameter for a disorder-free sample ($d_0 = 860$ nm). (b), The size of a ‘relaxed’ skyrmion vs. initial skyrmion size for different disorder strength. The error bars represent the variance of the size distribution and the black dashed line is a guide to the eye for the case without relaxation.

thickness fluctuations leads to about 30% and 20% fluctuations in effective anisotropy and domain wall energy, respectively. Such large fluctuations have a strong impact on the skyrmion spin texture. Although illustrative, magnetic simulations are performed at zero temperature, *i.e.* without including the effects of thermal fluctuations. As a result, a direct comparison between simulations and experiments does not allow to extract quantitative information about thickness fluctuations in the sample. Since thermal agitation helps to overcome energy barriers induced by pinning sites, the actual thickness fluctuations in the sample are most likely larger than 1%.

To further illustrate how the skyrmion size depends on disorder and magnetic field history, the skyrmion relaxation was simulated under the same 3 mT magnetic field while starting from a large skyrmion diameter $d_i = 1500$ nm. The resulting skyrmion size distribution is shown in Figure 3.11 (b) for various amplitudes of the thickness fluctuations. We now observe that the skyrmion size is larger than the one expected in a disorder-free sample. Such a measurement procedure was not accessible experimentally, as round, 1500-nm diameter skyrmions could not be stabilized before the application of the 3 mT magnetic field. However, a qualitative comparison can be done by comparing the first two images in Fig. 3.8, where the $1400\text{nm} \times 500\text{nm}$ domain at the center in zero field relaxes under 3 mT into a $1200\text{nm} \times 400\text{nm}$ domain.

The disorder-limited relaxation is well illustrated by plotting the variation of the skyrmion size obtained after relaxation (d_s) as a function of the initial size (d_i), as shown in Figure 3.11 (b). In the absence of disorder, the final size does not depend on the initial size and no magnetic history effect is found. In this case, the data

points would lie on the black dashed line in Figure 3.11 (b). When including disorder in the model we find the following: for an initial skyrmion size smaller than the equilibrium size ($d_i < d_0$), also the final size is smaller than the equilibrium ($d_s < d_0$). For an initial size larger than the equilibrium size ($d_i > d_0$), the final size is found to be larger as well ($d_s > d_0$). Moreover, the simulation show that the skyrmion relaxation becomes more and more efficient when the disorder decreases. We finally note that for the smallest initial size, relaxation is always found more efficient than for larger sized. This illustrates that the skyrmion energy variation versus its diameter is strongly asymmetric [79, 97], so that the force restoring the equilibrium size is stronger when $d_s < d_0$ compared to $d_s > d_0$.

In this chapter the capability of NV microscopy in quenching mode as a tool to investigate skyrmions at room temperature was demonstrated. This shows that NV microscopy holds great promise for skyrmion imaging in materials with low pinning, where other invasive techniques will ultimately fail. The large number of images skyrmions have revealed that, in contrast to the disorder-free medium, the skyrmion size and shape strongly vary. Importantly, the skyrmion size and its distribution also depend on the magnetic field history. Consequently, precaution is demanded, when extracting the equilibrium skyrmion size. A simple model of disorder based on thickness fluctuations has been shown to provide a good description of the obtained results. This work opens the way to a detailed understanding of the dynamics of skyrmions in real, disordered media [103, 101]. Indeed, the uniformity of the skyrmion size directly influences skyrmion dynamics [118], as the dissipation term in the Thiele equation grows with skyrmion size, whereas the gyrotropic term is independent, fixed by topology. This study also implies that, for applications using skyrmions, tight constraints apply to the thickness uniformity, a feature that is not so surprising in samples whose properties are interface-driven.

3.4 The future of skyrmionics

Material systems involving ultrathin ferromagnets with perpendicular magnetic anisotropy have already been studied extensively for magnetic domain wall dynamics with the common observations of strong pinning in the films. Experiments have revealed that the disorder leading to wall pinning can also have an influence on the skyrmion propagation. As we have seen in the previous chapter, imperfections in thin magnetic films have a non-negligible effect on skyrmion shape and size, on pinning and ultimately on their dynamics [101]. These results highlight important challenges that have to be tackled in order to make robust devices. Pinning due to disorder must not be neglected and the skyrmion topology is insufficient to oppose the effect. Device schemes that require control of the propagation direction will have to account for the resulting altered dynamic properties. Also the fluctuations in skyrmion size can become an issue causing noise for detection schemes that rely on the surface area of reversed magnetization or stray fields [129]. It was shown that the effect of local pinning can be accounted for by considering the thin film grain structure with local variation in the films thickness, a point which should be included into any future simulations. While pinning can be favorable for some kind of devices [137, 138] a key point for future investigations lies in the optimization and tuning of thin film host materials.

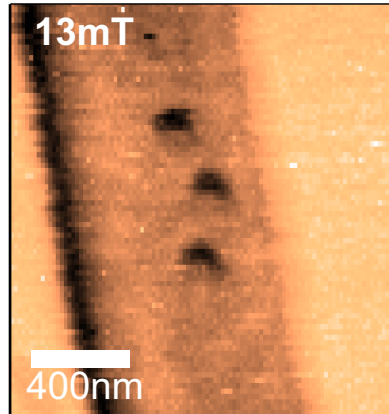


Figure 3.12 – **Skyrmions in thin film Co_2FeAl track** Magnetic skyrmions in a Heusler alloy thin film at room temperature recorded with the quenching mode of the NV magnetometer. The externally applied out-of-plane magnetic field of approximately 13 mT and the size of the skyrmions is in the range of ~ 100 nm

Apart from imperfections in thin films, there are other obstacles that have to be resolved on the way to the usage of skyrmions in storage devices: Eventually, the skyrmion Hall effect described in Section 3.2 leads to the motion of the skyrmions towards device edges and thus presents an issue. At the wire edges, skyrmions are easily annihilated by topographic defects. One possible solution has already been proposed and lies in the creation of antiferromagnetically exchange-coupled skyrmions [139]. Here the Magnus force on both sub-lattices is opposite and cancel each other, thus the skyrmions are no longer deflected towards the edge.

Rather than optimizing currently utilized materials, completely new skyrmion materials also have to be investigated. One example are Heusler alloys. They combine advantageous properties, such as high spin polarization and a small damping. This versatile material category is composed of four interpenetrating fcc lattices of metals that, in their pure state, are not magnetic, but together lead to ferro- and antiferromagnetic magnetized materials. Heusler alloys can be half-metals and have high Curie temperatures, which make them optimal for spintronics applications. A lot of Heusler compounds exhibit a non-centrosymmetric crystal structure, which is necessary for the presence of the DMI. Complex magnetic structures in which the magnetic moments are aligned non-collinearly have already been discovered [140, 141] in bulk. For spintronics applications, thin film Heusler alloys with interface induced DMI, would be especially interesting. However, the experimental proof of skyrmions in thin films was still missing. In collaboration with LPS and LSPM (Paris 13) we recently investigated a single layer of 1.5 nm thin Co_2FeAl film deposited on Pt and we observed skyrmions in nanotracks as shown in Figure 3.12. Due to the low damping in this material skyrmions are expected to move very fast. Experiments investigating the dynamics of the skyrmions in this sample with NV magnetometry are currently in progress.

Another interesting prospective in the field of skyrmionics are novel skyrmion control, beyond magnetic field and currents. For example, some multiferroic materials show DMI and can host skyrmions [142]. The existence of skyrmions in an insulating magnetoelectric material holds promise for new manipulation mechanisms via electric fields. Such magnetoelectric skyrmions may contribute the the design of completely novel skyrmion devices.

The material type of multiferroics mentioned in the last paragraph is not only interesting as skyrmion host medium. It has outstanding characteristics on its own which may be exploited to design yet utterly new low-power consuming memory storage technology. One of these materials, bismuth ferrite, will be the topic of the next Chapter.

Real-space imaging of non collinear antiferromagnetic order in the multiferroic bismuth ferrite

Contents

4.1	The antiferromagnetic multiferroic bismuth ferrite	85
4.1.1	Investigating antiferromagnetics and multiferroics	85
4.1.2	Crystal structure and magnetoelectric coupling	87
4.1.3	Electric and magnetic properties	89
4.2	Measuring and controlling the spin spiral of thin film BFO	93
4.2.1	Sample fabrication and characterization	93
4.2.2	Ferroelectric state revealed by piezoresponse force microscopy	93
4.2.3	First magnetic real space image uncovering the interplay between polarization and magnetization	94
4.3	Controlling the magnetic structure with electric fields	96
4.3.1	Observation of the switching of the spin spiral propagation direction	98
4.3.2	Amplitude of spin density wave revealed by qualitative stray field analysis	98
4.4	Conclusion and outlook	103

In the first part of this thesis, ferromagnetic materials hosting magnetic domain walls were investigated with respect to their application for low power consuming spintronic devices. In the previous chapter this idea was carried on and extended to a new magnetic texture: Magnetic skyrmions and their host medium were examined with the perspective of further pushing scaling limits and power consumption. These two new possible approaches for memory and logic devices rely on electric currents to drive the motion of domain walls or skyrmions. With the aim to further increase speed and reduce energy cost, utterly new materials are now

being investigated. One example are multiferroics. These materials possess the rare trait of exhibiting more than one ferroic order parameters simultaneously in a single phase. In this chapter, scanning NV magnetometry is utilized to study the multiferroic material bismuth ferrite (BiFeO_3 or short BFO). Especially interesting in BFO is the coupling between its (anti-)ferromagnetic and ferroelectric properties at room temperature. This magnetoelectric coupling can be exploited to create devices where the magnetization is controlled by electric fields rather than electrical currents [143]. To do so, a profound understanding of ferroelectric and magnetic properties of the material is indispensable. However, while the electric properties can readily be investigated, a real space image of its magnetic structure is elusive to date. We will exploit the extreme magnetic sensitivity and nanoscale spatial resolution of an all diamond scanning probe to study the magnetization structure of BFO. This work was conducted in close collaboration with

- V. Garcia, M. Bibes, S. Fusil, A. Barthélemy from the Unité Mixte de physique CNRS/Thales, Palaiseau
- M. Viret, from CEA, Gif-sur-Yvette
- J.-V. Kim from IEF, Orsay.

In Section 4.1 an overview over the material class is given. The thin film BFO sample studied in this work is characterized in detail in Section 4.2, where results of piezo force microscope imaging on the electronic polarization of the material are shown. A first magnetic image of the as-grown sample recorded with our magnetometer is resented. In Section 4.3 the first real space image of the spin spiral magnetic structure is presented and the switching of its propagation direction for different electric polarization is demonstrated. Furthermore, qualitative analysis of the stray field is conducted and conclusions on the existence and strength of the spin density wave accompanying the spin spiral are drawn. Finally, in Section 4.4 an outlook on open questions and future experiments on this material is given.

4.1 The antiferromagnetic multiferroic bismuth ferrite

Multiferroics are an outstanding and rare material class that exhibit more than one of the primary ferroic order parameters (ferromagnetism, ferroelectricity, ferroelasticity) simultaneously (See Figure 4.1). This definition is expanded to also include antiferromagnetic materials, as BFO. In the first section we explain the fundamentals of the antiferromagnetic multiferroic BFO. The material is embedded into the bigger framework of antiferromagnets and multiferroics, and its assets for spintronic applications is outlined (§4.1.1). In the following, a brief description of the magnetoelectric coupling is given and the crystal structure of BFO is described (§4.1.2). Lastly, the electric and magnetic properties of the multiferroic are explained (§4.1.3).

4.1.1 Investigating antiferromagnetics and multiferroics

Nearly 90% of known magnetic materials have dominant antiferromagnetic interactions, resulting in no or very small magnetization, and in addition most of them are insulators [144]. This strongly impedes their investigation, especially, when their magnetic order needs to be mapped at the nanoscale. While magnetic force

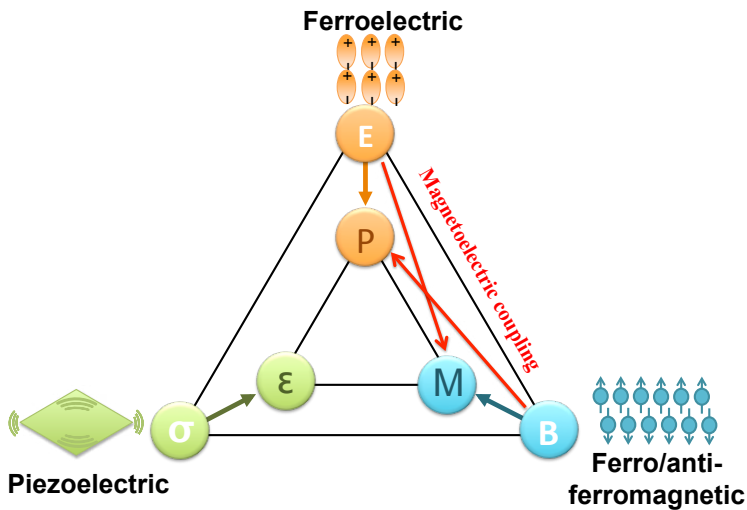


Figure 4.1 – **Electrical control of magnetism.** This schematic illustrating different types of coupling that can be present in multiferroics. Especially desirable is the coupling of electric and magnetic order. So far the only known multiferroic exhibiting the so called magnetoelectric coupling at room temperature is BFO. Controlling magnetism especially in thin films at room temperature by electric fields is a key challenge to diversify and augment the performance of spintronic devices.

microscopy [145] or X-ray photoemission electron microscopy [146] can reach a spatial resolution of a few tens of nanometers, their sensitivities are not compatible with the detection of weak magnetic signals commonly involved in antiferromagnets. Other techniques, like spin-polarized scanning tunnelling microscopy, can resolve the magnetic moments of single atoms [147] but are only applicable to conductive systems. Therefore, the spin texture of the vast majority of magnetically ordered materials cannot be directly imaged at the nanoscale. This is increasingly problematic since materials with complex antiferromagnetic orders show very appealing functionalities, which are absent in ferromagnets, and start to be exploited in a new generation of low-power spintronic devices [148].

Typical examples are multiferroics, in which (anti-)ferromagnetism coexists with ferroelectricity, enabling an efficient electrical control of magnetization through magnetoelectric coupling [149, 150, 151]. BFO is such a multiferroic material [152], which is currently emerging as a unique platform for spintronic [151] and magnonic devices [153] because its multiferroic phase is preserved well above room temperature. This material may boost the development of room temperature devices that can switch their magnetic properties with electric fields. It could serve as novel building block in microelectronic devices to avoid overheating due to Joule heating. The ferroelectric properties of BFO have been widely investigated by piezoresponse force microscopy (PFM), revealing unique electric domain structures and domain wall functionalities [154, 155]. However, the corresponding nanoscale magnetic textures and their potential for spin-based technology still remain concealed. In this chapter we demonstrate the first real-space imaging and electric field manipulation of complex antiferromagnetic order in a BFO thin film by using the NV scanning magnetometer.

The properties of our NV magnetometer are indispensable for investigating these materials magnetic properties: It is non-destructive (unlike Lorenz microscopy), non-invasive (unlike magnetic force microscopy), does not require synchrotron light (unlike photoemission electron microscopy), is applicable to insulators (unlike spin-polarized scanning tunnelling microscopy), and involves a table-top experiment that can operate under ambient

conditions. All these features, combined with its high sensitivity and nanoscale spatial resolution make it ideal for imaging the spin texture of complex antiferromagnetic or weak-ferromagnetic insulators that represent a large fraction of known magnetic substances which remain unobservable so far.

4.1.2 Crystal structure and magnetoelectric coupling

The crystal structure of BFO is a so-called perovskite. In general, a perovskite shows an ABO_3 structure as presented in Figure 4.2 (a). A metallic cation 'A' of rather big atomic radius (purple) occupies the corners of the cube. Another smaller metallic cation 'B' is positioned in the middle of the cube (green) and an anion 'O' is located in the middle of each face of the cube (pink). The anions, usually oxygen, form an octahedral structure (pink shaded). In a constellation, where the oxygen octahedron are connected to one another at the corners by sharing one of their oxygen atoms, the presence of polarized ions promotes the occurrence of ferroelectricity [156]. In the case of BFO, site 'A' is occupied by a strongly polarized Bi^{3+} and site 'B' with the magnetic Fe^{3+} cation. The complete crystal structure of BFO is described as a rhombohedrally distorted perovskite. Due to the clock and anticlockwise rotation of the oxygen octahedral cages around the $[111]$ direction, the BFO lattice is described with a rhombohedral unit cell. This is shown in Figure 4.2 (b), where the grey lines outline the rhombohedral unit cell. Since the rhombohedral distortion is small, the crystal orientation is frequently referred to as (pseudo) cubic unit cell with the lattice parameter $a_o = 0.96\text{\AA}$ and $\alpha = 89.47^\circ$ (black cubes in Figure 4.2 (b)). This description is chosen to represent crystallographic directions in the following sections. The structure of BFO deviates slightly from the ideal cubic perovskite structure in two points: First, a polar displacement of all the anion and cation sublattices relative to one another is present, which leads to the spontaneous electric

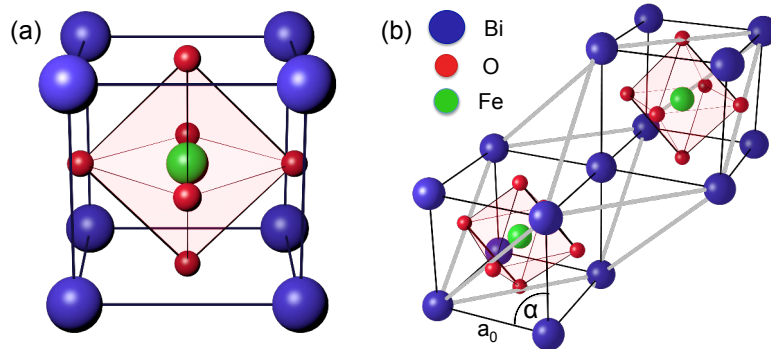


Figure 4.2 – **Crystal structure of BFO.** (a) Perovskite crystal structure. Two metallic cations occupy the corners and the middle of the cube (purple and green) and an anion is located in the middle of each face of the cube (pink). The anions form the pink shaded octahedral structure. (b) The BFO crystal structure with the pseudo cubic unit cell in black and the rhombohedral unit cell in grey. The oxygen octahedra are rotated with alternating sense around the $[111]$ direction and the cations are displaced along the $[111]$ direction with respect to the anions in the lattice.

polarization of the material. Second, an antiferrodistortive rotation of the oxygen octahedra occurs around the [111] direction with alternating sense of rotation [157, 158]. The incorporation of both of these distortions gives rise to the R_{3c} symmetry group of BFO, defining magnetic and electric properties and their coupling.

BFO is a multiferroic, displaying at the same time ferroelectricity, antiferromagnetism and ferroelasticity [159]. Of special interest is the magnetoelectric character of the material: The so-called magnetoelectric effect leads to the cross-coupling of magnetization \mathbf{M} and electric polarization \mathbf{P} to their conjugate fields, \mathbf{E} and \mathbf{H} (see Figure 4.1). This effect was already proposed by P. Curie in 1894 [160], calculated by Dzyaloshinski for Cr_2O_3 [161] and experimentally verified nearly 70 years later in Cr_2O_3 [162].

In order to obtain an easy mathematical understanding of the magnetoelectric coupling, a system in its equilibrium state is first described thermodynamically by its free energy $F(E_i, H_i)$. The expansion of the free energy as a power series in the electric and magnetic fields \mathbf{E} and \mathbf{H} is given in Equation 4.1 [163].

$$F(E_i, H_i) = F_0 - \underbrace{P_i^S E_i - M_i^S H_i}_{\text{spontaneous P and M}} - \underbrace{\frac{1}{2}\epsilon_0\epsilon_{ij}E_iE_j - \frac{1}{2}\mu_0\mu_{ij}H_iH_j}_{\text{permittivity and permeability effect}} - \underbrace{\alpha_{ij}E_iH_j}_{\text{linear magnetoelectric effect}} + \dots \quad (4.1)$$

For many materials, higher order magnetoelectric effects have to be taken into account. We omit them in this derivation to easily illustrate the basic relation of polarization (magnetization) and magnetic field (electric field). The partial derivative with respect to E_i and H_i gives the polarization P_i and the magnetization M_i at a given temperature:

$$P_i = -\frac{\partial F}{\partial E_i} = P_i^S + \epsilon_0\epsilon_{ij}E_j + \alpha_{ij}H_j + \dots \quad (4.2)$$

$$M_i = -\frac{\partial F}{\partial H_i} = M_i^S + \mu_0\mu_{ij}H_j + \alpha_{ij}E_j + \dots \quad (4.3)$$

where M_i^S and P_i^S are the static magnetization and polarization and ϵ_{ij} (μ_{ij}) is the electric (magnetic) susceptibility. The agent of the magnetoelectric coupling is the tensor α which describes the magnetoelectric effect that corresponds to a linearly induced polarization by a magnetic field and vice versa. Under a constant field the first order response of a magnetoelectric material is described by this magnetoelectric susceptibility. This tensor can be written as [164]:

$$\alpha_{ij} = \left(\frac{\partial P_i}{\partial H_j} \right) = \epsilon_0\epsilon_{ii} \left(\frac{\partial E_i}{\partial H_j} \right) \quad (4.4)$$

and when simplified the following representation of α_{ij} is obtained:

$$\alpha_{ij} = \sqrt{\epsilon_0\mu_0\epsilon_{ii}\mu_{jj}} \quad (4.5)$$

This equation shows that the magnetoelectric effect is expected to be large in materials which exhibit coexisting magnetic and ferroelectric phases with high susceptibilities [165]. However, such materials are extremely scarce. While ferroelectricity requires diamagnetic ions and thus empty d orbitals, a magnetic order usually requires

atoms with partially filled d orbitals and the two properties are seemingly incompatible.

A class of multiferroics that display large magnetoelectric coupling are single phase multiferroics. Large magnetoelectric effects were especially observed in multiferroic bulk crystals and have led to the proposition and demonstration of a variety of spintronic technologies [166, 167, 168, 169]. However, for the next-generation low power consuming devices, multiferroics should preferably be utilizable in thin film form. A major experimental breakthroughs in 2003 showed an enhanced magnetoelectric coupling in thin films of BiFeO₃ [170] at room temperature. By now, thin films of single phase can be produced routinely and their properties can be tailored with epitaxial strain [171]. The coupling of electrical and magnetic orders in thin film single phase BFO is mediated by the spin-orbit driven Dzyaloshinskii-Moriya interaction (introduced in Chapter 2) between adjacent Fe moments $E_{DM} = \vec{D} \cdot (\vec{M}_{Fe1} \times \vec{M}_{Fe2})$. The polar distortion along the [111] direction is responsible for the symmetry of the crystal, defining the direction of the DMI vector (along the symmetry axis [111]) and the magnetic structure of BFO is orthogonally coupled to the DMI vector. By reorienting the polarization it is possible to reorient the magnetic plane and thus the antiferromagnetic structure [172, 157]. In this work we focus on the characterization of thin film, single phase BFO. The exact properties and the interplay between polarization and magnetization in this particular system are explained in the next section.

4.1.3 Electric and magnetic properties

The displacement of the Bi ions relative to the FeO₆ octahedra in BFO gives rise to a strong ferroelectric polarization ($100 \mu\text{C}/\text{cm}^2$) along one of the [111] directions [152]. In this complex system, eight possible polar-

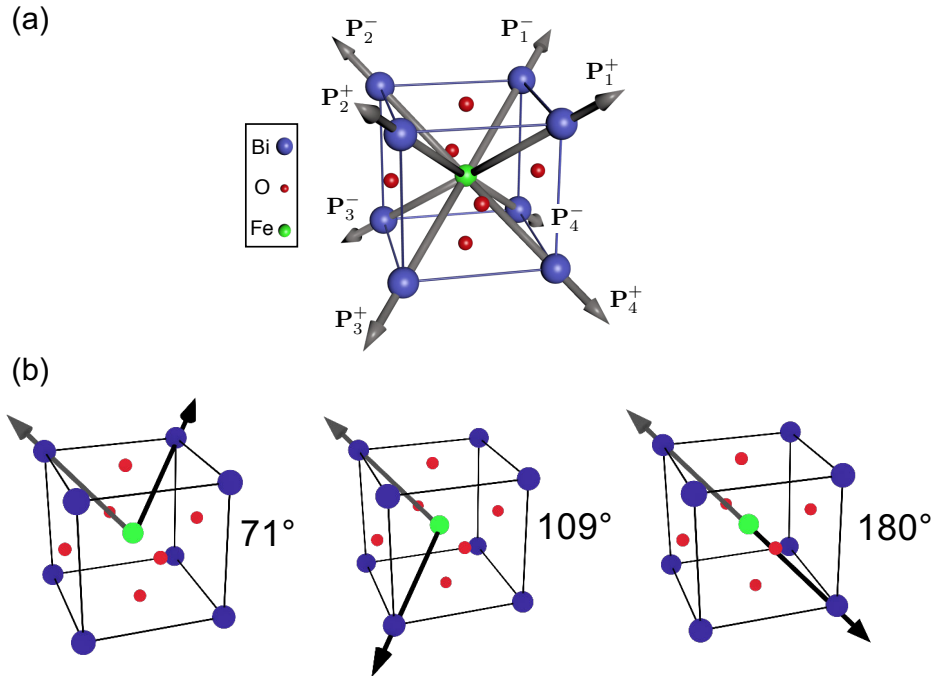


Figure 4.3 – **Polarization direction in BFO.** Image (a) shows the pseudocubic unit cell of BFO with its eight possible polarizations \mathbf{P}_i^\pm along the [111] directions. The eight possible directions for the polarization lead to three different types of electric domain walls. An example for 71°, 109°, and 180° wall is shown in (b). The angle is defined by the rotation between the two polarization directions.

ization orientations $\mathbf{P}_{i=1..4}^{\pm}$ are thus possible (See Figure 4.3 (a)). They permit the possible formation of three ferroelectric domain walls 71° , 109° , and 180° which are distinguished by the angle the polarization rotates across the domain wall as depicted in Figure 4.3 (b).

A piezoresponse force microscopy (PFM) can be used to determine the flavor of electric domains and domain walls by mapping the direction of the polarization. For a PFM measurement an electric voltage is applied with the tip and the mechanical response due to the local expansions or contractions of the sample are detected by the tip deflection. By using a lock-in amplifier and alternating current V_{ac} , the signal is demodulated in order to distinguish and image simultaneously topography and ferroelectric response. This causes an oscillatory deformation of the sample surface which amplitude and phase are determined with the lock-in detection method. For polar components orientated parallel to the electric field the resulting oscillating movement will be entirely in-phase with the modulated electric field and for an anti-parallel alignment the motion will be 180° out-of-phase. In this way it is possible to determine the orientation of the vertical components of polarization from analysis of the phase information (see Figure 4.4). In order to determine the third component of the polarization vector, along the long axis of the tip, the measurement of a region must be repeated with the sample rotated by 90° . This technique is utilized to observe, as well as to write electric domains. For the latter a small DC voltage is applied between the tip and bottom electrode, high enough to generate an electric field higher than the coercive voltage and thus induce local polarization reversal.

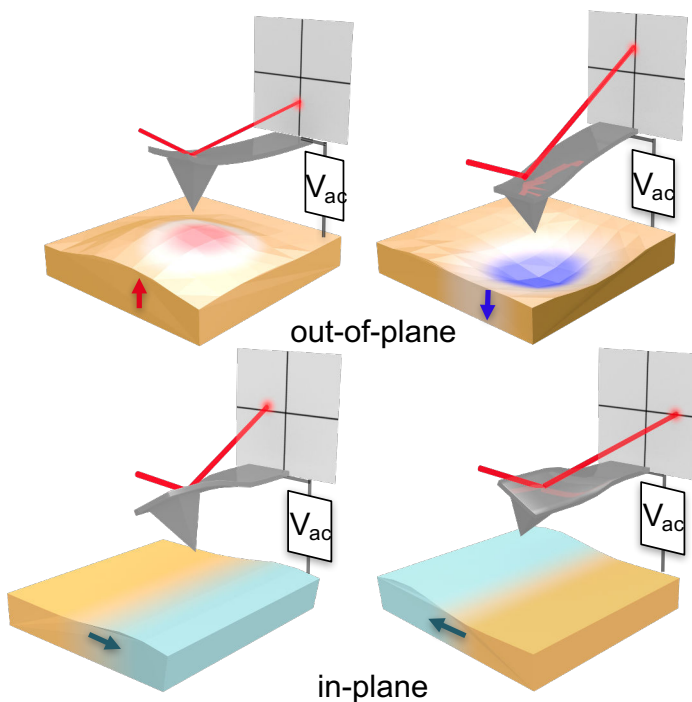


Figure 4.4 – **Working principle of the PFM.**

This technique employs a conductive tip to detect the ferroelectricity of a sample by monitoring the piezoelectric surface displacements. The tip of the PFM is scanned over a sample while applying a voltage between tip and sample. As response to the electrical stimulus the sample locally expands or contracts according to its polarization and the tip is deflected. This deflection is measured by a laser which is reflected from the back of the tip to a photodetector. The separation of in and out-of-plane components is possible through the use of this 4-quadrant photodiode detector. If the polarization has an out-of-plane component, an applied electric field causes a out-of-plane expansion or contraction of the lattice depending on electric field orientation with respect to the polarization direction. For the in-plane components, an out-of-plane electric field causes the regions to shear in a different way, resulting in the PFM tilting either to the left or the right.

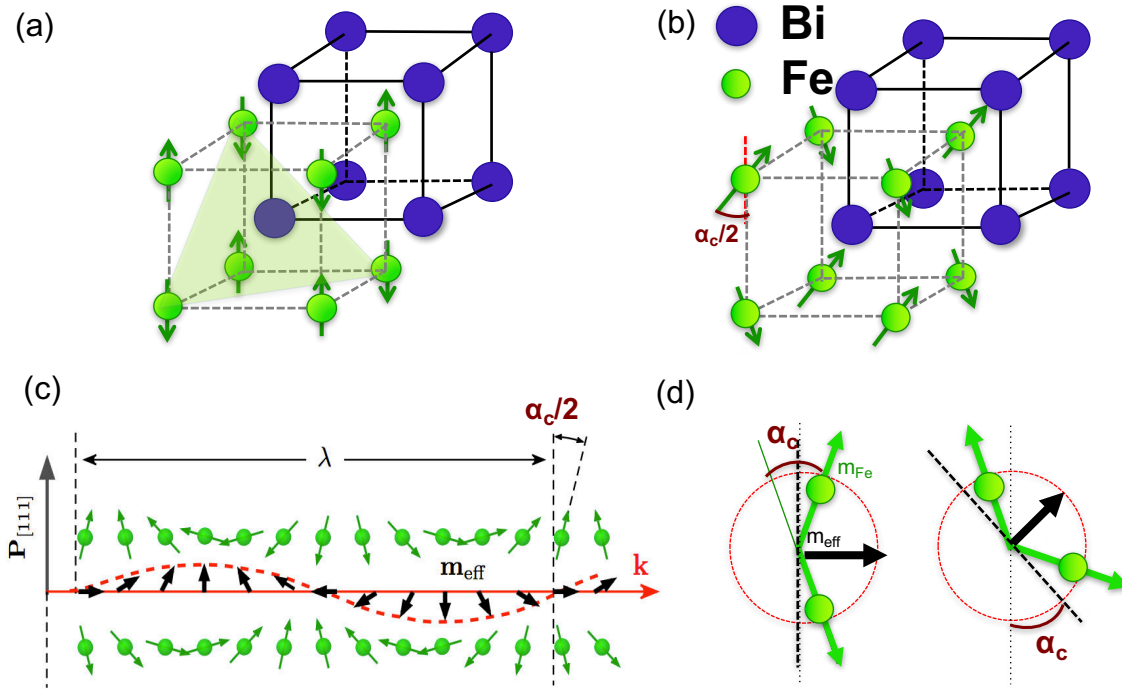


Figure 4.5 – **Magnetic structure of BFO.** (a) shows a G-type antiferromagnetic structure. The spins in (111) plane (light green) are aligned ferromagnetically, spins in adjacent (111) planes antiferromagnetically. (b) In addition the Fe³⁺ moments in BFO are canted by the canting angle α_c due to the torque provided by the DMI interaction [143]. (c) depicts the superimposed spin spiral modulation of the magnetic structure. Magnetoelectric coupling induces a cycloidal rotation of Fe³⁺ spins (green arrows). The canted antiferromagnetic alignment between consecutive atomic layers, characterized by the angle α_c , results in an effective magnetic moment \mathbf{m}_{eff} describing a cycloid with a wavelength λ (black arrows). (d) Neighboring spins of the spin spiral show a canting of α_c . It is thus possible to retrieve the canting angle from the spiral wavelength λ .

From the magnetic point of view, BFO was initially thought to be a conventional G-type antiferromagnet [173]. This indicates that the Fe magnetic moments are coupled ferromagnetically within the (111) planes and antiferromagnetically between adjacent planes, as illustrated in Figure 4.5 (a). In addition, the symmetry imposed by the rhombohedrally distorted perovskite and the rotation of the oxygen octahedral cages permit the formation of a net magnetic moment through a canting of the antiferromagnetic lattice via the torque provided by the DM interaction, as depicted in Figure 4.5 (b). This canting is described by the so-called canting angle α_c , sketched in Figure 4.5 (b) and is defined as the angle between antiferromagnetically coupled Fe atoms. High-resolution neutron diffraction later revealed a cycloidal antiferromagnetic order [174, 175] with a characteristic wavelength of $\lambda \sim 64$ nm (see Figure 4.5 (c)). Here the canting angle is defined as the rotation angle of the magnetic moment with respect to its nearest neighbor as specified in Figure 4.5 (d). In addition to the spin spiral, a spin density wave (SDW) was predicted theoretically [176] and proven experimentally [177]. The SDW follows the same propagation direction and wavelength as the cycloid. Its spin oscillating are in a plane normal to the cycloid (See Figure 4.11). The spin-spiral magnetic configuration was initially discovered for bulk BFO.

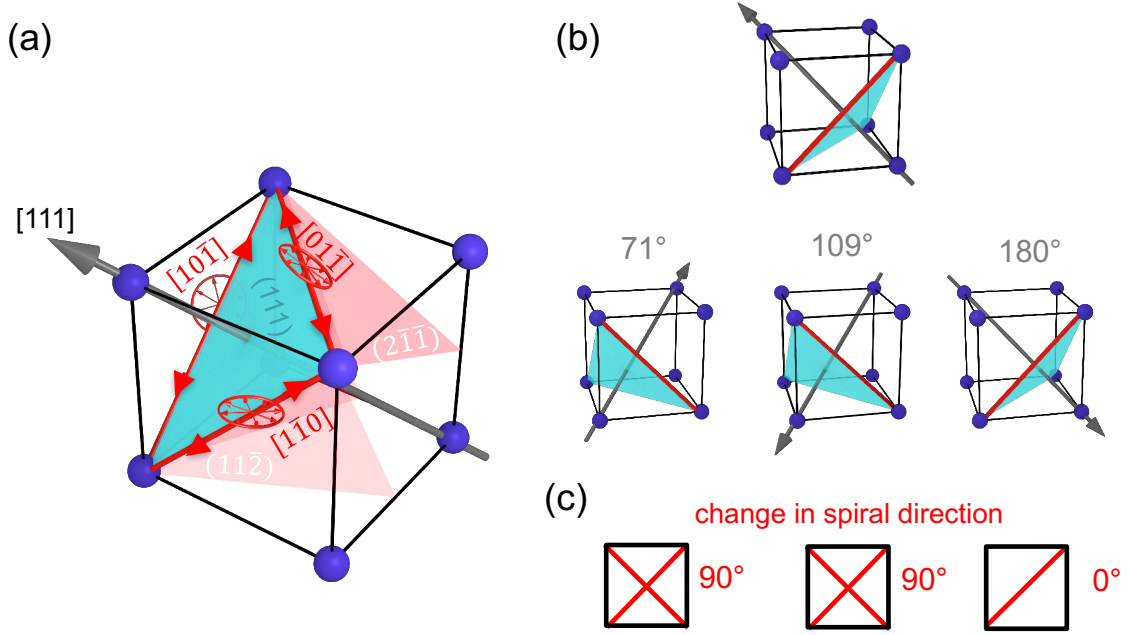


Figure 4.6 – **Coupling of polarization and magnetization.** (a) shows the pseudo cubic unit cell with BFO and one polarization direction (grey arrow). For this direction three different spiral directions (red lines), perpendicular to the polarization are possible. The spiral is rotating in a well defined plane (light red) as visible for two of the directions (the third plane for the $[10\bar{1}]$ direction is $(\bar{1}21)$). (b) illustrates the three different electric domain walls with the spiral propagation direction depicted in red. This leads to a change in the rotation direction of 90° in the case of 71° and 109° walls and no change in direction for the 180° as shown in (c)

Several works indicated that it is suppressed due to strain [165, 171, 178] leading to a homogeneous G-type antiferromagnetic order in thin films. However, it has recently been shown that the cycloidal spin order can be present in a 100 nm thick BFO films [179]. In our work it will be shown that the spin cycloid is even preserved in ~ 30 nm thin films, a promising result for device proposals based on the spin spiral magnetic order [153, 180, 181] as spin-wave-based logic gates.

After having had a look at polarization and magnetization structure in BFO separately, we are now interested in how these two properties are linked by the magnetoelectric coupling. The coupling causes that the spin cycloid propagation direction and the ferroelectric polarization vector are normal to each other. In addition, the rhombohedral symmetry of BFO allows three equivalent propagation directions of the cycloid ($\mathbf{k}_1, \mathbf{k}_2, \mathbf{k}_3$) for a given variant of ferroelectric domain [175, 173]. The magnetic moments rotate in a plane defined by the direction of polarization, \mathbf{P} and the cycloidal propagation vector \mathbf{k}_i . Figure 4.6 depicts this behavior: in 4.6 (a) one polarization direction with the possible spiral directions \mathbf{k}_i and corresponding spin rotation planes are shown. This is analogous for the other seven polarization directions. Although the three spiral directions are degenerate, usually only one is present per polarization (as detailed later). Assuming that only \mathbf{k}_1 , which is

defined as the propagation direction parallel to the sample surface, is observed for the three electric domain walls (shown in Figure 4.3 (b)) a change in the spin spiral direction of 90° (for 71° and 109° walls) or no change (in case of 180° walls) should be observed at an electric domain wall as illustrated in Figure 4.6. It should be noted that the spiral wavelength as seen from the surface is different for \mathbf{k}_1 (direction parallel to the surface) and $\mathbf{k}_2, \mathbf{k}_3$ since latter are propagating with an angle of 45° with respect to the surface. Furthermore, stress can induce a modification of the spin cycloid period and may be used as a tool to either destroy or preserve this magnetic order as magnetic ground state in nanoscale thin film [171, 179, 182].

4.2 Measuring and controlling the spin spiral of thin film BFO

In the next sections we will investigate a thin film BFO sample. First, the sample fabrication is outlined and the sample structure is presented (§4.2.1). The growth was performed by our collaborators at the UMR de physique/Thales, Palaiseau. Next, the results on the sample characterized with PFM are discussed. The as-grown sample shows a worm-like electric polarization structure formed by two different domain types (§4.2.2). A first real-space magnetic image of the NV-scanning magnetometer reveals the relation between polarization and magnetization (§4.2.3).

4.2.1 Sample fabrication and characterization

The sample investigated in this work is a thin BFO (001) film, which was grown by pulsed laser deposition on a $\text{DyScO}_3(110)$ orthorhombic substrate, using an ultrathin buffer electrode of SrRuO_3 . The film's structural properties were investigated by X-ray diffraction (XRD) showing that the film is epitaxial and single phase, exhibiting a well-crystallized structure and has a thickness of 32 nm. In this kind of films epitaxial strain leads to an array of striped ferroelectric domains whose typical width is in the range of ~ 100 nm (see Figure 4.8). In-depth PFM and X-ray diffraction analysis reveal that only two variants of polarization coexist (\mathbf{P}_3^- and \mathbf{P}_4^- as shown in Figure 4.3), separated by 71° domain walls as specified in the next section. In thin films the spin cycloid can be modulated or even destroyed by epitaxial strain. Considering the low lattice mismatch between BFO and DSO ($\sim 0.4\%$), the cycloidal antiferromagnetic order is however expected to be preserved in the studied epitaxial thin film. A gold microwave stripline was deposited on the sample to excite the NV center and different areas were marked in order to distinguish differently polarized domains as shown in Figure 4.7.

4.2.2 Ferroelectric state revealed by piezoresponse force microscopy

First, the ferroelectric configuration of the pristine BFO sample was identified by vectorial PFM, by probing the different in-plane variants when rotating the sample crystallographic axis compared to the PFM cantilever's long axis (Figure 4.8). These measurements were conducted by S. Fusil and V. Garcia at UMR physique/Thales. Alternated light/dark stripes are observed in the in-plane PFM phase image acquired with the cantilever aligned along the pseudo cubic [100] direction (Figure 4.8 (c)). This configuration does not lift the degeneracy between equivalent polarization variants for PFM response: all four variants with polarization pointing downwards

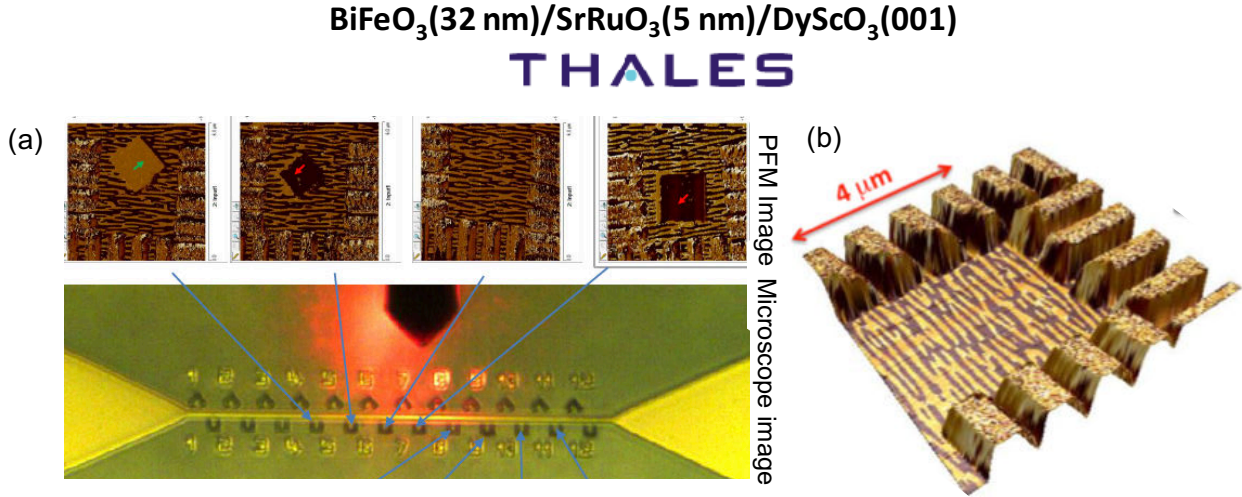


Figure 4.7 – **Structure of the investigated sample** (a) The thin film BFO sample was fabricated by the oxytronics, CNRS/Thales laboratory (Palaiseau, France). A gold antenna was fabricated on top of the sample and different squares were created and numbered close to this microwave line. In this way differently polarized areas (see next section) can be easily recognized and measured with the NV center, excited by the antenna. (b) Each area is $4 \times 4 \mu\text{m}$ and framed by ~ 100 nm high barriers.

(sketched in Figure 4.8 (b)) correspond to the same in plane amplitude response (Figure 4.8 (d)). \mathbf{P}_2^- and \mathbf{P}_3^- are pointing to the right of the cantilever, corresponding to the dark phase signal, while \mathbf{P}_1^- and \mathbf{P}_4^- are pointing to the left of the cantilever, corresponding to the light phase signal. At this stage, several kind of domain walls are still possible. When the cantilever is aligned along $[110]$ (Figure 4.8 (f)), the \mathbf{P}_2^- and \mathbf{P}_4^- in-plane responses are turned off and all responding domains (bright amplitude in Figure 4.8 (g)) are pointing to the left side of the cantilever (light phase signal in Figure 4.8 (h)), identifying \mathbf{P}_3^- domains. When the cantilever is aligned along $[\bar{1}10]$ (Figure 4.8 (i)), the \mathbf{P}_1^- and \mathbf{P}_3^- in-plane responses are turned off and all responding domains (bright amplitude in Figure 4.8 (j)) are pointing to the right of the cantilever (dark phase in Figure 4.8 (k)), identifying \mathbf{P}_4^- domains. With data from Figure 4.8 (g) and (j) it is concluded that the ferroelectric configuration in the BFO thin film is determined as alternated \mathbf{P}_3^- and \mathbf{P}_4^- variants in the form of stripes separated by 71° domain walls.

4.2.3 First magnetic real space image uncovering the interplay between polarization and magnetization

After having identified the electric polarization properties of the sample, we are now interested in its magnetic properties. The spin texture of the BFO sample is investigated through stray field measurements using the scanning NV magnetometer. For the present study, a single NV defect placed at the apex of a nanopillar of a diamond scanning-probe is utilized. This allows scanning the NV defect in close proximity to the sample [48] and provides high spatial resolution and magnetic field sensitivity. Scanning-NV magnetometry is the only

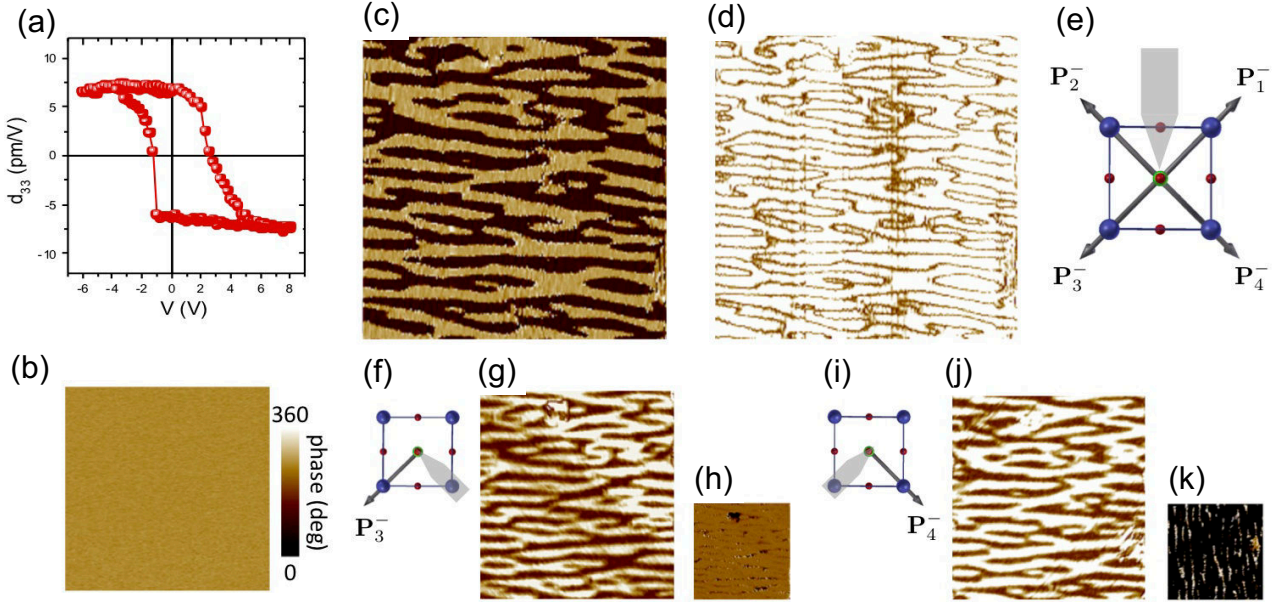


Figure 4.8 – **Determination of polarization variants in the BFO thin films.** (a) Local out-of-plane PFM hysteresis loop with bias voltage. Being imprinted toward positive bias voltage values it reveals the homogeneous pristine downward polarization in accordance with out-of-plane PFM imaging. (b) Homogeneous out-of-plane PFM phase corresponding to polarization variants pointing downward in a $6 \times 6 \mu\text{m}^2$ area. (c) In-plane PFM phase and (d) amplitude for the cantilever parallel to $[100]$. (e) Sketch of the PFM cantilever and the four possible in plane variants of polarization in BFO. (f) Sketch of the $[110]$ direction of the cantilever with the corresponding in-plane PFM (g) amplitude and (h) phase. (i), Sketch of the $[\bar{1}10]$ direction of the cantilever with the corresponding in-plane PFM (j) amplitude and (k) phase. All the images in (c) to (k) are acquired in the same $3 \times 3 \mu\text{m}^2$ area.

magnetic microscopy technique allowing to investigate directly the stray field of such an anti-ferromagnetic material and to give information on the real space, nanometer-scale magnetization pattern.

At each point of the scan, optical illumination combined with radiofrequency (RF) excitation enable measuring the ESR spectrum of the NV defect by recording its spin-dependent photoluminescence (PL) intensity. Any magnetic field emanating from the sample is then detected through a Zeeman shift of the ESR frequency, which is simply given by $\Delta_z = \gamma_e B_{\text{NV}} / 2\pi$, where $\gamma_e / 2\pi = 28 \text{ GHz/T}$ is the electronic spin gyromagnetic ratio and B_{NV} is the magnetic field projection along the NV defect quantization axis, as described in Chapter 1. The resulting magnetic sensitivity is in the range of a few $\mu\text{T}/\sqrt{\text{Hz}}$, while the spatial resolution is fixed by the distance d between the sample and the NV spin sensor [42]. This key parameter is independently measured through a calibration process above the edges of a uniformly magnetized ferromagnetic wire [92], leading to $d = 49.0 \pm 2.4 \text{ nm}$. The calibration measurement is described more precisely in Chapter 1 and in reference [54]. In the following, all experiments are performed under ambient conditions with a bias field $B_b = 1.4 \text{ mT}$ applied along the NV defect axis in order to increase the sensitivity and to determine the sign of the measured magnetic

fields [42]. Such a bias field is weak enough not to modify the magnetic order in BFO.

For preliminary magnetic characterization a simplified and fast version of the full-B images is employed. This so-called **dual iso-B** imaging mode is executed by measuring the PL difference between the two consecutively applied frequencies f_1 and f_2 (marked in Figure 4.9 (a)) for the given value of the magnetic field, i.e. $S_{isoB} = PL(f_2) - PL(f_1)$. As the sample is scanned by the diamond tip, the stray field (δB_{NV}) along the NV axis from the sample shifts the ESR frequency as the case for the normal full-B mode. The signal S_{isoB} is positive (resp. negative) if the projected magnetic field from the sample shifts the ESR signal towards f_1 (resp. f_2). The $400\text{nm} \times 400\text{nm}$ iso-B image shown in Figure 4.9 of the main text was obtained with 48×48 pixels corresponding to a pixel size of $8.33\text{nm} \times 8.33\text{nm}$. An integration time of 200 ms was used for each pixel. Thus, the time to record the iso-B image shown in the main text accounts to approximately 10 minutes and is much faster compared to the full-B mode, while still being able to detect the negative and positive shift of the signal.

The scanning-NV magnetometer was first operated in this *dual-iso-B* imaging mode over the virgin state of the sample. A typical *dual-iso-B* image recorded above the (001)-oriented BFO thin film is shown in Figure 4.9 (d). We observe a periodic variation of the magnetometer signal along the horizontal axis of Figure 4.9, which directly reveals the spatially oscillating magnetic field generated by the cycloidal modulation of the spin order. Moreover, the propagation direction of this spin cycloid is periodically modified along the vertical axis of Figure 4.9. The resulting zig-zag shaped magnetic field distribution mimics the shape and width (~ 100 nm) of the ferroelectric domains of the virgin state as determined by PFM and shown in Figure 4.8. With this measurement we reveal the first hint of the spin spiral and the manipulation of its propagation direction with polarization. However the virgin state of the grown sample with its stripe electric domain structure proves a complex system in order to draw more precise conclusion on the magnetic structure. For these reasons the PFM is used to imprint single electric domains with different polarization directions into the as-grown state. We take a closer look at these areas with the magnetometer in the following sections.

4.3 Controlling the magnetic structure with electric fields

Our goal in the last section is, to controllably alter the magnetic structure of BFO by using an electric field to write certain polarization directions. Two different electric monodomains are written into the as-grown sample and are subsequently investigated with the NV magnetometer (§4.3.1). The full magnetic field image over an electric monodomain is recorded. The expected magnetic field produced by a spin spiral is calculated and compared with the measured data. We conclude that, in addition to the spin cycloid, the predicted SDW has to be taken into account in order to explain the measured field strength (§4.3.2).

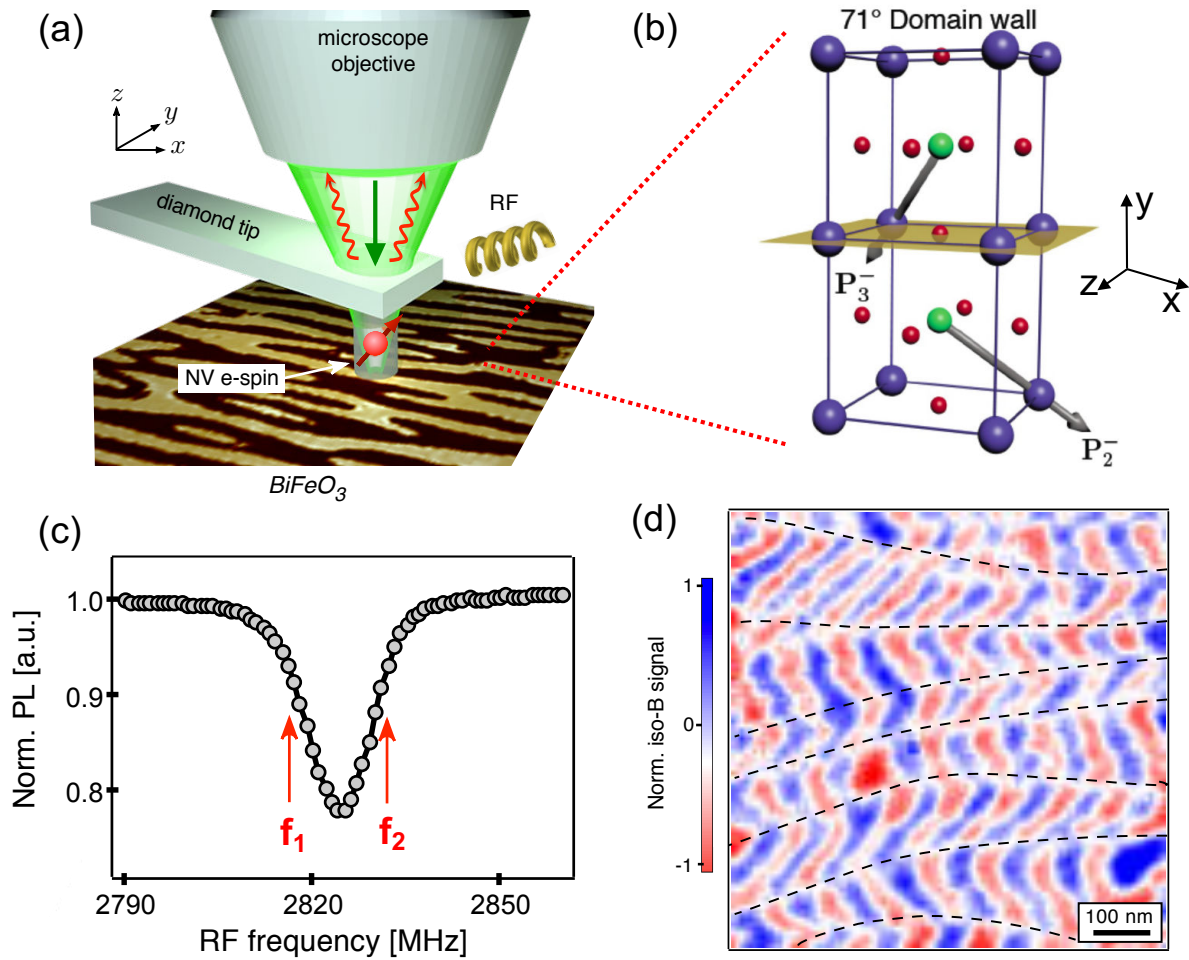


Figure 4.9 – Mapping the magnetic texture of BiFeO_3 with NV magnetometry. (a) The electronic spin of a single NV defect placed at the apex of a diamond scanning-probe tip is scanned over the BFO thin film sample in its virgin state. A gold antenna is placed on the sample to excite the NV center to perform quantitative field imaging. The PFM image below the tip is the virgin state of the BFO thin film with stripe-like electric domains. (b) The virgin state of the sample exhibits alternating P_3^- and P_4^- electric domains and thus 71° domain walls. (c) Typical ESR spectrum recorded while applying a bias field $B_b = 1.4$ mT along the NV axis. The red arrows indicate the two RF frequencies f_1 and f_2 used for the *dual-iso-B* imaging mode. (d) Magnetic field image recorded above the BFO film while operating the NV magnetometer in *dual-iso-B* imaging mode. The black dashed lines, which are drawn as a guide to the eye, are attributed to ferroelectric domain walls leading to abrupt rotations of the antiferromagnetic order.

4.3.1 Observation of the switching of the spin spiral propagation direction

To gain further insights into the properties of the spin cycloid in this BFO thin film, PFM was used to design a single micron-sized ferroelectric domain from the as-grown striped pattern (Figure (a)), taking advantage of the trailing electric field induced by the slow scan axis of the scanning probe. The magnetic field distribution recorded above such a ferroelectric monodomain exhibits a simple periodic structure, indicating the presence of a single spin cycloid (Figure 4.10 (b)). Importantly, the (001) surface projection of the spin cycloid propagation direction is normal to that of the ferroelectric polarization vector \mathbf{P}_1^+ . Among the three possible cycloid propagation directions, only \mathbf{k}_1 is normal to the (001) projection of \mathbf{P}_1^+ , the other two lying at 45° from the polarization vector (see inset in Figure 4.10 (c)). We therefore conclude that the spin cycloid propagates along \mathbf{k}_1 , *i.e.* in the plane of the BFO thin film. This result can be qualitatively explained by considering that epitaxial strain modifies the anisotropy along the film normal [171]. For BFO thin films grown on DSO, compressive strain induces an easy-plane contribution which stabilizes magnetic structures with their spins far from the [001] direction. Thus, the three possible cycloidal directions see their degeneracy lifted and the one propagating along $[\bar{1}10]$ becomes energetically favorable [171]. Using a two-dimensional fit of the magnetic image with a sinusoidal function, we infer a characteristic wavelength $\lambda = 70.6 \pm 1.4$ nm (Figure 4.10 (c)). The slightly enhanced period compared to the bulk value (~ 64 nm) is interpreted as due to the small compressive strain imposed by the substrate [182]. This result illustrates that the local magnetoelectric interaction between neighboring atoms at the origin of the spin cycloid does not require thick films of BFO, *i.e.* with thicknesses well above its characteristic wavelength, as previously speculated [179].

After demonstrating that the polarization and the cycloid propagation are intimately linked, we describe how this cycloid propagation direction can be manipulated using the magnetoelectric coupling. To this end, we define another ferroelectric domain with an in-plane component of the polarization rotated by 90° (\mathbf{P}_4^- in Figure 4.3 (a)). The magnetic image shows that the propagation direction of the spin cycloid is also rotated by 90° with a very similar wavelength $\lambda = 71.4 \pm 1.4$ nm, once again corresponding to the propagation direction \mathbf{k}'_1 lying in the (001) plane (Figure 4.10 (e) and (f)). These experiments illustrate how magnetoelectric coupling can be used to efficiently control and manipulate the antiferromagnetic order in a BFO thin film. They also confirm that the abrupt rotations of the antiferromagnetic order observed in Figure 4.9 (d) are occurring at ferroelectric domain walls.

4.3.2 Amplitude of spin density wave revealed by qualitative stray field analysis

As a final experiment, a fully quantitative magnetic field image was recorded above the ferroelectric monodomain shown in Figure 4.10 (a). Here the magnetic field component B_{NV} was obtained by measuring the Zeeman shift Δf_{NV} of the NV defect electron spin sublevels at each pixel of the scan. The resulting magnetic field map indicates a modulation with a typical amplitude in the range of ± 140 μT as plotted in Figure 4.11 (a). In order to understand quantitatively this experimental data, stray field produced by the BFO sample is computed. To do so, the spin cycloid is modeled by a rotating uncompensated magnetization vector $\mathbf{M}_{\text{eff}} = \mathbf{m}_{\text{eff}}/V$, where V

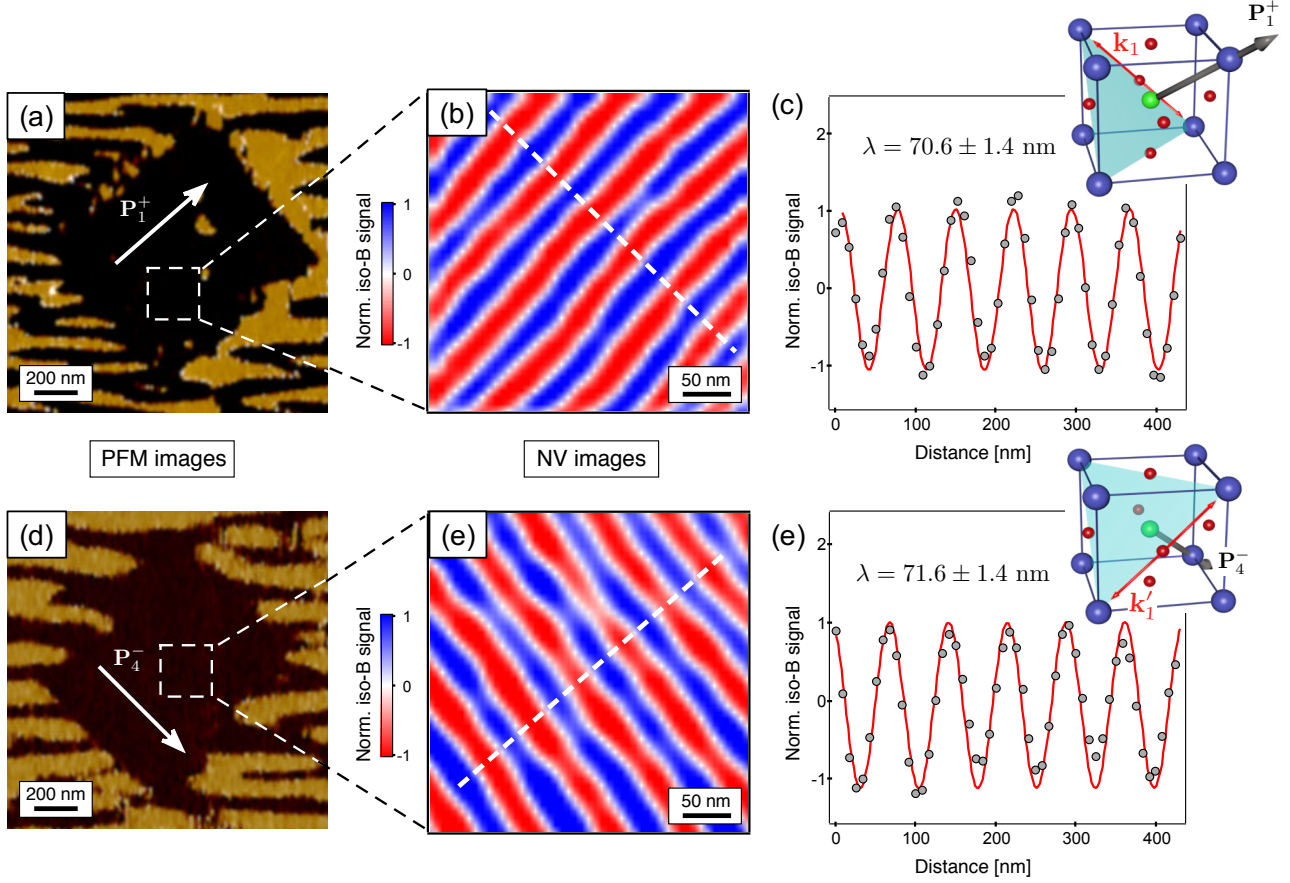


Figure 4.10 – **Electrical control of the spin cycloid.** (a) and (d) In-plane PFM images of ferroelectric micronsized domains with P_1^+ and P_4^- polarizations, respectively. The white arrows indicate the in-plane projection of the ferroelectric polarization vector. (b), (e) Corresponding magnetic field distributions recorded with the scanning-NV magnetometer operating in dual-iso-B imaging mode. (c), (f) Linecuts of the magnetic field distribution along the cycloid propagation direction (white dashed lines in (b) and (e), respectively). The cycloid wavelength λ is extracted through a two-dimensional fit of the experimental data with a sinusoidal function (red solid lines). The standard error (s.e.) of the measurement ($\sim 2\%$) is limited by the calibration of the scanner. The insets show top view sketches of the ferroelectric polarization vector together with the propagation vector of the spin cycloid k_1 (in (c)) and k_1' (in (f)).

is the volume of the pseudo-cubic cell of BFO and

$$\mathbf{m}_{\text{eff}}(\mathbf{r}') = m_{\text{eff}} [\cos(\mathbf{k}_1 \cdot \mathbf{r}') \mathbf{e}_{\mathbf{k}_1} + \sin(\mathbf{k}_1 \cdot \mathbf{r}') \mathbf{e}_{\mathbf{P}}] . \quad (4.6)$$

Here $|\mathbf{k}_1| = 2\pi/\lambda$, \mathbf{r}' denotes the coordinate in the BFO sample, while $\mathbf{e}_{\mathbf{k}_1}$ and $\mathbf{e}_{\mathbf{P}}$ are orthogonal unit vectors oriented along the cycloid propagation direction \mathbf{k}_1 and the ferroelectric polarization \mathbf{P} , respectively (see Figure 4.11(b)). The uncompensated magnetic moment per Fe atom is given by $m_{\text{eff}} = m_{\text{Fe}} \sin(\alpha_c/2)$, where $m_{\text{Fe}} = 4.1 \mu_B$ is the measured magnetic moment of Fe atoms in BFO at room temperature [175] and α_c is the canting angle between antiferromagnetically coupled Fe atoms (Figure 4.5 (c) and (d)). This angle is directly deduced from the measured cycloid wavelength: The tilt per nanometer is $\frac{360}{70nm} = 5.14^\circ$ and consequently the canting angle accounts to 2.04° . The pseudo-cubic unit cell of BFO holds one Fe^{3+} atom with a magnetic moment of $m_{\text{Fe}} = 4.1\mu_B$. Taking into account the canting and the antiferromagnetic alignment of neighboring atoms a net compensated moment of $m_{\text{eff}}^0 = m_{\text{Fe}} \sin(\frac{\alpha_c}{2}) = 0.73\mu_B$ per unit cell is obtained.

The Dzyaloshinskii-Moriya (DM) interaction resulting from the alternate rotation of the FeO_6 octahedra along the [111] direction is another source of non compensation of the magnetic moments in BFO [173, 157]. In the homogeneous G-type state obtained at high magnetic fields (> 20 T), this effect is known to generate a weak and uniform magnetization. In the cycloidal state, this magnetization is converted into a spin density wave (SDW) oscillating in the $[11\bar{2}]$ direction, which leads to a periodic wiggling of the cycloidal plane [177]. As sketched in Figure 4.11(b), the SDW can be simply modeled by an additional uncompensated magnetization vector $\mathbf{M}_{\text{DM}} = \mathbf{m}_{\text{DM}}/V$ such that

$$\mathbf{m}_{\text{DM}}(\mathbf{r}') = m_{\text{DM}} \cos(\mathbf{k}_1 \cdot \mathbf{r}') (\mathbf{e}_{\mathbf{k}_1} \times \mathbf{e}_{\mathbf{P}}) . \quad (4.7)$$

The value of the SDW amplitude m_{DM} remains a subject of debate. Although it is often considered small ($\sim 0.03 \mu_B$) or even negligible [173], polarized neutron scattering studies have revealed a maximum amplitude of $0.09 \mu_B$ in bulk BFO [177], which is slightly larger than the uncompensated moment m_{eff} due to the pure cycloid. The exact analytical calculation of the stray field produced above the BFO sample is given in Annexe C.

We postulate here that the magnetic structure generating the stray field is a wiggling cycloid as described elsewhere [173, 177]. The magnetic potential Φ produced by the magnetization pattern $\mathbf{M} = \mathbf{M}_{\text{DM}} + \mathbf{M}_{\text{eff}}$ is first calculated using Fourier methods for a monolayer of the BFO sample [183]. The resulting magnetic field is given by $\mathbf{B}^m = -\nabla\Phi$ and the total field \mathbf{B} produced at a distance z above the BFO sample surface is finally obtained by summing the contribution from each monolayer. In the laboratory frame (x, y, z) (for details see Annexe Figure C.1), the stray field components are given by

$$\begin{cases} B_x(\mathbf{r}) = -\mathcal{A} e^{-k_1 z} [C_1 m_{\text{eff}} \cos(\mathbf{k}_1 \cdot \mathbf{r}) - C_2 m_{\text{DM}} \sin(\mathbf{k}_1 \cdot \mathbf{r})] \\ B_y(\mathbf{r}) = \mathcal{A} e^{-k_1 z} [C_1 m_{\text{eff}} \cos(\mathbf{k}_1 \cdot \mathbf{r}) - C_2 m_{\text{DM}} \sin(\mathbf{k}_1 \cdot \mathbf{r})] \\ B_z(\mathbf{r}) = \sqrt{2}\mathcal{A} e^{-k_1 z} [C_1 m_{\text{eff}} \sin(\mathbf{k}_1 \cdot \mathbf{r}) + C_2 m_{\text{DM}} \cos(\mathbf{k}_1 \cdot \mathbf{r})] , \end{cases} \quad (4.8)$$

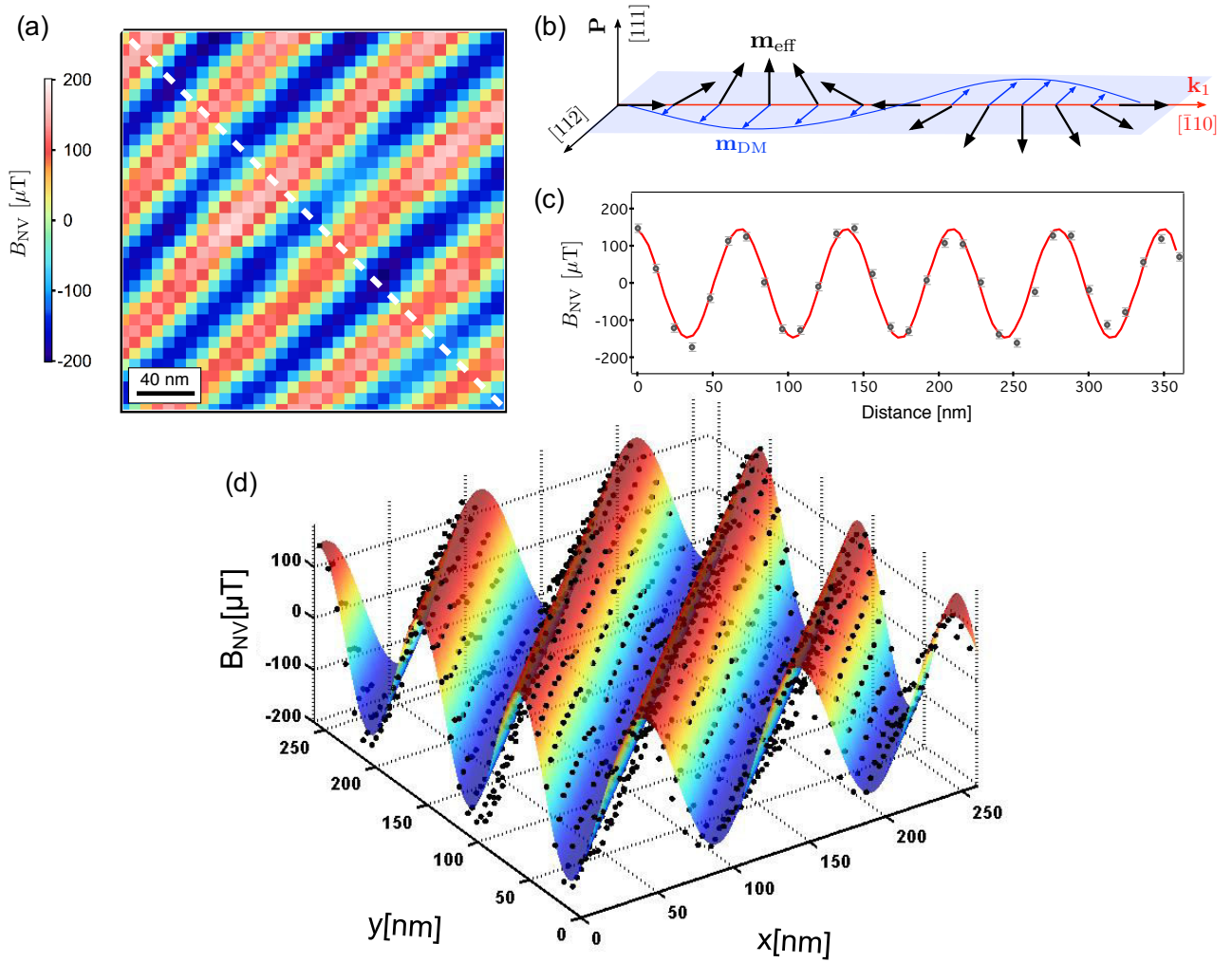


Figure 4.11 – Quantitative analysis of the spin cycloid magnetic texture. (a) Fully quantitative magnetic field distribution B_{NV} recorded above the ferroelectric monodomain shown in Figure 4.3 (a). (b), Schematic representation of the spin density wave (SDW) corresponding to an uncompensated magnetic moment \mathbf{m}_{DM} (blue arrows) oscillating in the $[11\bar{2}]$ direction, *i.e.* perpendicular to both the ferroelectric polarization vector and \mathbf{k}_1 . The uncompensated moment due to the pure cycloid \mathbf{m}_{eff} is shown with black arrows. (c), Linecut of the magnetic field distribution along the cycloid propagation direction (white dashed line in (a)). The black symbols are the experimental data with the standard error (s.e.) while the red solid line is the result of a fit using the analytical formula of the stray field produced by the BFO sample for $d = 49$ nm, $m_{\text{eff}} = 0.07 \mu_B$, $\lambda = 70$ nm, $a = 0.396$ nm, and $t = 32$ nm. The only free parameter is m_{DM} . (d) Equation (4.10) was used to perform a two-dimensional fit of the experimental data, while using m_{DM} as the *only free parameter*.

where $C_1 = 1 + 1/\sqrt{3}$, $C_2 = 2/\sqrt{6}$ for an anticlockwise chirality. (In the case of a clockwise spiral the stray field looks similar with the coefficient $C_1^{(cw)} = 1 - 1/\sqrt{3}$, as showed in the Annexe 4.3.2). The coefficient A reads as

$$\mathcal{A} = \frac{\mu_0}{\sqrt{2}V} \left[\frac{1 - e^{-k_1 t}}{1 - e^{-k_1 a}} \right] \sinh\left(\frac{ak_1}{2}\right). \quad (4.9)$$

Here a is the thickness of a BFO monolayer and t the total thickness of the sample. These magnetic field components are then projected along the independently measured NV defect axis in order to obtain an analytical formula for B_{NV} . This formula was used to perform a two-dimensional fit of the experimental data while using m_{DM} as the only fitting parameter (Figure 4.11 (d)).

$$B_{NV} = B_x \cos \phi \sin \theta + B_y \sin \phi \sin \theta + B_z \cos \theta, \quad (4.10)$$

where (θ, ϕ) are the spherical angles of the NV axis in the laboratory frame. A thorough analysis of uncertainties is given in the annexe, including those related to (i) the fitting procedure itself, (ii) the probe-to-sample distance d , (iii) the cycloid wavelength λ , (iv) the sample thickness t and (v) the NV defect orientation. This analysis

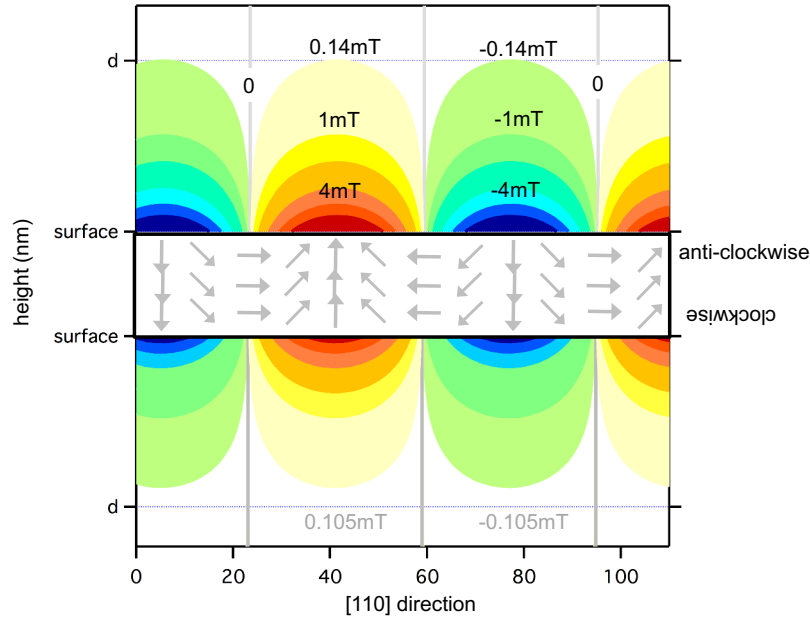


Figure 4.12 – **Effect of the chirality.** The effect of the chirality of the spin spiral in BFO is illustrated in this graph. The lines show contours with the same field value in mT. In the case of the investigated area, where the spiral rotation lies in the (-1-12) plane, the difference in field for the two chiralities (for the same polarization direction) is $\sim 35 \mu\text{T}$: For a clockwise spiral with otherwise identical parameters the produced field at the probe to sample distance accounts to $105 \mu\text{T}$. In the case of a spiral rotation in a plane perpendicular to the sample surface and parallel to its propagation direction (as the case for an observation from the [111] direction) the stray field for the clockwise spiral equals to zero (in the absence of a spin density wave).

leads to $m_{\text{DM}} = 0.16 \pm 0.06 \mu_{\text{B}}$, where the overall uncertainty of $\sim 40\%$ mainly results from the imperfect knowledge of the probe-to-sample distance. It should be noted that the stray field produced above the BFO sample also depends on the chirality of the spin cycloid [183]. Equation (4.8) is obtained for a spin cycloid with a *counter-clockwise* chirality. A similar analysis performed for a *clockwise* chirality would lead to a larger amplitude of the SDW, $m_{\text{DM}} = 0.21 \pm 0.08 \mu_{\text{B}}$ (see Annexe C). Figure 4.12 illustrates this for the case of the spin spiral in BFO propagating in direction \mathbf{k}_1 and rotating in the (-1-12) plane, calculated for the same parameters \mathbf{m}_{eff} and \mathbf{m}_{DM} . Since the stray field sensed by the NV at the probe to sample distance is even decreased for the clockwise chirality, in both cases, our study suggests a DM interaction significantly stronger than all reported values in the literature. This result could be explained by considering that the DM interaction is enhanced by the abrupt broken inversion symmetry occurring at the sample surface and then propagated in the BFO thin film by exchange interaction. This observation opens many perspectives for studying emergent interface-induced magnetic interactions resulting from a local breaking of inversion symmetry.

In summary, the interplay between ferroelectric domain structures and their boundary walls with the coupled antiferromagnetic order was demonstrated, by switching the polarization with electric fields and observing the corresponding changes in the magnetization (e.g spin spiral propagation direction) with the help of the NV magnetometer. This allows unprecedented insight into the magnetoelectric coupling between domains on the nanoscale, in the ferroelectric and antiferromagnetic system. The studied sample was BFO in a single phase, crystallized, 32 nm thin film configuration, in this from highly interesting for applications. Furthermore it was shown that surface-induced chiral interactions of the Dzyaloshinskii-Moriya type might lead to an enhanced amplitude of the spin density wave and are much stronger than previously thought due to symmetry-breaking in thin films.

4.4 Conclusion and outlook

The real space imaging of the magnetic structure in BFO and the demonstration of the magnetoelectro coupling is just the beginning of potential experiments that can be performed with the help of NV magnetometry on this type of material. With its unprecedented nanoscale magnetic field imaging capabilities, NV magnetometry makes its contribution to reveal and understand the multiferroic domain structure. An essential step for the materials potential use in future devices. In the recent literature different properties of BFO are investigated and proposed for future devices.

Domain walls in ferromagnets will play an important role in electronic devices due to their small dimension as discussed in Chapter 1 of this thesis. As we have seen, also in BFO exhibits domain walls (electric and magnetic) which are two dimensional nano objects of multiferroic type. It has been reported that ferroelectric walls in magnetoelectric multiferroics can be ferromagnetic and that the spin rotation across the walls can induce a local polarization. Furthermore, ferroelectric domain walls in BFO are predicted to exhibit room-temperature electronic conductivity [184]. The electronic transport across the domain wall can be modulated by an external

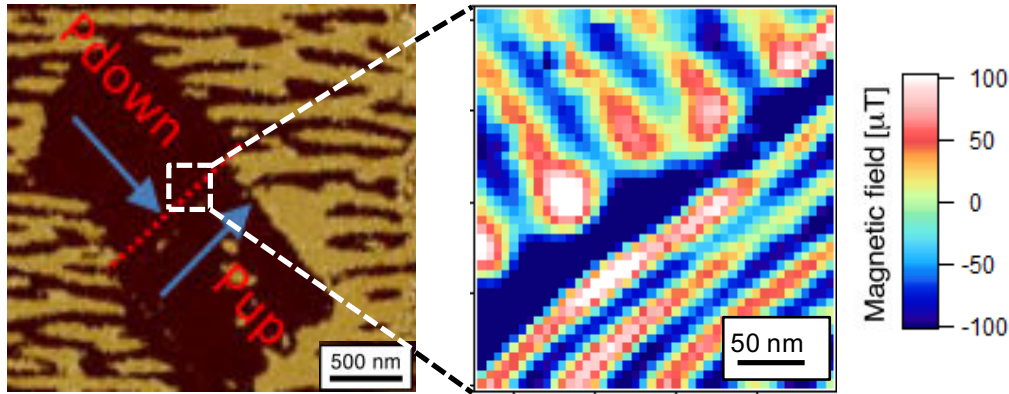


Figure 4.13 – **Imaging of domain walls in BFO.** The PFM image reveals a P_1^+ (Pup) and P_4^- (Pdown) domain and consequently a 109° domain wall. As expected the spiral propagation direction between the two domains changes by 90° . At the very position of the domain wall we observe an enhancement in magnetic field. It has to be noted that the probe to sample distance for this measurement was slightly increased compared to the full B image shown in Figure 4.11 and consequently the observed field amplitude is slightly smaller.

magnetic field resembling an anisotropic magnetoresistance effect [185]. At the same time BFO maintains its switchable electric polarization states. Thus the ferroelectric domain walls can be manipulated via an electric field and with them the magnetization. These multifaceted material functionalities have thinkable application in logic and memory devices: As the wall location can be controlled on the nanoscale, writable multiconfiguration devices that use nanoscale conductive channels are possible as proposed for example in reference [184]. However, the exact properties of domain walls, particularly their magnetic properties are poorly known and can - due to the nanoscale localization and dimensions of the walls - only be investigated with a non-averaging high resolution field sensing method. In order to make this magnetic structure accessible for devices, one of our future perspectives is to investigate magnetic domain walls in BFO with the NV magnetometer. First experiments have already been performed and are shown in Figure 4.13. Here the image at the wall between a P_1^+ and P_4^- polarized domain is shown. The magnetic image reveals the change in the spiral direction in correspondence with the change in the electric domain and an enhanced field at the wall (dominant dark blue and white color at the wall position). Also a slight change in magnetic field strength and spiral wavelength can be surmised between the two sides. It will be part of a future project to characterize and analyze different domain walls in detail with respect to their magnetic properties.

A second interesting aspect, which has been reported previously but is not yet well understood, is the transformation of the magnetic structure of BFO into various antiferromagnetic states. This includes modifying the spin spiral direction, wavelength and ordering patterns. Epitaxial strain for example, can suppress the cycloidal spin order, which is present in bulk samples. Furthermore, the spiral wavelength and direction can be modified with magnetic fields [186] or strain [182, 171]. Understanding these transitions is an important step in order to fully take advantage of the magnetoelectric effects and to uncontrollably tune the magnetic properties in

BFO. Such an analysis is an obvious task to be performed with the NV scanning magnetometer since the spiral wavelength (or its possible absence) can be determined fast and very precisely as already demonstrated in this chapter.

Another facet of the magnetic properties which will be investigated more closely in the future is the effect of the chirality of the spin spiral as briefly mentioned in Section 4.3.2 and Figure 4.12. Recently the switching of both the polarization and the magnetic chirality vector of BFO was investigated [187, 179]. The fact that the magnetic chirality can be switched by the application of an electric field is of fundamental interest but can also broaden the prospect of designing novel devices, as for example to encode information in chiral multiferroics domains as proposed by reference [188]. The magnetic stray field changes with the chirality and can thus be detected with the NV magnetometer as has been shown with the equation for the magnetic field produced by the spin spiral in Section 4.3.2 and in the Annexe C. In the case of the observed sample with [001] growth direction this effects leads to a difference in field in the order of 25%. In samples grown in the [111] direction this effect is even enhanced (in the absence of a SDW the field is zero for one chirality) and will be studied in the future.

In this work on thin film BFO, several important general points on the sample and measurement side of antiferromagnets and multiferroics were addressed. First, bismuth ferrite represents a prototypical and very promising multiferroic for applications, so new insight gained on its antiferromagnetic order will help to focus research efforts and stimulate other studies on similar material systems. Second, antiferromagnetic spintronics is a burgeoning field and potentially useful for low-power nanoelectronics, but at present suffers from the lack of direct experimental probes that have made ferromagnetic spintronics so useful. Third, there are still numerous materials with noncollinear spin order, whose properties are lacking understanding, especially when it comes to local variations in the magnetization structure by boundary effects or defects. These include fore example materials like B20 (Fe-Co)Si alloys [189, 190], Mn-FeGe compounds [191], FeGe thin films [192] and Cu_2OSeO_3 which all have typical magnetization features of several tens of nanometers. Our results pave the way toward the real-space imaging and manipulation of other non-collinear materials that have been discovered in the recent years, and also spin-density wave systems including high-TC copper- and iron-based superconductors (as NV magnetometry also works at cryogenic temperatures).

Even in the absence of canted moments as in BFO, NV magnetometry can image pure antiferromagnetic material. Generally, the oppositely aligned moments of the two spin sublattices in antiferromagnets results in a vanishing magnetic moment in the bulk, and in a vanishing stray field around the material. However, when approaching its surface, a finite displacement between the sub lattices results in the generation of small stray fields. This is for example the case in (0001)-oriented Cr_2O_3 . In this A-type antiferromagnet, the two sub lattices are vertically shifted by one lattice constant and form an uncompensated spin layer at the boundary. Recently performed experiments by our colleagues in Basel show magnetic stray field images arising from this antiferromagnet in close proximinty to the sapmle [193]. These results prove that NV magnetometry can readily be employed to investigate similar antiferromagnetic materials as NiO [194] and MnO [195]. Moreover, just as

ferromagnets, antiferromagnets also split into domains with rotating spins at domain walls. In some instances, this is expected to produce a local finite magnetization, weak but detectable with a non-averaging nano-sized probe, as the NV center.

Summary and Conclusion

In this thesis, we employed a scanning nitrogen vacancy magnetometer to investigate non-collinear magnetic order in thin film materials.

Firstly, we developed a new method to determine the strength of the Dzyaloshinskii-Moriya interaction in thin film magnetic heterostructures. It is based on the measurement of stray fields over domain walls performed with a NV center in a nanodiamond attached to an AFM. We showed that the strength and sign of the Dzyaloshinskii-Moriya interaction is tuned by changing the heavy metal substrate of the material. W|CoFeB and Pt|Co interfaces were determined to provide high DMI strength and are thus important host materials for fast moving chiral domain walls and skyrmions. This study will help in tailoring materials for spintronic applications.

To reveal the nanoscale texture of ferro- and antiferromagnetic thin films, our setup was equipped with an all-diamond scanning probe. This leads to an unprecedented spatial resolution. We implemented a non-invasive, all optical field sensing technique, which enabled to extend the magnetometers sensing capabilities to higher field regimes. With similar characteristics to those of a magnetic force microscope, but with the utilization of a nonmagnetic diamond tip instead, this apparatus was used to investigate soft magnetic materials hosting skyrmions. We have investigated the dependence of skyrmion size distribution and shape on the disorder in the host medium and magnetic history. These effects are essential for improving the accuracy of future simulations on skyrmion dynamics and for developing devices based on skyrmion motion.

Lastly, we have exploited the high quantitative magnetic field sensitivity of our technique to image an antiferromagnetic material on the nanoscale. For the first time, we revealed the 70nm spin spiral structure of bismuth ferrite in real space and demonstrate the manipulation of its magnetization via electric fields. By quantitatively measuring the magnetic stray field of this non-collinear antiferromagnet, we have confirmed the presence of a spin density wave and quantify its amplitude. These measurements will help to develop devices based on the magneto-electric coupling in multiferroic materials.

Our work, along with previous research [92, 196, 193], demonstrates the maturity of the NV based scanning probe technique. Similar setups are now being operated in several research groups around the world. An important step to make the method broadly accessible, and at the same time improve its performance, is the fabrication and commercialization [197]) of all-diamond scanning probes. The spatial resolution is currently limited by the probe to sample distance, which in average accounts to ~ 50 nm. By further improving the NV implantation process and the tip geometry, a spatial resolution inferior to 10 nm is feasible in the near future. Additionally, special tapered scanning probe pillars are now tailored for a highly efficient dipolar mode coupling, which will optimize photon collection efficiency and thus sensitivity. The NV magnetometer has by now evolved as an accessible and attractive tool for research institutes and companies working on magnetism. Especially when a non-perturbative study of nanoscopic magnetic structures with vanishing stray fields is required, scanning-NV magnetometry is unrivaled.

The successful implementation of novel concepts for data storage relies upon a solid microscopic understanding of the underlying materials. In the framework of this thesis, we have gained new insights into the magnetic configuration of technologically relevant thin films. Our technique was used to study magnetic phenomena at domain walls, and topological defects such as skyrmions in thin ferromagnetic layers. While ferromagnets are at the heart of everyday devices such as computers, their large magnetization and resulting energy cost for switching bring into question their suitability for reliable low-power spintronic devices. Future data storage and spintronic technologies are currently evolving towards antiferromagnet-based architectures. Antiferromagnets produce vanishing small magnetic stray fields. Thus, individual storage elements may be packed closer, leading to higher storage density compared to ferromagnets. Antiferromagnetic memories are also robust against external magnetic fields and radiation. However, at the same time, these virtues bring about a major problem: many of the imaging and characterization techniques that work well for ferromagnets are practically inoperative for antiferromagnets. To harness the unique traits of antiferromagnetic materials for next-generation spintronic devices, the nanoscale control and imaging capabilities that are now routine for ferromagnets must be developed for antiferromagnetic systems. As has been shown in this thesis through the example of BFO, NV magnetometry is a unique tool to investigate the antiferromagnetic order. There are still numerous materials with non-collinear and antiferromagnetic spin order, whose properties lack understanding. In particular when it comes to local variations in the magnetization structure by boundary effects and defects, NV magnetometry will help to better understand technologically relevant materials and thus open an exciting avenue towards the development of low-power spintronic and memory devices based on antiferromagnetic materials. Furthermore, many magnetic systems have transition temperatures in the 100 K range. For this purpose, our group has already optimized the NV magnetometry setup for operation down to 4 K. Corresponding measurements lie beyond the framework of this thesis and are part of future work.

Stray field simulations

In this chapter the necessary tools to simulate the NV response to a magnetic field are described. We start with the description of the field arising from the magnetization pattern in different samples. Then, the response of the NV center in terms of ODMR signal and fluorescence signal are determined.

A.1 Calculating the magnetic field from a magnetization pattern

In the case of the field over the edge of a magnetic stripe (Chapter 1) the analytical solution for the magnetic stray field can be calculated and utilized directly (for details see [54]). The same is the case for the spin spiral in BFO (Chapter 4). The calculation of the stray field coming from the spin spiral magnetization pattern is described in detail in Annexe C.

If no easy analytic formula for the magnetic field can be obtained, the magnetic field is calculated numerically from a given magnetization pattern. This magnetization pattern is modeled with Matlab or is generated by the software OOMMF, according to the underlying physics. For the domain walls in Chapter 1 and Chapter 2 the OOMMF code was utilized to create the magnetization pattern. For the simulation of the two skyrmions in Figure 3.7, the magnetization pattern was modeled with Matlab. The stray field is then calculated as described in the following.

A.2 Simulation of the magnetic field from a random magnetization pattern

In general an analytical solution to a certain magnetization pattern is not always easy to find and thus the field has to be calculated numerical. In this case we use the Colomb approach where the description of the

magnetization by magnetic charges makes it possible to write a dipolar field as the gradient of a potential V :

$$\mathbf{H}_{\text{dip}} = -\mathbf{grad}(V) \quad (\text{A.1})$$

analogous to the electrostatic description.

$$V(\mathbf{r}) = \frac{1}{4\pi} \iiint_{\mathcal{V}} \frac{\rho_M(\mathbf{r}')}{|\mathbf{r} - \mathbf{r}'|} d\mathcal{V} + \iint_{\partial\mathcal{V}} \frac{\sigma_M(\mathbf{r}')}{|\mathbf{r} - \mathbf{r}'|} d\mathcal{S} \quad (\text{A.2})$$

The magnetization pattern is divided up into parallelepiped and the field produced by every cell is calculated. Considering that the magnetization is random but uniform $\mathbf{m} = m_x \mathbf{u}_x + m_y \mathbf{u}_y + m_z \mathbf{u}_z$. The problem is further simplified by dividing the contribution of the three components according to the three axis of the unit cell. The problem is not broken down to the one of a uniformly magnetized condensator along x , y and z . By calculating the field from such a cell of size $2a \times 2b \times 2c$ and magnetized along x we get

$$V(x, y, z) = \frac{1}{4\pi} \left(\iint_{[-b,b] \times [-c,c]} \frac{dy' dz'}{\sqrt{(x-a)^2 + (y-y')^2 + (z-z')^2}} - \iint_{[-b,b] \times [-c,c]} \frac{dy' dz'}{\sqrt{(x+a)^2 + (y-y')^2 + (z-z')^2}} \right)$$

and after integration and calculation of the gradient:

$$B_{x,m_x} = \frac{-\mu_0}{4\pi} \sum_{i=\pm 1} \sum_{j=\pm 1} \sum_{k=\pm 1} ijk \operatorname{atan} \left(\frac{(y+jb)(z+kc)}{(x+ia)\sqrt{(x+ia)^2 + (y+jb)^2 + (z+kc)^2}} \right)$$

$$B_{y,m_x} = \frac{-\mu_0}{8\pi} \ln \left[\prod_{i=\pm 1} \prod_{j=\pm 1} \prod_{k=\pm 1} \left(\frac{(z+kc) - \sqrt{(x+ia)^2 + (y+jb)^2 + (z+kc)^2}}{(z+kc) + \sqrt{(x+ia)^2 + (y+jb)^2 + (z+kc)^2}} \right)^{ijk} \right]$$

$$B_{z,m_x} = \frac{-\mu_0}{8\pi} \ln \left[\prod_{i=\pm 1} \prod_{j=\pm 1} \prod_{k=\pm 1} \left(\frac{(y+jb) - \sqrt{(x+ia)^2 + (y+jb)^2 + (z+kc)^2}}{(y+jb) + \sqrt{(x+ia)^2 + (y+jb)^2 + (z+kc)^2}} \right)^{ijk} \right]$$

The field of the other components \mathbf{B}_{m_y} and \mathbf{B}_{m_z} can be retrieved by permuting the variables $\{a, b, c\}$ and $\{x, y, z\}$ in the equation.

With the analytic formula for the field produced by one cell the total field is obtained by summing the contribution of each cell weighted by its magnetization. This operation shows to be a simple convolution product which allows to efficiently apply the Fourier transform for the numerical calculations.

A.3 The ODMR response of the NV center

Once the total stray field is calculated, the response of the NV center to this field needs to be determined. To this end, the Hamiltonian described in Chapter 1.1.3 is diagonalized numerically.

$$\mathcal{H} = hDS_Z^2 + hE(S_X^2 - S_Y^2) + g\mu_B\mathbf{B} \cdot \mathbf{S}.$$

Like this the ESR frequencies f_+ and f_- of the NV center are retrieved, taking into account the intrinsic NV parameters D and E and the NV angles (θ, ϕ) . The Zeeman shift for each position over the sample is calculated and the entire magnetic field map as seen by the NV is obtained.

A.4 Photoluminescence resonance of the NV center to a static magnetic field

In order to simulate an image recorded in the quenching mode, we have to take a closer look at the photodynamics of a NV center in a magnetic field. The goal is, to calculate the NV fluorescence rate in a given magnetic field produced by a sample [55]).

The experimental observation of fluorescence quenching can be explained by the structure of the NV centers energy levels. The triplet ground state (GS) and excited state (ES) as well as the metastable (MS) state (Figure A.1). The optical transitions take place between the two triplet states as well as non-radiatively over the metastable singlet state. The states $|1^0\rangle, |2^0\rangle, |3^0\rangle, |4^0\rangle, |5^0\rangle, |6^0\rangle$ and $|7^0\rangle$ indicate the eigenstates in zero field. Neglecting E , these eigenstates correspond to the spin projection m_s on the quantization axis of the NV center. $|1^0\rangle, |2^0\rangle$ and $|3^0\rangle$ for the GS and $|4^0\rangle, |5^0\rangle, |6^0\rangle$ for the ES; $|7^0\rangle$ for MS. The zero-field transition rate from $|i^0\rangle$ to $|j^0\rangle$ is noted k_{ij^0} . In zero field the system has effectively five levels since $|2^0\rangle, |3^0\rangle$ and $|5^0\rangle, |6^0\rangle$ are degenerated. According to [132] the photodynamics of the NV center at room temperature and at zero field are described by supposing the conservation of m_s for optical transitions between the triplet states. The radiative transition rates are independent of their according m_s ($k_{41}^0 = k_{52}^0 = k_{63}^0 = k_r^0$) and the optical pumping rate β from GS to ES are proportional to the relaxation rate ($k_{ij} = \beta k_{ij}^0$ for $j = 1, 2, 3$ and $i = 4, 5, 6$). The non-radiative transitions between MS and triplet states only depends on the absolute value of m_s ($k_{57}^0 = k_{67}^0$ and $k_{72}^0 = k_{73}^0$).

As described in Chapter 1.3.3, an off-axis (with respect to the NV quantization axis) external field caused a spin mixing of the eigenstates (in GS and ES). The model in a non-zero field is hence the one depicted in Figure A.1 (b) where all transition rates k_{ij} are different and nonzero. In a first step, the eigenstates of the ES $|i\rangle$ are expressed in the base of the eigenstates of the GS $|i^0\rangle$ and the transition rates k as function of the rate in zero field k^0 . The photodynamics of the NV center in an applied magnetic field hence depend on the transition rates in zero field, the optical pumping β and the external magnetic field B . The Hamiltonian

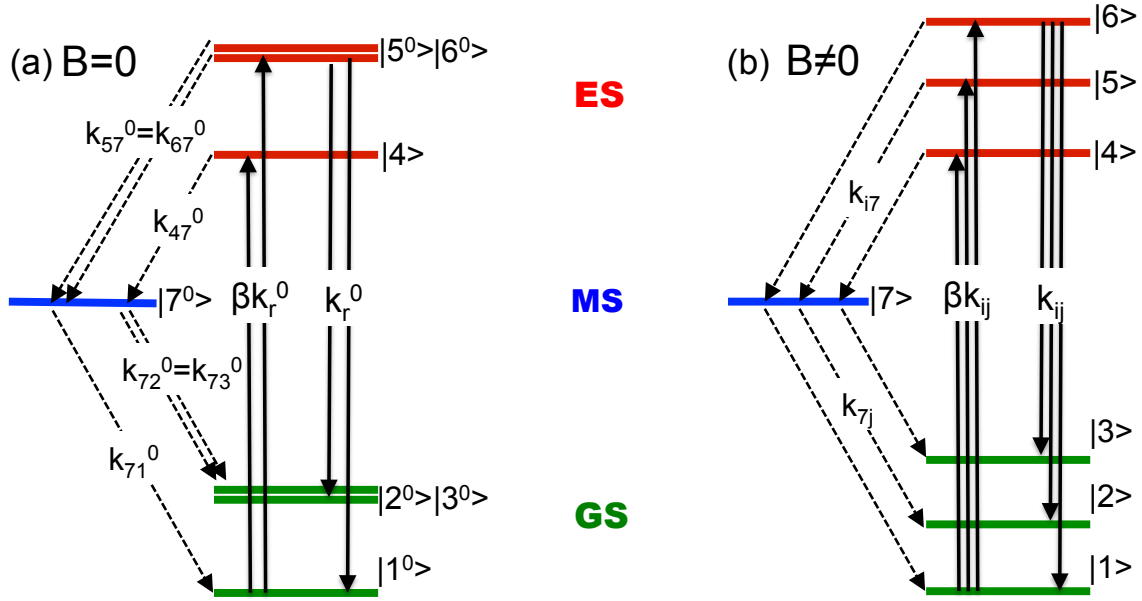


Figure A.1 – **Photodynamics of the NV center.** Energy structure with seven energy levels for modeling the photodynamics of the NV center in the presence of a magnetic field. The groundstate (GS) and the excited state (ES) are triplet states and linked by radiative transition conserving the projection of the spin state m_s . The metastable state (MS) provides a non-radiative path for relaxation (dotted arrows). (a) In zero field all the five parameters $k_r^0, k_{47}^0, k_{57}^0=k_{67}^0, k_{71}^0, k_{72}^0=k_{73}^0$ are used to describe the NV center dynamics. (b) If a magnetic field is applied all the transition rates k_{ij} are likely to be non-zero due to electron spin mixing in both ground and excited state.

to describe the GS and ES is neglecting the term due to the transversal splitting E which is justified for high fields B

$$H = \hbar D_{G,E} S_z^2 + g \mu_B \mathbf{B} \cdot \mathbf{S}, \quad (\text{A.3})$$

where D is the axial zero field splitting (different for GS and ES $D_G = 2.87$ GHz and $D_E = 1.42$ GHz). For a given field B the eigenstates $|i\rangle$ can be expressed by the eigenstates in zero field by

$$|i\rangle = \sum_{j=1}^7 \alpha_{ij}(\mathbf{B}) |j^0\rangle \quad (\text{A.4})$$

where the coefficients $\alpha_{ij}(\mathbf{B})$ are calculated by using the Hamiltonian for GS and ES and supposing that $|7\rangle = |7^0\rangle$. By applying Fermi's golden rule

$$k_{ij}(B) = \Gamma_0 |\langle j | W | i \rangle|^2 = \Gamma_0 \left| \sum_{p=1}^7 \sum_{q=1}^7 \alpha_{ip} \alpha_{jq}^* \langle q^0 | W | p^0 \rangle \right|^2 \quad (\text{A.5})$$

where Γ_0 is a normalization factor including the density of states and W is the perturbation Hamiltonian responsible for the transition. The transition rates in zero field are given by $k_{pq}^0 = \Gamma_0 |\langle q^0 | W | p^0 \rangle|^2$. Finally the

relation between transition rates with and without field reads

$$k_{ij}(\mathbf{B}) = \sum_{p=1}^7 \sum_{q=1}^7 |\alpha_{ip}|^2 |\alpha_{jq}|^2 k_{pq}^0 \quad (\text{A.6})$$

and the steady state fluorescence rate is given by

$$R(\mathbf{B}) = \eta_e \sum_{p=4}^6 \sum_{q=1}^3 k_{ij}(B) n_i \quad (\text{A.7})$$

where η_e is the collection efficiency of the optical detection system, The magnetic field dependent transition rates k_{ij} are given by equation A.4 and the coefficients n_i are obtained by solving the rate equation problem for the steady state:

$$\frac{dn_i}{dt} = \sum_{j=1}^7 (k_{ji}n_j - k_{ij}n_i) \quad (\text{A.8})$$

with $\sum_{j=1}^7 = 1$.

To simulate the optical response of the NV center, the magnetic field of a sample is calculated and the component perpendicular to the NV center axis is determined. The photophysical parameters of the NV defect (Zero-field transition rates transition rates β and η_e) have to be measured in order to compute its optical response as a function of B field. Details for this measurement can be found in [55, 198]. With the input of the intrinsic NV parameters (D , E , Θ , Φ , d , k_{ij}) and Formula A.7 the optical response of the NV center at each point over the sample is determined. It has to be noted, that photophysical parameters of the NV center are affected by the electromagnetic environment to the AFM tip, to the sample, etc. and are therefore prone to changes and errors. This is one reason why this optical imaging mode is hardly quantitative and can only give a very rough estimation of the stray field.

Error calculation

B.1 Probe to sample distance

The distance d between the NV spin sensor and the sample surface was inferred by recording the stray magnetic field produced above the edges of a uniformly magnetized ferromagnetic wire. A typical Zeeman-shift profile recorded while scanning the NV defect across a 500-nm-wide wire of Pt|Co(0.6nm)|AlO_x was shown in Figure 1.15. The probe to sample distance is then extracted by fitting the experimental data following the procedure described in Ref. [54]. Since the uncertainty in the probe to sample distance translates into the biggest error in stray field a thorough error analysis was carried out. The presented values are the ones for the all-diamond scanning-probe which was used for the study on Skyrmions (Chapter 03) and BFO (Chapter 04).

B.1.1 Uncertainty in the probe to sample distance

To determine the error in the probe to sample distance we examine on the one hand the NV center's intrinsic parameters (θ, ϕ, E, D) as well as the geometric parameters of the calibration stripe (width w and height δd). The error in d is attributed to these six independent parameters p_i . Nominal value \bar{p}_i and standard error σ_{p_i} of each of them are shown in Supplementary Table B.1. By varying one parameter while keeping the

parameter p_i	nominal value \bar{p}_i	uncertainty σ_{p_i}
w	500nm	20nm
δd	25nm	2nm
θ	128.2°	1°
ϕ	80.2°	1°
D	2860.4 Mhz	0.2 MHz
E	8.4 MHz	0.2MHz

Table B.1 – Summary of the uncertainty on the value of each parameter for the calibration on Pt/Co/AlO_x for the NV center used in the experiment. The uncertainty in the width w and height δd of the calibration stripe as well as the uncertainty in the knowledge of the intrinsic NV parameters are taken into account.

other parameters' nominal value fixed we estimate the relative uncertainty in the fit outcome linked to each independent parameter. The uncertainty caused by each parameter is:

$$\epsilon_{d/p_i} = \frac{d_{\bar{p}_i + \sigma_{p_i}} - d_{\bar{p}_i - \sigma_{p_i}}}{2d_{\bar{p}_i}}. \quad (\text{B.1})$$

This leads to a total error of $\epsilon_{d_{sys}} = \sqrt{\sum \epsilon_{d/p_i}^2} = 4.5\%$. The statistical error of the measurement is determined by fitting a set of independent linecuts while fixing all parameters to their nominal value \bar{p}_i . The error given by the standard deviation of the fitted distance equals to 1.5 %. The total error is eventually given by:

$$\epsilon_{d_{tot}} = \sqrt{\epsilon_{d_{stat}}^2 + \sum \epsilon_{d_{sys}}^2} = 5\% \quad (\text{B.2})$$

The probe to sample distance is consequently $d = 49 \pm 2.4$ nm.

B.2 Amplitude of the spin density wave in BFO

Here, we analyze the uncertainty on the fit outcome m_{DM} , which results (i) from the fitting procedure and (ii) from uncertainties on the parameters $p_i = \{\lambda, m_{\text{eff}}, t, d, \theta, \phi\}$ that are involved in the expression of B_{NV} . In the following, the parameters p_i are expressed as $p_i = \bar{p}_i + \sigma_{p_i}$ where \bar{p}_i denotes the nominal value of parameter p_i and σ_{p_i} its standard error. These parameters are evaluated as follows :

- The cycloid wavelength λ can be precisely extracted through an independent two-dimensional fit of the experimental data with a simple sinusoidal function. We obtain $\lambda = 70.0 \pm 1.4$ nm for the quantitative magnetic field image shown in Figure 4. The uncertainty ($\sim 2\%$) comes from the calibration of the (x, y) scanner.
- From the measured cycloid wavelength, we infer a characteristic canting angle of $\frac{360^\circ}{\lambda} = 5.14 \pm 0.10^\circ/\text{nm}$, leading to $\alpha_c = 2.04 \pm 0.02^\circ$ between neighboring antiferromagnetically coupled Fe atoms, which are separated by $a = 0.395$ nm. The resulting uncompensated magnetic moment per Fe atom is given by $m_{\text{eff}} = m_{\text{Fe}} \sin(\alpha_c/2) = 0.073 \pm 0.001 \mu_B$.
- The thickness of the BFO sample is extracted through X-ray diffraction (XRD) measurements. The peak-to-peak spacing of Laue fringes indicates a sample thickness $t = 32 \pm 2$ nm.
- The NV defect quantization axis is measured by recording the ESR frequency as a function of the amplitude and orientation of a calibrated magnetic field, leading to spherical angles ($\theta = 128 \pm 1^\circ, \phi = 80 \pm 1^\circ$) in the laboratory frame (x, y, z) .
- The probe-to-sample distance d is inferred through a calibration measurement described in the previous section, leading to $d = 49.0 \pm 2.4$ nm.

We first evaluate the uncertainty of the fitting procedure. To this end, a two-dimensional fit of the experimental data was performed with Equation (4.10) while fixing all the parameters p_i to their nominal values

\bar{p}_i , leading to $m_{\text{DM}} = 0.160 \pm 0.002 \mu_{\text{B}}$. The relative uncertainty linked to the fitting procedure is therefore given by $\epsilon_{\text{fit}} = 1.2\%$. We note that the intrinsic accuracy of the magnetic field measurement is in the range of $\delta B_{\text{NV}} \sim 10 \mu\text{T}$. This leads to an uncertainty of the SDW amplitude $\delta m_{\text{DM}} \sim 0.01 \mu_{\text{B}}$, corresponding to a relative uncertainty $\epsilon_{\text{m}} = 6\%$.

In order to estimate the relative uncertainty ϵ_{p_i} introduced by each parameter p_i , the two-dimensional fit was performed with one parameter p_i fixed at $p_i = \bar{p}_i \pm \sigma_{p_i}$, all the other five parameters remaining fixed at their nominal values. The corresponding fit outcomes are denoted $m_{\text{DM}}(\bar{p}_i + \sigma_{p_i})$ and $m_{\text{DM}}(\bar{p}_i - \sigma_{p_i})$. The relative uncertainty introduced by the errors on parameter p_i is then finally defined as

$$\epsilon_{p_i} = \frac{m_{\text{DM}}(\bar{p}_i + \sigma_{p_i}) - m_{\text{DM}}(\bar{p}_i - \sigma_{p_i})}{2m_{\text{DM}}(\bar{p}_i)}. \quad (\text{B.3})$$

This analysis was performed for each parameter p_i and the resulting uncertainties ϵ_{p_i} are summarized in Extended Data Fig. 6c. The cumulative uncertainty ϵ is finally given by

$$\epsilon = \sqrt{\epsilon_{\text{fit}}^2 + \epsilon_{\text{m}}^2 + \sum_i \epsilon_{p_i}^2}, \quad (\text{B.4})$$

where all errors are assumed to be independent.

We finally obtain $\epsilon = 41\%$ and $m_{\text{DM}} = 0.16 \pm 0.06 \mu_{\text{B}}$. We note that the dominating source of uncertainty is given by the imperfect knowledge of the probe-to-sample distance ($\epsilon_d = 39\%$).

Derrivation of the analytical formula for the magnetic field produced by the spin spiral in BFO

Contents

C.1	General Methodology	117
C.2	Magnetization pattern	118
C.3	Analytical description of the magnetic field	119
C.4	Comparison with numerical simulations	121
C.5	Effect of the cycloid chirality.	121

In Chapter 4.3.2 an analytic fit function is used to extract the strength of the spin density wave m_{DM} . In this Chapter the derivation of the analytic equation for the magnetic field present over a electric mono domain in the thin BFO film is described in detail.

C.1 General Methodology

In order to derive an analytic equation for the magnetic field produced by the cycloidal spin arrangement in BFO is represented by a magnetization M . The magnetic potential Φ produced by a single layer of the sample then calculated using the Fourier transform, and the resulting field \mathbf{B}^m is obtained by applying the relation $\mathbf{B}^{mono} = -\nabla\Phi$. The overall stray field B at a distance z above the sample is determined by adding up the contributions from all monolayers (see Figure C.2). The magnetic field thus obtained is eventually projected along the NV defect quantization axis and gives directly the analytic formula for the field sensed by the NV center B_{NV} . This one is used to fix the experimental data. The geometry of experiment and calculation is schematically depicted in Figure C.1.

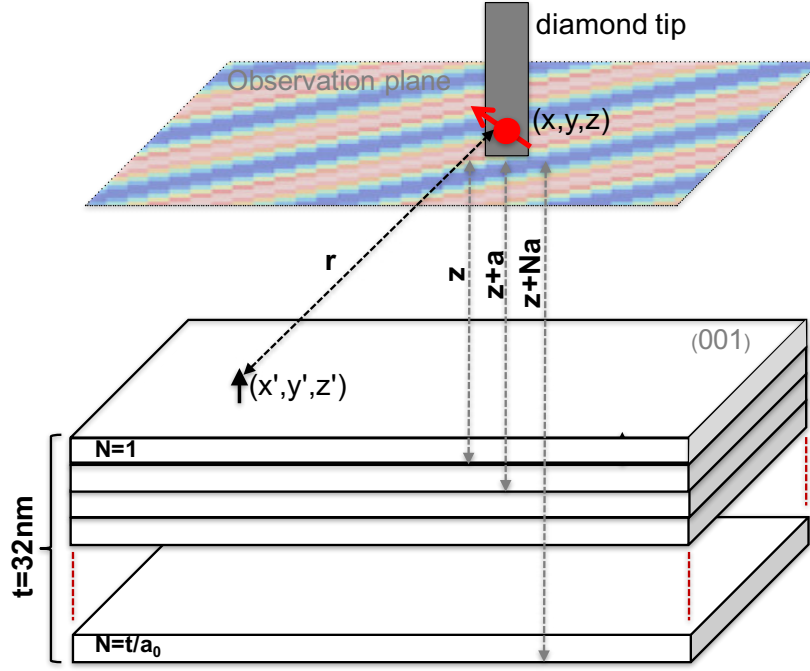


Figure C.1 – **Schematic of the geometry for the stray field calculation.** The 32 nm thick samples is divided up into slices with the thickness of the lattice constant of BFO. First the potential and then the magnetic field from one layer is calculated at a distance z above the sample. After, the contribution from all layers are added up with the distance to the NV center changing with each layer. Eventually we obtain a formula describing the magnetic field from the spiral in a plane above the sample.

C.2 Magnetization pattern

As introduced in Section 4.3.2 the magnetic structure in BFO can be modeled by considering an uncompensated moment \mathbf{m}_{eff} describing a spin cycloid and a spin density wave with the strength \mathbf{m}_{DM} . The total magnetization is following described with by $\mathbf{M} = (\mathbf{m}_{\text{eff}} + \mathbf{m}_{\text{DM}})/V$, with

$$\mathbf{m}_{\text{eff}}(\mathbf{r}') = m_{\text{eff}} [\cos(\mathbf{k}_1 \cdot \mathbf{r}') \mathbf{e}_{\mathbf{k}_1} + \sin(\mathbf{k}_1 \cdot \mathbf{r}') \mathbf{e}_{\mathbf{P}}] \quad (\text{C.1})$$

$$\mathbf{m}_{\text{DM}}(\mathbf{r}') = m_{\text{DM}} \cos(\mathbf{k}_1 \cdot \mathbf{r}') (\mathbf{e}_{\mathbf{k}_1} \times \mathbf{e}_{\mathbf{P}}) \quad (\text{C.2})$$

Here $\|\mathbf{k}_1\| = k_1 = 2\pi/\lambda$ and V is the volume of the unit cell a . As written, the equation describes the spin rotation in the 'spiral frame' with the orthogonal unit vectors $\mathbf{e}_{\mathbf{k}_1}$ and $\mathbf{e}_{\mathbf{P}}$ oriented along the cycloid propagation direction \mathbf{k}_1 and the ferroelectric polarization \mathbf{P} , respectively as represented in Figure C.1. A rotation matrix is used to translate this magnetization into the laboratory frame of reference (x, y, z) , in which the NV quantization axis is defined.

C.3 Analytical description of the magnetic field

We start by calculating the magnetic potential $\Phi(x, y, z)$ produced by a monolayer of the BFO film with a thickness of one unit cell $a = 0.396nm$. The magnetic potential is given by

$$\Phi(x, y, z) = \iiint_{x', y' = -\infty}^{x', y' = +\infty} \int_{z' = -a/2}^{z' = +a/2} -\frac{\mu_0}{4\pi} \mathbf{M}(x', y') \cdot \nabla \left(\frac{1}{\sqrt{(x-x')^2 + (y-y')^2 + (z-z')^2}} \right) dx' dy' dz' \quad (C.3)$$

Equation C.3 includes a two dimensional convolution defined as:

$$f(x, y) * g(x, y) = \iint_{x', y' = -\infty}^{x', y' = +\infty} f(x', y') g(x-x', y-y') dx' dy'$$

and can therefore be rewritten as:

$$\Phi(x, y, z) = -\frac{\mu_0}{4\pi} \int_{z' = -a/2}^{z' = +a/2} \left[(M_x * \frac{\partial}{\partial x} \frac{1}{r_0}) + (M_y * \frac{\partial}{\partial y} \frac{1}{r_0}) + (M_z * \frac{\partial}{\partial z} \frac{1}{r_0}) \right] dz' \quad (C.4)$$

where

$$\frac{1}{r_0} = \frac{1}{\sqrt{x^2 + y^2 + (z-z')^2}}$$

Taking the Fourier transform of Equation C.4 and using the convolution theorem $\mathcal{F}[f * g] = \mathcal{F}[f]\mathcal{F}[g]$, we obtain

$$\mathcal{F}(\Phi) = -\frac{\mu_0}{4\pi} \int_{z' = -a/2}^{z' = +a/2} \left[\mathcal{F}(M_x) \mathcal{F}\left(\frac{\partial}{\partial x} \frac{1}{r_0}\right) + \mathcal{F}(M_y) \mathcal{F}\left(\frac{\partial}{\partial y} \frac{1}{r_0}\right) + \mathcal{F}(M_z) \mathcal{F}\left(\frac{\partial}{\partial z} \frac{1}{r_0}\right) \right] dz' \quad (C.5)$$

Here M_x, M_y, M_z are the components of the magnetization and consist of sine and cosine terms as shown in equation C.6 and C.7 whose Fourier transform is given by the Dirac δ functions.

$$\mathcal{F}(\cos(\mathbf{k}_1 \mathbf{r})) = \frac{\delta(\mathbf{k} - \mathbf{k}_1) + \delta(\mathbf{k} + \mathbf{k}_1)}{2}, \quad \mathcal{F}(\sin(\mathbf{k}_1 \mathbf{r})) = \frac{\delta(\mathbf{k} - \mathbf{k}_1) - \delta(\mathbf{k} + \mathbf{k}_1)}{2i} \quad (C.6)$$

$$\mathcal{F}\left(\frac{\partial}{\partial x} \frac{1}{r}\right) = i 2\pi k_x \frac{e^{-|\mathbf{k}|(z-z')}}{|\mathbf{k}|}, \quad \mathcal{F}\left(\frac{\partial}{\partial y} \frac{1}{r}\right) = i 2\pi k_y \frac{e^{-|\mathbf{k}|(z-z')}}{|\mathbf{k}|}, \quad \mathcal{F}\left(\frac{\partial}{\partial z} \frac{1}{r}\right) = -2\pi |\mathbf{k}| \frac{e^{-|\mathbf{k}|(z-z')}}{|\mathbf{k}|} \quad (C.7)$$

The Fourier transform of the $\frac{1}{r}$ term is obtained by the procedure for example described in Reference [199]. The magnetic potential produced by a monolayer of the sample is then determined through an inverse Fourier transform, leading to

$$\Phi(x, y, z) = \frac{\mu_0 \sinh(a\pi/\lambda)}{V k_1} e^{-k_1 z} \left\{ C_1 m_{\text{eff}} \sin(\mathbf{k}_1 \cdot \mathbf{r}) + C_2 m_{\text{DM}} \cos(\mathbf{k}_1 \cdot \mathbf{r}) \right\} \quad (C.8)$$

where $C_1 = (1 + \frac{2}{\sqrt{12}})$ and $C_2 = \frac{2}{\sqrt{6}}$. The magnetic field \mathbf{B}^m produced at a distance z above a monolayer is then calculated using the relation $\mathbf{B}^m = -\nabla\Phi$. The resulting stray field components read as:

$$\begin{aligned} B_x^{mono} &= -\frac{\mu_0 \sinh(ak_1/2)}{\sqrt{2}V} e^{-|k_1|z} \left\{ C_1 m_{\text{eff}} \cos(\mathbf{k}_1 \cdot \mathbf{r}) - C_2 m_{\text{DM}} \sin(\mathbf{k}_1 \cdot \mathbf{r}) \right\} \\ B_y^{mono} &= +\frac{\mu_0 \sinh(ak_1/2)}{\sqrt{2}V} e^{-|k_1|z} \left\{ C_1 m_{\text{eff}} \cos(\mathbf{k}_1 \cdot \mathbf{r}) - C_2 m_{\text{DM}} \sin(\mathbf{k}_1 \cdot \mathbf{r}) \right\} \\ B_z^{mono} &= +\frac{\mu_0 \sinh(ak_1/2)}{V} e^{-|k_1|z} \left\{ C_1 m_{\text{eff}} \sin(\mathbf{k}_1 \cdot \mathbf{r}) + C_2 m_{\text{DM}} \cos(\mathbf{k}_1 \cdot \mathbf{r}) \right\} \end{aligned} \quad (\text{C.9})$$

The total magnetic field from the sample is obtained by summing the contribution of each monolayer:

$$\begin{aligned} B_x^{total} &= \sum_{j=0}^{N-1} -\frac{\mu_0 \sinh(ak_1/2)}{\sqrt{2}V} e^{-k_1(z+ja)} \left\{ C_1 m_{\text{eff}} \cos(\mathbf{k}_1 \cdot \mathbf{r}) - C_2 m_{\text{DM}} \sin(\mathbf{k}_1 \cdot \mathbf{r}) \right\} \\ B_y^{total} &= \sum_{j=0}^{N-1} +\frac{\mu_0 \sinh(ak_1/2)}{\sqrt{2}V} e^{-k_1(z+ja)} \left\{ C_1 m_{\text{eff}} \cos(\mathbf{k}_1 \cdot \mathbf{r}) - C_2 m_{\text{DM}} \sin(\mathbf{k}_1 \cdot \mathbf{r}) \right\} \\ B_z^{total} &= \sum_{j=0}^{N-1} +\frac{\mu_0 \sinh(ak_1/2)}{V} e^{-k_1(z+ja)} \left\{ C_1 m_{\text{eff}} \sin(\mathbf{k}_1 \cdot \mathbf{r}) + C_2 m_{\text{DM}} \cos(\mathbf{k}_1 \cdot \mathbf{r}) \right\} \end{aligned} \quad (\text{C.10})$$

where N is the number of atomic layers of the BFO sample. The above equation can be further simplified to:

$$\begin{aligned} B_x^{total} &= -A e^{-k_1 z} \left\{ C_1 m_{\text{eff}} \cos(\mathbf{k}_1 \cdot \mathbf{r}) - C_2 m_{\text{DM}} \sin(\mathbf{k}_1 \cdot \mathbf{r}) \right\} \\ B_y^{total} &= +A e^{-k_1 z} \left\{ C_1 m_{\text{eff}} \cos(\mathbf{k}_1 \cdot \mathbf{r}) - C_2 m_{\text{DM}} \sin(\mathbf{k}_1 \cdot \mathbf{r}) \right\} \\ B_z^{total} &= +\sqrt{2}A e^{-k_1 z} \left\{ C_1 m_{\text{eff}} \sin(\mathbf{k}_1 \cdot \mathbf{r}) + C_2 m_{\text{DM}} \cos(\mathbf{k}_1 \cdot \mathbf{r}) \right\} \end{aligned} \quad (\text{C.11})$$

where

$$A = \frac{\mu_0}{\sqrt{2}V} \left[\frac{1 - e^{-k_1 t}}{1 - e^{-k_1 a}} \right] \sinh\left(\frac{ak_1}{2}\right). \quad (\text{C.12})$$

Here $t = Na$ is the total thickness of the BFO sample.

This magnetic field distribution is finally projected along the NV defect axis in order to obtain an analytical formula for B_{NV} , which is given

$$B_{\text{NV}} = B_x \cos \phi \sin \theta + B_y \sin \phi \sin \theta + B_z \cos \theta, \quad (\text{C.13})$$

where (θ, ϕ) are the spherical angles of the NV axis in the laboratory frame. Equation (C.13) was used to perform a two-dimensional fit of the experimental data, while using m_{DM} as the *only free parameter*. The quality of the fit is illustrated in the main text in Figure 4.11 (d).

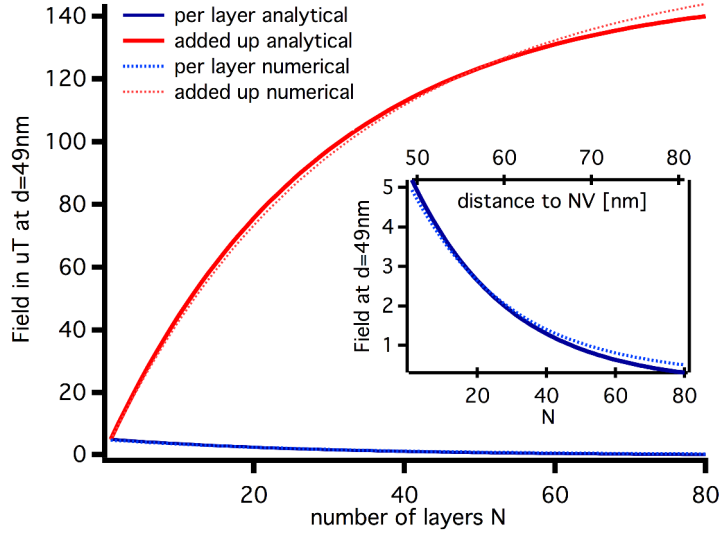


Figure C.2 – **Magnetic field dependence on distance** This graph shows the the magnetic stray field above one point of the sample for the numeric simulation (dashed line) and for the analytic calculation (solid line). The red curve is the field evolution with distance from the sample considering the field emanated from all layers of the sample. The blue graph shows how each layer with thickness a and varying distance Na is contributing to the field. The decay of the field from the spin spiral is exponential and the deeper layers of the samples with a distance to the NV center of around 80 nm merely contribute with a field of a μT

C.4 Comparison with numerical simulations

The only assumption for the derivation of the analytical fitfunction is that the 2D surface for which the field is calculated is supposed to have infinite size. To confirm the validity of this presumption we compare the analytic approach with a numeric simulations of the emitted field from the spin spiral. In this case the magnetization was discretized into uniformly magnetized computation cells with a mesh size $w \ll (d, \lambda)$. The magnetic field distribution produced by each magnetization cell was calculated at a distance d above the sample using magnetostatics theory. The field as seen by the NV center was determined by summing the contributions of all cells and layers before projecting it along the NV quantization axis. The numeric simulation proves to be in very good agreement (deviation of less than 1%) with the analytical calculation as soon as its lateral dimension exceed $2 \times \lambda$ (Figure C.2). We conclude that for a calculation size of $3 \times \lambda$ the obtained values for the field from a finite surface converge the ones for a infinite surface.

C.5 Effect of the cycloid chirality.

In the previous sections, the calculation of the stray field above the BFO sample was performed for a spin cycloid with a counterclockwise (c-cw) chirality. It was emphasized that the stray field depends on the chirality of the spin cycloid. By considering a clockwise (cw) chirality, the uncompensated magnetic moment induced by

the spin cycloid is modified as

$$\mathbf{m}_{\text{eff}}^{(\text{cw})}(\mathbf{r}') = m_{\text{eff}} [\cos(\mathbf{k}_1 \cdot \mathbf{r}') \mathbf{e}_{\mathbf{k}_1} - \sin(\mathbf{k}_1 \cdot \mathbf{r}') \mathbf{e}_{\mathbf{P}}] \quad (\text{C.14})$$

On the other hand, the magnetization distribution resulting from the SDW is independent of the chirality. The resulting magnetic field distribution is then given by

$$\begin{cases} B_x = -\mathcal{A} e^{-k_1 z} \left\{ C_1^{(\text{cw})} m_{\text{eff}} \cos(\mathbf{k}_1 \cdot \mathbf{r}) - C_2 m_{\text{DM}} \sin(\mathbf{k}_1 \cdot \mathbf{r}) \right\} \\ B_y = +\mathcal{A} e^{-k_1 z} \left\{ C_1^{(\text{cw})} m_{\text{eff}} \cos(\mathbf{k}_1 \cdot \mathbf{r}) - C_2 m_{\text{DM}} \sin(\mathbf{k}_1 \cdot \mathbf{r}) \right\} \\ B_z = +\sqrt{2} \mathcal{A} e^{-k_1 z} \left\{ C_1^{(\text{cw})} m_{\text{eff}} \sin(\mathbf{k}_1 \cdot \mathbf{r}) + C_2 m_{\text{DM}} \cos(\mathbf{k}_1 \cdot \mathbf{r}) \right\} \end{cases} \quad (\text{C.15})$$

where $C_1^{(\text{cw})} = 1 - 1/\sqrt{3}$. The only difference between this magnetic field distribution and the one obtained for a counterclockwise chirality is the constant $C_1^{(\text{cw})}$. Since $C_1^{(\text{cw})} < C_1$, the stray magnetic field produced by the pure cycloid is weaker for the clockwise chirality. Fitting the experimental data with such a chirality of the spin cycloid leads to $m_{\text{DM}} = 0.21 \pm 0.08 \mu_{\text{B}}$. The cycloid chirality could be measured in future experiments by analyzing the stray field amplitude on each side of a single ferroelectric domain wall. In this work, postulating either chirality leads to the similar conclusion that the DM interaction is significantly stronger than all reported values in the literature.

Bibliography

- [1] Executive summary, data growth, business opportunities, and the it imperatives. <https://www.emc.com/leadership/digital-universe/2014iview/executive-summary.htm>.
- [2] Gordon Moore. Cramming more components onto integrated circuits. *Electronics*, 38(8), 1965.
- [3] Gordon Moore. Progress in digital integrated electronics. *IEEE*, pages 11–13, 1975.
- [4] Mistry Kaizad. Intel’s 10 nm technology. <https://newsroom.intel.com/press-kits/leading-edge-intel-technology-manufacturing/>, 03 2017.
- [5] Stuart S. P. Parkin, Masamitsu Hayashi, and Luc Thomas. Magnetic domain-wall racetrack memory. *Science*, 320(5873):190–194, 2008.
- [6] C. Moreau-Luchaire, C. Moutafis, N. Reyren, J. Sampaio, C. A. F. Vaz, N. Van Horne, K. Bouzehouane, K. Garcia, C. Deranlot, P. Warnicke, P. Wohlhüter, J.-M. George, M. Weigand, J. Raabe, V. Cros, and A. Fert. Additive interfacial chiral interaction in multilayers for stabilization of small individual skyrmions at room temperature. *Nat. Nanotech.*, 11:444–448, 2016.
- [7] S. Woo, K. Litzius, B. Krüger, M.-Y. Im, L. Caretta, K. Richter, M. Mann, A. Krone, R. Reeve, M. Weigand, P. Agrawal, P. Fischer, M. Kläui, and G. S. D. Beach. Observation of room temperature magnetic skyrmions and their current-driven dynamics in ultrathin co films. *Nat. Mater.*, 15:501–506, 2016.
- [8] Albert Fert, Vincent Cros, and Joao Sampaio. Skyrmions on the track. *Nat. Nano.*, 8(3):152–156, 03 2013.
- [9] Manuel Bibes and Agnes Barthelemy. Multiferroics: Towards a magnetoelectric memory. *Nat Mater*, 7(6):425–426, 06 2008.
- [10] J. M. Taylor, P. Cappellaro, L. Childress, L. Jiang, D. Budker, P. R. Hemmer, A. Yacoby, R. Walsworth, and M. D. Lukin. High-sensitivity diamond magnetometer with nanoscale resolution. *Nature Physics*, 4(10):810–816, 2008.

- [11] G. Balasubramanian, I. Y. Chan, R. Kolesov, M. Al-Hmoud, J. Tisler, C. Shin, C. Kim, A. Wojcik, P. R. Hemmer, A. Krueger, T Hanke, A. Leitenstorfer, R. Bratschitsch, J. Jelezko, and J. Wrachtrup. Nanoscale imaging magnetometry with diamond spins under ambient conditions. *Nature*, 455:648, 2008.
- [12] J. R. Maze, P. L. Stanwix, J. S. Hodges, S. Hong, J. M. Taylor, P. Cappellaro, L. Jiang, M. V. Gurudev Dutt, E. Togan, A. S. Zibrov, A. Yacoby, R. L. Walsworth, and M. D. Lukin. Nanoscale magnetic sensing with an individual electronic spin in diamond. *Nature*, 455(7213):644–647, 2008.
- [13] C. L. Degen. Scanning magnetic field microscope with a diamond single-spin sensor. *Applied Physics Letters*, 92(24):243111, 2008.
- [14] L. Rondin, J. -P Tetienne, P. Spinicelli, C. Dal Savio, K. Karrai, G. Dantelle, A. Thiaville, S. Rohart, J. -F Roch, and V. Jacques. Nanoscale magnetic field mapping with a single spin scanning probe magnetometer. *Applied Physics Letters*, 100(15):153118, 2012.
- [15] L. Rodin. *Réalisation d'un magnétomètre a centre colorée NV du diamant*. PhD thesis, ENS Cachan, 2012.
- [16] J.P. Tetienne. *Un microscope de champ magnétique basé sur le défaut azote-lacune du diamant : réalisation et application a l'étude de couches ferromagnétiques ultraminces*. PhD thesis, ENS Cachan, 2014.
- [17] A. Dréau, M. Lesik, L. Rondin, P. Spinicelli, O. Arcizet, J.-F. Roch, and V. Jacques. Avoiding power broadening in optically detected magnetic resonance of single nv defects for enhanced dc magnetic field sensitivity. *Phys. Rev. B*, 84:195204, 2011.
- [18] J.-P. Tetienne, T. Hingant, J.-V. Kim, L. Herrera Diez, J.-P. Adam, K. Garcia, J.-F. Roch, S. Rohart, A. Thiaville, D. Ravelosona, and V. Jacques. Nanoscale imaging and control of domain-wall hopping with a nitrogen-vacancy center microscope. *Science*, 344(6190):1366–1369, 2014.
- [19] P. Appel, E. Neu, M. Ganzhorn, A. Barfuss, M. Batzer, M. Gratz, M. Tschope, and P. Maletinsky. Fabrication of all diamond scanning probes for nanoscale magnetometry. *AIP*, 87:063703, 2016.
- [20] A. Wachowiak, J. Wiebe, M. Bode, O. Pietzsch, M. Morgenstern, and R. Wiesendanger. Direct observation of internal spin structure of magnetic vortex cores. *Science*, 298(5593):577–580, 2002.
- [21] P. Fischer, M. Im, S. Kasai, K. Yamada, T. Ono, and A. Thiaville. X-ray imaging of vortex cores in confined magnetic structures. *Phys. Rev. B*, 83:212402, 2011.
- [22] D. Vasyukov, Y. Anahory, L. Embon, D. Halbertal, J. Cuppens, L. Neeman, A. Finkler, Y. Segev, Y. Myasoedov, M.L. Rappaport, M.E. Huber, and Zeldov E. A scanning superconducting quantum interference device with single electron spin sensitivity. *Nat. Nano.*, 8:639, 2013.
- [23] J. R. Kirtley. Fundamental studies of superconductors using scanning magnetic imaging. *Reports on Progress in Physics*, 73(12):126501, 2010.

- [24] S.K. Sekatskii and Letokhov V.S. Nanometer-resolution scanning optical microscope with resonance excitation of the fluorescence of the samples from a single-atom excited center. *Jetp Lett.*, 63(319), 1996.
- [25] B.M. Chernobrod and G.P. Berman. Spin microscope based on optically detected magnetic resonance. *Journal of Applied Physics*, 97(1):014903, 2005.
- [26] A.M. Zaitsev. *Optical properties of diamond, a data handbook*. Springer, 2000.
- [27] J. R. Maze, A. Gali, E. Togan, Y. Chu, A. Trifonov, E. Kaxiras, and M. D. Lukin. Properties of nitrogen-vacancy centers in diamond: the group theoretic approach. *New Journal of Physics*, 13(2):025025, 2011.
- [28] M. W. Doherty, N. B. Manson, P. Delaney, and L. C. L. Hollenberg. The negatively charged nitrogen-vacancy centre in diamond: the electronic solution. *New Journal of Physics*, 13(2):025019, 2011.
- [29] N.B. Manson, J.P. Harrison, and M.J. Sellars. Nitrogen-vacancy center in diamond : Model of the electronic structure and associated dynamics. *Phys. Rev. B*, 74:104303, 2006.
- [30] Marcus W. Doherty, Neil B. Manson, Paul Delaney, Fedor Jelezko, Joerg Wrachtrup, and Lloyd C. L. Hollenberg. The nitrogen-vacancy colour centre in diamond. *arXiv:1302.3288*, 2013.
- [31] M. Orrit and J. Bernard. Single pentacene molecules detected by fluorescence excitation in a p-terphenyl crystal. *Phys. Rev. Lett.*, 65:2716–2719, 1990.
- [32] M. Nirmal and et al. Fluorescence intermittency in single cadmium selenide nanocrystals. *Nature*, 383:802–804, 1996.
- [33] W. E. Moerner and M. Orrit. Illuminating single molecules in condensed matter. *Science*, 283(5408):1670–1676, 1999.
- [34] Benoit Mahler, Piernicola Spinicelli, Stephanie Buil, Xavier Quelin, Jean-Pierre Hermier, and Benoit Dubertret. Towards non-blinking colloidal quantum dots. *Nat Mater*, 7(8):659–664, 08 2008.
- [35] C. Kurtsiefer, S. Mayer, P. Zarda, and H. Weinfurter. Stable solid-state source of single photons. *Phys. Rev. Letter*, 85(2):290, 2000.
- [36] Nitin Mohan, Chao-Sheng Chen, Hsiao-Han Hsieh, Yi-Chun Wu, and Huan-Cheng Chang. In vivo imaging and toxicity assessments of fluorescent nanodiamonds in caenorhabditis elegans. *Nano Letters*, 10(9):3692–3699, 2010.
- [37] A. Gruber, A. Dräbenstedt, C. Tietz, L. Fleury, J. Wrachtrup, and C. Von Borczyskowski. Scanning confocal optical microscopy and magnetic resonance on single defect centers. *Science*, 276(5321):2012–2014, 1997.
- [38] Xing-Fei He, Neil B. Manson, and Peter T. H. Fisk. Paramagnetic resonance of photoexcited N-V defects in diamond. II. hyperfine interaction with the ^{14}N nucleus. *Phys. Rev. B*, 47:8816–8822, Apr 1993.

- [39] P. Neumann, R. Kolesov, V. Jacques, J. Beck, J. Tisler, A. Batalov, L. Rogers, N. B. Manson, G. Balasubramanian, F. Jelezko, and J. Wrachtrup. Excited-state spectroscopy of single nv defects in diamond using optically detected magnetic resonance. *New Journal of Physics*, 11(1):013017, 2009.
- [40] V.M Acosta, E. Bauch, M.P. Ledbetter, A. Waxman, L.-S. Bouchard, and D. Budker. Temperature dependence of the nitrogen-vacancy magnetic resonance in diamond. *PRL*, 104:070801, 2010.
- [41] M. L. Goldman, M. W. Doherty, A. Sipahigil, N. Y. Yao, S. D. Bennett, N. B. Manson, A. Kubanek, and M. D. Lukin. State-selective intersystem crossing in nitrogen-vacancy centers. *Physical Review B*, 91(16), Apr 2015.
- [42] L. Rondin, J.-P. Tetienne, T. Hingant, J.-F. Roch, P. Maletinsky, and V. Jacques. Magnetometry with nitrogen-vacancy defects in diamond. *Rep. Prog. Phys.*, 77(5):056503, 2014.
- [43] Y. Dovzhenko, F. Casola, S. Schlotter, T.X. Zhou, F. B'uttner, R.L. Walsworth, G.S.D. Beach, and A. Yacoby. Imaging the spin texture of a skyrmion under ambient conditions using an atomic-sized sensor. *arXiv:1611.00673*, 2017.
- [44] T. Akiyama. Symmetrically arranged quartz tuning fork with soft cantilever for intermittent contact mode atomic force microscopy. *Rev. Sci. Instrum.*, 74:112, 2003.
- [45] L. Rondin, G. Dantelle, A. Slablab, F. Grosshans, F. Treussart, P. Bergonzo, S. Perruchas, T. Gacoin, M. Chaigneau, H.-C. Chang, V. Jacques, and J.-F. Roch. Surface-induced charge state conversion of nitrogen-vacancy defects in nanodiamonds. *Physical Review B*, 82(11):115449, 2010.
- [46] Aurélien Cuche, Aurélien Drezet, Yannick Sonnefraud, Orestis Faklaris, François Treussart, Jean-François Roch, and Serge Huant. Near-field optical microscopy with a nanodiamond-based single-photon tip. *Opt. Express*, 17(22):19969–19980, Oct 2009.
- [47] L. Rondin, J.-P. Tetienne, P. Spinicelli, C. Dal Savio, K. Karrai, G. Dantelle, A. Thiaville, S. Rohart, J.-F. Roch, , and V. Jacques. Nanoscale magnetic field mapping with a single spin scanning probe magnetometer. *Appl. Phys. Lett.*, 100:153118, 2012.
- [48] P. Maletinsky, S. Hong, M. Grinolds, B. Hausmann, M. Lukin, R. Walsworth, M. Loncar, and A. Yacoby. A robust scanning diamond sensor for nanoscale imaging with single nitrogen-vacancy centres. *Nat. Nanotechnol.*, 7:320 – 324, 2012.
- [49] <http://www.srim.org/>.
- [50] A. Dréau, M. Lesik, L. Rondin, P. Spinicelli, O. Arcizet, J.-F. Roch, and V. Jacques. Avoiding power broadening in optically detected magnetic resonance of single NV defects for enhanced dc magnetic field sensitivity. *Physical Review B*, 84(19):195204, 2011.
- [51] S. A. Wolf, I. Rosenberg, R. Rapaport, and N. Bar-Gill. Purcell-enhanced optical spin readout of nitrogen-vacancy centers in diamond. *Phys. Rev. B*, 92:235410, Dec 2015.

- [52] F. A. Inam, T. Gaebel, C. Bradac, L. Stewart, M. J. Withford, J. M. Dawes, J. R. Rabeau, and M. J. Steel. Modification of spontaneous emission from nanodiamond colour centres on a structured surface. *New Journal of Physics*, 13(7):073012, 2011.
- [53] Jennifer T. Choy, Birgit J. M. Hausmann, Thomas M. Babinec, Irfan Bulu, Mughees Khan, Patrick Maletinsky, Amir Yacoby, and Marko Loncar. A diamond nanowire single-photon source. *Nature Nanotech.*, 5:195199, 2009.
- [54] T. Hingant, J.-P. Tetienne, L. J. Martínez, K. Garcia, D. Ravelosona, J.-F. Roch, and V. Jacques. Measuring the magnetic moment density in patterned ultrathin ferromagnets with submicrometer resolution. *Phys. Rev. Applied*, 4:014003, Jul 2015.
- [55] J.-P. Tetienne, L. Rondin, P. Spinicelli, M. Chipaux, T. Debuisschert, J.-F. Roch, and V. Jacques. Magnetic-field-dependent photodynamics of single NV defects in diamond: an application to qualitative all-optical magnetic imaging. *New Journal of Physics*, 14(10):103033, 2012.
- [56] M. Kläui, C. A. F. Vaz, J. A. C. Bland, W. Wernsdorfer, G. Faini, E. Cambril, and L. J. Heyderman. Domain wall motion induced by spin polarized currents in ferromagnetic ring structures. *Appl. Phys. Lett.*, 83:105, 2003.
- [57] I. M. Miron, G. Gaudin, S. Auffret, B. Rodmacq, A. Schuhl, S. Pizzini, J. Vogel, and P. Gambardella. Current-driven spin torque induced by the Rashba effect in a ferromagnetic metal layer. *Nature Mat.*, 9:230–234, 2010.
- [58] K.-S. Ryu, L. Thomas, S.-H. Yang, and S. Parkin. Chiral spin torque at magnetic domain walls. *Nat. Nano.*, 8:527, 2013.
- [59] Satoru Emori, Uwe Bauer, Sung-Min Ahn, Eduardo Martinez, and Geoffrey S D Beach. Current-driven dynamics of chiral ferromagnetic domain walls. *Nat. Mater.*, 12(7):611–616, 2013.
- [60] E. Martinez, S. Emori, and G. S. D. Beach. Current-driven domain wall motion along high perpendicular anisotropy multilayers: The role of the rashba field, the spin hall effect, and the dzyaloshinskii moriya interaction. *Applied Physics Letters*, 103(7), 2013.
- [61] A. Thiaville, S. Rohart, E. Jué, V. Cros, and A. Fert. Dynamics of dzyaloshinskii domain walls in ultrathin magnetic films. *Europhys. Lett.*, 100(5):57002, 2012.
- [62] W. Brown. Theory of the approach to magnetic saturation. *Phys. Rev.*, 44:736–743, 1940.
- [63] M. Yamanouchi, A. Jander, P. Dhagat, S. Ikeda, F. Matsukura, and H. Ohno. Domain structure in cofeb thin films with perpendicular magnetic anisotropy. *IEEE Magn. Lett.*, 2:3000304–3000304, Dec 2011.
- [64] Kai Di, Vanessa Li Zhang, Hock Siah Lim, Ser Choon Ng, Meng Hau Kuok, Xuepeng Qiu, and Hyunsoo Yang. Asymmetric spin-wave dispersion due to dzyaloshinskii-moriya interaction in an ultrathin Pt|CoFeB film. *Phys. Rev. Lett.*, 106:052403, 2015.

- [65] J. A. Osborn. Demagnetization factors for the general ellipsoid. *Phys. Rev.*, 67:11–12, 1945.
- [66] A. Hubert and R. Schäfer. *Magnetic Domains - The Analysis of Magnetic Microstructures*. Springer, Berlin, 1998.
- [67] J.A.C. Bland and B. Heinrich. *Ultrathin magnetic structures I*. springer, 2005.
- [68] L. Neel. Anisotropie magnetique superficielle et surstructures d'orientation. *Le J. Phys. Le Radium*, 15:225–239, 1954.
- [69] S.V. Tarasenko, A. Stankiewicz, V.V. Tarasenko, and J. Ferré. Bloch wall dynamics in ultrathin ferromagnetic films. *Journal of Magnetism and Magnetic Materials*, 189(1):19 – 24, 1998.
- [70] Soong-Geun Je, Duck-Ho Kim, Sang-Cheol Yoo, Byoung-Chul Min, Kyung-Jin Lee, and Sug-Bong Choe. Asymmetric magnetic domain-wall motion by the Dzyaloshinskii-Moriya interaction. *Phys. Rev. B*, 88:214401, Dec 2013.
- [71] F. Bloch. Zur Theorie des Austauschproblems und der Remanenzerscheinung der Ferromagnetika. *Z. Phys.*, 74:295, 1932.
- [72] Claude Chappert, Albert Fert, and Frederic Nguyen Van Dau. The emergence of spin electronics in data storage. *Nat. Mater.*, 6(11):813–823, 2007.
- [73] S. A. Wolf, D. D. Awschalom, R. A. Buhrman, J. M. Daughton, S. von Molnar, M. L. Roukes, A. Y. Chtchelkanova, and D. M. Treger. Spintronics: A spin-based electronics vision for the future. *Science*, 294(5546):1488–1495, 2001.
- [74] M. Heide, G. Bihlmayer, and S. Blügel. Dzyaloshinskii-moriya interaction accounting for the orientation of magnetic domains in ultrathin films: Fe/W (110). *Phys. Rev. B*, 78(14):140403, 2008.
- [75] H.Y. Kwon, K.M. Bu, Y.Z Wu, and C. Won. Effect of anisotropy and dipole interaction on long-range order magnetic structures generated by dzyaloshinskii moriya interaction. *J. Magn. Magn. Mater.*, 324(13):2171 – 2176, 2012.
- [76] I. Dzyaloshinsky. A thermodynamic theory of weak ferromagnetism of antiferromagnetics. *J. Phys. Chem. Solids*, 4:241–255, Feb 1957.
- [77] Tôru Moriya. New mechanism of anisotropic superexchange interaction. *Phys. Rev. Lett.*, 4:228–230, Mar 1960.
- [78] Tôru Moriya. Anisotropic superexchange interaction and weak ferromagnetism. *Phys. Rev.*, 120:91–98, 1960.
- [79] S. Rohart and A. Thiaville. Skyrmion confinement in ultrathin film nanostructures in the presence of dzyaloshinskii-moriya interaction. *Phys. Rev. B*, 88:184422, 2013.

- [80] S. Emori, U. Bauer, S.-M. Ahn, E. Martinez, and G.S.D. Beach. Current-driven dynamics of chiral ferromagnetic domain walls. *Nat. Mater.*, 12(7):611–616, 2013.
- [81] Soong-Geun Je, Duck-Ho Kim, Sang-Cheol Yoo, Byoung-Chul Min, Kyung-Jin Lee, and Sug-Bong Choe. Asymmetric magnetic domain-wall motion by the dzyaloshinskii moriya interaction. *Phys. Rev. B*, 88:214401, Dec 2013.
- [82] A. Hrabec, N. A. Porter, A. Wells, M. J. Benitez, G. Burnell, S. McVitie, D. McGrouther, T. A. Moore, and C. H. Marrows. Measuring and tailoring the dzyaloshinskii moriya interaction in perpendicularly magnetized thin films. *Phys. Rev. B*, 90:020402, 2014.
- [83] Jacob Torrejon, Junyeon Kim, Jaivardhan Sinha, Seiji Mitani, Masamitsu Hayashi, Michihiko Yamanouchi, and Hideo Ohno. Interface control of the magnetic chirality in CoFeB/MgO heterostructures with heavy-metal underlayers. *Nat. Commun.*, 5, 08 2014.
- [84] K. Garello, I. M. Miron, C. O. Avci, F. Freimuth, Y. Mokrousov, S. Blügel, S. Auffret, O. Boulle, G. Gaudin, and P. Gambardella. Symmetry and magnitude of spin orbit torques in ferromagnetic heterostructures. *Nat. Nano.*, 8:587–593, 2013.
- [85] M. Vaňatka, J.-C. Rojas-Sánchez, J. Vogel, M. Bonfim, M. Belmeguenai, Y. Roussigné, A. Stashkevich, A. Thiaville, and S. Pizzini. Velocity asymmetry of dzyaloshinskii domain walls in the creep and flow regimes. *J. Phys.: Condensed Matter*, 27(32):326002, 2015.
- [86] R. Lavrijsen, D. M. F. Hartmann, A. van den Brink, Y. Yin, B. Barcones, R. A. Duine, M. A. Verheijen, H. J. M. Swagten, and B. Koopmans. Asymmetric magnetic bubble expansion under in-plane field in Pt/Co/Pt: Effect of interface engineering. *Phys. Rev. B*, 91:104414, 2015.
- [87] Mohamed Belmeguenai, Jean-Paul Adam, Yves Roussigné, Sylvain Eimer, Thibaut Devolder, Joo-Von Kim, Salim Mourad Cherif, Andrey Stashkevich, and André Thiaville. Interfacial dzyaloshinskii moriya interaction in perpendicularly magnetized Pt/Co/AlO_x ultrathin films measured by brillouin light spectroscopy. *Phys. Rev. B*, 91:180405, 2015.
- [88] R. Soucaille, M. Belmeguenai, J. Torrejon, J.-V. Kim, T. Devolder, Y. Roussigné, S.-M. Chérif, A. A. Stashkevich, M. Hayashi, and J.-P. Adam. Probing the dzyaloshinskii moriya interaction in CoFeB ultrathin films using domain wall creep and brillouin light spectroscopy. *Preprint arXiv:1604.05475*, 2016.
- [89] M. Heide, G. Bihlmayer, and S. Blügel. Dzyaloshinskii moriya interaction accounting for the orientation of magnetic domains in ultrathin films: Fe/W(110). *Phys. Rev. B*, 78(9):140403(R), 2008.
- [90] S. Meckler, N. Mikuszeit, A. Preßler, E. Y. Vedmedenko, O. Pietzsch, and R. Wiesendanger. Real-space observation of a right-rotating inhomogeneous cycloidal spin spiral by spin-polarized scanning tunneling microscopy in a triple axes vector magnet. *Phys. Rev. Lett.*, 103:157201, 2009.

- [91] Gong Chen, Tianping Ma, Alpha T. N'Diaye, Heeyoung Kwon, Changyeon Won, Yizheng Wu, and Andreas K. Schmid. Tailoring the chirality of magnetic domain walls by interface engineering. *Nat. Commun.*, 4, 10 2013.
- [92] J. P. Tetienne, T. Hingant, L. J. Martínez, S. Rohart, A. Thiaville, L. Herrera Diez, K Garcia, J. P. Adam, J. V. Kim, J. F. Roch, I. M. Miron, G. Gaudin, L. Vila, B. Ocker, D. Ravelosona, and V. Jacques. The nature of domain walls in ultrathin ferromagnets revealed by scanning nanomagnetometry. *Nat. Commun.*, 6, 04 2015.
- [93] J.-P. Tetienne, T. Hingant, L. Rondin, S. Rohart, A. Thiaville, E. Jué, G. Gaudin, J.-F. Roch, and V. Jacques. NV-center imaging of bubble domains in a 6-Å film of cobalt with perpendicular magnetization. *J. Appl. Phys.*, 115:17D501, 2014.
- [94] J. Sinha, M. Hayashi, A. J. Kellock, S. Fukami, M. Yamanouchi, H. Sato, S. Ikeda, S. Mitani, S. Yang, S. S. P. Parkin, and H. Ohno. Enhanced interface perpendicular magnetic anisotropy in Ta/CoFeB/MgO using nitrogen doped ta underlayers. *Appl. Phys. Lett.*, 102:242405, 2013.
- [95] C. Burrowes, N. Vernier, J.-P. Adam, L. Herrera Diez, K. Garcia, I. Barisic, G. Agnus, S. Eimer, Joo-Von Kim, T. Devolder, A. Lamperti, R. Mantovan, B. Ockert, E. E Fullerton, and D. Ravelosona. Low depinning fields in Ta-CoFeB-MgO ultrathin films with perpendicular magnetic anisotropy. *Appl. Phys. Lett.*, 103(18), 2013.
- [96] K. Yamada, J.-P. Jamet, Y. Nakatani, A. Mougin, A. Thiaville, T. Ono, and Jacques Ferré. Influence of instabilities on high-field magnetic domain wall velocity in (Co/Ni) nanostrips. *Appl. Phys. Express*, 4(11):113001, 2011.
- [97] O. Boulle, J. Vogel, H. Yang, S. Pizzini, D. de Souza Chaves, A. Locatelli, T. O. Mentis, A. Sala, L. D. Buda-Prejbeanu, O. Klein, M. Belmeguenai, Y. Roussigné, A. Stashkevich, S. M. Chérif, L. Aballe, M. Foerster, M. Chshiev, S. Auffret, I. M. Miron, and G. Gaudin. Room-temperature chiral magnetic skyrmions in ultrathin magnetic nanostructures. *Nat. Nano.*, 11:449–454, 2016.
- [98] Kai Di, Vanessa Li Zhang, Hock Siah Lim, Ser Choon Ng, Meng Hau Kuok, Jiawei Yu, Jungbum Yoon, Xuepeng Qiu, and Hyunsoo Yang. Direct observation of the dzyaloshinskii moriya interaction in a Pt/Co/Ni film. *Phys. Rev. Lett.*, 114:047201, 2015.
- [99] H. T. Nembach, J. M. Shaw, M. Weiler, E. Jué, and T. J. Silva. Linear relation between heisenberg exchange and interfacial dzyaloshinskii moriya interaction in metal films. *Nat. Phys.*, 11:825–829, 2015.
- [100] A. A. Stashkevich, M. Belmeguenai, Y. Roussigné, S. M. Cherif, M. Kostylev, M. Gabor, D. Lacour, C. Tiusan, and M. Hehn. Experimental study of spin-wave dispersion in Py/Pt film structures in the presence of an interface dzyaloshinskii moriya interaction. *Phys. Rev. B*, 91:214409, 2015.

- [101] Kai Litzius, Ivan Lemesh, Benjamin Krüger, Pedram Bassirian, Lucas Caretta, Kornel Richter, Felix Büttner, Koji Sato, Oleg A Tretiakov, Johannes Förster, et al. Skyrmion hall effect revealed by direct time-resolved X-ray microscopy. *Nature Phys.*, 2016.
- [102] A. Hrabec, J. Sampaio, M. Belmeguenai, I. Gross, R. Weil, S.M. Chérif, A. Stashkevich, V. Jacques, A. Thiaville, and S. Rohart. Current-induced skyrmion generation and dynamics in symmetric bilayers. *Nat. Comm.*, 8:15765, 2017.
- [103] Wanjun Jiang, Xichao Zhang, Guoqiang Yu, Wei Zhang, Xiao Wang, M Benjamin Jungfleisch, John E Pearson, Xuemei Cheng, Olle Heinonen, Kang L Wang, et al. Direct observation of the skyrmion hall effect. *Nature Phys.*, 2016.
- [104] S. Mühlbauer, B. Binz, F. Jonietz, C. Pfleiderer, A. Rosch, A. Neubauer, R. Georgii, and P. Böni. Skyrmion lattice in a chiral magnet. *Science*, 323:915–919, 2009.
- [105] Wanjun Jiang, Pramey Upadhyaya, Wei Zhang, Guoqiang Yu, M. Benjamin Jungfleisch, Frank Y. Fradin, John E. Pearson, Yaroslav Tserkovnyak, Kang L. Wang, Olle Heinonen, Suzanne G. E. te Velthuis, and Axel Hoffmann. Blowing magnetic skyrmion bubbles. *Science*, 349(6245):283–286, 2015.
- [106] Anjan Soumyanarayanan, M. Raju, A. L. Gonzalez Oyarce, Anthony K. C. Tan, Mi-Young Im, A. P. Petrovic, Pin Ho, K. H. Khoo, M. Tran, C. K. Gan, F. Ernult, and C. Panagopoulos. Tunable room-temperature magnetic skyrmions in Ir/Fe/Co/Pt multilayers. *Nat Mater*, 16:898–904, 2017.
- [107] A. Fert, N. Reyren, and V. Cros. Magnetic skyrmions: advances in physics and potential applications. *Nature Materials*, 2:17031, 06 2017.
- [108] Christopher H. Marrows. An inside view of magnetic skyrmions. 2015.
- [109] X. Z. Yu, N. Kanazawa, W. Z. Zhang, T. Nagai, T. Hara, K. Kimoto, Y. Matsui, Y. Onose, and Y. Tokura. Skyrmion flow near room temperature in an ultralow current density. *Nat. Commun.*, 3:988, 08 2012.
- [110] J Sampaio, V Cros, S Rohart, A Thiaville, and A Fert. Nucleation, stability and current-induced motion of isolated magnetic skyrmions in nanostructures. *Nat. Nanotech.*, 8(11):839–844, 2013.
- [111] J. Iwasaki, M. Mochizuki, and N. Nagaosa. Current-induced skyrmion dynamics in constricted geometries. *Nature Nano.*, 2013.
- [112] S. Seki and M. Mochizuki. *Skyrmions in Magnetic Materials*. Springer, 1979.
- [113] A.P. Malozemoff and J.C. Slonczewski. *Magnetic domain walls in bubble materials*, volume 81. Academic Press New York, 1979.
- [114] T. Suzuki. A study of magnetization distribution of submicron bubbles in sputtered Ho-Co thin films. *Applied Physics Letters*, 31-34(8):1009–1010, 1983.

- [115] Y. S. Lin, P. J. Grundy, and E. A. Giess. Bubble domains in magnetostatically coupled garnet films. *Applied Physics Letters*, 23(8):485–487, 1973.
- [116] Niklas Romming, André Kubetzka, Christian Hanneken, Kirsten von Bergmann, and Roland Wiesendanger. Field-dependent size and shape of single magnetic skyrmions. *Phys. Rev. Lett.*, 114:177203, May 2015.
- [117] Y. Dovzhenko, F Casola, S. Schlotter, T. X. Zhou, F. Buettner, R.L. Walsworth, G.S.D. Beach, and Yacoby A. Imaging the spin texture of a skyrmion under ambient conditions using an atomic-sized sensor. *arXiv:1611.00673*, 2016.
- [118] William Legrand, Davide Maccariello, Nicolas Reyren, Karin Garcia, Christoforos Moutafis, Constance Moreau-Luchaire, Sophie Collin, Karim Bouzehouane, Vincent Cros, and Albert Fert. Room-temperature current-induced generation and motion of sub-100nm skyrmions. *Nanoletters*, 17, 2017.
- [119] IM Miron, P-J Zermatten, G Gaudin, S Auffret, B Rodmacq, and A Schuhl. Domain wall spin torquemeter. *Physical review letters*, 102(13):137202, 2009.
- [120] Luqiao Liu, O. J. Lee, T. J. Gudmundsen, D. C. Ralph, and R. A. Buhrman. Current-induced switching of perpendicularly magnetized magnetic layers using spin torque from the spin hall effect. *Phys. Rev. Lett.*, 109:096602, Aug 2012.
- [121] Junichi Iwasaki, Masahito Mochizuki, and Naoto Nagaosa. Universal current-velocity relation of skyrmion motion in chiral magnets. *Nature Com.*, 4, 02 2013.
- [122] A. A. Thiele. Applications of the gyrocoupling vector and dissipation dyadic in the dynamics of magnetic domains. *Journal of Applied Physics*, 45(1):377–393, 1974.
- [123] A. Bellec, S. Rohart, M. Labrune, J. Miltat, and A. Thiaville. Domain wall structure in magnetic bilayers with perpendicular anisotropy. *Europhys. Lett.*, 91(1):17009, 2010.
- [124] N. Romming, C. Hanneken, M. Menzel, J. E. Bickel, B. Wolter, K. von Bergmann, A. Kubetzka, and R. Wiesendanger. Writing and deleting single magnetic skyrmions. *Science*, 341:6146, 2013.
- [125] K. Everschor-Sitte, M. Sitte, T. Valet, J. Sinova, and A. Abanov. Skyrmion production on demand by homogeneous DC currents. *arXiv preprint*, page arXiv:1610.08313, 2016.
- [126] Kwang-Su Ryu, Luc Thomas, See-Hun Yang, and Stuart S. P. Parkin. Chiral spin torque at magnetic domain walls. *Nat. Nanotech.*, 8(7):527–533, 2013.
- [127] P.J. Metaxas, J.P. Jamet, A. Mougín, M. Cormier, J. Ferré, V. Baltz, B. Rodmacq, B. Dieny, and R.L. Stamps. Creep and flow regimes of magnetic domain-wall motion in ultrathin Pt/Co/Pt films with perpendicular anisotropy. *Phys. Rev. Lett.*, 99(21):217208, 2007.

- [128] S. Lemerle, J. Ferré, C. Chappert, V. Mathet, T. Giamarchi, and P. Le Doussal. Domain wall creep in an Ising ultrathin magnetic film. *Phys. Rev. Lett.*, 80:849, 1998.
- [129] Joo-Von Kim and Myoung-Woo Yoo. Current-driven skyrmion dynamics in disordered films. *Applied Physics Letters*, 110(13):132404, 2017.
- [130] N. D. Lai, D. Zheng, F. Jelezko, F. Treussart, and J.-F. Roch. Influence of a static magnetic field on the photoluminescence of an ensemble of nitrogen vacancy color centers in a diamond single crystal. *Appl. Phys. Lett.*, 95:133101, 2009.
- [131] R. J. Epstein, F.M. Mendoza, Y.K. Kato, and D.D. Awschalom. Anisotropic interactions of a single spin and dark spin spectroscopy in diamond. *Nat. Phys.*, 1:94, 2005.
- [132] L. Robeldo, H. Bernien, T. Van der Sar, and R. Hanson. Spin dynamics in the optical cycle of single nitrogen vacancy centres in diamond. *New Journal of Physics*, 13:025013, 2011.
- [133] Arne Vansteenkiste, Jonathan Leliaert, Mykola Dvornik, Mathias Helsen, Felipe Garcia-Sanchez, and Bartel Van Waeyenberge. The design and verification of MuMax3. *AIP Advances*, 4:107133, 2014.
- [134] C. Reichhardt, D. Ray, and C. J. Olson Reichhardt. Collective transport properties of driven skyrmions with random disorder. *Phys. Rev. Lett.*, 114:217202, 2015.
- [135] E. Jue, A. Thiaville, S. Pizzini, J. Miltat, J. Sampaio, L. D. Buda-Prejbeanu, S. Rohart, J. Vogel, M. Bonfim, O. Boulle, S. Auffret, I. M. Miron, and G. Gaudin. Domain wall dynamics in ultrathin Pt|Co|AlOx microstrips under large combined magnetic fields. *Phys. Rev. B*, 93:014403, 2016.
- [136] T.H. Pham, J. Vogel, J. Sampaio, M. Vanatka, J.C. Rojas-Sanchez, M. Bonfim, D.S. Chaves, F. Choueikani, P. Ohresser, E. Otero, A. Thiaville, and S. Pizzini. Very large domain wall velocities in Pt|Co|GdOx and Pt|Co|Gd trilayers with dzyaloshinskii-moriya interaction. *Europhys. Lett.*, 113:67001, 2016.
- [137] Fook Hiu Tung, Wei Liang Gan, and Wen Siang Lew. Gateable skyrmion transport via field-induced potential barrier modulation. *Scientific Reports*, 6:21099, 2016.
- [138] C. Hanneken, A. Kubetzka, K. von Bergmann, and R. Wiesendanger. Pinning and movement of individual nanoscale magnetic skyrmions via defects. *New Journal of Physics*, 18(055009), 2016.
- [139] Xichao Zhang, Yan Zhou, and Motohiko Ezawa. Magnetic bilayer-skyrmions without skyrmion hall effect. *Nat. Commun.*, 7:10293, 01 2016.
- [140] Ajaya K. Nayak, Vivek Kumar, Tianping Ma, Peter Werner, Eckhard Pippel, Roshnee Sahoo, Françoise Damay, Ulrich K. Rößler, Claudia Felser, and Stuart S. P. Parkin. Magnetic antiskyrmions above room temperature in tetragonal heusler materials. *Nature*, 548(7669):561–566, 08 2017.

- [141] Olga Meshcheriakova, Stanislav Chadov, A K. Nayak, U K. Rößler, Jürgen Kübler, G André, A A. Tsirlin, J Kiss, Steffen Hausdorf, Adel Kalache, W Schnelle, M Nicklas, and Claudia Felser. Large non-collinearity and spin-reorientation in the novel mn2rhn heusler magnet. *Phys. Rev. Lett.*, 113:087203, 04 2014.
- [142] S. Seki, X. Z. Yu, S. Ishiwata, and Y. Tokura. Observation of skyrmions in a multiferroic material. *Science*, 336(6078):198–201, 2012.
- [143] J. T. Heron, D. G. Schlom, and R. Ramesh. Electric field control of magnetism using BiFeO₃-based heterostructures. *Appl. Phys. Rev.*, 1:021303, 2014.
- [144] J. M. D. Coey. Noncollinear spin structures. *Can. J. Phys.*, 65:1210–1242, 1987.
- [145] U. Hartmann. Magnetic force microscopy. *Annu. Rev. Mater. Sci.*, 29:53–87, 1999.
- [146] A. Locatelli and E. Bauer. Recent advances in chemical and magnetic imaging of surfaces and interfaces by XPEEM. *J. Phys.: Condens. Matter*, 20:093002, 2008.
- [147] R. Wiesendanger. Spin mapping at the nanoscale and atomic scale. *Rev. Mod. Phys.*, 81:1495, 2009.
- [148] T. Jungwirth, X. Marti, P. Wadley, and J. Wunderlich. Antiferromagnetic spintronics. *Nature Nano.*, 11:231–241, 2016.
- [149] S.-W. Cheong and M. Mostovoy. Multiferroics: a magnetic twist for ferroelectricity. *Nature Mater.*, 6:13–20, 2007.
- [150] T. Lottermoser, T. Lonkai, U. Amann, D. Hohlwein, J. Ihringer, and M. Fiebig. Magnetic phase control by an electric field. *Nature*, 430:541–544, 2004.
- [151] J. T. *et al.* Heron. Deterministic switching of ferromagnetism at room temperature using an electric field. *Nature*, 516:370–373, 2014.
- [152] G. Catalan and J. F. Scott. Physics and applications of bismuth ferrite. *Adv. Mater.*, 21:2463–2485, 2009.
- [153] P. Rovillain, R. de Sousa, Y. Gallais, A. Sacuto, M. A. Méasson, D. Colson, A. Forget, M. Bibes, A. Barthélémy, and M. Cazayous. Electric-field control of spin waves at room temperature in multiferroic BiFeO₃. *Nat Mater*, 9(12):975–979, 12 2010.
- [154] Nina Balke, Benjamin Winchester, Wei Ren, Ying Hao Chu, Anna N. Morozovska, Eugene A. Eliseev, Mark Huijben, Rama K. Vasudevan, Petro Maksymovych, Jason Britson, Stephen Jesse, Igor Kornev, Ramamoorthy Ramesh, Laurent Bellaiche, Long Qing Chen, and Sergei V. Kalinin. Enhanced electric conductivity at ferroelectric vortex cores in BiFeO₃. *Nat Phys*, 8(1):81–88, 01 2012.
- [155] G. Catalan, J. Seidel, R. Ramesh, and J. F. Scott. Domain wall nanoelectronics. *Rev. Mod. Phys.*, 84:119, 2012.

- [156] J.B. Neaton, Ederer C., Waghmare U.V., Spaldin N. A., and Rabe K. M. First-principles study of spontaneous polarization in BiFeO_3 . *Phys. Rev. B*, 71(7):014113, 2005.
- [157] Claude Ederer and Nicola Spaldin. Weak ferromagnetism and magnetoelectric coupling in bismuth ferrite. *Phys. Rev. B*, 71:060401, Feb 2005.
- [158] A. F. Popkov, M. D. Davydova, K. A. Zvezdin, S. V. Solov'yov, and A. K. Zvezdin. Origin of the giant linear magnetoelectric effect in perovskitelike multiferroic BiFeO_3 . *Phys. Rev. B*, 93:094435, Mar 2016.
- [159] H. Schmid. Some symmetry aspects of ferroics and single phase multiferroics. *J. Phys.: Condens. Matter*, 20:434201, 2008.
- [160] P. Curie. Sur la symétrie dans les phénomènes physiques, symétrie d'un champ électrique et d'un champ magnétique. *J. Phys. Theor. Appl.*, 3:393–415, 1894.
- [161] I. Dzyaloshinski. On the magneto-electrical effect in antiferromagnets. *JETP*, 37:881–882, 1959.
- [162] D. N. Astrov. Magnetoelectric effect in chrommium oxide. *Soviet physics JETP*, 13:729–733, 1961.
- [163] Manfred Fiebig. Revival of the magnetoelectric effect. *Journal of Physics D: Applied Physics*, 38(8):R123, 2005.
- [164] Vopson M. M, Fetisov Y.K., Caruntu G., and Srinivasan G. Measurement techniques of the magneto-electric coupling in multiferroics. *materials*, 10(963), 2017.
- [165] Nicola A. Spaldin and R. Ramesh. Electric-field control of magnetism in complex oxide thin films. *MRS Bulletin*, 33(11):1047–1050, 2008.
- [166] Junyi Zhai, Zengping Xing, Shuxiang Dong, Jiefang Li, and D. Viehland. Detection of pico-tesla magnetic fields using magneto-electric sensors at room temperature. *Applied Physics Letters*, 88(6):062510, 2006.
- [167] M. I. Bichurin, I. A. Kornev, V. M. Petrov, A. S. Tatarenko, Y. V. Kiliba, and G. Srinivasan. Theory of magnetoelectric effects at microwave frequencies in a piezoelectric magnetostrictive multilayer composite. *PRB*, 64(9):094409, 2001.
- [168] Shuxiang Dong, J. F. Li, and D. Viehland. Voltage gain effect in a ring-type magnetoelectric laminate. *Applied Physics Letters*, 84(21):4188–4190, 2004.
- [169] Shuxiang Dong, Jie-Fang Li, and D. Viehland. Circumferentially magnetized and circumferentially polarized magnetostrictive/piezoelectric laminated rings. *Journal of Applied Physics*, 96(6):3382–3387, 2004.
- [170] J. Wang, J.B. Neaton, H. Zheng, V. Nagarajan, S. B. Ogale, T. Liu, D. Viehland, V. Veithzanathan, D. G. Schlom, U.V. Waghmare, N. A. Spaldin, K.M. Rabe, M. Wuttig, and R. Ramesh. Epitaxial BiFeO_3 multiferroic thin film heterostructures. *Science*, 299:1719–1722, 2003.

- [171] D. Sando, A. Agbelele, D. Rahmedov, J. Liu, P. Rovillain, C. Toulouse, I. C. Infante, A. P. Pyatakov, S. Fusil, E. Jacquet, C. Carrétéro, C. Deranlot, S. Lisenkov, D. Wang, J.-M. Le Breton, M. Cazayous, A. Sacuto, J. Juraszek, A. K. Zvezdin, L. Bellaiche, B. Dkhil, A. Barthélémy, and M. Bibes. Crafting the magnonic and spintronic response of BiFeO₃ films by epitaxial strain. *Nat Mater*, 12(7):641–646, 07 2013.
- [172] Craig J. Fennie. Ferroelectrically induced weak ferromagnetism by design. *Phys. Rev. Lett.*, 100:167203, 2008.
- [173] J.-G Park, M. D. Le, J. Jeong, and S. Lee. Structure and spin dynamics of multiferroic BiFeO₃. *J. Phys. Cond. Mat.*, 26:433202, 2014.
- [174] I. Sosnowska, T. P. Neumaier, E. Steichele, T. Peterlin-Neumaier, and E. Steichele. Spiral magnetic ordering in bismuth ferrite. *J. Phys. C*, 15:4835–4846, 1982.
- [175] D. Lebeugle, D. Colson, A. Forget, M. Viret, A. M. Bataille, and A. Gukasov. Electric-field-induced spin flop in BiFeO₃ single crystals at room temperature. *Phys. Rev. Lett.*, 100:227602, 2008.
- [176] D. Rahmedov, Dawei Wang, Jorge Íñiguez, and L. Bellaiche. Magnetic cycloid of BiFeO₃ from atomistic simulations. *Phys. Rev. Lett.*, 109:037207, Jul 2012.
- [177] M. Ramazanoglu and *et al.* Local weak ferromagnetism in single-crystalline ferroelectric BiFeO₃. *Phys. Rev. Lett.*, 107:207206, 2011.
- [178] H. Bea, M. Bibes, S. Petit, J. Kreisel, and A. Barthelemy. A structural distortion and magnetism of BiFeO₃ epitaxial thin films: A raman spectroscopy and neutron diffraction study. *Phil. Mag. Lett.*, 87(4):165–174, 2007.
- [179] Joel Bertinshaw, Ronald Maran, Sara J. Callori, Vidya Ramesh, Jeffery Cheung, Sergey A. Danilkin, Wai Tung Lee, Songbai Hu, Jan Seidel, Nagarajan Valanoor, and Clemens Ulrich. Direct evidence for the spin cycloid in strained nanoscale bismuth ferrite thin films. 7:12664, 09 2016.
- [180] T. Schneider, A. A. Serga, B. Leven, B. Hillebrands, R. L. Stamps, and M. P. Kostylev. Realization of spin-wave logic gates. *Applied Physics Letters*, 92(2):022505, 2008.
- [181] J. F. Scott. Data storage: Multiferroic memories. *Nat Mater*, 6(4):256–257, 2007.
- [182] A. Agbelele, D. Sando, C. Toulouse, C. Paillard, R. D. Johnson, R. Ruffer, A. F. Popkov, C. Carretero, P. Rovillain, J.-M. Le Breton, B. Dkhil, M. Cazayous, Y. Gallais, M.-A. Measson, A. Sacuto, P. Manuel, A. K. Zvezdin, A. Barthelemy, J. Juraszek, and M. Bibes. Strain and magnetic field induced spin-structure transitions in multiferroic BiFeO₃. *Adv. Mater.*, 29:1602327, 2017.
- [183] N. Mikuszeit, S. Meckler, R. Wiesendanger, and R. Miranda. Magnetostatics and the rotational sense of cycloidal spin spirals. *Phys. Rev. B*, 84:054404, 2011.

- [184] J. Seidel, L. W. Martin, Q. He, Q. Zhan, Y. H. Chu, A. Rother, M. E. Hawkrige, P. Maksymovych, P. Yu, M. Gajek, N. Balke, S. V. Kalinin, S. Gemming, F. Wang, G. Catalan, J. F. Scott, N. A. Spaldin, J. Orenstein, and R. Ramesh. Conduction at domain walls in oxide multiferroics. *Nat Mater*, 8(3):229–234, 03 2009.
- [185] Ji Hye Lee, Ignasi Fina, Xavi Marti, Young Heon Kim, Dietrich Hesse, and Marin Alexe. Spintronic functionality of BiFeO₃ domain walls. *Advanced Materials*, 26(41):7078–7082, 11 2014.
- [186] Shiro Kawachi, Atsushi Miyake, Toshimitsu Ito, Sachith E. Dissanayake, Masaaki Matsuda, William Ratcliff, Zhijun Xu, Yang Zhao, Shin Miyahara, Nobuo Furukawa, and Masashi Tokunaga. Successive field-induced transitions in bifeo₃ around room temperature. *Phys. Rev. Materials*, 1:024408, Jul 2017.
- [187] S. Bhattacharjee, D. Rahmedov, D. Wang, J. Iniguez, and L. Bellaiche. Ultrafast switching of the electric polarization and magnetic chirality in BiFeO₃ by an electric field. *Phys. Rev. Lett.*, 1012:147601, 2014.
- [188] I. Fina, L. Fabrega, X. Marti, F. Sanchez, and J. Fontcuberta. Chiral domains in cycloidal multiferroic thin films: Switching and memory effects. *Phys. Rev. Lett.*, 107:257601, 2011.
- [189] J. Beille, J. Voiron, F. Towfiq, M. Roth, and Z. Y. Zhang. Helimagnetic structure of the Fe x Co 1-x Si alloys. *Journal of Physics F: Metal Physics*, 11(10):2153, 1981.
- [190] K. Shibata, X. Z. Yu, T. Hara, D. Morikawa, N. Kanazawa, K. Kimoto, S. Ishiwata, Y. Matsui, and Y. Tokura. Towards control of the size and helicity of skyrmions in helimagnetic alloys by spin-orbit coupling. *Nat Nano*, 8(10):723–728, 2013.
- [191] S. V. Grigoriev, N. M. Potapova, S.-A. Siegfried, V. A. Dyadkin, E. V. Moskvina, V. Dmitriev, D. Menzel, C. D. Dewhurst, D. Chernyshov, R. A. Sadykov, L. N. Fomicheva, and A. V. Tsvyashchenko. Chiral properties of structure and magnetism in Mn_{1-x}Fe_xGe compounds: When the left and the right are fighting, who wins? *Phys. Rev. Lett.*, 110:207201, May 2013.
- [192] S.L. Zhang, I. Stasinopoulos, T. Lancaster, F. Xiao, A. Bauer, F. Rucker, A. A. Baker, A. I. Figueroa, Z. Salman, F. L. Pratt, S. J. Blundell, T. Prokscha, A. Suter, J. Waizner, M. Garst, D. Grundler, G. van der Laan, C. Pfleiderer, and T. Hesjedal. Room-temperature helimagnetism in FeGe thin films. *Scientific Reports*, 7, May 2017.
- [193] P. Appel, B.J. Shields, T. Kosub, D. Makarov, and Maletinsky P. Real space stray field imaging of antiferromagnets. *to be published*, 2017.
- [194] A. Barbier, C. Mocuta, W. Neubeck, M. Mulazzi, F. Yakhou, K. Chesnel, A. Sollier, C. Vettier, and F. de Bergevin. Surface and bulk spin ordering of antiferromagnetic materials: NiO(111). *Phys. Rev. Lett.*, 93:257208, 2004.
- [195] B. Hermsmeier, J. Osterwalder, D.J. Friedman, B. Sinkovic, T. Tran, and C.S. Fadley. Spin-polarized photoelectron diffraction and valence-band photoemission from MnO(001). *Phys. Rev. B*, 42:11895, 1990.

-
- [196] L. Thiel, D. Rohner, M. Ganzhorn, P. Appel, E. Neu, B. Müller, R. Kleiner, D. Koelle, and P. Maletinsky. Quantitative nanoscale vortex imaging using a cryogenic quantum magnetometer. *Nat Nano*, 11(8):677–681, 08 2016.
- [197] <https://qnami.ch/products/>.
- [198] L. Robledo, H. Bernien, T. van der Sar, and R. Hanson. Spin dynamics in the optical cycle of single nitrogen?vacancy centres in diamond. *New J. Phys.*, 13:025013, 2011.
- [199] Richard J. Blakely. *Potential Theory in Gravity and Magnetic Applications*. Cambridge University Press, Cambridge, 1997.

Titre : Etude de structures de spin non colinéaires dans des matériaux magnétiques ultraminces par magnetometrie NV à balayage

Résumé : Les films magnétiques ultra-minces font partie intégrante des technologies d'aujourd'hui, comme l'illustre leur omniprésence dans de nombreuses applications courantes telles que les disques durs. A cause de leurs dimensions réduites, les propriétés magnétiques spécifiques à ces échelles conduisent à la formation de structures de spin exotiques et de taille nanométrique. Pour explorer ces matériaux en détail, nous utilisons un magnétomètre à balayage développé dans notre laboratoire et qui est basé sur un défaut de spin unique dans le diamant. Ce capteur non-invasif peut mesurer à l'échelle nanométrique à la fois le champ magnétique et la topographie, et fonctionne aux conditions ambiantes. En développant une méthode d'évaluation originale du champ magnétique, nous déterminons la structure interne de parois de domaines ferromagnétiques et quantifions la force de l'interaction Dzyaloshinskii-Moriya dans des hétérostructures à couches minces. Ensuite, nous mettons en évidence le rôle clé du désordre et de l'histoire magnétique sur la stabilisation des skyrmions dans un échantillon de bicouche magnétique. Enfin, nous visualisons dans l'espace réel une spirale de spin de 70nm de période dans le matériau multiferroïque BiFeO_3 et nous manipulons sa direction de propagation avec des champs électriques. Les connaissances tirées de ces études aideront à exploiter au maximum les capacités des matériaux magnétiques à couche ultra-mince et à les mettre en œuvre dans de nouveaux dispositifs de spintronique.

Title : Exploring non-collinear spin structures in thin magnetic films with Nitrogen-Vacancy scanning magnetometry

Abstract : Thin film magnetic materials are an integral part of today's technology and widespread applications like the magnetic hard drive disk mirror their potential. Due to their reduced dimensions, size-specific magnetic properties induce the formation of nanoscale, exotic spin structures. To explore such materials in detail, we utilize a home-built nitrogen vacancy scanning magnetometer, based on a single defect in diamond. This non-perturbative probe combines nanoscale magnetic field- and spatial resolution and works under ambient conditions. We develop a new way to determine the inner structure of magnetic domain walls and quantify the strength of the Dzyaloshinskii-Moriya interaction in thin film heterostructures. We reveal the key role of disorder and magnetic history on the stabilization of skyrmions in a magnetic bilayer sample. Finally, we reveal the 70nm-pitch spin spiral in the multiferroic bismuth ferrite in real space and manipulate its propagation direction with electric fields. The insight gained from these studies will help to exploit the full capacity of thin film magnetic materials for spintronic application.

